


Numéro National de Thèse: 2017LYSEN008

THÈSE DE DOCTORAT DE L'UNIVERSITÉ DE LYON
opérée par
l'École Normale Supérieure de Lyon

École Doctorale N°52
Physique et Astrophysique de Lyon

Discipline: Physique

Soutenue publiquement le 31/03/2017, par :
Mme. Laura STREPPA

Characterizing mechanical properties of living C2C12 myoblasts with single cell indentation experiments: application to Duchenne muscular dystrophy

---

Devant le jury composé de :

Mme.	Françoise ARGOUL	Directrice de Recherche	(Directrice de thèse)
M.	Laurent SCHAEFFER	Professeur des Universités	(Co-encadrant)
M.	Karl ROUGER	Maitre de conférence	(Rapporteur)
M.	Claude VERDIER	Directeur de Recherche	(Rapporteur)
Mme.	Corinne ALBIGES RIZO	Directrice de Recherche	(Examinateur)
M.	Ludovic BELLON	Chargé de Recherche	(Examinateur)
Mme.	Anne DEVIN	Directrice de Recherche	(Examinateur)

Contents

1 Introduction **1**

1.1 Forewords . . . 1
1.2 The animal cell and its cytoskeleton . . . 1
1.3 Cell mechanics and atomic force microscopy (AFM) . . . 4
1.4 Outline of the thesis . . . 7

2 Rheology of myoblasts: from general concepts to AFM experiments **9**

2.1 Introduction to rheology . . . 9
2.2 Fundamental definitions . . . 9
2.2.1 Normal stress and shear stress . . . 9
2.2.2 Deformation . . . 11
2.2.3 Creep and relaxation . . . 11
2.3 One-dimensional viscoelastic models . . . 13
2.3.1 Hookean solids . . . 13
2.3.2 Newtonian liquids . . . 14
2.3.3 Viscoelastic materials . . . 16
2.3.3.a Maxwell model . . . 17
2.3.3.b Kelvin–Voigt model . . . 17
2.3.3.c Standard linear solid (SLS) model . . . 18
2.3.4 Generalization of the viscoelastic models . . . 18
2.4 Three-dimensional mechanical models . . . 20
2.4.1 Hookean solids . . . 20
2.4.2 Newtonian liquids . . . 21
2.4.3 Viscoelastic materials . . . 21
2.5 Three-dimensional indentation modeling with a conical AFM tip . . . 22
2.5.1 Creep and relaxation experiments with a conical indenter . . . 22
2.5.2 Conical indenter moving at constant velocity . . . 25
2.6 Confrontation of the mechanical models with AFM indentation experiments . . . 30
2.6.1 Description of the AFM force-indentation curves (FICs) . . . 30
2.6.2 Experimental validation of constant tip velocity FICs . . . 32
2.6.3 Impact of viscous drag on FICs . . . 32
2.6.4 Parametrization and modeling of AFM experimental FICs . . . 40
2.6.4.a Deciphering the elastoplastic response of myoblasts . . . 41
2.6.4.b Deciphering the viscoelastic response of myotubes . . . 44
2.6.4.c Work integrals and dissipation loss . . . 45
2.6.4.d Discussion . . . 48

3 C2C12 myoblasts: from structural to mechanical properties 51
3.1 Structural properties of C2C12 myoblasts . . . 51
3.1.1 Myoblasts and satellite cells . . . 51
3.1.2 Cell cycle . . . 54
3.1.3 Morphology . . . 56
3.1.4 Cytoskeleton organization . . . 57
3.1.4.a Microtubules . . . 58
3.1.4.b Intermediate filaments . . . 59
3.1.4.c Microfilaments . . . 60
3.1.5 Impact of the culture dish surface properties on C2C12 myoblasts . . . 65
3.1.6 Migration . . . 69
3.1.7 Myoblast differentiation and myotube properties . . . 73
3.2 Mechanical properties of muscle cells: a literature survey . . . 80
3.2.1 Single cell mechanical studies . . . 81
3.2.2 The role of ATP in single cell mechanics and CSK active processes . . . 84
3.2.2.a ATP as a versatile source of energy for living organisms . . . 84
3.2.2.b Impact of ATP depletion on single cell mechanics . . . 85
3.2.3 Enlightening the major role of NMMII through its inhibition by blebbistatin . . . 88
3.2.4 Viscoelasticity of C2C12 myoblasts: Young modulus estimations with AFM 89
3.2.5 Viscoelasticity of myotubes and muscle tissues: AFM studies . . . 91
3.3 Revisiting the interpretation of FICs collected on single living cells: application to myoblasts . . . 92
3.3.1 Deciphering the temporal signature of living cell adaptation to local stress from AFM FICs . . . 93
3.3.1.a Evidencing local rupture events in FICs recorded on myoblasts and myotubes . . . 93
3.3.1.b Refined time-frequency analysis for tracking FIC disruption events 100
3.3.1.c Comparing the global shear relaxation modulus $\langle G \rangle$ and the dissipation loss D_l of FICs without and with disruption events . . . 102
3.3.1.d Reconstruction of histograms from local rupture event characteristic features . . . 105
3.3.1.e From ATP depletion to blebbistatin inhibition of NMMII: highlighting the dynamic cross-linker role of NMMII . . . 112

4 Structural and mechanical characterization of human primary myoblasts 117
4.1 Skeletal muscle and neuromuscular junction organization . . . 117
4.2 Overview of neuromuscular diseases and muscular dystrophies . . . 121
4.3 The Duchenne muscular dystrophy (DMD) . . . 123
4.3.1 DMD etiology and epidemiology . . . 124
4.3.2 Dystrophin location and function in myofibers and myoblasts . . . 125
4.3.3 Comparison of the cross-linking complexes at the extracellular and nuclear membranes . . . 127
4.3.4 DMD pathogenesis, structural alterations and clinical manifestations . . . 128
4.3.5 DMD diagnosis and treatment . . . 131

4.4 Structural and morphological properties of healthy and DMD primary human myoblasts . . . 132
4.4.1 Morphology of HD and DMD myoblasts . . . 133
4.5 Application of the AFM-based method to the characterization of healthy and DMD human myoblast mechanical properties . . . 137
4.5.1 Mechanical properties of healthy primary human myoblasts . . . 139
4.5.2 Mechanical properties of human DMD myoblasts . . . 143
4.5.3 Comparison of the statistics and strength of disruption events from HD and DMD myoblasts . . . 147

5 Materials and methods 153
5.1 Cell culture and differentiation . . . 153
5.1.1 C2C12 myoblast culture . . . 153
5.1.2 C2C12 myoblast differentiation . . . 153
5.1.3 Primary human myoblast culture . . . 154
5.1.4 Cell fixation . . . 154
5.1.5 ATP depletion . . . 154
5.1.6 Blebbistatin treatment . . . 155
5.2 Sample preparation . . . 155
5.2.1 Collagen coating of petri dishes . . . 155
5.2.2 Gold coated micro-slide cleaning and cell deposition . . . 155
5.2.3 SSPM cell chamber preparation . . . 155
5.3 Optical microscopies for cell visualisation . . . 156
5.3.1 Differential interference contrast microscopy . . . 156
5.3.2 Fluorescence confocal microscopy . . . 156
5.3.2.a Fluorescent staining . . . 157
5.3.3 Surface plasmon microscopy . . . 157
5.4 Atomic force microscopy . . . 158
5.4.1 AFM equipment . . . 158
5.4.2 AFM probes and their calibration . . . 158
5.4.3 AFM FIC recording . . . 160
5.4.3.a FICs recorded with different cantilever scan velocities . . . 160
5.4.3.b FICs recorded at fixed cantilever scan velocities . . . 160
5.4.3.c Maps of FICs acquisition . . . 160
5.4.4 FIC analysis . . . 160
5.4.4.a Hydrodynamic drag and baseline drift correction . . . 161
5.4.4.b Wavelet-based decomposition of FICs . . . 161
5.4.4.c Contact point detection . . . 165
5.4.4.d Cantilever spring constant correction . . . 165
5.4.4.e Integral representation of force-indentation curves . . . 165

6 Conclusions and perspectives 167
6.1 Conclusions . . . 167
6.2 Perspectives . . . 169

List of Acronyms

2-DG	2-Deoxy-D-Glucose
AAV	Adeno-Associated Virus
ABP	Actin Binding Protein
ACE	Angiotensin-Converting Enzyme
ACh	ACetylcholine
AChR	Receptor for ACh
ADF	Actin-Depolymerizing Factor
ADP	Adenosine DiPhosphate
AFM	Atomic Force Microscopy
ALS	Amyotrophic Lateral Sclerosis
AMCA	AminoMethylCoumarin Acetate
AMP	Adenosine MonoPhosphate
AMA	AntiMycin A
ANC	ANChors
Arp2/3	Actin-Related Protein-2/3
ATP	Adenosine TriPhosphate
BCE	Before Common Era
BMD	Becker Muscular Dystrophy
BSA	Bovine Serum Albumins
C	Compression
CC	Cell Cortex
CCPD	Collagen Coated Petri Dish
CK	Creatine Kinase
CLL	Chronic Lymphocytic Leukemia
CML	Chronic Myelogenous Leukemia
CRISPR	Clustered Regularly Interspaced Short Palindromic Repeats
CSK	Cytoskeleton
CSMC	Cultured rat aortic Smooth Muscle Cell
CWT	Continuous Wavelet Transform
DAPC	Dystrophin-Associated Protein Complex
DAPI	4′,6-DiAmidino-2-PhenylIndole
DGC	Dystrophin-Glycoprotein Complex
DHPR	DiHydroPyridine Receptor
DIC	Differential Interference Contrast
DM	Differentiation Medium
DMD	Duchenne Muscular Dystrophy
DMEM	Dulbecco's Modified Eagle Medium
DMSO	Dimethyl Sulfoxide
DNA	DeoxyriboNucleic Acid
DOCK1	Dedicator of Cytokinesis protein 1
DPSS	Diode-Pumped Solid State
DWT	Discrete Wavelet Transform
EB	End Binding
ECM	Extra Cellular Matrix
EDB	Exor Digitorum Brevis
EDL	Extensor Digitorum Longus
EDMD	Emery-Dreifuss Muscular Dystrophies
EGF	Epidermal Growth Factor
EGFP	Enhanced Green Fluorescent Protein
ENUC-D	Extra Nuclear Domain
EP	End Plates
ETC	Electron Transport Chain
F	Filopodium
FA	Focal Adhesion
FBS	Fetal Bovine Serum
FIC	Force versus Indentation Curve
FSMC	Freshly isolated rat aortic Smooth Muscle Cell
G0	Gap 0 phase
G1	Gap 1 phase
G2	Gap 2 phase
GM	Growth Medium
GTP	Guanosine TriPhosphate
HIII	third Hinge
hbFGF	human basic Fibroblast Growth Factor
HBMSC	Human Bone Marrow Stromal Cells
HD	Healthy Donor
hiPSC	human induced Pluripotent Stem Cell
HS	Horse Serum
hSkMC	human Skeletal Muscle Cell

HUVEC	Human Umbilical Vein Endothelial Cell
IF	Intermediate Filament
IGF-I	Insulin-like Growth Factor I
iPS	induced Pluripotent Stem cell
L	Lamellipodium
LDH	Lactate DeHydrogenase
LTM	Laser Tracking Microrheology
M	Mitosis phase
MAP4	Microtubule-Associated Protein 4
MD	Muscular Dystrophy
MDCK	Madin-Darby Canine Kidney
MF	MicroFilament
MPC	Muscle Precursor Cells
MSC	Mesenchymal Stem Cell
MRF	Myogenic Regulatory Factors
MS	Mechanical Stretch
MT	MicroTubule
mTOR	mammalian Target Of Rapamycin
MuSK	Muscle Specific tyrosine Kinase
MYOG	MYOGenin
NA	Numerical Aperture
NMD	NeuroMuscular Diseases
NMJ	Neuromuscular Junction
NMM II	Non Muscle Myosin II
NOS	Nitric Oxide Synthases
NPF	Nucleation Promoting Factor
NUC-D	NUClear Domain
OMIM	Online Mendelian Inheritance in Man
OS	Optical Stretch
OXPHOS	OXidative PHOSphorylation
PAK	p21 Activated Kinase
PBS	Phosphate Buffer Saline
PCR	Polymerase Chain Reaction
PFA	ParaFormAldehyde
PIP2	PhosphatidylInositol 4,5-bisPhosphate
PM	Proliferation Medium
PT	Particle Tracking
RBC	Red Blood Cell
RER	Rough Endoplasmic Reticulum
RI	Refractive Index
RNA	RiboNucleic Acid
ROS	Reactive Oxygen Species
RyR	Ryanodine Receptor
S	Synthesis phase
S1P	Sphingosine 1-Phosphate
SAC	Stretch Activated Channels
SC	Satellite Cell
SEM	Scanning Electron Microscope
SF	Stress Fiber
SI	International System of units
SLS	Standard Linear Solid
SMA	Spinal Muscular Atrophy
SNARE	Soluble N-ethylmaleimide-sensitive factor Attachment REceptor
SNL	Sharp Nitride Lever
SPD	Standard Petri Dish
SPR	Surface Plasmon Resonance
SR	Sarcoplasmic Reticulum
SSPM	Scanning Surface Plasmon Microscope
TEM	Transmission Electron Microscopy
TER	Trans-Epithelial Resistance
TIC	Tumor-Initiating Cell
TJ	Tight Junction
TNF	Tumor Necrosis Factor
TPM	TwoPoint Microrheology
UV	UltraViolet
VASP	VAsodilator-Stimulated Phosphoprotein
VIC	Valve Interstitial Cell
WASp	Wiskott-Aldrich Syndrome protein
WT	Wavelet Transform

To all people affected
by Duchenne muscular dystrophy

Chapter 1

Introduction

1.1 Forewords

The seed of this thesis work originates from the interaction of two researchers from the Ecole Normale Supérieure of Lyon, Françoise Argoul from the Laboratory of Physics and Laurent Schaeffer from the Laboratory of Molecular and Cellular Biology. Two main issues were raised as the guiding lines of this thesis projects: (i) Can we develop an original approach for probing locally the mechanics of living muscle progenitors which will take into account their active, non stationary fundamental characteristics? (ii) Will this type of approach allow us to distinguish normal myoblasts from transformed myoblasts (with chemical agents, through differentiation into myotubes, or in pathological situations such as muscular dystrophies)? The originality of this project was to embrace several disciplines and their associated methods: muscle physiology, medical approaches of myopathies, cellular and molecular biology, biochemistry, biophysics, rheology, modeling and mathematical analysis of complex dynamics during cellular indentation experiments. Even if optical microscopies such as differential interference contrast (DIC) microscopy, scanning surface plasmon microscopy (SSPM) and fluorescence confocal microscopy have been used to capture cellular and nuclear morphologies as well as intracellular organization of muscle progenitor cells, we have concentrated our efforts on the experimental methods and theoretical concepts for living cell indentation with sharp nano-indenters to improve our ability to capture in real time the compliance of a living cell to a mechanical stress.

1.2 The animal cell and its cytoskeleton

As the smallest unit of living organisms, the cell was originally discovered by Robert Hooke in 1665 on a slice of cork [Cooper, 2003] and subsequently by Antony van Leeuwenhoek in 1674 from his observations of "animalcules" (*i.e.* micro-organisms) [Porter, 1976]. The cell was recognized as the smallest self-replicative living unit with a complex well-regulated organization and which communicates with the extracellular environment from which it can extract energy and materials necessary for its maintenance and growth [Nelson, 2008]. Later on, the ability of cells to respond and adapt to extracellular chemical stimuli was demonstrated, pointing out the dynamic nature of living cells. The advent of genetics and molecular biology opened new perspectives in understanding how hereditary information contained within the genetic code is used by eukaryotic cells to translate DNA in proteins [Crick, 1958, 1970]. If the development of the polymerase chain reaction (PCR) technique for the *in vitro* synthesis of oligonucleotides by Kary

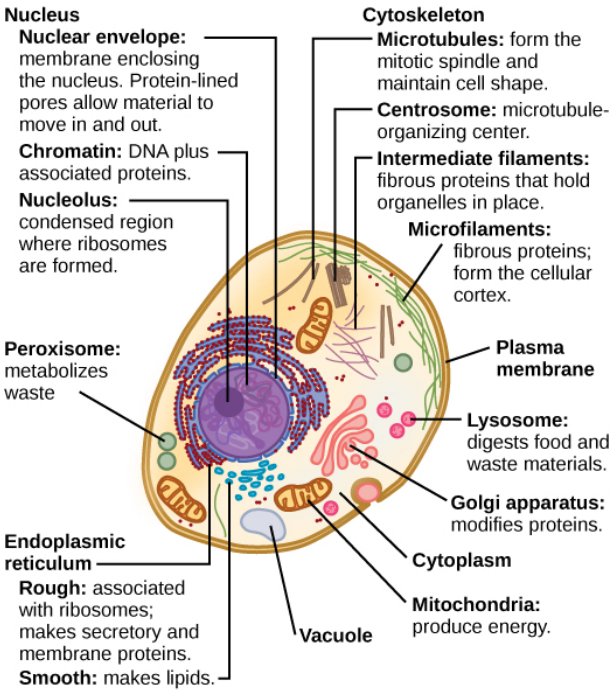

Figure 1.1: **Schematic of an animal cell and its organelles.** Typical cell biology diagram of the cell organization in functional compartments. Adapted from OpenStax College, Eukaryotic Cells. [OpenStax-CNX Web site] 2016.

B. Mullis [Mullis, 1986] marked the beginning of the modern molecular biology and a revolution in this field, the emergence of cell mechanics as a whole domain of research shed a new light on cells as living mechanical machines. Progressively, cell mechanical studies helped defining new biomechanical paradigms: (i) living cells are able to sense mechanical cues, (ii) they can respond to such stimuli, (iii) the cell mechanical properties rely on the dynamical organization of the cell cytoskeleton, (iv) cell mechanics is essential in many critical cell biological processes (*e.g.* morphology, migration, adhesion, differentiation, growth, division, ...) [Crouzier, 2009, 2011; Fourel, 2016], (v) cell mechanics is altered in aging [Phillip, 2015] and in pathological conditions [Kumar & Weaver, 2009], (vi) these alterations can participate in the pathogenesis and in the progression of a disease, and (vii) the mechanical properties of the extracellular matrix can impact the cell function [Jansen, 2015].

The functional compartmentalisation of an animal cell is illustrated in Fig. 1.1. The main structural compartments of an animal cell are: (i) the cell membrane (*i.e.* thin selectively permeable lipid bilayer containing transmembrane receptors, channels, ...), (ii) the cytoplasm (*i.e.* the intracellular gelatinous cytosol and its organelles), (iii) the nucleus (*i.e.* nucleoplasm delimited by the nuclear envelope), and (iv) the cytoskeleton (CSK, *i.e.* dynamical intracellular network of interconnected filaments and regulatory proteins). These structural compartments and their dynamical regulation confer to the cell its mechanical properties. Unlike plant cells, animal cells do not have an elastic wall. Therefore, they require specialized structures to maintain their integrity. These specialized structures, namely the cell membrane and the CSK, are the major actors of the cell mechanics. Originally considered as a structural cell compartment to maintain cell shape and organelle positions, the CSK and its dynamical organization is nowadays recognised to play a central role in the regulation of the cell mechanical proper-

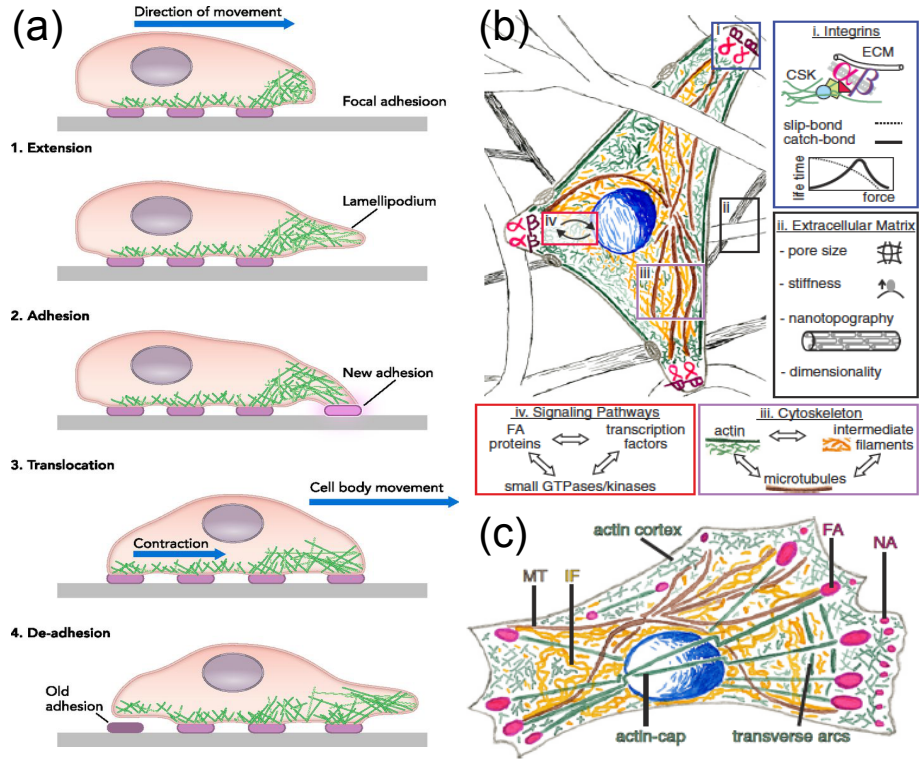

Figure 1.2: **Schematic of an animal cell migration and its interaction with the extracellular matrix.** Typical cell mechanics diagram of the steps of cell migration of an adherent cell (a), a cell mechanosensitive interaction with 3D (b) and 2D (c) extracellular matrix. The subpanels (i-iv) show the main cell components involved in mechanosensing. Actin filaments are drawn in green, intermediate filaments (IFs) in yellow, microtubules (MTs) in brown, focal adhesions (FAs) and nascent adhesions (NAs) in pink, α and β are integrin subunits. Adapted from (a) Physiology [Tschumperlin, 2013] and (b-c) Biochimica et Biophysica Acta (BBA)-Molecular Cell Research [Jansen, 2015].

ties (motility, coupling with the extracellular matrix, mechanosensing, force transmission and mechanotransduction) [Fletcher & Mullins, 2010]. Among all the molecules and cell compartments identified as involved in cell mechanics, actin filaments (*i.e.* microfilaments) are key actors in many cellular processes, such as cellular reshaping, locomotion (Fig. 1.2(a)), adhesion, phagocytosis, ... [Blanchoin, 2014]. In particular, actin dynamics was shown to be the driving force for cell protrusion [Pollard & Borisy, 2003]. Actin filaments also participate in mechanosensing (Fig. 1.2(b)) in cooperation with stretch-activated ion channels and proteins (*e.g.* paxillin, vinculin, integrins, ...) located at specialized transmembrane sites (*i.e.* focal adhesions) [Bershadsky, 2006; Moore, 2010; Pasapera, 2010; Jansen, 2015; Millon-Frémillon, 2008]. Actin filament bundles linked to focal complexes (Fig. 1.2(c)) are known as stress fibers (SFs). Thanks to the non muscle myosin (NMM II) molecular motor and the cross-linker α-actinin, these large bundles of actin filaments generate tension, sustain forces, and respond to external stimuli by remodeling and reinforcing the cell [Burridge & Wittchen, 2013]. Mechanical inputs

can enter the cell machinery, be transmitted to the nucleus where they can act as epigenetic determinants of nuclear processes and in turn retroact on cytoplasmic signalling pathways [Marko & Poirier, 2003; Pajerowski, 2007; Dahl, 2008].

1.3 Cell mechanics and atomic force microscopy (AFM)

The first studies of cell mechanics date back to the XVIIth century, with the qualitative description of the movement of cilia and the Brownian motion of intracellular organelles [Pelling & Horton, 2008]. The importance of the mechanical properties of muscles and their interpretation in terms of force and movement became an evidence with experiments on frog leg muscles [Zatsiorsky & Prilutsky, 2012]. Since then, the importance of mechanics in biology has been increasingly recognised. At the end of the XIXth century, a quantitative mechanical characterization of biological materials was accomplished thanks to the combination of macro-scale experiments and mathematical modeling (*e.g.* models for elastic and viscoelastic material indentation, beam bending, Hertz model, ...) [Pelling & Horton, 2008]. At the beginning of the XXth century, biological material science emerged as a fundamental research field for the development of bio-inspired, bio-mimetic and biomedical materials [Meyers, 2008]. Quantitative researches focused on the whole muscle mechanics and its macroscopic interactions with the skeletal system and tendons [Ralston, 1947; Gareis, 1992; Hawkins & Bey, 1997; Gandevia, 1998; Rassier, 2010]. Progressively, the miniaturization of experimental techniques allowed more local studies, e.g. muscle fibers could be isolated and tested as single mechanical entities [Glerum, 1990]. Lately, nano-scale biophysical experimental techniques, along with progresses in cellular and molecular biology, opened a whole domain of research on single cell mechanics. In particular, if the invention of the optical microscope opened our eyes on micron-scale structures in living systems, the development of nanoscopic tools such as the scanning probe microscopies (including atomic force microsccopy) [Binnig, 1986] revolutionized our approach of sub-micron to nanometer size processes. Since then, two main lines of research have been developed in cell mechanics, a global one at the cellular and tissular scale, and a local one at the subcellular scales that addresses the mechanical properties of the cell compartments and molecular assemblies [Kuznetsova, 2007]. In parallel, analytical tools, mathematical modeling and computational techniques have also been developed and improved [Rodriguez, 2013; Moeendarbary & Harris, 2014]. Nowadays the interest of the biology and physicist communities in cellular and tissular mechanics keeps on growing [Janmey & McCulloch, 2007; Hoffman & Crocker, 2009; Fletcher & Mullins, 2010; Moeendarbary & Harris, 2014; Darling & Di Carlo, 2015].

Currently, several experimental methods have been developed for cell mechanics. They can be classified in two main groups [Rodriguez, 2013]: (i) intrusive techniques that apply a force to the cells before measuring their responses (Fig. 1.3(a)), and (ii) non intrusive techniques that sense the forces exerted by the cells upon deformable materials (Fig. 1.3(b)). The force application approaches can be classified according to the type of applied force: (i) aspiration techniques that apply a negative pressure to a whole cell or its compartments [Lee & Liu, 2014], (ii) indenting techniques with cantilevers or micro-needles (cell poker or AFM) [Kuznetsova, 2007], (iii) optical or magnetic force manipulation of cells or beads interacting with cell compartments [Hoffman, 2006], (iv) compression devices, (v) shear flow chambers, (vi) acoustic waves, (vii) electromechanical and electrochemical force gradients [Rodriguez, 2013]. The force sensing approaches use different force sensitive probes: wrinkling membranes, beads dispersed in a polymeric gel (traction force microscopy), single probe cantilevers (AFM), arrays of vertical

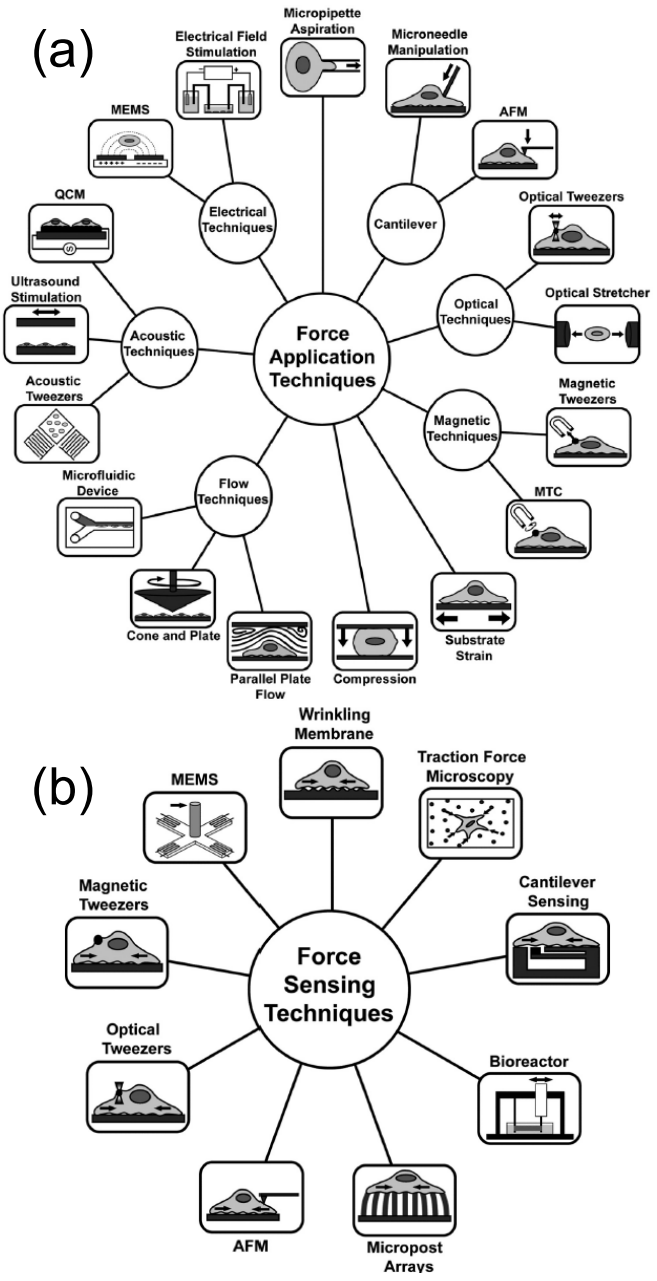

Figure 1.3: **Currently available experimental techniques for cell mechanics.** The experimental approaches can be classified in force application techniques (a) and force sensing techniques (b). Note that some techniques can be used in both approaches depending on their operation mode. Adapted from Applied Mechanics Reviews [Rodriguez, 2013].

cantilevers (micropost arrays), ... Each of these techniques has different characteristics and different resolutions in time, space and force. The choice of an appropriate experimental technique should be made in regard to the biological target, but this choice is sometimes delicate due to the multi-scale organization of biological systems (Fig. 1.4).

Among the available techniques for cell mechanics, AFM, optical and magnetic tweezers obtained remarkable successes thanks to their versatility. While an optical microscope exploits the transport of light through a sample to reconstruct an image, scanning probe microscopes

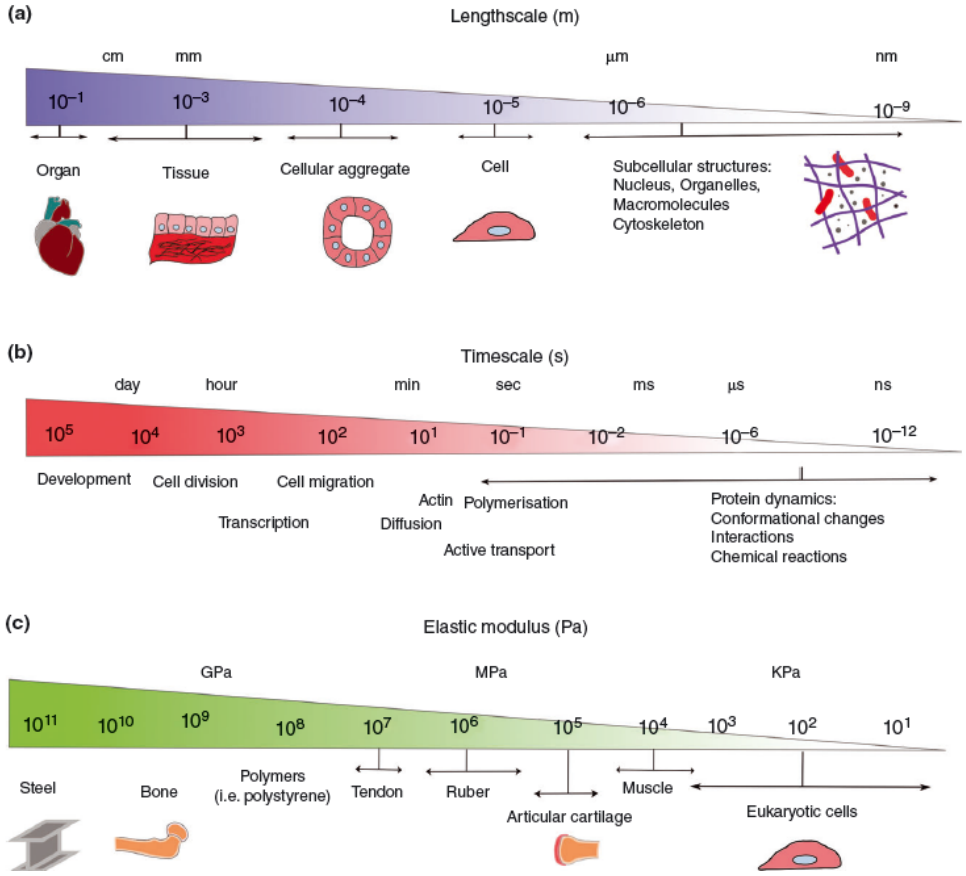

Figure 1.4: **Typical spatial, temporal and elasticity modulus characteristic scales of biological systems.** These parameters need to be taken into account for choosing the more convenient experimental, analytical and modeling approaches in cell mechanics. Adapted from Wiley Interdisciplinary Reviews: Systems Biology and Medicine [Moeendarbary & Harris, 2014].

such as AFM use an interaction force between the probe (*i. e.* the cantilever tip) and the sample. Initially designed as an imaging technique to reconstruct three-dimensional surface topography with an angstrom vertical resolution and a nanometer lateral resolution, AFM can also be used to manipulate single molecules and to measure forces with a high sensitivity (picoNewton resolution). AFM force measurements have been applied to the characterization of the micro-rheology and mechanical properties (*e. g.* elasticity, viscoelasticity, adhesion, storage and loss modulus, ...) of living cells [Collinsworth, 2002; Li, 2008; Frederix, 2009; Nawaz, 2012; Abidine, 2013; Sokolov, 2013; Laurent, 2014; Digiuni, 2015; Martinez-Torres, 2016; Laperrousaz, 2016a].

AFM indentation experiments can be performed on single cells or a population of cells with a nanometer resolution to extract their *in vitro* distributions of mechanical parameters while controlling their environment (*e.g.* chemical, mechanical, electrical properties of cell substrates, liquid or gel chamber, culture medium additives ...) [Costa, 2004a; Santos & Castanho, 2004; Alessandrini & Facci, 2005; Kuznetsova, 2007; Kirmizis & Logothetidis, 2010; Spedden & Staii, 2013; Vahabi, 2013; Cartagena & Raman, 2014; Haase & Pelling, 2015; Qing, 2016]. Minimum preparation of the samples is necessary before and during AFM indentation experiments. These

advantages distinguish AFM from other cell mechanics techniques, and nowadays AFM is one of the reference tools in cell mechanics.

The mechanical properties of eukaryotic living cells have been widely studied in the last decades with a great diversity of experimental approaches. Nevertheless, the interpretation of the experimental data is not easy due to the complex rheological or mechanical behaviour of cells. Contradictory results have been published in the literature, not only among studies using different experimental techniques, but also among those that used similar experimental techniques. These difficulties can be explained by the specificities of a living material. The mechanical behaviour of a given cell can vary drastically according to the experimental conditions; it depends also on the type of cell and in in which phase of the cell cycle the tested cell is. Even worse, a population of cells generated from a unique cell culture can display a strong variability in its mechanical properties.

1.4 Outline of the thesis

This thesis is organized in 6 chapters, including the present introduction (Chapter 1).

Chapter 2 introduces the concepts and formalisms for cell mechanics and rheology and AFM indentation experiments. From standard one-dimensional viscoelastic models, theoretical predictions for the indentation of a viscoelastic material by a conical or pyramidal tip are described. The prediction of these models are used to parametrize experimental force-indentation curves (FICs) collected at fixed scan velocity with an AFM on C2C12 myoblasts and myotubes. The possible impact of both the liquid chamber and the layer of adherent cells on the FICs is analysed by running experiments at different cantilever scan velocities. A global classification of myoblasts and myotubes in term of elastoplastic and viscoelastic cells is proposed.

Chapter 3 pushes further the wavelet-based time-scale analytical tools introduced in Chapter 2 to characterize both global and local shear moduli, and to detect local singular disruption events that appear during the cell indentation. With this methology we propose an original and innovative method for tracking local cytoskeleton events which can occur during the intrusion of a sharp cantilever inside a living cell. This methodology is used to compare normal myoblasts to their differentiated myotubes, to myoblasts with altered actomyosin cytoskeleton properties by ATP depletion, and to blebbistatin treated myoblasts. This mechanical study is complemented by a morphological characterization of these cells by DIC and confocal fluorescence microscopy.

Chapter 4 applies the methodology developed in Chapter 3 to human primary myoblasts from healthy donors and patients affected by the Duchenne muscular dystrophy (DMD). It addresses the fundamental question of how the lack of dystrophin, typical to DMD, can impair the mechanical function of muscle fibers and how the muscle progenitors (single cell mechanics) can also be corrupted. White light transmission and confocal fluorescence microscopies are used to visualise the transformation of the morphological characteristics of these primary muscle progenitors.

Chapter 5 gives a description of the materials and methods implemented for this PhD project.

Chapter 6 summarizes the main results of this thesis work, emphasizing their importance in a more general context of living system rheology. Finally, some directions for future theoretical and experimental researches are proposed.

Chapter 2

Rheology of myoblasts: from general concepts to AFM experiments

2.1 Introduction to rheology

Rheology, from the Greek word "rheos" meaning "to flow", is the science of creep and deformation of matter under applied forces. The interest in the mechanical properties of matter originated from technical problems that human beings had to face, such as how to excavate a cave or to carve the wood. Heraclitus (535−475 BCE) was already philosophizing about the fact that everything changes as time goes on; his famous aphorism $\pi\alpha\nu\tau\tilde{\alpha}\ \rho\varepsilon\acute{\iota}$: (panta rhei - everything flows) survived through centuries. Also Archimedes (250 BCE), Newton (1687) and Young (1807) contributed to the progress of this domain much before the birth of rheology as a science. The formal establishment of rheology as a scientific discipline and the term itself were introduced during a preliminary meeting of the nascent Society of Rheology in Columbus (April 1929) by Bingham [Bingham, 1922] and Reiner [Reiner, 1960]. Nowadays this discipline is still developing and finds applications in various domains such as mechanical engineering, physics, chemistry, medicine, biotechnology, pharmacy, food processing and biology. Rheology relies on a fundamental relationship between stress and strain of a material. For example, for linear elastic materials, stress and strain satisfy a linear relationship. The mechanical response of a material to an applied stress or strain can be considered as linear at small deformations. At larger deformations, nonlinear behavior up to local rupture events may occur. In this chapter we will focus exclusively on the linear response of viscoelastic materials. The concepts of creep and relaxation will be introduced and illustrated on five simple linear viscoelastic 1D models. The 1D solutions of these models will be generalized to 3D configurations mimicking indentation experiments with conical cantilever tips performed in our AFM experiments. These models will be used to discuss the shape of the AFM force-indentation curves (FICs) recorded on myoblasts and myotubes and their modification when changing the cantilever tip velocity.

2.2 Fundamental definitions

2.2.1 Normal stress and shear stress

The stress is a physical quantity that characterizes the internal resistance of a material to an applied load. When a load is applied to a material, its atoms are forced out of their equilibrium

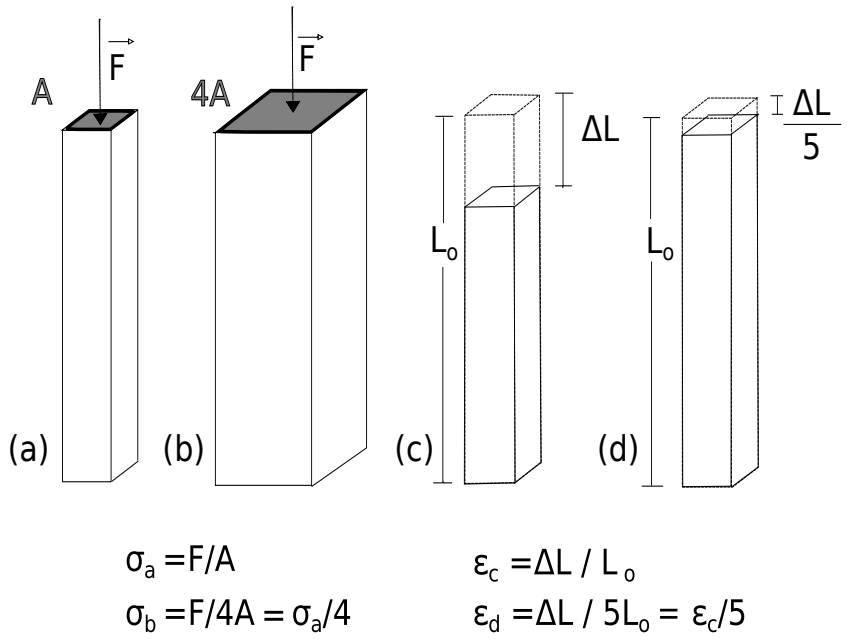

Figure 2.1: **Illustration of stress and strain relationships**. (a) $\vec{F}$ is normally applied over the area A. (b) $\vec{F}$ is normally applied over a four times larger area $4A$. (c) and (d) illustrate different strains ε for a fixed stress σ.

positions. The energy transferred to the material can either (i) be stored in the deformation of interatomic elastic bounds and then used back to recover the original material shape after removing the load or (ii) dissipated in the form of heat, sound, plastic deformation and kinetic energy [Vincent, 2012]. The stress σ is conventionally defined as the ratio of the applied force (F) over the deformed cross sectional area (A) (Fig. 2.1):

$$\sigma = \frac{F}{A} \,. \tag{2.1}$$

The stress has a dimension of a force per unit of area expressed in N/m^2 or Pa (Pascal), where 1 Pa = 1 N/m^2 according to the International System of Units (SI, from the French expression "Le Système International d'Unités"). The stress is a function of both the force F and the area A; therefore if the same force is applied over a bigger area, the material will experience a smaller stress. This phenomenon is illustrated in Fig. 2.1 (a) and (b) where the same force ($\vec{F}$) is normally exerted over an area A and a four time larger area $4A$, respectively. For the same applied force, the stress σ_b experienced by the second body is four time smaller than σ_a.

When the direction of the applied force ($\vec{F}$) is not normal to the surface, shearing is involved in the deformation experienced by the material. Normal stresses (Fig. 2.2 (a) and (b)) correspond to uniaxial loads, where forces are perpendicular to the surface (z axis in Fig. 2.2). Among normal stresses if the force vectors ($\vec{F}$ and $\vec{F}'$) are directed toward each other (Fig. 2.2 (a)), the material is experiencing a compressive stress. The ability of a material to react to compressive stress or pressure is called compressibility. For example, gases are compressible while metals and liquids are incompressible. On the contrary, if the force vectors are directed apart from each other (Fig. 2.2 (b)), the material is stretched under a tensile stress. Shear stresses instead correspond to tangential forces parallel to the surface of force application (parallel to the x-y plane in Fig. 2.2 (c)).

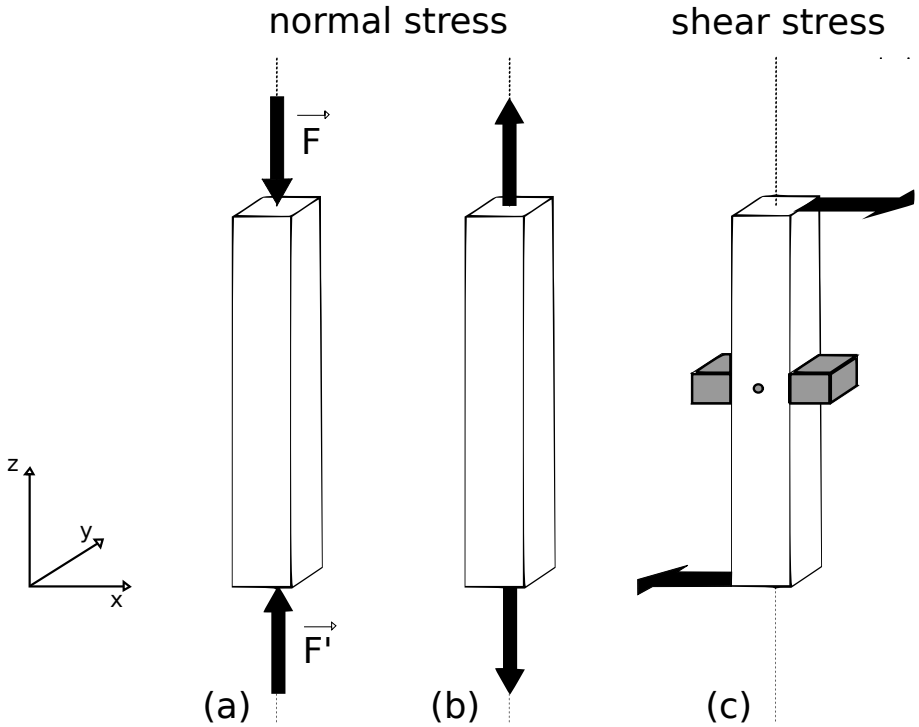

Figure 2.2: **Normal stress and shear stress**. (a) Normal compressive stress. (b) Normal tensile stress. (c) Tangential shear stress.

2.2.2 Deformation

A deformation corresponds to a variation of shape or size of a body when subjected to an external force. There are several ways to express the strain: engineering strain, stretch ratio, Almansi-Hamel (Eulerian) strain, Green-St. Venant strain and true strain [Karimi, 2014]. In the classical infinitesimal theory of elasticity, the most common definition of nominal strain is the engineering strain, which is given by the ratio of the material length change (ΔL) over its original length (L_o):

$$\varepsilon = \frac{\Delta L}{L_o} \, . \tag{2.2}$$

The nominal strain ε is therefore a dimensionless variable quantitying the material deformation; it is negative if the material is compressed and positive if it is stretched. If two different materials such as a metal and a foam are experiencing the same compressive stress, the strain of the former will be much smaller as compared to the strain of the later. Considering a metal below its melting point, metallic bounds keep its atoms in a close packed ordered crystalline structure and they are not as free to move as compared to those of a foam. Thus the amount of strain that a material can withstand for a given stress is related to its internal structure (cross-link strengths) and its deformability.

2.2.3 Creep and relaxation

The term creep describes the slow and gradual flow of a material under constant stress [Findley & Davis, 2013]. A creep experiment will therefore consist in recording the strain of a material under a constant stress. For a linear elastic material, when a constant stress is

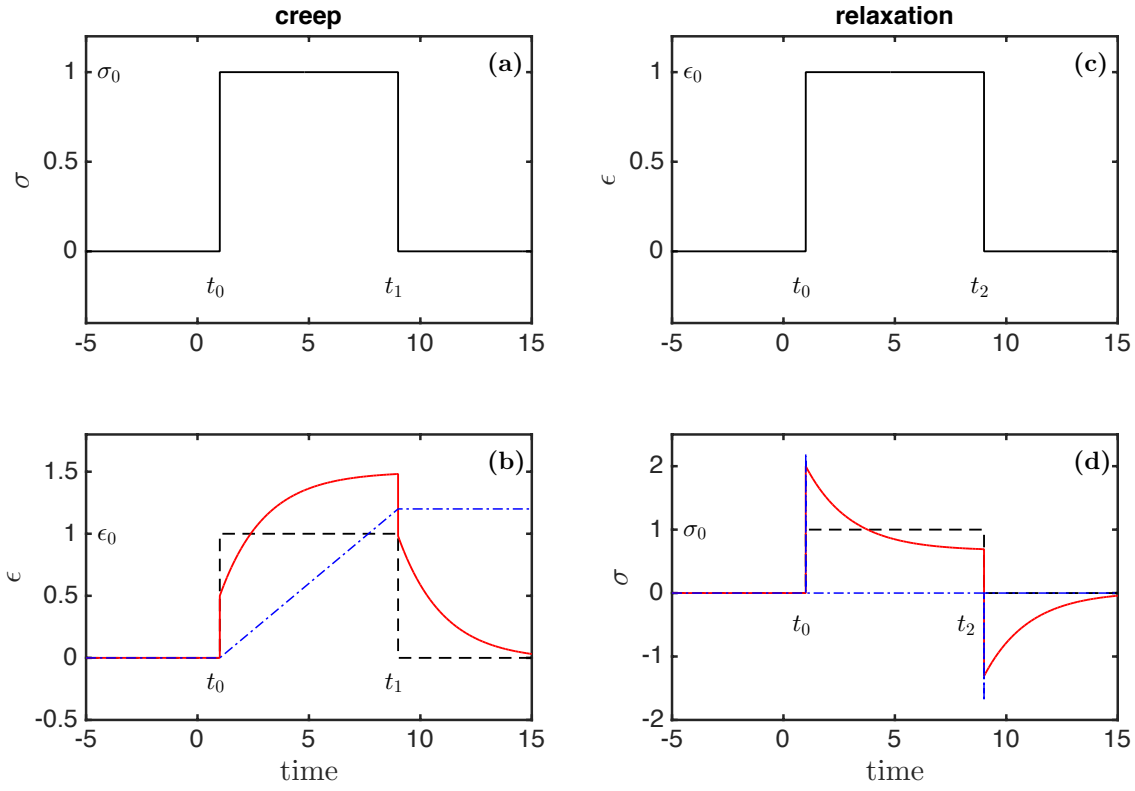

Figure 2.3: **Examples of creep-recovery and relaxation-recovery experiments**. Stress (a) and strain (c) constraints exerted in time. Three materials are depicted, respectively elastic (black dashed line), viscous (blue dashed dotted line) and viscoelastic (red line). (b) Strain of the three materials during creep ($t_0 < t < t_1$) and recovery ($t_1 < t$) phases. (d) Stress applied to the three materials during relaxation ($t_0 < t < t_2$) and recovery ($t_2 < t$) phases.

applied (at $t = t_0$ in Fig. 2.3 (a) and (b)) the strain jumps instantaneously to a constant value. Contrastingly, in the case of viscous materials, the strain increases linearly with time. Once the load is removed ($t > t_1$ in Fig. 2.3 (a) and (b)), in the recovery phase, the deformation vanishes instantaneously for linear elastic materials, persists for viscous materials and decreases progressively for viscoelastic materials.

The term relaxation describes the evolution of the stress of a material under constant strain (Fig. 2.3 (c) and (d)). Again, according to the nature of the tested material, the applied stress can vary substantially in time as shown in Fig. 2.3 (d). Similarly to creep experiments, the elastic material stress follows instantaneously the strain in relaxation experiments. Upon a fixed strain, viscous and viscoelastic materials experience first an excess of stress (positive at t_0 and negative at t_2), followed by either a fast decay or a slow relaxation.

These two types of creep and relaxation experiments are routinely used in several domains of applied sciences such as mechanical, spatial and nuclear engineering, food industry, pharmacology and biotechnology.

2.3 One-dimensional viscoelastic models

Since real materials may display a wide variety of mechanical behaviour, it will be helpful for our forthcoming discussions to have in mind a classification of linear stress-strain responses using pedagogical one-dimensional (1D) models. These models are constructed from elastic (spring) and viscous (dashpot) elements as shown in Fig. 2.4. A spring (Fig. 2.4(a)) represents an ideal elastic material or Hookean solid and a dashpot (Fig. 2.4(b)) represents an ideal fluid or Newtonian liquid. Fig. 2.4(c,d,e) illustrates viscoelastic models made up from a combination of elastic (spring) and viscous (dashpot) components: (c) Maxwell, (d) Kelvin–Voigt and (e) standard linear solid (SLS) models.

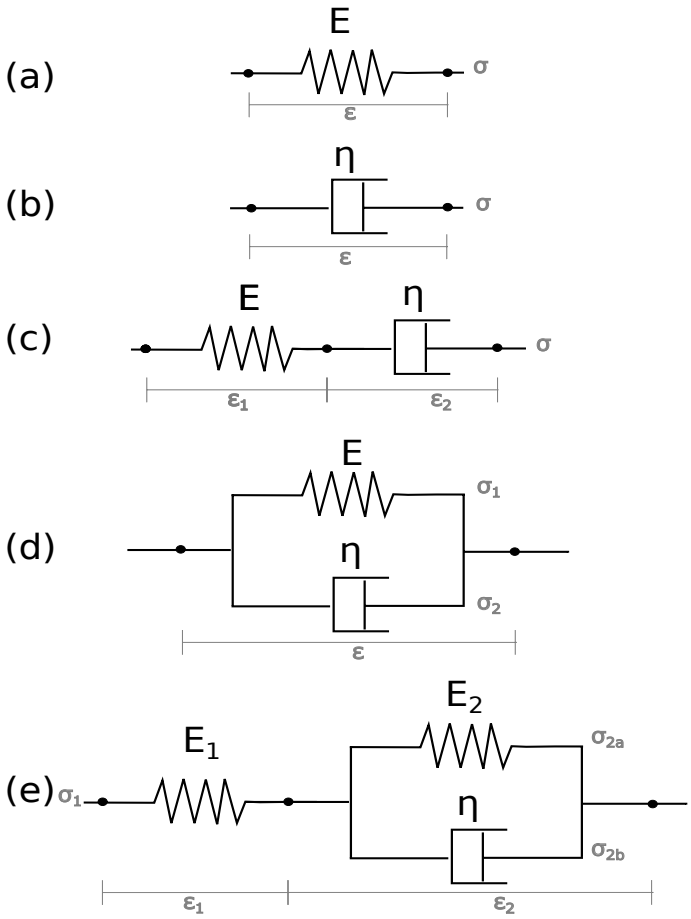

Figure 2.4: **Spring and dashpot representation of elastic, viscous and viscoelastic 1D models**. (a) Spring model for linear elastic materials (Hookean solids). (b) Dashpot model for linear viscous fluids (Newtonian liquids). Examples of linear viscoelastic models: (c) Maxwell, (d) Kelvin–Voigt and (e) standard linear solid (SLS) models.

2.3.1 Hookean solids

In purely elastic materials, also called Hookean solids, the energy introduced by applying a force (resp. deformation) is stored by the material and can be recovered upon release of the force (resp. deformation). An important property of elastic materials is that the strain is reversible as shown in Fig. 2.3(b) in the recovery part of the curve ($t > t_1$). In 1D the stress-to-strain

relationship is described by the Hooke's law:

$$\sigma = E\,\varepsilon\ , \tag{2.3}$$

where the Young's modulus E is constant and characterizes the resistance (stiffness) of an elastic material to an axial deformation. Linear elastic materials respond instantaneously to a mechanical load with a deformation proportional to the stress: a doubling of stress doubles the strain. The stress versus strain curve is a straight line with a slope equal to the Young's modulus E. In 1D, the Hooke's law can also be expressed in terms of the material compliance D:

$$\varepsilon = D\,\sigma\ , \tag{2.4}$$

where $D = 1/E$. Hookean solids are represented by a spring (Fig. 2.4 (a)). Knowing the Young's modulus of the material under investigation, it is possible to predict its behaviour during a creep experiment. If a constant stress σ_0 is applied at $t = 0$ (Fig. 2.5(a)), its strain will also be constant and proportional to the stress for $t > 0$:

$$\epsilon(t) = \frac{\sigma_0}{E}\ . \tag{2.5}$$

The evolution of the strain of an Hookean solid during a creep experiment computed with Eq. (2.5) is shown in Fig. 2.5(a'), for the parameter values $\sigma_0 = 1$ kPa and $E = 10$ kPa, consistent with the experimental estimates for C2C12 myoblasts [0.72-28 kPa] [Collinsworth, 2002; Zhang, 2004; Sbrana, 2008; Takemoto, 2012; Al-Rekabi & Pelling, 2013; Sun, 2014; Li, 2016]. This result shows that a linear elastic material responds instantaneously to a constant stress.

Similarly, during a relaxation experiment, to impose a constant strain ε_0 to an elastic material requires an instantaneous jump of the stress:

$$\sigma(t) = \varepsilon_0 E\ . \tag{2.6}$$

The stress of a Hookean solid during a relaxation experiment computed *via* Eq. (2.6) is shown in Fig. 2.5 (a‴) for $\varepsilon_0 = 0.1$ and $E = 10$ kPa.

Remark Most solid materials behave as purely elastic for small strains and may behave non-linearly for larger strain values. In these conditions they are characterised by an elasto-plastic response; beyond some stress threshold called the yield stress, their deformation is irreversible. If the yield stress is reached, they exhibit a residual strain when the load is removed. This type of strain is called plastic strain. The plastic to elasto-plastic transition depends on the temperature. For example metals or wood at high temperature do not exhibit an elastic but a viscoplastic behaviour. Among biological materials, bones [Rho, 1993] and plant cell walls [Chanliaud, 2002] are examples of elasto-plastic materials.

2.3.2 Newtonian liquids

In a purely viscous material, also called Newtonian liquid, the energy injected in the material by the applied force is totally dissipated. As a consequence, the strain is not recovered upon release of the stress (Fig. 2.3(b)). In 1D, the stress-to-strain relationship is described by the

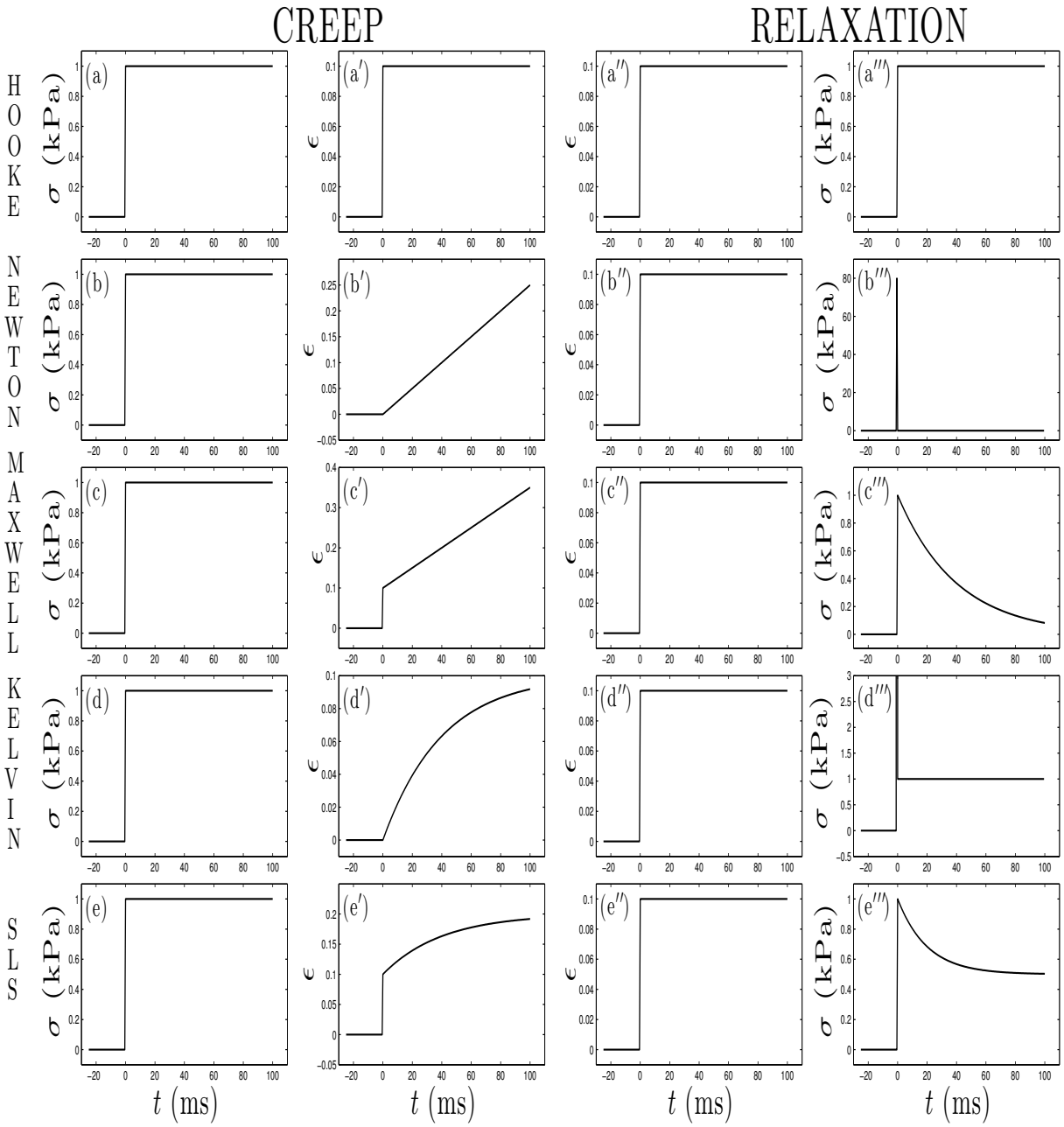

Figure 2.5: **Temporal responses of the five viscoelastic 1D models during creep and relaxation experiments**. Strain (σ) and stress (ε) evolutions of a Hookean solid (a-a‴), a Newtonian fluid (b-b‴), a Maxwell model (c-c‴), a Kelvin–Voigt model (d-d‴) and a standard linear solid model (e-e‴) during creep (first and second columns) and relaxation (third and fourth columns) experiments. For creep, the stress was fixed at 1kPa. For relaxation, the strain was fixed at 0.1. Parameter values: $E = E_1 = E_2 = 10$ kPa, $\eta = 400$ Pa.s.

following equation originally proposed by I. Newton [Newton, 1833]:

$$\sigma = \eta \, \frac{d\varepsilon}{dt} \, , \tag{2.7}$$

where η is the Newtonian viscosity or dynamic viscosity (in Pa.s) of the fluid and $d\varepsilon/dt$ is the local strain rate. Therefore in a Newtonian liquid, the stress is proportional to the local strain rate, the rate of its deformation, with a constant coefficient equal to η. While the stiffness is the resistance of a material to deformation, the viscosity is the resistance to motion of a fluid. For example, the viscosity of honey ($0.421-23.405$ Pa.s) is much larger than the one of water (1 mPa.s). η depends on many parameters including moisture and temperature [Yanniotis, 2006]. Newtonian fluids are represented by a dashpot in Fig. 2.4(b). Knowing the viscosity η of a fluid, one can predict its behaviour during a creep experiment from Eq. (2.7). If a constant stress σ_0 is applied at $t = 0$, the strain of the viscous material will increase linearly with time as:

$$\varepsilon(t) = \sigma_0 \, D(t) = \sigma_0 \frac{t}{\eta} \, , \tag{2.8}$$

meaning that the creep compliance $D(t)$ increases linearly with t. The behaviour of a Newtonian fluid during a creep experiment computed *via* Eq. (2.8) is shown in Fig. 2.5(b') for parameters values $\sigma_0 = 1$ kPa and $\eta = 400$ Pa.s, consistent with estimations reported for mouse myoblasts [Sako, 2010].

Interestingly, during a relaxation experiment, if a constant strain ε_0 is applied at $t = 0$, the amount of stress required for this deformation is singular at $t = 0$ and null for $t > 0$

$$\sigma(t) = \eta \, \delta(t) \, . \tag{2.9}$$

The stress evolution of a Newtonian fluid during a relaxation experiment computed with Eq. (2.9) is shown in Fig. 2.5 (b$'''$) for $\varepsilon_0 = 0.1$ and $\eta = 400$ Pa.s. When a constant strain is applied to a Newtonian fluid at $t = 0$, this fluid experiences an infinite stress at $t = 0$ before dropping down to zero for $t > 0$. Mathematically, this behaviour can be represented by the unit impulse or Dirac delta function $\delta(t)$, where $\delta(t) = \infty$ for $t = 0$ while $\delta(t) = 0$ for $t \neq 0$. Let us point out that $\delta(t)$ is a distribution that satisfies the following equation:

$$\int_{-\infty}^{+\infty} \delta(t) \, dt = 1 \, . \tag{2.10}$$

A fluid will be classified as a non-Newtonian fluid when its viscosity is no longer constant but varies with the strain rate $\gamma = \dfrac{d\varepsilon}{dt}$:

$$\sigma = \eta(\gamma) \, \gamma \ . \tag{2.11}$$

Notable biological examples of non-Newtonian fluids are blood [Baskurt & Meiselman, 2003; Shibeshi & Collins, 2005], mucus [Lai, 2009] and synovial fluid (osteoarthritic patients) [Bhuanantanondh, 2012]. Cerebrospinal [Bloomfield, 1998] and synovial fluids in patients with rheumatoid arthritis are instead Newtonian fluids [Bloch & Dintenfass, 1963].

2.3.3 Viscoelastic materials

Viscoelastic materials exhibit both viscous (dashpot) and elastic (spring) characteristics. Several mechanical models of viscoelastic materials were constructed by assembling in different

ways these basic building blocks. Depending on the building block number and their assemblage, the models exhibit different mechanical behaviour. When a mechanical load is applied to a viscoelastic material, viscous damping of mechanical energy yields a separation of the loading and unloading curves. Almost all body tissues, cells, polymers, extracellular matrices, proteins are biological examples of viscoelastic materials [Sasaki, 2012; Pal, 2014; Thoumine & Ott, 1997; Sanjeevi, 1982; Jamison, 1968].

2.3.3.a Maxwell model

The Maxwell model is a two-element model for viscoelastic materials that puts in series a linear spring and a linear dashpot (Fig. 2.4(c)). This conformation confers to the model two characteristics: (i) the stress on the spring is the same as the stress on the dashpot and equals the total stress; (ii) the total strain equals the sum of the spring and dashpot strains. From this construction, a stress-strain differential equation can be written:

$$\frac{\sigma}{\eta} + \frac{1}{E}\frac{d\sigma}{dt} = \frac{d\varepsilon}{dt} \, . \tag{2.12}$$

The integration of Eq. (2.12) gives the creep-response in terms of a creep compliance function $D(t)$:

$$\varepsilon(t) = \sigma_0 \, D(t) = \sigma_0 \left[\frac{1}{E} + \frac{t}{\eta}\right] \, . \tag{2.13}$$

The strain response given by Eq. (2.13) is shown in Fig. 2.5 (c'), for the parameters values: $\sigma_0 = 1$ kPa, $E = 10$ kPa and $\eta = 400$ Pa.s. This figure shows that the Maxwell model strain is the sum of a spring strain of Fig. 2.5 (a') and a dashpot strain of Fig. 2.5 (b').

If instead during a relaxation experiment, a constant strain ε_0 is applied at $t = 0$, the solution of Eq. (2.12) gives an exponential decreasing function of time of the stress:

$$\sigma(t) = \varepsilon_0 \, E(t) = \varepsilon_0 \, E \, e^{-\frac{t}{\tau_R}} \, , \tag{2.14}$$

where E(t) is called the relaxation modulus function and $\tau_R = \dfrac{\eta}{E}$ is a characteristic relaxation time. The stress evolution of a Maxwell model during a relaxation experiment predicted by Eq. (2.14) is shown in Fig. 2.5 (c‴) with the parameters: $\varepsilon_0 = 0.1$, $E = 10$ kPa and $\eta = 400$ Pa.s.

2.3.3.b Kelvin–Voigt model

The Kelvin–Voigt model also combines a linear spring and a linear dashpot but in parallel (Fig. 2.4 (d)). This conformation confers to the model two features: (i) the total stress is the sum of the spring and the dashpot stresses; (ii) the spring strain equals the dashpot strain and corresponds also to the total strain. The differential equation fulfilled by the stress σ and the strain ε is:

$$\frac{\sigma}{\eta} = \frac{d\varepsilon}{dt} + \frac{E}{\eta}\varepsilon \, . \tag{2.15}$$

Solving Eq. (2.15) for a constant stress σ_0 applied at $t = 0$ (creep experiment) gives the temporal evolution of the strain:

$$\varepsilon(t) = \sigma_0 D(t) = \frac{\sigma_0}{E}(1 - e^{-\frac{t}{\tau_R}}) \, , \tag{2.16}$$

where $\tau_R = \eta/E$ is called the retardation time and characterizes the time taken for the strain to accumulate. $\varepsilon(t)$ predicted by Eq. (2.16) is shown in Fig. 2.5(d') for the parameter values $\sigma_0 = 1$ kPa, $E = 10$ kPa and $\eta = 400$ Pa.s. The Kelvin–Voigt model response during a creep experiment is no longer instantaneous (as compared to the Hooke's model) and the viscous term η introduces a smooth exponential evolution of the strain with a characteristic time $\tau_R = \eta/E$.

If a constant strain ε_0 is applied at $t = 0$ on a Kelvin–Voigt model (relaxation experiment), solving Eq. (2.15) leads to the following temporal evolution of the stress:

$$\sigma(t) = E\,\varepsilon(t) \; + \; \eta \;\; \delta(t) \, . \tag{2.17}$$

$\sigma(t)$ predicted by Eq. (2.17) is shown in Fig. 2.5 (d‴) for parameters values $\varepsilon_0 = 0.1$ and $\eta = 400$ Pa.s. The Dirac term $\delta(t)$ in $\sigma(t)$ means that a sudden jump in strain at $t = 0$ requires an infinite strain rate, which is quite unrealistic in real experimental situations. To circumvent this problem, the addition of another elastic component in series with the Kelvin-Voigt spring-dashpot has been proposed, as reported in the next section.

2.3.3.c Standard linear solid (SLS) model

The SLS model is a three-element model of viscoelastic materials composed by a linear spring and a Kelvin–Voigt model (Fig. 2.4(e)). This conformation confers to the model two main features: (i) the spring stress equals Kelvin–Voigt element stress (total stress); (ii) the total strain is the sum of the spring and the Kelvin–Voigt strains. The stress σ and the strain ε fulfill the differential equation:

$$(E_1 + E_2)\sigma + \eta\frac{d\sigma}{dt} = E_1 E_2 \varepsilon + E_1 \eta \frac{d\varepsilon}{dt} \, , \tag{2.18}$$

where E_1 is the elastic modulus of the spring, E_2 and η are respectively the elastic modulus and the viscosity of the Kelvin–Voigt model. Given E_1, E_2 and η, when a constant stress σ_0 is applied at $t = 0$, the solution of Eq. (2.18) for the strains reads [Flügge, 1975; Li, 1995]:

$$\varepsilon(t) = \sigma_0 D(t) = \sigma_0 \left(\frac{E_1 + E_2}{E_1 E_2} - \frac{1}{E_2}\, e^{-\frac{t}{\tau_R}} \right) \, , \tag{2.19}$$

where the characteristic retardation time $\tau_R = \eta/E_2$. $\varepsilon(t)$ computed with Eq. (2.19) is shown in Fig. 2.5 (e'), for the parameters values: $E_1 = E_2 = 10$ kPa and $\eta = 400$ Pa.s.

If a constant strain ε_0 is applied at $t = 0$ (relaxation experiment), the solution of Eq. (2.18) for the stress $\sigma(t)$ reads:

$$\sigma(t) = \frac{E_1}{E_1 + E_2} \left[E_1\, e^{-\frac{t}{\tau_R}} + E_2 \right] \varepsilon_0 \, , \tag{2.20}$$

where the relaxation time $\tau_R = \eta/(E_1 + E_2)$. $\sigma(t)$ computed with Eq. (2.20) is shown in Fig. 2.5 (e‴) for $\varepsilon_0 = 0.1$. When comparing creep and relaxation responses (Fig. 2.5(e') and

(e‴)), the switch of the system from its initial to its final state is characterized by two different characteristic times $\tau_R = \eta/E_2$ and $\tau_R = \eta/(E_1 + E_2)$.

2.3.4 Generalization of the viscoelastic models

If the mechanical properties of the material are unknown and cannot be simplified as in the previous reported models, a generalization of Eqs (2.3) and (2.4) for elastic and viscous elements was proposed by Lakes [Lakes, 2009], assuming that $D(t)$ and $E(t)$ are no longer constant but depend on time:

$$\varepsilon(t) = D(t)\,\sigma(t)\ , \tag{2.21}$$

$$\sigma(t) = E(t)\,\varepsilon(t)\ . \tag{2.22}$$

Then, the previous linear differential equations can be rewritten as temporal integrals. For example, the differential equation of the Maxwell model (Eq. (2.12)):

$$\frac{d\sigma}{dt} + \frac{E_o}{\eta}\sigma = E_o\,\frac{d\varepsilon}{dt}\ , \tag{2.23}$$

can be solved using a standard integrating factor method. By multiplying the two sides of Eq. (2.23) by $\exp(E_o t/\eta)$, we get:

$$\left(\frac{d\sigma}{dt} + \frac{E_o}{\eta}\sigma\right) e^{\dfrac{E_o t}{\eta}} = E_o\, e^{\dfrac{E_o t}{\eta}}\,\frac{d\varepsilon}{dt}\ , \tag{2.24}$$

which can be straightforwardly transformed into:

$$\frac{d}{dt}\left[e^{\dfrac{E_o t}{\eta}}\,\sigma(t)\right] = E_o\, e^{\dfrac{E_o t}{\eta}}\,\frac{d\varepsilon(t)}{dt}\ . \tag{2.25}$$

Assuming that $\sigma(t \to -\infty)$ does not diverge exponentially, Eq. (2.25) can be integrated in the interval $t \in [-\infty,\, T]$:

$$\left[e^{\dfrac{E_o t}{\eta}}\,\sigma(t)\right]_{-\infty}^{T} = e^{\dfrac{E_o T}{\eta}}\,\sigma(T) = \int_{-\infty}^{T} E_o e^{\dfrac{E_o t}{\eta}}\,\frac{d\varepsilon(t)}{dt}dt\ , \tag{2.26}$$

leading to the following expression for $\sigma(T)$:

$$\sigma(T) = \int_{-\infty}^{T} E_o e^{\dfrac{E_o(t-T)}{\eta}}\,\frac{d\varepsilon(t)}{dt}dt\ . \tag{2.27}$$

Then, after the following changes in the notations ($T \to t$ and $t \to \tau$), we get:

$$\sigma(t) = \int_{-\infty}^{t} E(t-\tau)\frac{d\varepsilon(\tau)}{d\tau}d\tau\ , \tag{2.28}$$

where

$$E(t) = E_o \exp(-E_o t/\eta) \tag{2.29}$$

is called shear relaxation modulus. Eq. (2.28) is known as a hereditary integral [Schapery, 1984].

Hereditary integrals were generally proposed respectively for creep (strain) and relaxation (stress) [Lakes, 2009]:

$$\varepsilon(t) = \sigma(0)D(t) + \int_{0^+}^{t} D(t-\tau)\frac{d\sigma(\tau)}{d\tau}d\tau \ , \tag{2.30}$$

and

$$\sigma(t) = \varepsilon(0)E(t) + \int_{0^+}^{t} E(t-\tau)\frac{d\varepsilon(\tau)}{d\tau}d\tau \ . \tag{2.31}$$

From Eq. (2.30), in a creep experiment, the strain response $\varepsilon(t)$ to a jump of stress from $\sigma(t \leqslant 0) = 0$ to $\sigma(t > 0) = \sigma_0$ provides direct access to the temporal compliance $D(t)$:

$$\varepsilon(t) = D(t)\sigma_0 \ . \tag{2.32}$$

Similarly, from Eq. (2.31), we get the shear relaxation modulus $E(t)$ directly from the stress solution $\sigma(t)$:

$$\sigma(t) = E(t)\varepsilon_0 \ . \tag{2.33}$$

2.4 Three-dimensional mechanical models

In this section, we generalize the creep and relaxation 1D models to three dimensions, introducing a 3D creep compliance J(t) and a 3D shear relaxation modulus G(t). In particular, since conical AFM tips were used in the experiments reported in this thesis manuscript, we will mainly focus on conical indentation situations.

2.4.1 Hookean solids

Let us consider a body (*i.e.* a rectangular parallelepiped) in the 3D Euclidean space $\mathbb{R}^3$ characterised by the three Cartesian axes X, Y and Z (Fig. 2.6). If different forces are applied to the different faces of the parallelepiped with different angles, it is possible to resolve each force in terms of strain components parallel to each axis. The 3D stress (resp. strain) is expressed as a Cauchy tensor σ_{ij} (resp. $\varepsilon_{k,l}$). In 3D, the linear Hooke's laws (Eqs (2.3) and (2.5)) take the following tensorial forms:

$$\varepsilon_{i,j} = J_{i,j,k,l} \ \sigma_{k,l} \ , \tag{2.34}$$

and

$$\sigma_{i,j} = G_{i,j,k,l} \ \varepsilon_{k,l} \ , \tag{2.35}$$

where $J_{i,j,k,l}$ is the fourth-order elastic compliance tensor and $G_{i,j,k,l}$ is the fourth-order elastic moduli tensor (the indices $i, j, k, l = 1, 2, 3$ correspond to the X, Y and Z axes of the Euclidean space).

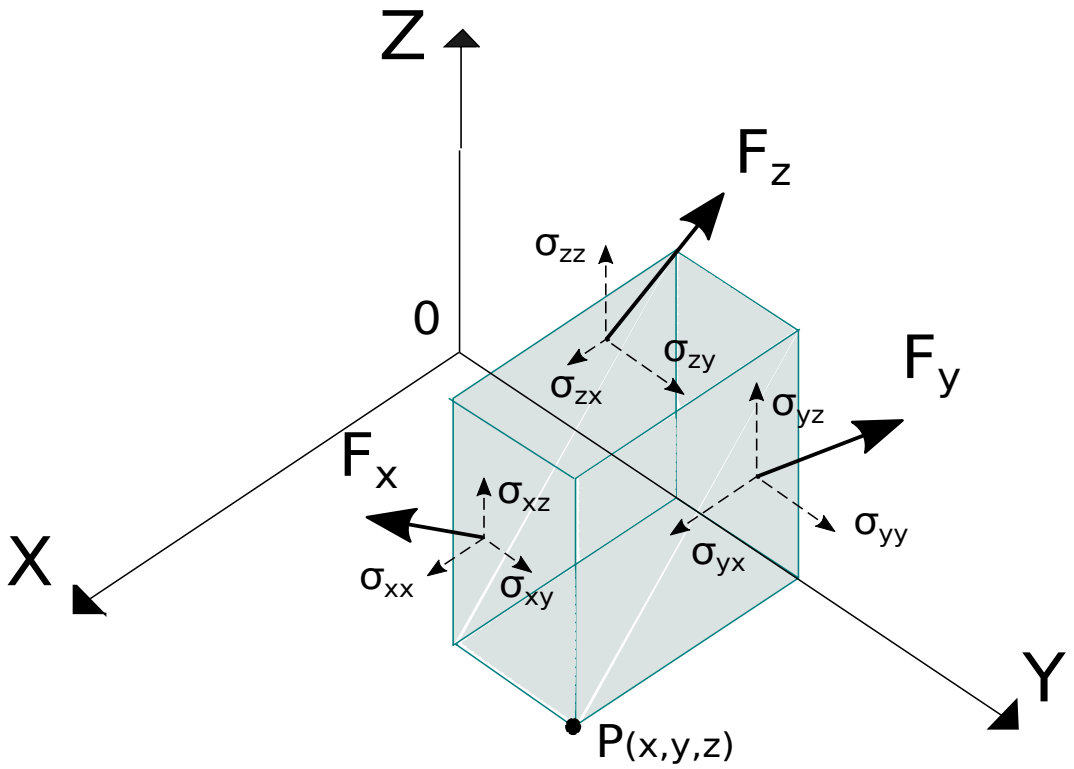

Figure 2.6: **Three dimensional representation of the stress tensor on a rectangular parallelepiped**. Three forces F_x, F_y and F_z are applied with a certain angle on the three faces that are normal respectively to the X, Y and Z axes. At each face of the parallelepiped (*e.g.* the x face perpendicular to the X axis), the stress tensor is decomposed into three stress components (*e.g.* σ_{xx}, σ_{xy} and σ_{xz}) which are respectively parallel to the three X, Y and Z axes.

2.4.2 Newtonian liquids

For an isotropic Newtonian fluid at rest in 3D, the pressure stress tensor σ_{pre} is diagonal:

$$\sigma_{pre} = -p\mathbf{I} = \begin{bmatrix} -p & 0 & 0 \\ 0 & -p & 0 \\ 0 & 0 & -p \end{bmatrix} , \tag{2.36}$$

where p is the hydrostatic pressure and $\mathbf{I}$ the third-order identity matrix such that I_{ij} is 1 if $i = j$ and 0 if $i \neq j$. Similarly to the 1D case, the 3D stress of a Newtonian fluid is proportional to the applied strain rate and takes a tensorial form (for details see [Findley & Davis, 2013]:

$$\sigma_{i,j} = 2\ \eta_{i,j,k,l}\ \gamma_{k,l}\ , \qquad \gamma_{k,l} = \frac{d\varepsilon_{k,l}}{dt}\quad . \tag{2.37}$$

Overall, the 3D total stress tensor $\sigma_{i,j}$ is given by [Kirby, 2010]:

$$\sigma_{i,j} = -pI + 2\ \eta_{i,j,k,l}\ \gamma_{k,l}\ . \tag{2.38}$$

2.4.3 Viscoelastic materials

As in 1D, 3D Hookean solid and Newtonian fluid models have a limited capability to describe material behaviour when compared to experimental data. The viscoelastic constitutive models are more appropriate to account for the 3D behaviour of a wide class of materials. The 3D hereditary integral for creep, generalized from Eq. (2.30), reads [Christensen, 2012]:

$$\varepsilon_{ij}(x_i,t) = \int_0^t J_{ijkl}(x_i, t-\tau)\frac{d\sigma_{k,l}(x_i,\tau)}{d\tau}d\tau \ , \tag{2.39}$$

where $J_{ijkl}(t)$ is the tensorial compliance. In the same way, Eq. (2.31) can be generalized in 3D using a tensorial stress relaxation function $G_{ijkl}(t)$:

$$\sigma_{ij}(x_i,t) = \int_0^t G_{ijkl}(x_i, t-\tau)\frac{d\varepsilon_{k,l}(x_i,\tau)}{d\tau}d\tau \ . \tag{2.40}$$

2.5 Three-dimensional indentation modeling with a conical AFM tip

2.5.1 Creep and relaxation experiments with a conical indenter

For 3D creep and relaxation experiments performed with an indenter, the morphology of the indenter needs to be considered since it determines the cross-sectional area A where the force is applied. Thus, the local stress, defined as the ratio of the local force F over the deformed area A (Eq. (2.1)), varies according to the geometry of the indenter (*e.g.* conical, pyramidal, paraboloidal or spherical). For an axisymmetric rigid cone (Fig. 2.7), in contact with an isotropic elastic material, the force required to indent the material with a depth h is a parabolic function of h [Sneddon, 1965; Cheng & Cheng, 2004]:

$$F = \frac{2\tan\alpha}{\pi(1-\nu^2)}\,E\,h^2 = K_c\,E\,h^2 \ , \tag{2.41}$$

where E is the Young modulus, ν the Poisson's ratio and α the half-opening angle of the conical indenter (Fig. 2.7(b)). The prefactor $K_c = 2\tan\alpha/(\pi(1-\nu^2))$ depends on both the mechanical anisotropy of the sample (ν) and the geometry of the cone (α). For isotropic materials, the Poisson's ratio ν varies between 0.5 (for incompressible materials as water or rubber) and -1 [Greaves, 2011]. Negative values of ν correspond to transversal extension upon stretching (auxetic materials) [Lakes, 1993]. When considered incompressible and isotropic, living cells have a Poisson ratio ν in the range [0.3-0.5] [Charras & Horton, 2002a; Costa, 2004a; Sirghi, 2008]. For isotropic 3D materials, the shear relaxation modulus G is related to the 1D relaxation modulus E (Young modulus):

$$G = \frac{E}{2\,(1+\nu)} \ . \tag{2.42}$$

Thus Eq. (2.41) can be rewritten as:

$$F = \frac{4\tan\alpha}{\pi(1-\nu)}\,G\,h^2 \ . \tag{2.43}$$

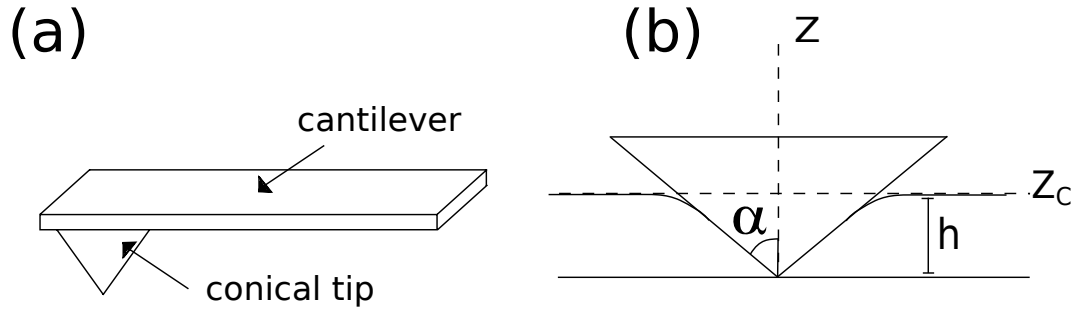

Figure 2.7: **Schematic representation of an AFM conical indenter.** (a) AFM rectangular cantilever with a sharp conical tip. (b) Cross-section of the contact surface of a conical tip for a given indentation depth h. α is the half-opening angle of the conical indenter, Z the vertical axis, Z_C the original surface position.

Viscoelastic materials respond to stress with time-varying mechanical parameters ($G(t)$ and $J(t)$) (see section 2.4.3). For an isotropic and conical indenter shape, the hereditary integral expression (Eq. (2.40)) takes the following simple integral form [Lu, 2003; Cheng & Cheng, 2004; Huang & Lu, 2006; Knauss, 2008; Cheng & Yang, 2009]:

$$F(t) = \frac{4\tan\alpha}{\pi(1-\nu)} \int_0^t G(t-\tau) \frac{dh^2(\tau)}{d\tau} d\tau \ . \tag{2.44}$$

This formula describes the force $F(t)$ for a conical indentation of a linear viscoelastic at a given velocity. A similar viscoelastic constitutive equation has been derived for spherical indenters [Hunter, 1960; Graham, 1965]. For a constant strain jump at $t = 0$, Eq. (2.44) can be straightforwardly solved using the property of the Dirac distribution integral (Eq. (2.10)):

$$F(t) = \frac{4\tan\alpha}{\pi(1-\nu)} G(t) h_0^2 \ . \tag{2.45}$$

From Eq. (2.45), the 3D relaxation solutions $F(t)$ for the five viscoelastic models introduced in section 2.3 can be computed from the 1D relaxation stress functions $\sigma(t)$. The shear relaxation moduli $G(t)$ and the forces $F(t)$ for these five models are reported in Table 2.1.

Similarly, the 3D creep compliance $J(t)$ (creep experiments) can be formulated from the 1D creep compliance $D(t)$ (Eq. (2.32)) [Shimizu, 1999]:

$$J(t) = 2(1+\nu)\, D(t) \ . \tag{2.46}$$

Thus, for a constant force F_0 applied at $t = 0$ on a viscoelastic material with a conical shape indenter, the integral of Eq. (2.39) takes the following form:

$$h^2(t) = \frac{\pi(1-\nu)}{4\tan\alpha} \int_0^t J(t-\tau) \frac{dF(\tau)}{d\tau} d\tau = \frac{\pi(1-\nu)}{4\tan\alpha} J(t) F_0 \ . \tag{2.47}$$

The corresponding indentation solution $h(t)$ is then given by a square-root law of the compliance $J(t)$:

$$h(t) = \sqrt{\frac{\pi(1-\nu)}{4\tan\alpha} J(t) F_0} \ . \tag{2.48}$$

model	G(t)	F(t)
Hooke	$\frac{E}{2(1+\nu)}$	$\frac{2\tan\alpha}{\pi(1-\nu^2)}Eh_0^2$
Newton	$\frac{\eta\delta(t)}{2(1+\nu)}$	$\frac{2\tan\alpha}{\pi(1-\nu^2)}\eta\delta(t)h_0^2$
Maxwell	$\frac{Ee^{-\frac{tE}{\eta}}}{2(1+\nu)}$	$\frac{2\tan\alpha}{\pi(1-\nu^2)}Ee^{-\frac{tE}{\eta}}h_0^2$
Kelvin	$\frac{E+\eta\delta(t)}{2(1+\nu)}$	$\frac{2\tan\alpha}{\pi(1-\nu^2)}(E+\eta\delta(t))h_0^2$
SLS	$\frac{E_1}{2(E_1+E_2)(1+\nu)}\left(E_1e^{-\frac{t(E_1+E_2)}{\eta}}+E_2\right)$	$\frac{2\tan\alpha}{\pi(1-\nu^2)}\left[\frac{E_1}{E_1+E_2}\left(E_1e^{-\frac{t(E_1+E_2)}{\eta}}+E_2\right)\right]h_0^2$

Table 2.1: **Three-dimensional relaxation shear moduli $G(t)$ and forces $F(t)$ for a conical indenter applying a constant strain h_0 at $t = 0$ on the five viscoelastic models (Fig. 2.4)**. $G(t)$ (first column) and $F(t)$ (second column), computed from Eq. (2.45) and the 1D relaxation stress functions $\sigma(t)$ of the five viscoelastic models (Section 2.3).

In Table 2.2 are reported the creep compliances $J(t)$ and indentation solutions $h(t)$ for the five viscoelastic models (Section 2.3). The creep and relaxation behaviour of these models for a force F_0=1 nN and an indentation depth h_0 =100 nm are illustrated in Fig. 2.8.

For Hookean solids, one recovers for $h(t)$ (Fig. 2.8(a')) and $F(t)$ (Fig. 2.8(a‴)) the instantaneous responses of these elastic materials to stress and strain as originally obtained in 1D (Fig. 2.5(a') and (a‴)). For Newtonian fluids, the indentation $h(t)$ response to a constant force F_0 increases as a square-root law of time (Fig. 2.8(b')), differently to the linear response obtained in 1D (2.5(b')). In contrast, the conical shape of the indenter does not affect the relaxation response $F(t)$ of a Newtonian fluid (Fig. 2.8(b‴)) as compared to the 1D response $\sigma(t)$ (Fig. 2.5(b‴)). From Eqs (2.46) and (2.48), the 3D creep $h(t)$ responses of the three viscoelastic models with a conical shape indenter behave as the square-root of the 1D compliance $D(t)$ (Fig. 2.8(c',d',e')). For the relaxation experiments, the forces $F(t)$ (Fig. 2.8(c‴,d‴,e‴)) are identical (up to a constant factor) to the 1D strain responses $\sigma(t)$ (Fig. 2.5(c‴,d‴,e‴)).

2.5.2 Conical indenter moving at constant velocity

In this section, we investigate the response $F(t)$ of the five mechanical models when probed with a conical indenter moving at constant velocity V_0. The theoretical conditions are supposed to mimic the experimental AFM indentation of myoblasts and myotubes, reported in Section 2.6.

model	**J(t)**	**h(t)**
Hooke	$\frac{2(1+\nu)}{E}$	$\sqrt{\frac{\pi(1-\nu^2)}{2\tan\alpha}\frac{F_0}{E}}$
Newton	$\frac{2(1+\nu)t}{\eta}$	$\sqrt{\frac{\pi(1-\nu^2)}{2\tan\alpha}\frac{F_0 t}{\eta}}$
Maxwell	$2(1+\nu)\left(\frac{1}{E}+\frac{t}{\eta}\right)$	$\sqrt{\frac{\pi(1-\nu^2)}{2\tan\alpha}\left(\frac{1}{E}+\frac{t}{\eta}\right)F_0}$
Kelvin	$\frac{2(1+\nu)}{E}\left(1-e^{-\frac{tE}{\eta}}\right)$	$\sqrt{\frac{\pi(1-\nu^2)}{2\tan\alpha}\left(1-e^{-\frac{tE}{\eta}}\right)\frac{F_0}{E}}$
SLS	$\left(\frac{E_1+E_2}{E_1E_2}-\frac{1}{E_2}e^{-\frac{E_2 t}{\eta}}\right)[2(1+\nu)]$	$\sqrt{\frac{\pi(1-\nu^2)}{2\tan\alpha}\left(\frac{E_1+E_2}{E_1E_2}-\frac{1}{E_2}e^{-\frac{E_2 t}{\eta}}\right)F_0}$

Table 2.2: **Three-dimensional compliance $J(t)$ and indentation $h(t)$ for a conical indenter applying a constant force F_0 at $t = 0$ on the five viscoelastic models (Fig. 2.4)**. $J(t)$ (first column) and $h(t)$ (second column), computed from Eq. (2.47) and the 1D relaxation strain functions $\varepsilon(t)$ of the five viscoelastic models (Section 2.3).

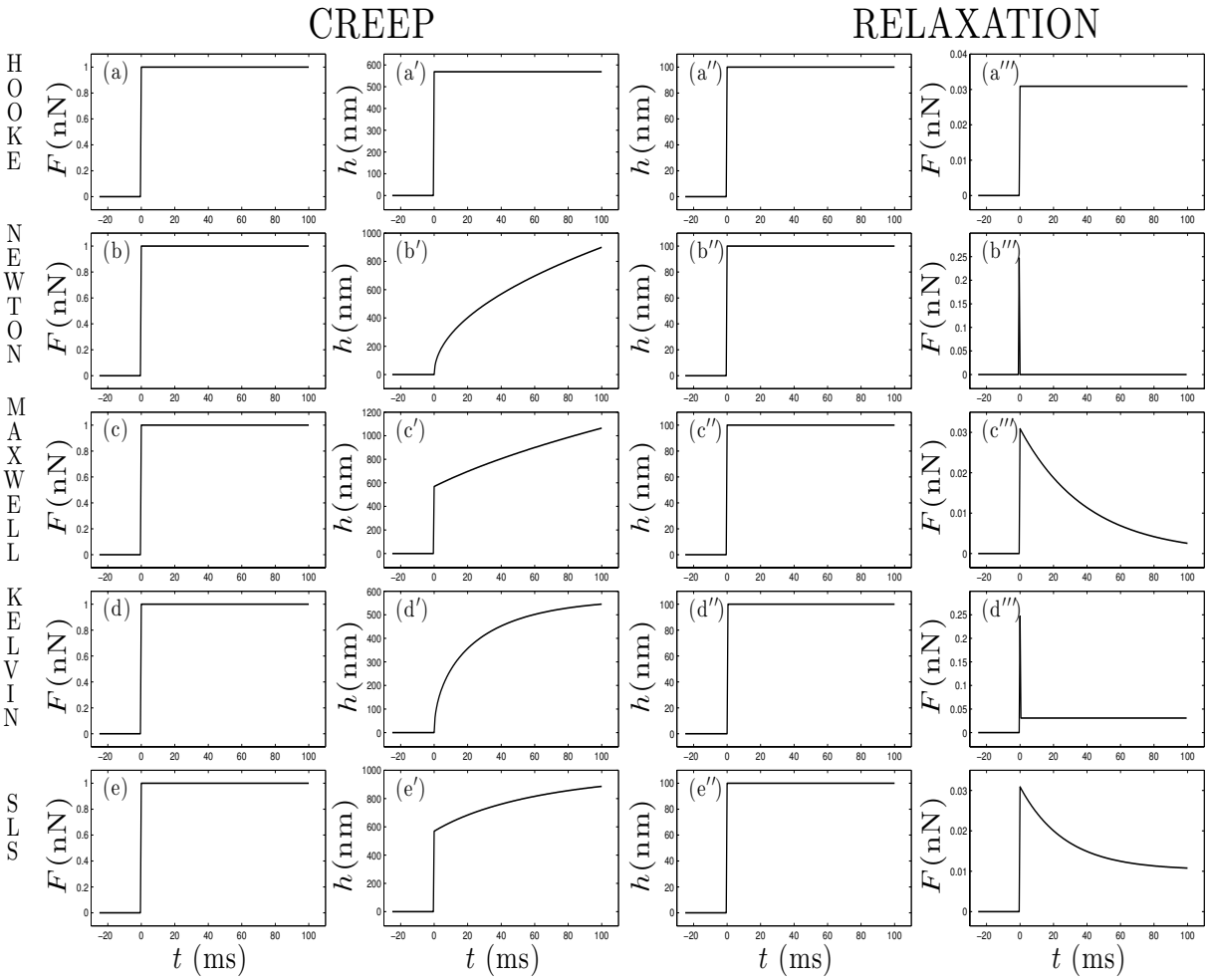

Figure 2.8: **Temporal responses of the five viscoelastic models during creep and relaxation experiments with a conical shape indenter.** Indentation ($h(t)$) and force ($F(t)$) responses for a Hookean solid (a-a‴), a Newtonian fluid (b-b‴), a Maxwell model (c-c‴), a Kelvin-Voigt model (d-d‴), and a SLS model (e-e‴). For creep, F_0 was fixed at 1 nN. For relaxation, the indentation h_0 was fixed at 100 nm. Parameter values: $E = E_1 = 10$ kPa, $E_2 = 5$ kPa, $\eta = 400$ Pa.s, $\alpha = 20°$ and $\nu = 0.5$.

If the AFM cantilever is moving at constant velocity V_0, then the indentation writes:

$$h(t) = \begin{cases} 0 & \text{for} \quad t < 0 \,, \\ V_0 t & \text{for} \quad t \geqslant 0 \,. \end{cases} \tag{2.49}$$

Thus, for $t > 0$, Eq. (2.44) becomes [Cheng & Yang, 2009]:

$$F(t) = \frac{8{V_0}^2 \tan\alpha}{\pi(1-\nu)} \int_0^t G(t-\tau)\tau d\tau \,. \tag{2.50}$$

When differentiating Eq. (2.50) with respect to time, we obtain

$$\int_0^t G(\tau)d\tau = \frac{\pi(1-\nu)}{8{V_0}^2 \tan\alpha} \frac{dF(t)}{dt} \,. \tag{2.51}$$

When further differentiating Eq. (2.51), we get the following relation between the shear relaxation modulus $G(t)$ and the second derivative of the force $F(t)$ with respect to time:

$$G(t) = \frac{\pi(1-\nu)}{8{V_0}^2 \tan\alpha} \frac{d^2F(t)}{dt^2} \ . \tag{2.52}$$

Since $h = V_0 t$ for $t > 0$, Eq. (2.52) can be rewritten as:

$$G(h) = \frac{\pi(1-\nu)}{8 \tan\alpha} \frac{d^2F(h)}{dh^2} \ . \tag{2.53}$$

This equation shows that when conical shape indenters are pushed inward the material with constant velocity, the shear relaxation modulus is straightforwardly computed from the second derivative of the force F [Shimizu, 1999; Cheng & Cheng, 2004].

In Table 2.3, are listed the expressions of the force $F(t)$ obtained for the five viscoelastic models when introducing in Eq. (2.50) the shear relaxation modulus expressions for $G(t)$ previously reported in Table 2.1. Since in the AFM experiments, we record the force F as a function of indentation h, we have reported in Table 2.4 the expressions of the force-indentation curves (FICs) $F(h)$ and their first and second order derivatives with respect to the indentation h for the five viscoelastic models. A typical illustration of these FICs is reported in Fig. 2.9 for the set of parameters $V_0 = 1$ μm.s^{-1}, $E = E_1 = E_2 = 10$ kPa, $\eta = 400$ Pa.s, $\alpha = 20°$ and $\nu = 0.5$.

The Hooke model predicts a parabolic shape of the FIC $F(h)$ (Fig. 2.9 - first line) which is precisely the Sneddon model (Eq. (2.41)) and which does not depend on the velocity V_0. The FIC second derivative is constant for $t > 0$ and gives direct access to the Young modulus E. The Newtonian model predicts a linear increase of $F(h)$ upon indentation, with a slope proportional to V_0 (Fig. 2.9 - second line). Concerning the Maxwell model solution (Fig. 2.9 - third line), a characteristic relaxation time $\tau_R = \eta/E$ comes into play (Table 2.4). At short times ($t \ll \tau_R$), when performing the following approximation:

$$e^{-\frac{t}{\tau_R}} = e^{-\frac{Et}{\eta}} \approx 1 - \frac{Et}{\eta} + \frac{1}{2}\left(\frac{t^2E^2}{\eta^2}\right) \ , \tag{2.54}$$

we get rid of the viscous term η, and recover the quadratic (in h) Sneddon model (Eq. (2.41)) at the lowest order in h. On the opposite, at longer times ($t \gg \tau_R$), then

$$e^{-\frac{t}{\tau_R}} \approx 0 \ , \tag{2.55}$$

and the Maxwell model FIC behaves linearly with h like for a Newtonian fluid. Thus, the Maxwell model behaves as an elastic spring when it has not enough time to react to the mechanical stimulus, whereas on longer time experiments the viscous component becomes prominent in controlling its mechanical response. The Kelvin-Voigt model relaxation solution is the sum of an elastic and a viscous term. On the opposite to the Maxwell model, a viscous (resp. elastic) is obtained at short (resp. long) times (Fig. 2.9 - fourth line). For the SLS model, the time

model	**F(t)**
Hooke	$\frac{2\tan\alpha}{\pi(1-\nu^2)}\, E\, t^2\, V_0^2$
Newton	$\frac{4\tan\alpha}{\pi(1-\nu^2)}\, \eta\, t\, V_0^2$
Maxwell	$\frac{4\tan\alpha}{\pi(1-\nu^2)} \left(t - \tau_R + \tau_R e^{-\frac{t}{\tau_R}} \right) \eta\, V_0^2$ (*)
Kelvin	$\frac{2\tan\alpha}{\pi(1-\nu^2)} \left(Et + \eta\right)\, t\, V_0^2$
SLS	$\frac{2\tan\alpha}{\pi(1-\nu^2)} \left[\frac{E_1 E_2}{E_1+E_2} \left(\frac{t}{\tau_R}\right)^2 + 2\frac{E_1^2}{E_1+E_2} \left(\frac{t-\tau_R}{\tau_R} + e^{-\frac{t}{\tau_R}} \right) \right] V_0^2\, \tau_R^2$ (**) ()

(*) $\tau_R = \dfrac{\eta}{E}$, (**) $\tau_R = \dfrac{\eta}{E_1+E_2}$, () [Cheng & Cheng, 2004]

Table 2.3: **Three-dimensional relaxation solutions $F(t)$ for the five viscoelastic models probed using a conical indenter moving with constant speed V_0.** The expressions of $F(t)$ were obtained by introducing the specific relaxation moduli $G(t)$ for each model (Table 2.1) inside Eq. (2.50).

$\tau_R = \dfrac{\eta}{E_1+E_2}$ separates two parabolic Hookean like FIC regimes [Cheng & Cheng, 2004]:

$$F(h) = \begin{cases} \dfrac{2\tan\alpha}{\pi(1-\nu^2)} E_1 h^2 & \text{for } t \ll \tau_r\ , \\ \\ \dfrac{2\tan\alpha}{\pi(1-\nu^2)} \dfrac{E_1 E_2}{E_1+E_2} h^2 & \text{for } t \gg \tau_r\ , \end{cases} \tag{2.56}$$

that correspond to a constant shear modulus $G = E_1$ and $G = \dfrac{E_1 E_2}{E_1+E_2}$ respectively.

Altogether, we can conclude that for 3D conical indentation experiments performed at constant velocity V_0, there are two ways to estimate the shear relaxation modulus $G(h)$: (i) by computing the second derivative of the force with respect to h (Eq. (2.53)) or (ii) by fitting the FICs with the relaxation solutions $F(h)$ listed in Table 2.4. In any case, the dependence of the FICs on the velocity V_0 will be the signature of some viscous component underlying the mechanical properties of the considered material. Distinguishing viscous from elastic components

(a) *Hooke*	$F(h) = \frac{2\tan\alpha}{\pi(1-\nu^2)} E h^2$
	$F'(h) = \frac{4\tan\alpha}{\pi(1-\nu^2)} E h$
	$F''(h) = \frac{2\tan\alpha}{\pi(1-\nu^2)} E$
(b) *Newton*	$F(h) = \frac{4\tan\alpha}{\pi(1-\nu^2)} V_0 \eta h$
	$F'(h) = \frac{4\tan\alpha}{\pi(1-\nu^2)} V_0 \eta$
	$F''(h) = \frac{4\tan\alpha}{\pi(1-\nu^2)} V_0 \eta \delta(h)$
(c) *Maxwell*	$F(h) = \frac{4\tan\alpha}{\pi(1-\nu^2)} V_0 \eta \left[h - h_R \left(1 - e^{-\frac{h}{h_R}} \right) \right]$
	$F'(h) = \frac{4\tan\alpha}{\pi(1-\nu^2)} V_0 \eta \left(1 - e^{-\frac{h}{h_R}} \right)$
	$F''(h) = \frac{4\tan\alpha}{\pi(1-\nu^2)} V_0 \eta e^{-\frac{h}{h_R}}$
(d) *Kelvin*	$F(h) = \frac{4\tan\alpha}{\pi(1-\nu^2)} E \left(h^2 + 2 h h_R \right)$
	$F'(h) = \frac{4\tan\alpha}{\pi(1-\nu^2)} E \left(h + h_R \right)$
	$F''(h) = \frac{4\tan\alpha}{\pi(1-\nu^2)} E \left(1 + h_R + \delta(h) \right)$
(e) *SLS*	$F(h) = \frac{4\tan\alpha}{\pi(1-\nu^2)} \frac{E_1}{E_1+E_2} \left\{ E_2 \frac{h^2}{2} + h_{R_1} \left[h - h_{R_1} \left(1 - e^{-\frac{h}{h_{R_1}}} \right) \right] \right\}$
	$F'(h) = \frac{4\tan\alpha}{\pi(1-\nu^2)} \frac{E_1}{E_1+E_2} \left[E_2 h + E_1 h_{R_1} \left(1 - e^{-\frac{h}{h_{R_1}}} \right) \right]$
	$F''(h) = \frac{4\tan\alpha}{\pi(1-\nu^2)} \frac{E_1}{E_1+E_2} \left(E_2 + E_1 e^{-\frac{h}{h_{R_1}}} \right)$

$h_R = V_0 \tau_R = V_0 \frac{\eta}{E}$, $\qquad h_{R_1} = V_0 \tau_{R_1} = \frac{V_0 \eta}{E_1}$

Table 2.4: **FICs $F(h)$ and their first and second derivatives for the five viscoelastic models, probed with a conical indenter moving at constant velocity V_0.** The expressions for $F(h)$ were obtained from the expressions of $F(t)$ in Table 2.3 with $h = V_0 t$.

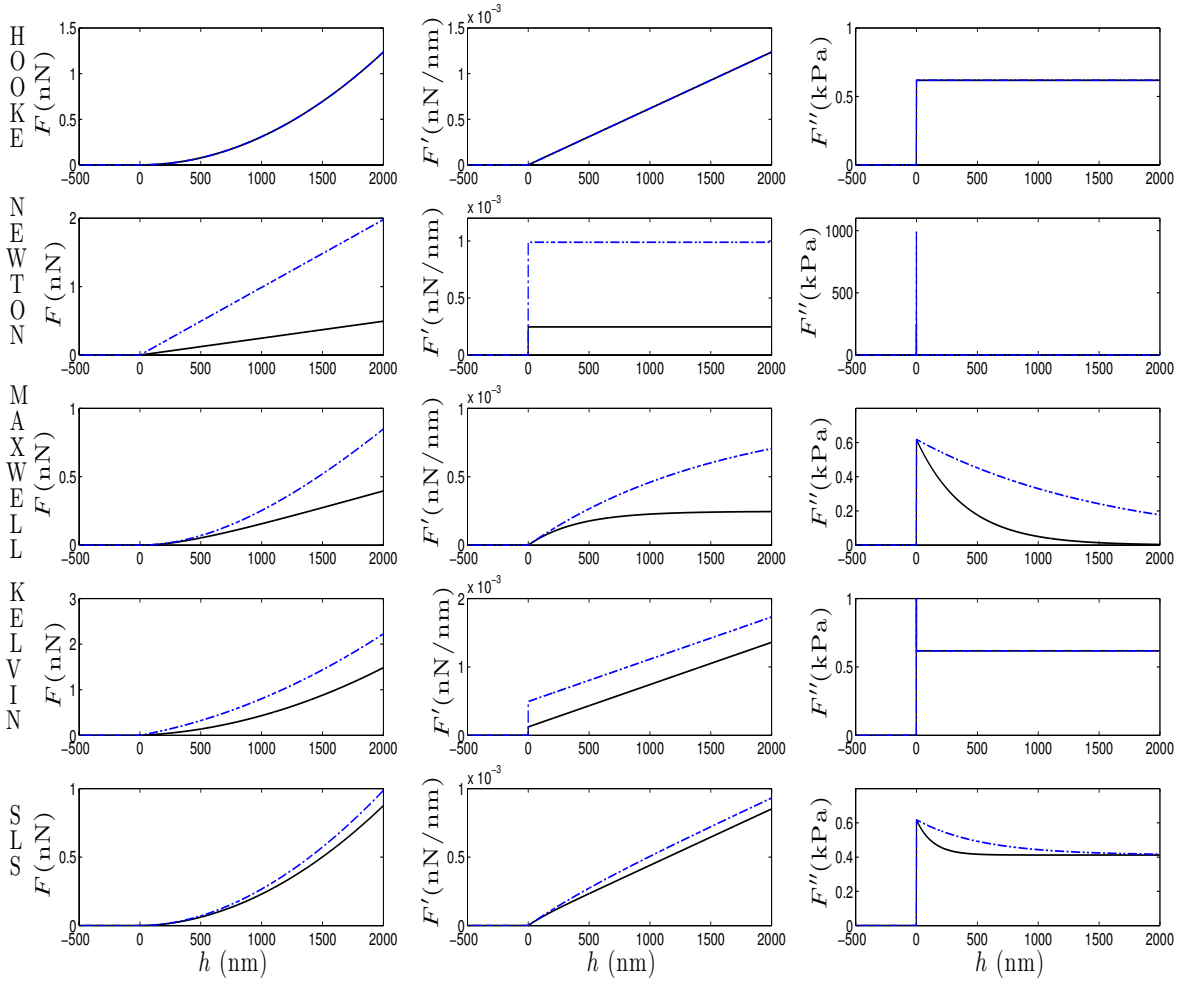

Figure 2.9: **Plots of the FICs for the five viscoelastic models (Table 2.4).** First line: Hooke model. Second line: Newton model. Third line: Maxwell model. Fourth line: Kelvin-Voigt model. Fifth line: SLS model. $F(h)$ vs h (first column), $F'(h)$ vs h (second column), $F''(h)$ vs h (third column). Parameter values: $V_0 = 1\mu$m/s (black solid lines) and 4 μm/s (blue dashed-dotted lines), $E = E_1 = 1$ kPa, $E_2 = 2$ kPa, $\eta = 400$ Pa.s, $\alpha = 20°$ and $\nu = 0.5$.

will therefore require to perform experiments with different indenter velocities, as reported in Section 2.6 for the analysis of myoblasts and myotubes.

2.6 Confrontation of the mechanical models with AFM indentation experiments

To quantify the mechanical properties of myoblasts and myotubes, we performed two sets of AFM experiments: (i) fixed velocity indentation experiments, from which we retrieved the temporal evolution of the shear relaxation modulus $G(t)$ and (ii) fixed stress experiments from which we retrieved the temporal evolution of the compliance $J(t)$. In this section, we use the first technique to compare experimental and theoretical (predictions of the five viscoelastic models) FICs.

2.6.1 Description of the AFM force-indentation curves (FICs)

AFM has been used as a mechanical nano-indenter [Kuznetsova, 2007; Kirmizis & Logothetidis, 2010; Haase & Pelling, 2015] to collect the stress to strain relationship of living adherent C2C12 myoblasts and myotubes in their growth medium (GM). Through this operation mode, the tip located at the far end of the micrometric cantilever is moved perpendicularly toward the probed sample *via* piezoelectric actuators. Knowing the stiffness of the cantilever and recording its deflection and position, it is possible to measure the tip-sample interaction forces as a function of the tip-sample distance [Leite, 2003, 2007; Sirghi, 2008]. Both loading (the tip moving toward the sample) and unloading (withdrawing the tip from the sample) FICs can be recorded. The position of the cantilever is given by the variable Z (μm). The vertical deflection (ΔD) (nm) of the cantilever is proportional to the force applied to the sample; it can be converted to a tip-sample interaction force ΔF (nN) knowing the stiffness of the cantilever k (N/m) through the Hooke's law: $\Delta F = k\Delta D$ and the sensitivity of the photodiode quadrant. As reported in Chapter 5 (Materials and Methods), the stiffness k of the cantilever can be calibrated by the thermal noise method [Hutter & Bechhoefer, 1993; Sader, 1999; Stark, 2001]. In this section, the AFM tip is driven at constant speed (V_0) perpendicularly to the sample plane (along the Z direction) until a defined deflection value (*i.e.* a setpoint force value) is reached at cantilever position Z_{sp}. Then the cantilever is withdrawn at the same constant speed (-V_0) back to its starting Z position. These non-stationary fixed velocity indentation experiments allow a rapid survey of the temporal changes of the shear relaxation modulus $G(t)$ which is related to the second derivative of the FICs (Section 5.4.4.b) [Cappella & Dietler, 1999; Huang & Lu, 2006; Attard, 2007; Tripathy & Berger, 2009; Chen, 2014; Digiuni, 2015; Laperrousaz, 2016a].

In Fig. 2.10(a-c) are reported loading and unloading FICs recorded on a glass micro slide in air, on a collagen-coated petri dish in liquid (growth medium, GM) and on an adherent C2C12 myoblast in liquid (GM) respectively. As shown in Fig. 2.10(a'-c'), the loading curves can be divided in three main parts: (i) a non-contact part (green), (ii) an in-contact part (magenta), and (iii) a transition between the non-contact and the in-contact parts, which may be discontinuous in air (jump-to-contact, Fig. 2.10(a',a")) or continuous in liquid (black dots in Fig. 2.10(b',b") and (c',c")). The non-contact parts are relatively flat portions of the curves that will be used as a force reference F_0 (Fig. 2.10, black dashed lines) since the interaction of the cantilever with the sample is negligible. As discussed in the following sections, these parts of the FICs depend on the cantilever scan velocity (hydrodynamic drag) which will require some readjustment of the non-contact FICs baseline (Section 2.6.3). During the cantilever movement downward the sample surface, the tip starts interacting with the sample and the FIC departs from the zero-line. The Z position where the FICs slope exceeds some threshold defines the so-called contact point Z_c. Characterizing this non-contact/ in-contact transition zone with picoNewton (pN) resolution was used to provide a description of the interaction forces between the cantilever tip and the sample surface at the atomic level [Weisenhorn, 1992; Leite, 2007]. Depending on the distance between the tip and the sample surface, their dielectric polarizabilities and their surface charges, attractive and/or repulsive forces may be involved in the FICs. A typical example of capillary adhesion force in air is given in Fig. 2.10 (a-a"), where the attractive force is exerted on the tip by a water meniscus. Indeed when AFM is operated in air, depending on the humidity, a water meniscus between the tip and the sample surface can be formed by capillary condensation [Schenk, 1998; Rozhok, 2004]. When the cantilever tip penetrates the substrate water film, a small capillary film is formed on its surface and bends the cantilever downward that manifests in

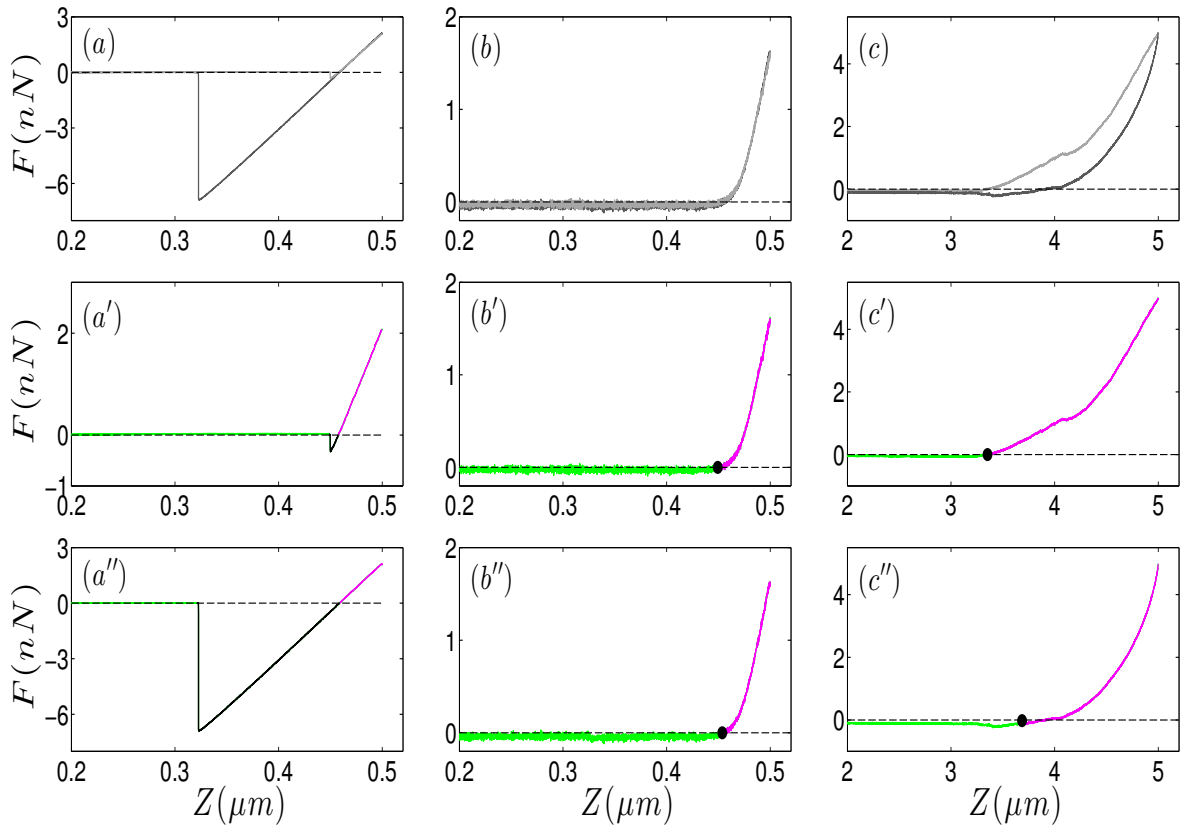

Figure 2.10: **Examples of different FICs collected with the fixed velocity AFM operation mode**. FICs collected on a glass micro-slide in air (a-a"), a collagen-coated petri dish in liquid (growth medium) (b-b"), and an adherent C2C12 myoblast in liquid (growth medium) (c-c"). In light (resp. dark) grey is shown the loading (resp. unloading) curve (a-c). The same data are shown when splitting loading (a'-c') and unloading (a"-c") curves. In green (resp. magenta) are drawn the non-contact (resp. contact) regions. The black dot marks the transition between the in-contact and the non-contact parts of the FICs. The scans were performed using the same SNL-10 triangular cantilever (nominal $k = 0.06$ N/m) moving at the same constant velocity ($V_0 = 1$ μm/s).

a drop of the force (Fig. 2.10 (a')). During the unloading curve, the capillary film has migrated further along the tip surface and it requires a larger force to separate the tip from the sample surface (Fig. 2.10 (a")). The last portion of the loading FICs corresponds to the in-contact part, which represents the region between the contact point Z_c and the setpoint of maximum vertical deflection (*i.e.* the maximum force) Z_{sp}. The analysis of this part of the FICs will provide quantitative informations about the mechanical properties of the sample. In this regard, AFM can be considered as an elastography instrument [Costa, 2004a]. In the next sections, we will focus on the in-contact portions of the FICs captured on single living cells (myoblasts and myotubes).

2.6.2 Experimental validation of constant tip velocity FICs

Before further analyzing AFM FICs operated at different constant scan velocities, we must check whether the AFM electronic feedback loop switches correctly from positive (toward the

sample) to negative (outward the sample) velocities. In Fig. 2.11, we plot the three quantities $Z(t)$, $F(t)$ and $dZ(t)/dt$ during loading and unloading scans, recorded from different spots of a nuclear region of a C2C12 myoblast cell, at the two scan velocities: 0.25 μm/s (first and second lines) and 10 μm/s (third and fourth lines). For a low scan velocity, $Z(t)$ exhibits a gap

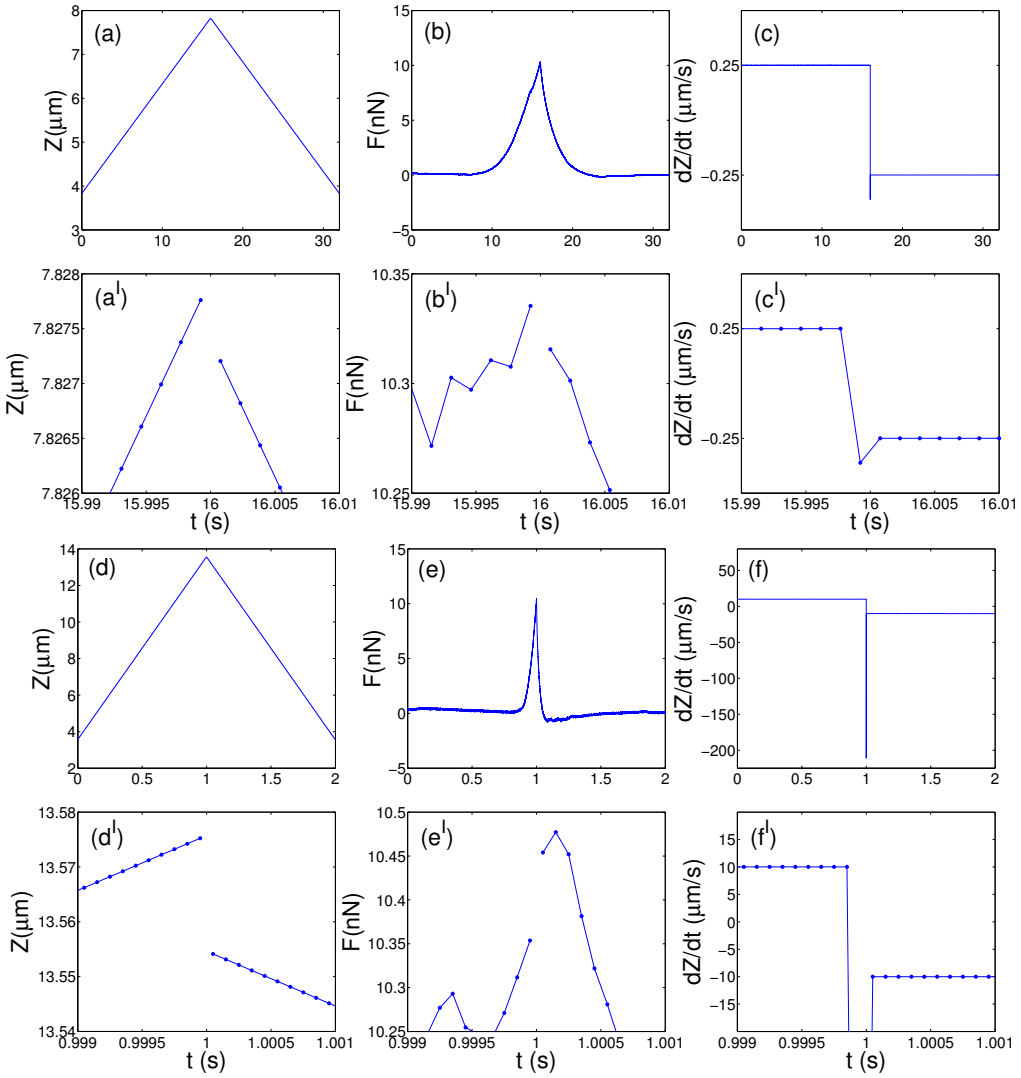

Figure 2.11: $Z(t)$, $F(t)$ **and** dZ/dt **recorded at slow (resp. high) constant scan velocity during a complete indentation cycle on the nuclear region of the same myoblast cell**. (a-c) Low speed scan ($V_0 = 0.25$ μm/s). (a'-c') Zoom on the (a-c) curves around the scan reversal time $t = 16$ s. (d-f) High speed scan ($V_0 = 10$ μm/s). (d'-f') Zoom on the (d-f) curves around the scan reversal time.

$\Delta Z_g \sim 0.6$ nm at scan reversal time $t = 16$ s (Fig. 2.11 (a')). Note that ΔZ_g is not larger than the vertical resolution of the piezoelectric transducer. Surprisingly, at the faster scan velocity (10 μm/s), ΔZ_g reaches a much greater value ~ 21 nm (Fig. 2.11 (d')). This ΔZ_g is probably due to hysteresis effects in the piezoelectric tubes which cannot be compensated at this fast scan velocity. Another amazing observation is that the force gap upon scan reversal ΔF_g is also much larger at faster scan velocity $\Delta F_g \sim 0.1$ nN (Fig. 2.11 (e')) than at slower scan velocity $\Delta F_g \sim -0.02$ nN (Fig. 2.11 (b')). The ratio $\mathcal{R}_g = \Delta F_g / \Delta Z_g$ also depends on the scan velocity, namely $\mathcal{R}_g = 0.005$ nN/nm for $V_0 = 10$ μm/s and $\mathcal{R}_g = -0.03$ nN/nm for $V_0 = 0.25$ μm/s. Both

these $\mathcal{R}_g$ values are smaller in magnitude than the cantilever nominal stiffness $k = 0.06$ nN/nm, meaning that the viscosity of the sample (a living myoblast cell) is slowing down the reversal of the FICs curves. The $dZ(t)/dt$ curves (Fig. 2.11(c,c') and (f,f')) confirm that upon scan reversal the piezoelectric scanner is quite instantaneously switching from a positive to a negative velocity. The negative peak in the $dZ(t)/dt$ curves at scan reversal corresponds to a fast braking of the AFM control system to achieve a negative acceleration of the cantilever. To summarize, from these experimental curves recorded at different scan velocities, we can conclude that: (i) the scan speed is maintained during the whole scan (stability in both downward and upward scans), and (ii) the transition between loading and unloading scans is limited to one single time step.

2.6.3 Impact of viscous drag on FICs

To analyze the effects of the liquid chamber viscosity on FICs, we used triangular cantilevers (Bruker's Sharp Nitride Lever (SNL), D cantilever). Besides random thermal excitations from the liquid chamber, the cantilever may capture two other forces: (i) the viscous drag force that slows down the penetration of the cantilever beam though the liquid chamber, and (ii) the visco-elasticity or visco-plasticity of the living C2C12 myoblast that refrains the penetration of the cantilever tip inside its body. Here, the central domain of a myoblast was indented above its nucleus (denoted as NUC-D) with increasing scan velocities ($V_0 = 0.1$ to 10 μm/s). 10 loading and unloading FICs were recorded for each scan velocity (Fig. 2.12). For each scan velocity, the sampling rate was adjusted to collect the same number of data points ($\approx 2\ 10^4$). The travel distance of the cantilever was adjusted to the scan velocity (the slower the scan, the shorter the distance): 3 μm for $V_0 = 0.1$ μm/s, 4 μm for $V_0 = 0.25$ and 0.5 μm/s, 5 μm for V_0 =1, 2, 4 and 6 μm/s and 10 μm for $V_0 >$ 6 μm/s. As already reported in liquid AFM experiments [Radmacher, 1996; Sader, 1998; Vinogradova, 2001; Alcaraz, 2002; Janovjak, 2005; Mendez-Mendez, 2014], a solid cantilever moving through a liquid is slowed down by an hydrodynamic drag force. This hydrodynamic drag causes the cantilever to bend in the opposite direction to its displacement. In other words, the friction between the cantilever and the surrounding liquid leads to a shift of the cantilever deflection in the opposite direction of its movement. This phenomenon is well known and it has also been used as an alternative technique to calibrate the cantilever spring constant k [Maeda & Senden, 2000; Craig & Neto, 2001].

Hydrodynamic drag forces can be estimated from the non-contact parts of the FICs as an hysteresis between the loading and the unloading curves [Hoh & Engel, 1993; Radmacher, 1996]. The phenomenon is highlighted in Fig. 2.13, where the FICs of Fig. 2.12 are zoomed around $h = Z - Z_c \in [-500$ nm, 100 nm]. The hydrodynamic drag force (F_d) for a sphere moving toward a wall in a liquid chamber is described by the following formula [Brenner, 1961; Alcaraz, 2002; Janovjak, 2005; Despeyroux & Ambari, 2012; Mendez-Mendez, 2014]:

$$F_d(H) = \frac{6\pi\eta a^2}{H} V_0 \ , \tag{2.57}$$

where η is the viscosity of the medium, a the sphere radius, H the distance between the sphere and the wall, and V_0 the relative velocity between the sphere and the liquid. This relationship can be extended to AFM cantilevers of different shapes by introducing in Eq. (2.57) an effective radius a_{eff} of the cantilever and an effective size H_{eff} of the cantilever tip, leading to an effective cantilever-sample separation $H + H_{\text{eff}}$ where H is the separation of the cantilever tip with the

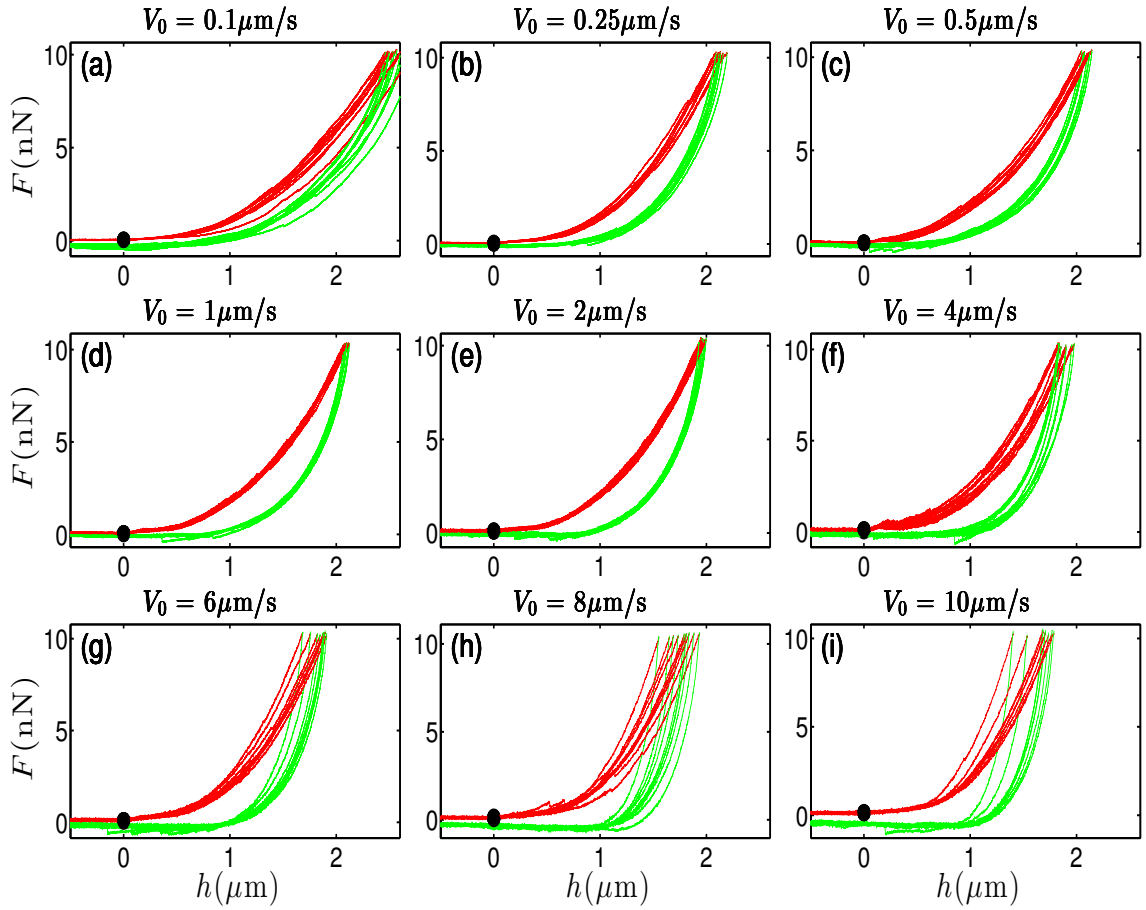

Figure 2.12: **FICs recorded on a living C2C12 myoblast nuclear domain (NUC-D) for different scan velocities**. Loading (resp. unloading) FICs are plotted in red (resp. green). The black dots mark the contact position $Z = Z_c$. For each scan velocity $V_0 = 0.1$ μm/s (a) to $V_0 = 10$ μm/s (i), 10 FICs were recorded sequentially. The indentation depth is defined as $h = Z - Z_c$ (the Z axis is oriented downward).

solid substrate [Roters & Johannsmann, 1996; Alcaraz, 2002]:

$$F_d(H) = \frac{6\pi\eta a_{\text{eff}}^2}{H + H_{\text{eff}}} V_0 \, . \tag{2.58}$$

From Eq. (2.58), an equivalent drag factor $b(H)$ can be defined as:

$$b(H) = \frac{F_d}{V_0} = \frac{6\pi\eta a_{\text{eff}}^2}{H + H_{\text{eff}}} \, . \tag{2.59}$$

Thus the drag force depends on the cantilever geometry, the viscosity of the medium, the scan velocity and the cantilever tip to substrate distance. Due to the velocity gradient imposed by the null fluid velocity at the substrate surface (hydrodynamic boundary layer), the drag force F_d increases when approaching the cantilever to the sample surface [Happel & Brenner, 1983; Craig & Neto, 2001; Hodges, 2002; Mendez-Mendez, 2014]. The extra-term H_{eff} introduced in Eq. (2.58) limits the divergence of F_d when H tends to zero, since the presence of the cantilever tip limits the approach of the cantilever body to the solid substrate. When the sample is no

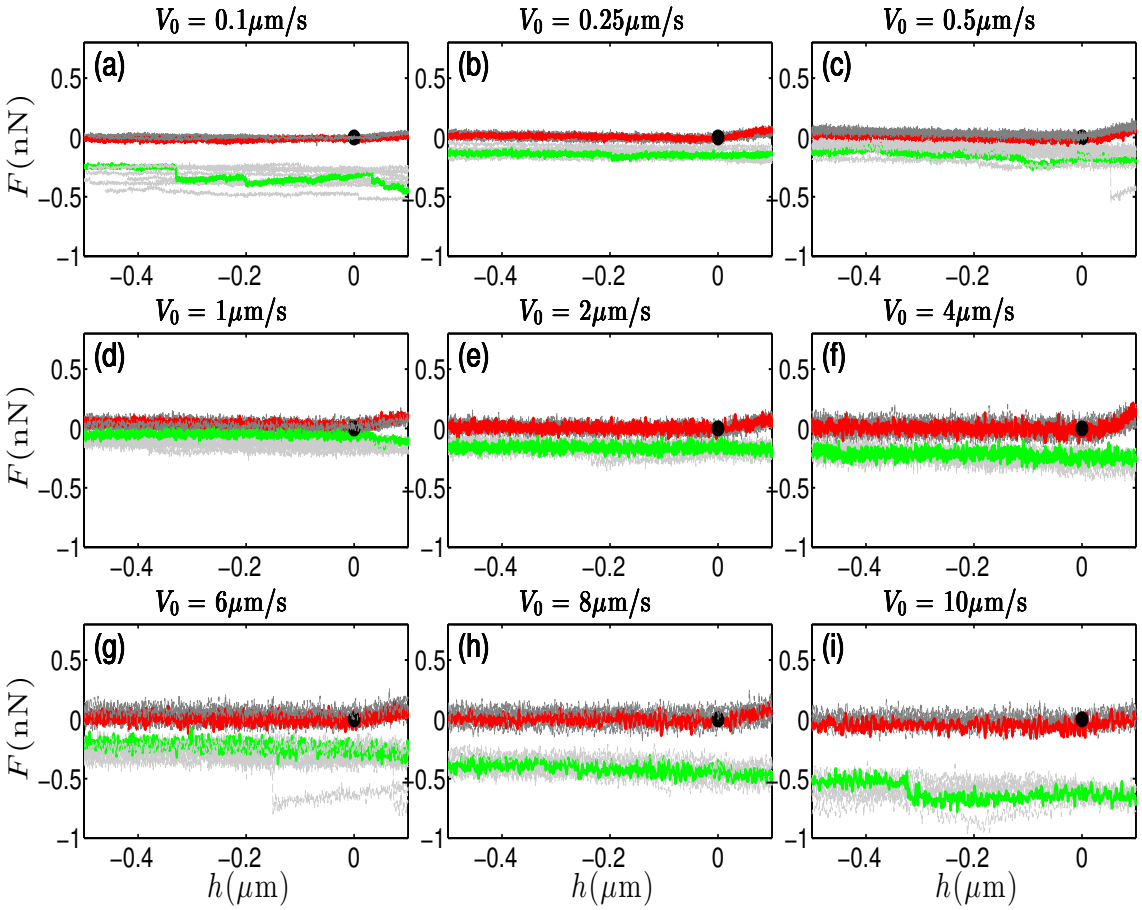

Figure 2.13: **Effect of the hydrodynamic drag on the non-contact parts of FICs recorded for different scan velocities**. For each dataset in Fig. 2.12, the separation between the loading and the unloading curves is shown for scan velocities ranging from 0.1 μm/s (a) to 10 μm/s (i). One individual loading FIC (red) was selected from a set of 10 FICs (dark grey). One individual unloading FIC (green) was selected from a set of 10 FICs (light grey). The contact point is marked with a black dot.

longer a rigid body but rather a soft visco-elastic material, it can be deformed by the fluid pushed ahead of the cantilever when its moves toward its interface within the liquid chamber. Thanks to a spectral decomposition of cantilever fluctuations at different distances from soft and visco-elastic polymethyl methacrylate (PMMA) layers, Roters and Johannsmann [Roters & Johannsmann, 1996] showed that the viscous drag damping is enhanced, as compared to a hard sample surface. In that case, it is necessary to introduce an effective viscosity η_{eff} that includes both the chamber liquid viscosity and the sample material visco-elasticity.

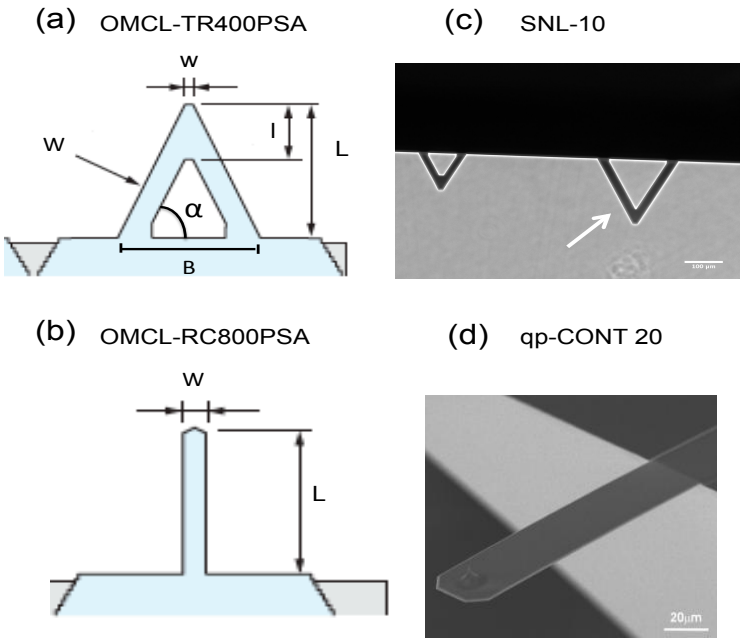

Figure 2.14: **Comparison of cantilever geometries.** Schematic of (a) the triangular (OMCL-TR400PSA) and (b) the rectangular (OMCL-RC800PSA) cantilevers used by Alcaraz *et al.* [Alcaraz, 2002]. (c) DIC image the triangular (SNL-10) cantilever. (d) SEM image of the rectangular (qp-CONT 20) cantilever. These images were downloaded from the Olympus (a,b), Bruker (c) and Nanosensors (d) websites.

shape	model	B (μm)	L (μm)	l (μm)	W (μm)	w (μm)	k (N/m)	H_{real} (μm)	H_{eff} (μm)	α (°)	a_{eff} (μm)
△	SNL-10	180	205	48	25	12.5	0.06	5.5	10.8 ± 1.3 **	65	21 ± 6 **
△	TR400PSA	166	200	75	27.9	6	0.02	2.9	5.7 ± 0.6 *	67	22 ± 6 *
□	qp-CONT 20	-	125	-	35	-	0.1	7	4.4 ± 0.2 **	-	12.3 ± 3 **
□	RC800PSA	-	200	-	20	-	0.05	2.9	1.8 ± 0.1 *	-	12 ± 3 *

Table 2.5: **Cantilever specifications** . TR400PSA and RC800PSA cantilevers parameters were obtained from the Olympus website, and H_{eff} and a_{eff} from Alcaraz *et al.* [Alcaraz, 2002]. SNL-10 and qp-CONT cantilevers geometrical parameters were estimated from transmission microscopy images, the parameters B, l and w were obtained from Bruker and Nanosensors websites. a_{eff} and H_{eff} for SNL-10 and qp-CONT (**) cantilever were extrapolated from those of Alcaraz *et al.* (*) [Alcaraz, 2002] (see text).

We used the parameters a_{eff} and H_{eff} estimated by Alcaraz *et al.* [Alcaraz, 2002] via Eq. (2.58) for triangular (OMCL-TR400PSA) and rectangular (OMCL-RC800PSA) cantilevers to compute

a_{eff}, H_{eff} and the drag factor $b(H)$ (Eq (2.59)) for triangular (SNL-10) and rectangular (qp-CONT 20) cantilevers used in the AFM experiments reported in this manuscript (Fig. 2.14).

The geometrical and mechanical (k) characteristics of these different cantilevers are reported in Table 2.5. We estimated the α angle of the triangular cantilevers (Fig. 2.14 (a)) to 65° and 67° for SNL-10 and TR400PSA cantilevers respectively (Table 2.5). We calculated the values of a_{eff} for our rectangular and triangular AFM cantilevers by assuming that the ratio of their real surface S_{real} to their effective surface $2\pi a_{\text{eff}}^2$ was invariant for a given cantilever shape. S_{real} is the surface of the cantilever that experiences the friction with the liquid medium (light blue in Fig. 2.14 (a) and (b)). Similarly, we estimated the effective tip height H_{eff} by assuming that the ratio $H_{\text{real}}/H_{\text{eff}}$ is constant for a given geometry (Table 2.5).

Eq. (2.58) gives a simple prediction for the variation of the drag force $F_d(H)$ with the distance H of the tip of the cantilever with the substrate surface. The presence of adherent cells on the solid substrate and their density (confluency) may also change the flow boundary condition when the cantilever is approaching the surface. If we consider the substrate (and not the cell surface) as the boundary plane for the hydrodynamic circulation, we have:

$$H = -h + H_{\text{cell layer}} \ , \tag{2.60}$$

where $h = Z - Z_c$ is the distance of the tip to the surface of the cell (h is negative when the tip if far from the cell and positive when it indents the cell) and $H_{\text{cell layer}}$ an effective height of the cell layer. In practice, since we do not know the effective thickness of the cell layer $H_{\text{cell layer}}$, we will instead estimate the variations of F_d and b as a function of the variable h. Introducing Eq. (2.60) in Eqs (2.58), we get:

$$F_d(h) = \frac{6\pi\eta_{\text{eff}} a_{\text{eff}}^2}{-h + H_{\text{cell layer}} + H_{\text{eff}}} V_0 \ . \tag{2.61}$$

$H^*_{\text{eff}} = H_{\text{cell layer}} + H_{\text{eff}}$ is an effective tip height that includes also the thickness of the cell layer. η_{eff} is the effective viscosity of the liquid medium close to this layer (a few micron distance).

The AFM experiments reported in this chapter were performed using triangular cantilevers SNL-10 (Bruker). The drag force F_d was first estimated from loading and unloading FICs (Fig. 2.13) collected on four different cell culture samples (two with myoblast cells and two with myotubes), for four values of the indentation distance $h = Z - Z_c$ values [-200 nm, -100 nm, -50 nm and 0 nm] and varying the cantilever scan velocity V_0 (Figs 2.15 and 2.16). F_d can actually be estimated from the difference of the approach and retract force curves, since by symmetry this difference gives twice the drag force when the tip is far enough from the cell layer. On the two examples with confluent myoblast layers, the drag force F_d increases linearly with V_0, for V_0 larger than 0.5 μm/s, consistently with Eq. (2.61) (Fig. 2.15(b,d)). For very low scan velocity (*i.e.* V_0= 0.1 μm/s), V_0 diverges, suggesting that the living myoblast layer may sense the pressure driven by the hydrodynamic drag and slow down the fluid circulation (higher viscous drag). The drag factor $b = F_d/V_0$, estimated from the slopes $\Delta F_d/\Delta V_0$ to $\sim (4 \pm 1)10^{-3}$ N s/m is larger than previous estimations on glass substrates and water filled chambers ($\sim$ 1.5 10^{-6} N s/m) [Alcaraz, 2002]. On the two examples with confluent myotube layers, the drag force F_d does not change much with V_0 for $V_0 > 2$ μm/s (Fig. 2.16(b,d)). According to Eq. (2.58), this suggests that $\eta_{\text{eff}} V_0$ is invariant, in other words that the effective viscosity η_{eff} of the liquid layer in front of the myotube layer decreases with the scan velocity $\eta_{\text{eff}} \sim 1/V_0$, as the signature of a pseudo visco-plasticity of the myotube cell layer. As for the myoblast layers, the slight

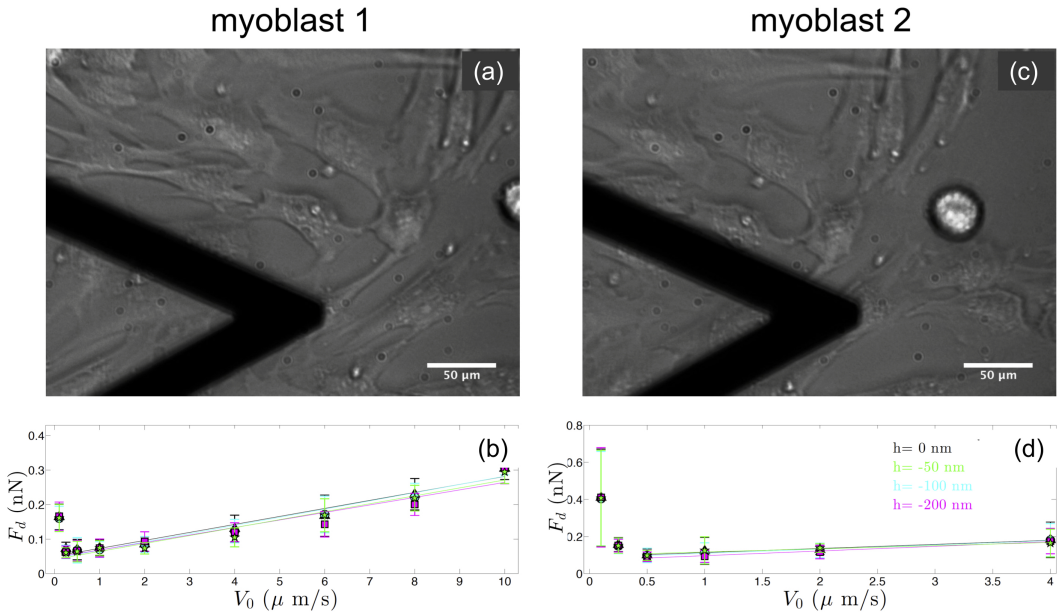

Figure 2.15: **Drag force versus scan velocity when indenting living C2C12 myoblast cells (high confluency).** F_d was measured in the non-contact part of the FICs at $h = 0$ (black), -50 (green), -100 (light blue) and -200 nm (pink). (a,c) Optical transmission images of the two myoblast cell layers. (b,d) Mean over 10 FIC recordings of F_d versus the cantilever tip velocity V_0.

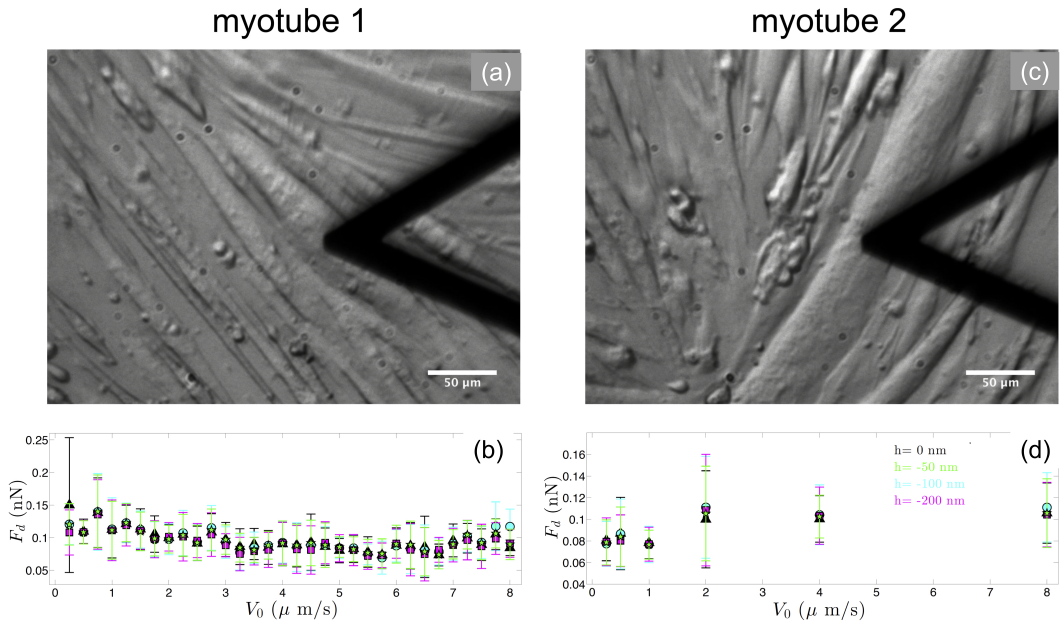

Figure 2.16: **Drag force versus scan velocity when indenting living C2C12 myotubes (high confluency).** F_d was measured in the non-contact part of the FICs at $h = 0$ (black), -50 (green), -100 (light blue) and -200 nm (pink). (a,c) Optical transmission images of the two myotube cell layers. (b,d) Mean over 10 FIC recordings of F_d versus the cantilever tip velocity V_0.

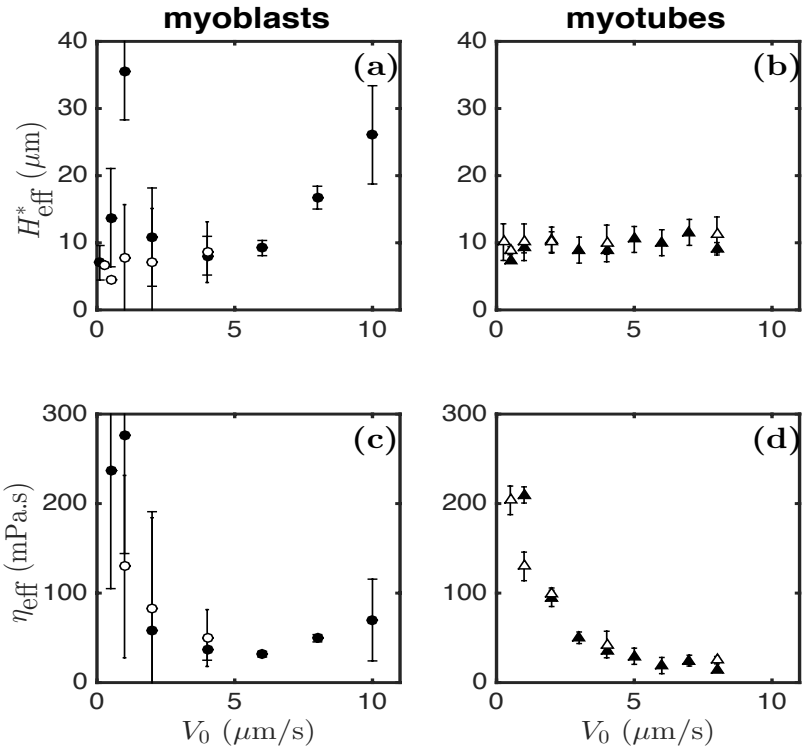

Figure 2.17: **Hydrodynamic drag parameters $H^*_{\rm eff}(V_0)$ and $\eta_{\rm eff}(V_0)$ estimated for myoblast and myotube cell layers with different cantilever scan velocities**. (a,c) Confluent myoblast cell layers: myoblast 1 (black dots) and myoblast 2 (white dots) (Fig. 2.15). (b,d) Confluent myotube cell layers: myotube 1 (black triangles) and myotube 2 (white triangles) (Fig. 2.16). The error bars were estimated from the error of the mean computed from 10 FICs.

increase of the drag force F_d at lower scan velocities ($V_0 < 2$ μm/s) suggests that the myotube layer requires an extra-drag force (due to some deformation of the cell layer), leading to a larger effective viscosity $\eta_{\rm eff}$.

To push further this analysis, we performed a linear parametrization of the $F_d(h)$ curves computed from the difference of the approach and retract FICs, with the hypothesis that $h/H^* \ll 1$ (F_d varies very slowly with h for 500 nm $< |h| <$ 1500 nm). From Eq. (2.61), we get:

$$(F_{app} - F_{ret})/2 = F_d(h) \sim \frac{6\pi\eta_{\rm eff}a^2_{\rm eff}}{H^*_{\rm eff}}(1 + \frac{h}{H^*_{\rm eff}})V_0 = A + Bh \ . \tag{2.62}$$

For each FIC, we computed the prefactor B which depends on V_0, $\eta_{\rm eff}$, $a_{\rm eff}$ and $H^*_{\rm eff}$ and the ratio of the constant term A and the prefactor B, $A/B = H^*_{\rm eff}$. Using the value $a_{\rm eff}$ estimated in Table 2.5: $a_{\rm eff} \sim 21$ μm, we plotted the evolution of both $H^*_{\rm eff}$ and $\eta_{\rm eff}$ as a function of the cantilever velocity (Fig. 2.17). We notice immediatly that the effective viscosity of the liquid layer ahead of the two groups of cell layers is much larger than the viscosity of water $\eta_w \sim 1$ mPa.s at 0 °C (about 50 times larger for the myoblast layers and 15 times larger for the myotube layers). The cell growth medium (GM) is mainly composed of high glucose (4.5 g/L) Dulbecco's modified eagle's medium (DMEM), supplemented by 20 % fetal bovine serum (FBS). The viscosity of DMEM $\eta_{\rm DMEM} \sim 0.78$ mPa.s at 37 °C [Bacabac, 2005] rises ~ 6 % when supplemented with

10 % serum [Hinderliter, 2010]. The viscosity of aqueous solutions of glucose is not different from that of water for glucose concentrations lower than 4.5 g/l [Converti, 1999; Bui & Nguyen, 2004]. Thus, the observed amplification of η_{eff} cannot be explained by the addition of serum and glucose to the DMEM.

This complete analysis confirms and reinforces the conclusions drawn from Figs 2.15 and 2.16, namely that at the lowest scan velocity both cell layers introduce an additional damping due to a larger effective viscosity η_{eff}. Henceforth, when the adherent cell layer is dense (confluency), an extra viscoelastic layer that changes the flow boundary conditions must be considered. When the viscosity of this layer $\eta_{\text{cell layer}}$ is large enough as compared to the chamber liquid viscosity η, it will amplify the slowing down of the fluid circulation close to the cell layer surface [Roters & Johannsmann, 1996]. This slowing down will be noticeable when the duration of the scan is larger than the characteristic relaxation time $\tau_R = \eta_{\text{cell layer}}/E_{\text{cell layer}}$, *i.e.* at low scan velocity V_0 ($E_{\text{cell layer}}$ is an effective elastic modulus of the cell layer). The impact of the cell layers on the hydrodynamic drag is different at larger scan velocity; whereas the effective viscosity η_{eff} of the myotube layers keeps decreasing for larger V_0 (Fig. 2.17(d)), η_{eff} of the myoblast 1 cell layer tends to increase for $V_0 > 5\mu$/s. The H^*_{eff} values estimated from this parametrization (Fig. 2.17(a,b)) are remarkably close to those estimated in Table 2.5. Another important information is given by the error-bars of these parameters estimated from 10 consecutive FICs for each cell layer and scan velocity. The dispersion of H^*_{eff} and η_{eff} values is much larger for myoblast cell layers (Fig. 2.17(a,c)) than for myotube cell layers (Fig. 2.17(b,d)), indicating a greater irreproducibility of the approach and retract force curves for the myoblast cell layers.

Similar hydrodynamically induced artifacts on AFM FICs have already been reported in the literature [Alcaraz, 2002; Sarangapani, 2010]. For instance, when $V_0 < 10$ μm/s, the drag force may overwhelm Van der Waals forces [Janovjak, 2005]. Therefore, for keeping AFM efficacy for cell mechanics characterization [Santos & Castanho, 2004; Alessandrini & Facci, 2005; Kuznetsova, 2007; Frederix, 2009; Vahabi, 2013; Cartagena & Raman, 2014; Haase & Pelling, 2015], it is important to correct properly the drag force F_d [Liu, 2010]. Contrarily to Alcaraz *et al.* [Alcaraz, 2002], we suggest to perform this estimation at reasonable distance from the contact point $h = 0$ ($h < -500$ nm), since the viscoelasticity of the cell layer could introduce artifacts (by adding an apparent drag force) in the detection of the contact point (divergence of η_{eff} at lower velocities). Our careful characterization of the drag force F_d shows that even if we perform the FICs at lower scan velocities (typically 1 μm/s in the next chapters), we have to take into account the correction of the drag since the amplification of the drag may come precisely from the cell layer and not from the liquid chamber (the softer the cell layer, the greater this amplication). The estimated larger η_{eff} values are therefore a clear marker of the implication of the living cell layer in the hydrodynamic flow boundary conditions. In the following, we will systematically perform a drag correction of the FICs before contact ($h > -500$ nm) and extrapolate the predicted $F_d(h)$ shape in the indentation regime ($h > -500$ nm).

2.6.4 Parametrization and modeling of AFM experimental FICs

In this section, we focus on the in-contact part of the FICs described in Section 2.6.3. We first compare the changes of the shape of these in-contact FICs when increasing V_0 and we address the validity of the 3D mechanical models introduced in Section 2.5 to account for the observed behavior. In a second part, we compare the mechanical works (integrals of the force curves) during cell loading and unloading and we discuss the different mechanisms that can produce

the observed dissipation losses when indenting living cells. From this preliminary comparison of myoblast cells and myotubes, we illustrate the variety of viscous damping or failure mechanisms that a cell can select to respond to a forced deformation.

2.6.4.a Deciphering the elastoplastic response of myoblasts

From now on (in this chapter and the next ones) all the FICs will be corrected for the hydrodynamic drag (as described in Section 2.6.3) and we will concentrate our effort on the in-contact part, when the cantilever tip is indenting the cell. Figs 2.18 and 2.19 show typical FICs recorded on living myoblasts in their growth medium (GM) buffer. The shape of these curves is quite reminiscent of a parabolic shape predicted for purely elastic materials (Hooke model equations in Table 2.4). The parametrization of FICs relies on a correct determination of the contact point (Section 5.4.4.c). Z_c can be estimated simultaneously to the parametrisation of the first derivatives of the FICs (Figs 2.20 and 2.21). The force derivatives were computed using a Gaussian derivative analyzing wavelet (Eqs (5.8 and (5.11)), the width of which was chosen to smear out the background fluctuations of the out of contact part of the FICs: $2\sqrt{2}s_g^{(1)} = 110$ nm. Note also that the force curves represented in Figs 2.18, 2.19, 2.22 and 2.23 were also filtered by a Gaussian wavelet (Eq. 5.10) with a much smaller width: $2\sqrt{2}s_g^{(0)} = 9$ nm. We observe on Fig. 2.20 that these FIC derivatives change with the cantilever velocity V_0, which means that they cannot correspond to a simple elastic material (Hooke model) (Table 2.4)). If the FICs of Fig. 2.18 adopt a parabolic shape, their derivatives should be linear. Actually, at very low scan velocity (< 0.5 μm), the FIC derivatives can be parametrized with a linear increasing function, but above this threshold, the range of validity of a linear behaviour shrinks to smaller Z interval. To keep a correct parametrisation of the whole FICs, we introduce a higher order nonlinear term (quadratic for the FIC derivative, cubic for the FIC):

$$\frac{dF(Z)}{dZ} = C_0 + C_1 Z + C_2 Z^2 \ , \tag{2.63}$$

corresponding to a cubic function for the FIC:

$$F(Z) = F_0 + C_0 Z + C_1 Z^2 + C_2 Z^3 \ . \tag{2.64}$$

There is a particular value of Z where the function dF/dZ computed from Eq. (2.63) crosses or becomes tangent to the horizontal axis, this value corresponds to the contact point Z_c. With this parametrization method, we get a direct estimation of the contact point Z_c (as compared to the thresholding method proposed in Section 5.4.4.c). Actually, Eq. (2.63) is strictly valid for $Z > Z_c$. Parametrizing FIC derivatives (rather than FICs) is more efficient because it diminishes the order of the polynomial, and the number of parameters; as a result, it offers a better stability and convergence of the minimization method.

This nonlinear parametrization (Eq. 2.63) was performed for both myoblasts 1 and 2 (Fig. 2.15(a) and (c)). The linear term coefficient C_1 can be assimilated to a Young modulus (see Hooke model equation for the derivative - Table 2.4):

$$E = \frac{\pi(1-\nu^2)}{4\tan\alpha} C_1 \ . \tag{2.65}$$

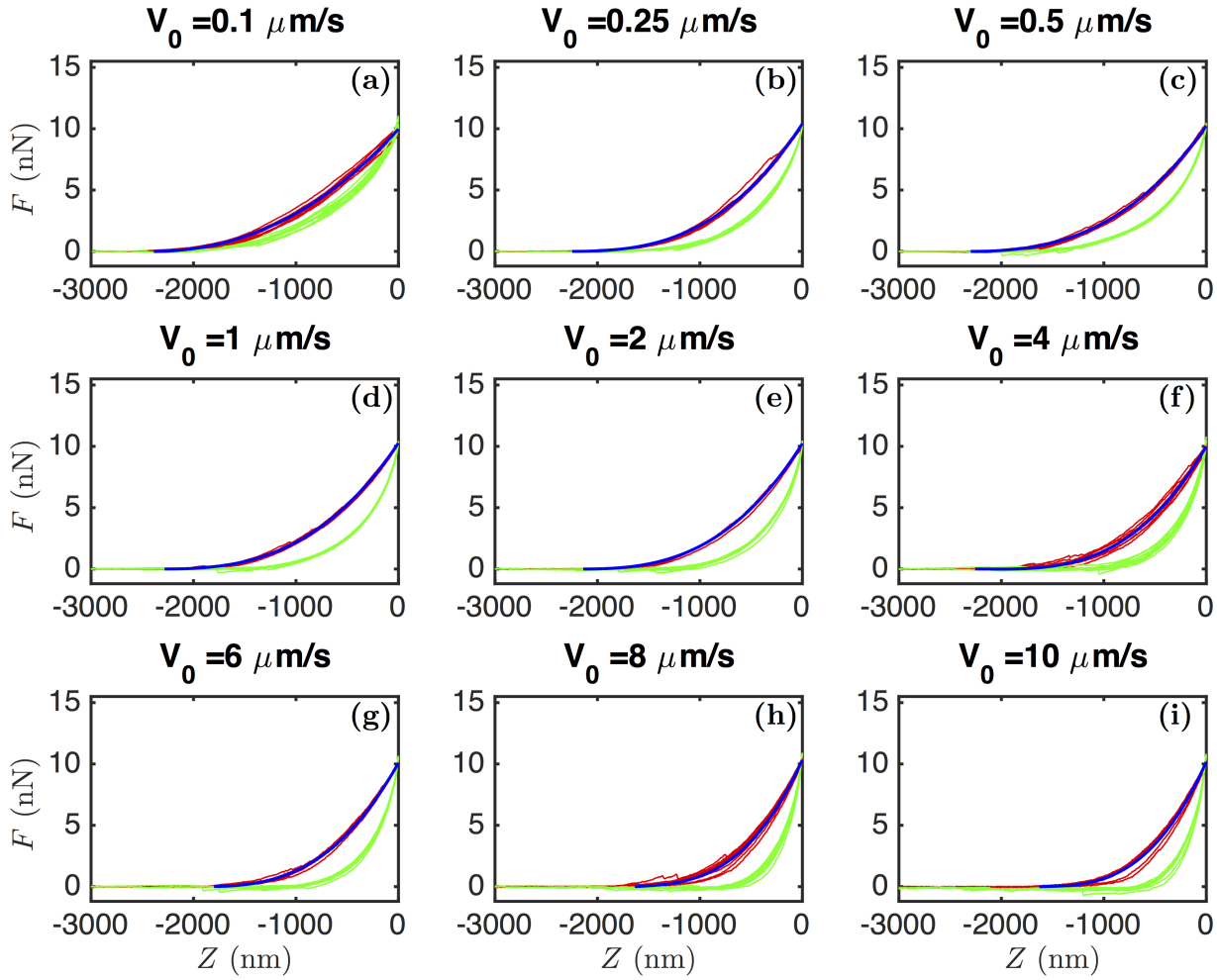

Figure 2.18: **FICs collected from myoblast 1 (Fig. 2.15(a)) for different** V_0.

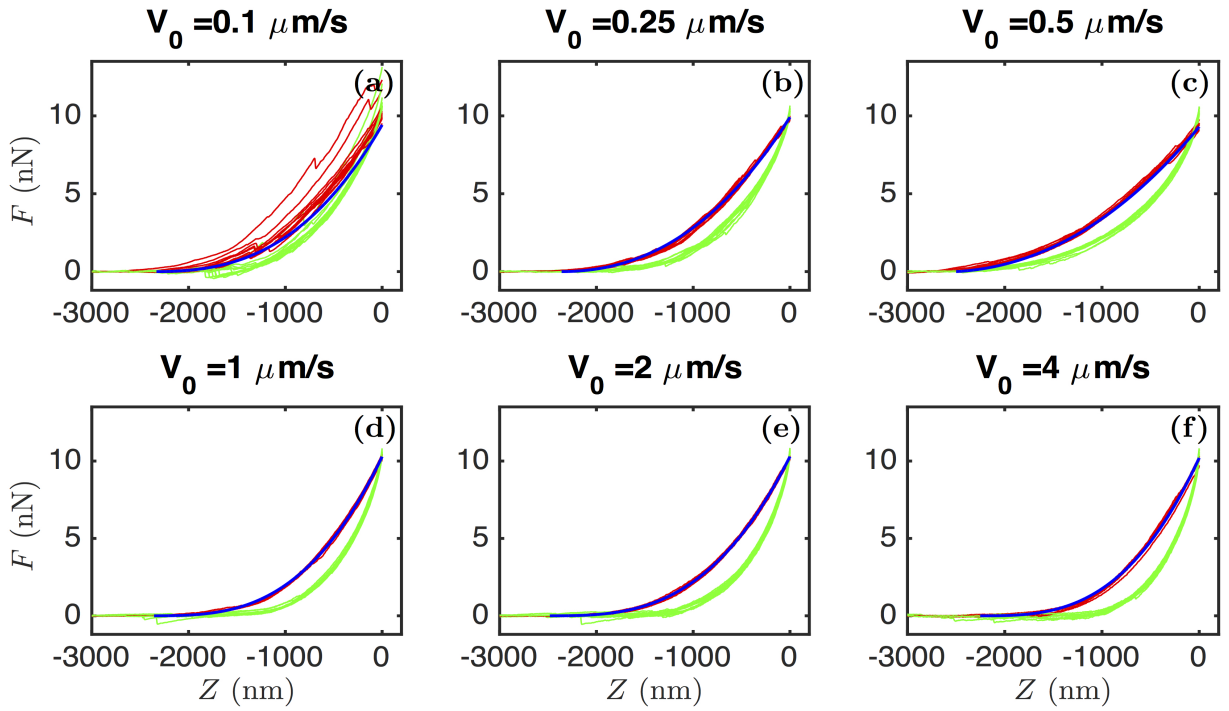

Figure 2.19: **FICs collected from myoblast 2 (Fig. 2.15(c)) for different** V_0. Both FIC series (Figs 2.18 and 2.19) were filtered from the raw FICs using a Gaussian wavelet of width $2\sqrt{2}s_g^{(0)} = 9$ nm (Eq. (5.10)). Black curve: mean of the loading FICs; blue curve: integral of the parametrization of the FIC derivatives with Eq. (2.63).

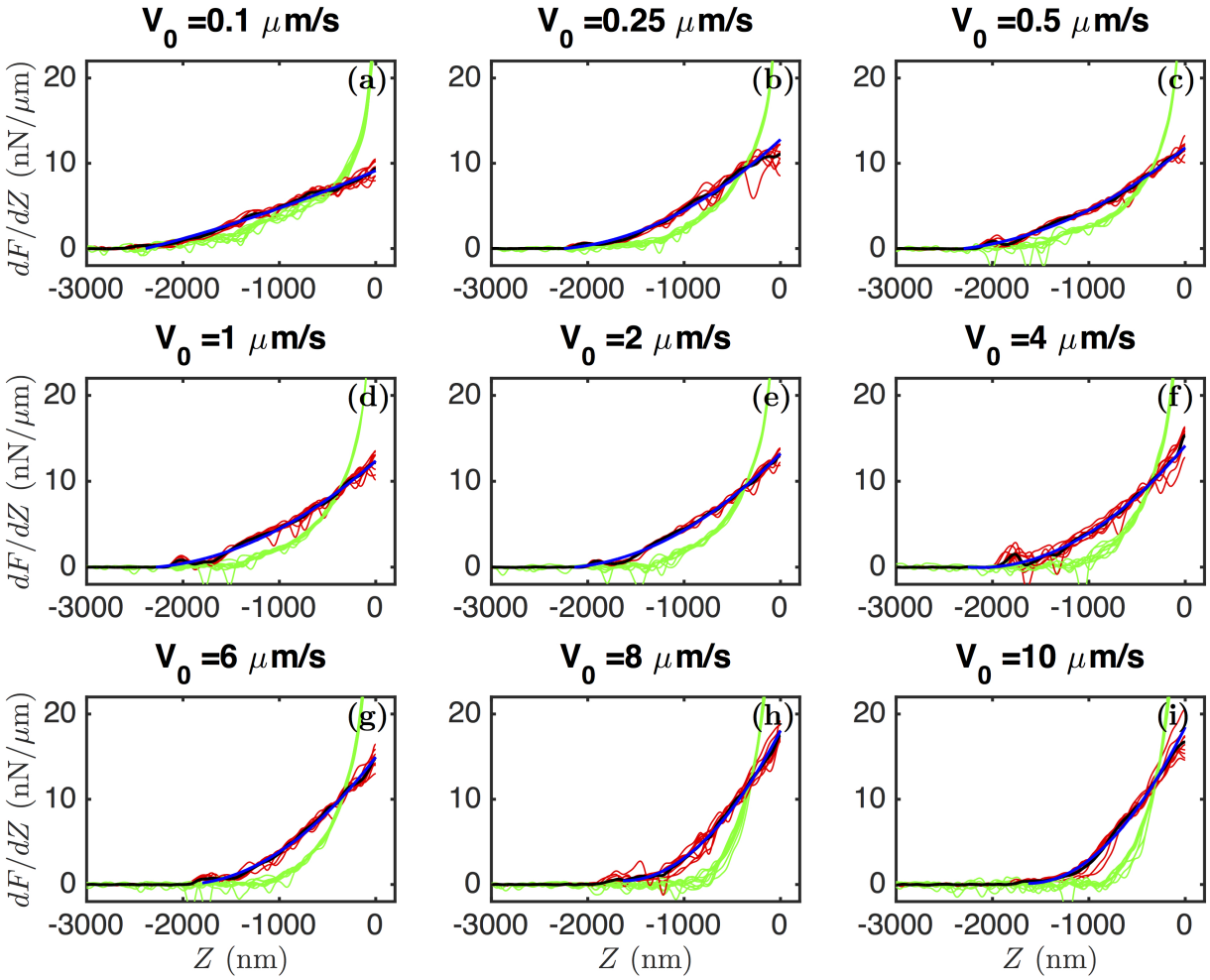

Figure 2.20: **FIC derivatives collected from myoblast 1 (Fig. 2.15(a)) for different** V_0.

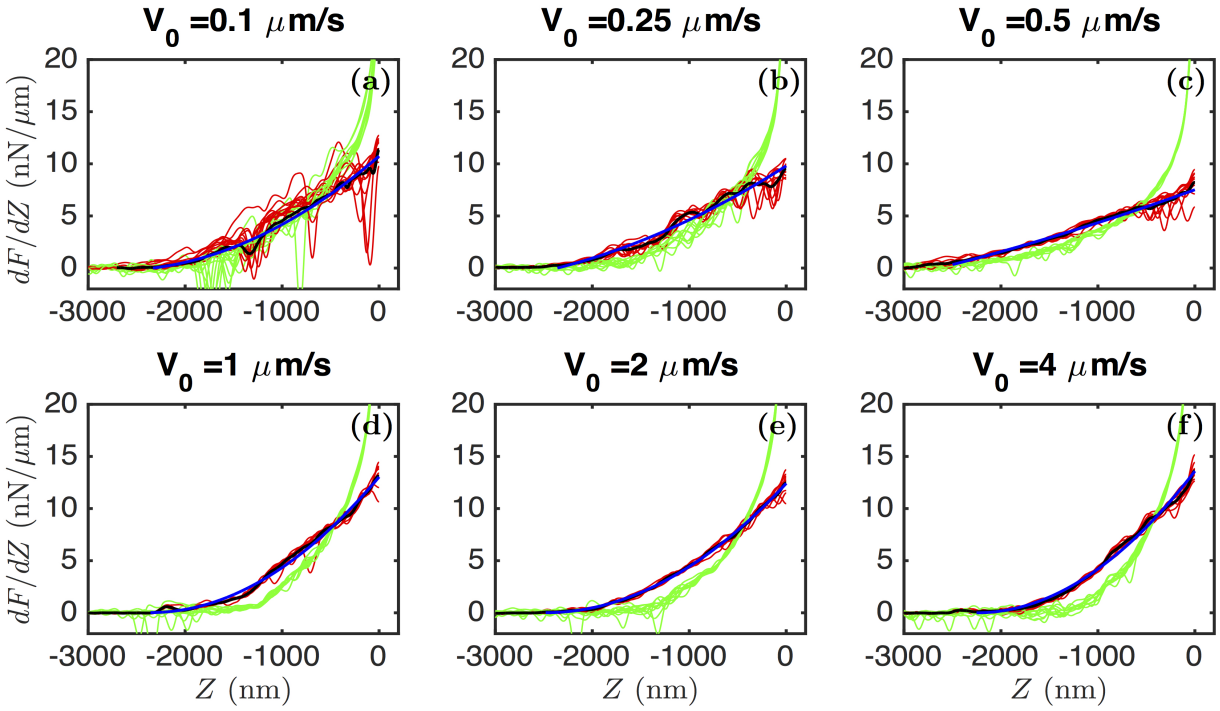

Figure 2.21: **FIC derivatives collected from myoblast 2 (Fig. 2.15(c)) for different** V_0. Both FIC derivative series (Figs 2.20 and 2.21) were computed from the raw FICs using a Gaussian derivative wavelet of width $2\sqrt{2}s_g^{(1)} = 110$ nm (Eq. (5.11)). Black curve: mean of the loading FIC derivatives; blue curve its parametrization with Eq. (2.63).

We scaled the nonlinear term coefficient C_2 similarly:

$$\lambda = \frac{\pi(1-\nu^2)}{4\tan\alpha} C_2 \ , \tag{2.66}$$

E will be given in Pascal (Pa) and λ in Pa/nm. The ratio E/λ has the dimension of a length, it corresponds precisely to a characteristic indentation length h_{NL} where the linear and nonlinear terms in Eq. (2.63) are equal. The larger h_{NL}, the closer the cell response to a Hooke-like elastic response. The fact that the FIC derivatives are curved upward when V_0 increases indicates that the nonlinear coefficient λ increases faster than E with V_0. This behavior does not correspond to a pure elastic material, it is the signature of a stiffening of the cell for faster deformation rates (strain-rate stiffening). Interestingly, we also notice in Figs 2.18 and 2.19 that the separation of the loading and unloading curves (in the in-contact zone) increases with V_0, meaning that mechanical work injected for the cell deformation is not restored upon downloading (energy loss). This effect is surprising since we would rather expect a very small or negligible impact of the strain rate on the relaxation response if these cells were pure elastic materials (Hooke model). Materials with a viscous component, for exemple Maxwell, Kelvin Voigt or SLS models (Table 2.4) are the only ones which show such a dependancy. However, the shape of the experimental FIC derivative is very different from the predictions of the Maxwell and SLS models (the FIC derivative should be curved downward and not upward at larger deformations) or of the Kelvin-Voigt model (the FIC derivative has a constant slope independent of V_0). We must therefore consider another origin, namely the plasticity of the cells, to explain these observations. Given that these myoblast cells cannot use a viscous component to slow down their deformation and that they become more rigid for larger indentation and larger scan velocity V_0 (Fig. 2.26(a,c)), we can suspect that their cross-linked filamentous cytoskeleton structure that brings off this additional nonlinearity may finally break locally (local breaks) to open the space for the penetration of the cantilever tip. These local failures and their accumulation for larger strain rate might produce an elasto-plastic response (higher nonlinearity). All these observations are summarized in Fig. 2.26 where the mechanical response of myoblasts 1 and 2 and myotubes 1 and 2 are reported. Let us emphasize the necessity to consider living cells as dynamical and active materials. These two cases of myoblasts show that for $V_0 > 0.5$ μm/s, these cells likely behave as passive breakable cross-linked networks which cannot relax fast enough to open the necessary space for the cantilever entry; an inevitable local fracture must occur. One may wonder if this reinforcement of the cells could be the consequence of the chronology that we have adopted to record these sets of FICs at different V_0. We started by the slower velocities and increased progressively V_0, we also kept the same position for the indentation (with a precision of $\sim$ 200 nm in the plane X, Y). For each scan velocity V_0, we recorded only 10 FICs to minimize the cell perturbation and we waited for at least one minute to change the velocity V_0 and collect a new set of FICs. For the slowest velocities, two minutes delay was used between each FIC set recording.

2.6.4.b Deciphering the viscoelastic response of myotubes

As for the two myoblasts 1 and 2 just above, we have reproduced the same analysis for the FICs and their derivatives for myotubes 1 and 2 (Fig. 2.16(a) and (c)). The two figures reporting the evolution of the FICs with V_0 (Figs 2.22 and 2.23) enlighten a drastic change in the behavior of these two cells. Even if the length of the whole in-contact curves (to reach the same force set-

point) does not change drastically (except for the lowest velocities $V_0 \leq 0.5$ μm/s), the curvature of these FICs is markedly decreased as compared to myoblasts. This preliminary observation is confirmed by the FIC derivatives (Figs 2.24 and 2.25), showing that not only the FIC derivatives are always smaller that those observed for the myoblasts, but that the curvature of the FIC derivatives is negative (their slope decreases with the deformation). This slow damping of the FIC derivative is reminiscent of the response of a Maxwell-type (or more generally a SLS-type) viscoelastic material (Table 2.4), where the viscous and elastic components are placed in series. We took the simplest of these two viscoelastic models (Maxwell) to parametrize these FICs. The derivative of the FICs reads as an exponential relaxation curve:

$$\frac{dF}{dZ} = D_0 + D_1 \left[1 - \exp\left(\frac{-(Z - D_2)}{D_3}\right)\right] , \tag{2.67}$$

where the coefficients D_1 and D_3 can be expressed in terms of the elastic modulus E_{cell} and the viscosity η_{cell} of the cell:

$$\eta_{\text{cell}} = \frac{\pi(1-\nu^2)}{4V_0 \tan\alpha} D_1 , \quad \text{and} \quad E_{\text{cell}} = \frac{V_0 \eta_{\text{cell}}}{h_R} = \frac{V_0 \eta_{\text{cell}}}{D_3} = \frac{\pi(1-\nu^2)}{4\tan\alpha} \frac{D_1}{D_3} . \tag{2.68}$$

D_2 corresponds to the contact point Z_c. D_1/D_3 is the slope of dF/dZ at $Z = Z_c$. The relaxation length $h_R = D_3$ describes the indentation length h where dF/dZ is reduced by $(1 - 1/e) \sim 63\%$, as compared to the value D_1 it would have reached at this indentation without damping. The fact that the FIC derivative tends to saturates is a strong indication that there must be a viscous damping process, superimposed to an elastic component for these two myotubes. This characteristic damping length h_R does not seem to change much with the cantilever scan velocity for the myotube 1 (except for the smallest V_0 values < 1 μm/s). However, for the myotube 2 (Fig. 2.25) the FIC derivative is less damped for larger V_0 values, corresponding to h_R values much larger than the whole length of indentation (~ 2 μm) (Fig. 2.25(d-f)). Given that h_R depends on V_0, E and η, we cannot conclude from the variation of h_R how the viscosity η_{cell} of the myotubes changes with V_0, since E_{cell} may also change with the scan velocity. Comparing the shapes of the loading (red) and unloading (green) FICs in Figs 2.22 and 2.23, we note that their separation is smaller than for the myoblasts and that this separation does not change much for $V_0 > 1$ μm/s, suggesting that the loss of mechanical energy is smaller for the two myotubes than for the two myoblasts.

2.6.4.c Work integrals and dissipation loss

Before concluding this study by a quantitative confrontation of the mechanical parameters estimated for the whole set of FICs (myoblasts and myotubes) (Fig. 2.26), we need to introduce a last quantity that describes the loss of mechanical work upon indentation (loading) and recovery (unloading) phases. Actually, if the process of indentation was fully reversible (ideal case of an elastic material), the loading and unloading FICs should superimpose. This is not really what we have observed on the FICs reported in this Chapter 2, consistently with previous experimental studies by other groups [Radmacher, 1996; Parre & Geitmann, 2005a,b]. We define the dissipation loss ratio D_l as the normalized sum of the work integrals between the loading and unloading FICs:

$$D_l = \frac{W_l + W_u}{W_l} . \tag{2.69}$$

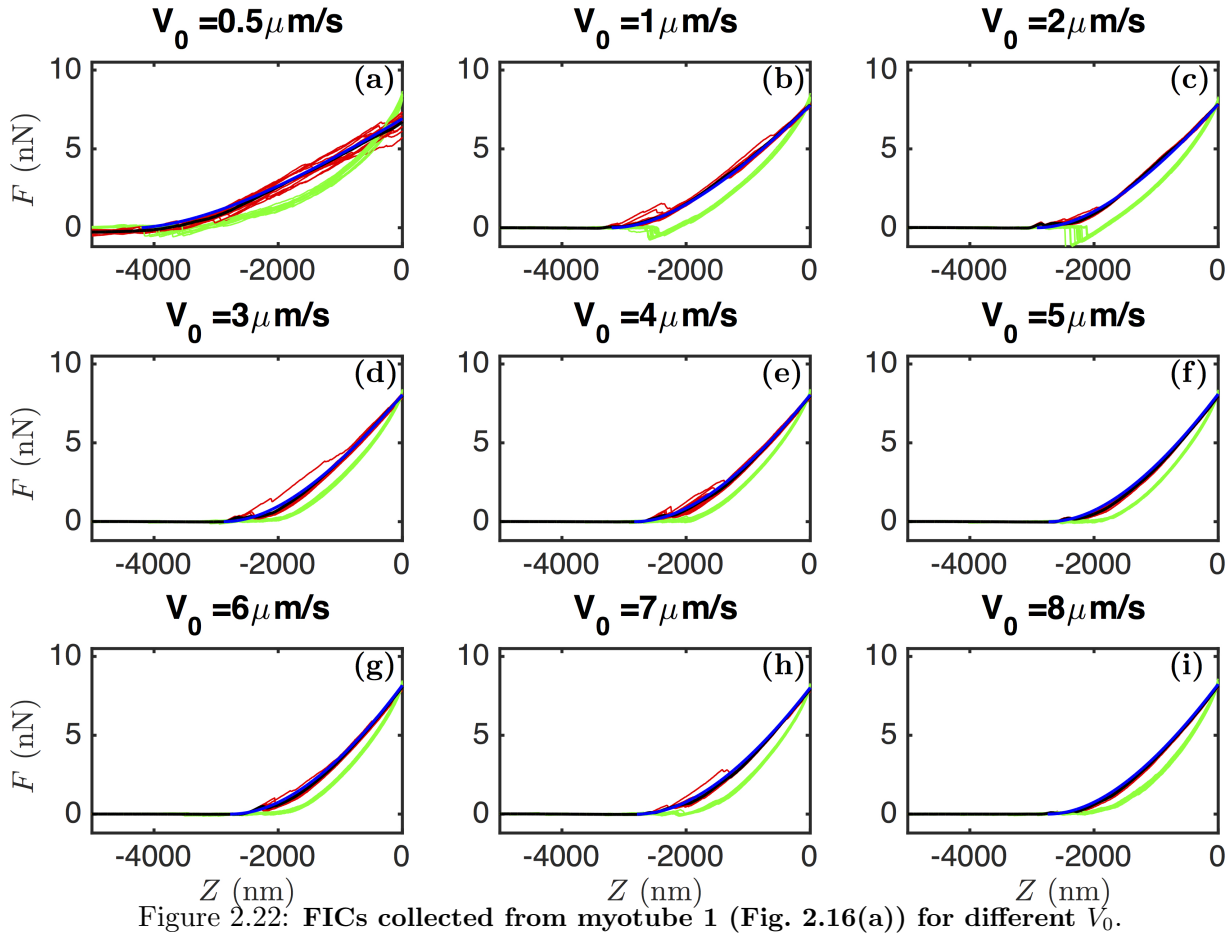

Figure 2.22: **FICs collected from myotube 1 (Fig. 2.16(a)) for different** V_0.

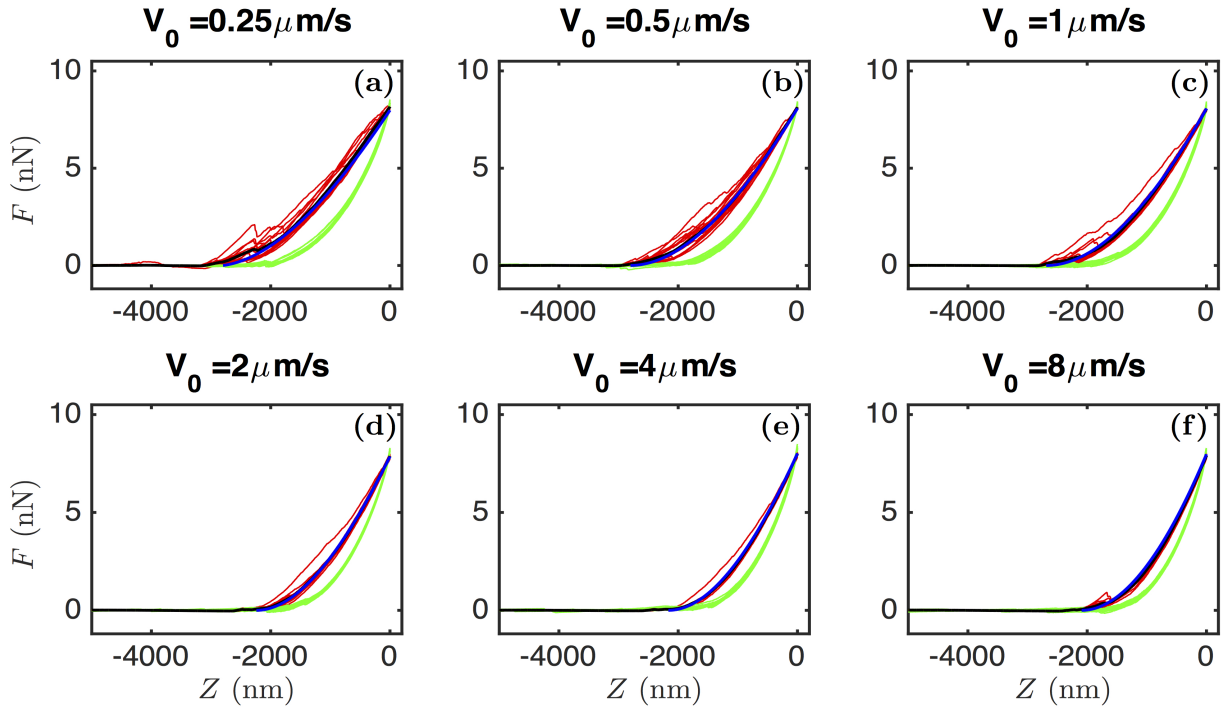

Figure 2.23: **FICs collected from myotube 2 (Fig. 2.16(c)) for different** V_0. Both FIC series (Figs 2.22 and 2.23) were filtered from the raw FICs using a Gaussian wavelet of width $2\sqrt{2}s_g^{(0)} = 9$ nm (Eq. (5.10)). Black curve: mean of the loading FICs; blue curve: integral of the parametrization of the FIC derivatives with Eq. (2.63).

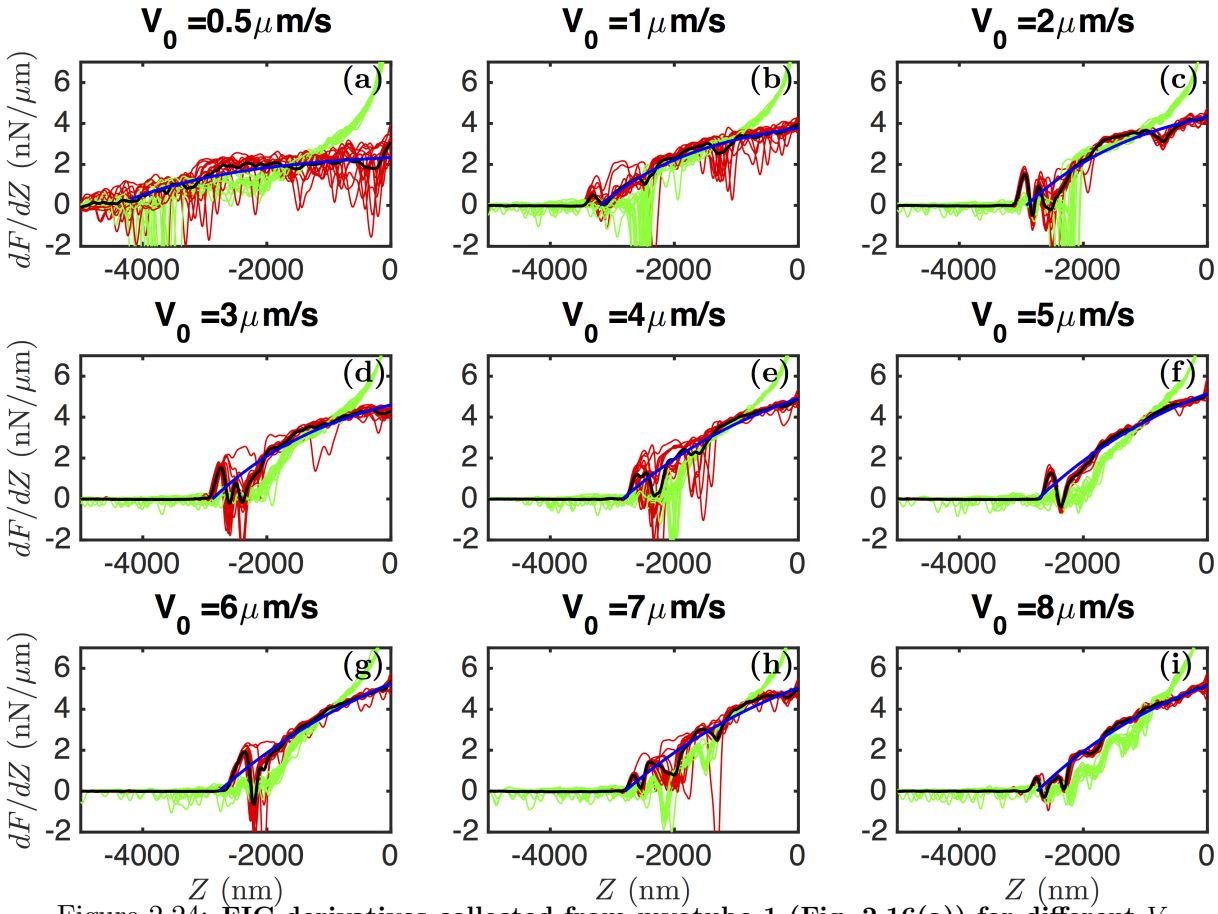

Figure 2.24: **FIC derivatives collected from myotube 1 (Fig. 2.16(a)) for different** V_0.

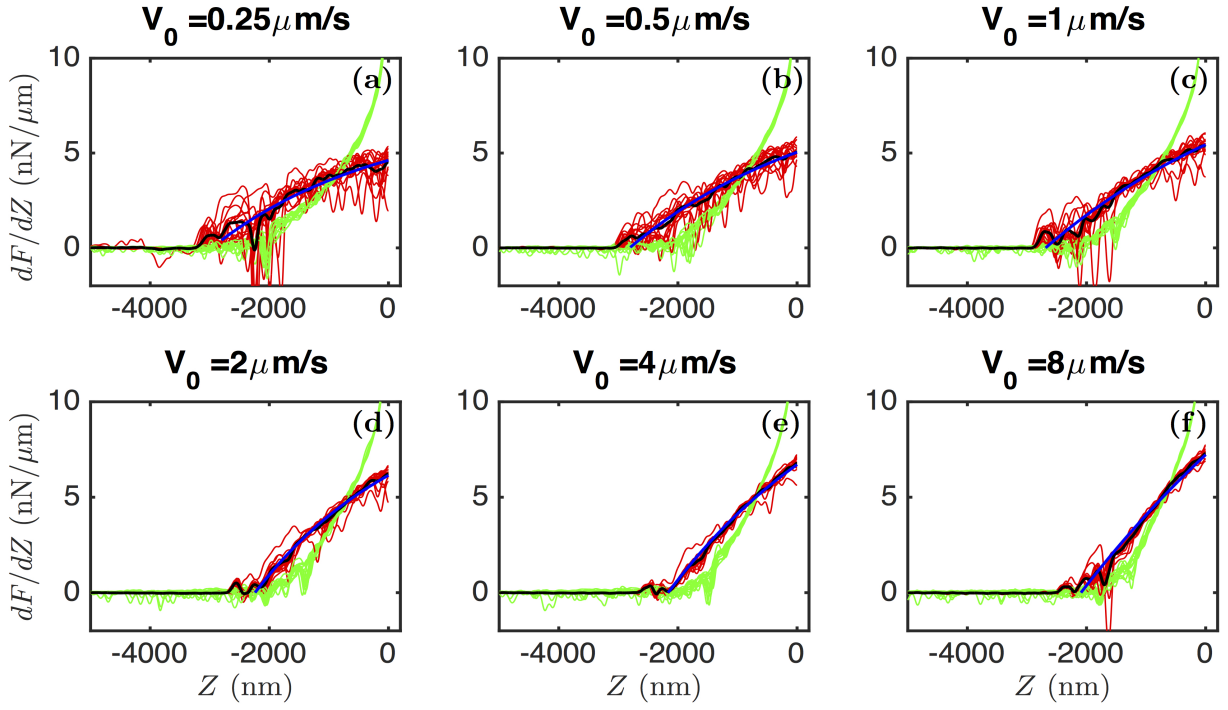

Figure 2.25: **FIC derivatives collected from myotube 2 (Fig. 2.16(c)) for different** V_0. Both FIC derivative series (Figs 2.24 and 2.25) were computed from the raw FICs using a Gaussian derivative wavelet of width $2\sqrt{2}s_g^{(1)} = 110$ nm (Eq. (5.11)). Black curve: mean of the loading FIC derivatives; blue curve: its parametrization with Eq. (2.63).

This ratio quantifies the percentage of mechanical energy that is not restored upon unloading the cantilever tip. The magnitude of D_l does not tell us how this mechanical energy is lost, it simply gives us a mechanical yield of the cell to a fixed velocity deformation.

The loading work integral W_l of the indentation force is computed from the contact point Z_c to the set point Z_{sp}:

$$W_l = \int_{Z_c}^{Z_{sp}} F(Z)dZ \ , \quad W_l > 0 \ . \tag{2.70}$$

The unloading work integral W_u of the retraction force is computed from the set point Z_{sp} to the position Z_f where it crosses the horizontal line ($F = 0$) or becomes tangent to it:

$$W_u = \int_{Z_{sp}}^{Z_f} F(Z)dZ \ , \quad W_u < 0 \ . \tag{2.71}$$

This lower bound in the Z interval for computing W_u is a way to minimise a possible bias coming from adhesion of the cantilever tip with the sample, as observed in Fig. 2.22(b,c). This effect is more likely to occur at small scan velocity where the cantilever tip spend more time in contact with the cell and get covered by extracellular matrix or cell membrane elements which promote this adhesion.

2.6.4.d Discussion

Fig. 2.26 is a good illustration of the type of quantitative informations which can be extracted from the combination of experimental, modeling and analysis methods that we developed in this chapter. If we had limited our FIC analysis to the estimate of a single elastic parameter (the Young modulus E), we would not have been able to distinguish properly viscous and plastic properties of these cells. If we had run the FIC recording at a fixed scan velocity V_0, we would have obtained Young modulus values $E \gtrsim 15$ kPa for the myoblasts and $E \sim 5$ kPa for the myotubes (Fig. 2.26(a,b)), from which we would have concluded that these two myoblast cells behave as stiffer than the two myotubes. The computation of the dissipation loss D_l would not have been discriminative at low scan velocity $V_0 \lesssim 1$ μm/s, where D_l varies as much from cell to cell than from cell type to cell type (for $V_0 = 1$ μm/s, $D_l = 0.45 \pm 0.02$ and 0.35 ± 0.02 for myoblasts 1 and 2 respectively, as compared to $D_l = 0.3 \pm 0.02$ and 0.35 ± 0.02 for myotubes 1 and 2 respectively). The shape of the FIC curves and their parametrization by elastic (linear or nonlinear) or viscoelastic models offered us a better mean to distinguish two main groups of cell behavior. On the one hand, the elasto-plastic-like cells which become more and more rigid and breakable when V_0 increases (Fig. 2.26(a,c,e)) and on the other hand the viscoelastic-like cells with a viscosity that diminishes with the rate of deformation (Fig. 2.26(b,d,f)). This decrease of η_{cell} with V_0 reminds the decrease of the effective viscosity η_{eff} of the liquid medium above the myotube cell layers (Fig. 2.17(d)). If the orders of magnitude of η_{cell} and η_{eff} differ by 6 decades, they both decrease by one order of magnitude when increasing V_0. η_{cell} must be understood as a global viscosity which includes the whole connectivity of the cell (cytoskeleton, membrane cortex) and its ability to slow down the impact of external mechanical stresses. The relaxation length h_R increases very slowly for myotube 1 when varying V_0 from 2 μm/s to 6 μm/s (Fig. 2.26(f)), whereas η_{cell} decreases by one order of magnitude (Fig. 2.26(d)). This suggests that the myotube 1 is getting more and more "liquid-like" while increasing V_0. Such a behavior can be compared to shear-thinning materials for which η decreases with the shear rate. On the opposite, for the myoblast 1, the nonlinear coefficient λ increases faster than η_{cell} (Fig. 2.26(c)),

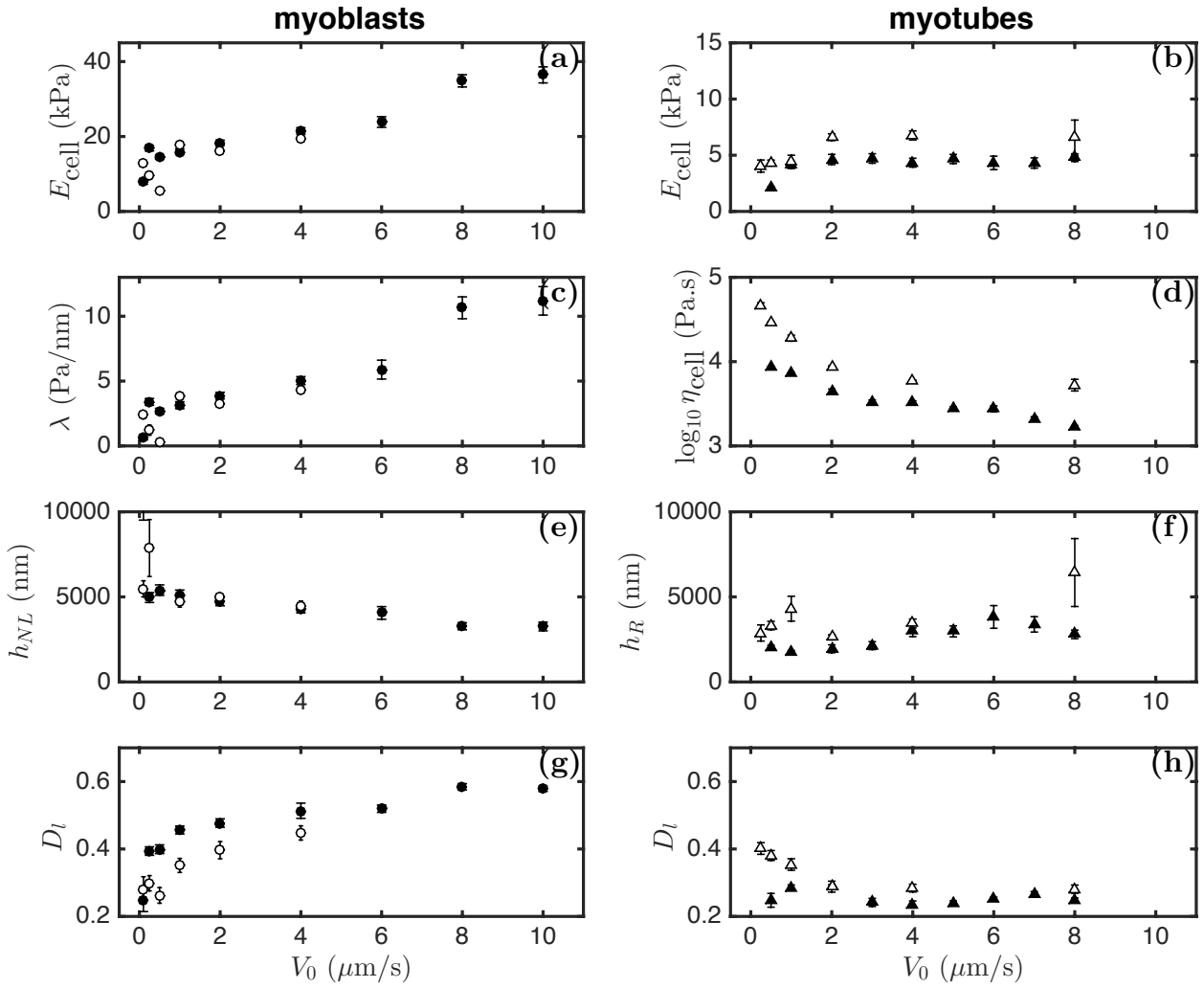

Figure 2.26: **Compilation of the mechanical parameters estimated from the four experiments on myoblasts and myotubes, performed at different scan velocity** V_0. Left column: myoblast 1(black dot) and myoblast 2 (white dot), right column: myotube 1 (black triangle) and myotube 2 (white triangle)). (a,b) Effective elastic modulus E_{cell}. (c) Nonlinear coefficient λ describing the plasticity of the myoblasts (Eq. (2.66)). (d) Effective viscosity η_{cell} of the myotubes (Eq. (2.68)) (in log-lin representation). (e) h_{NL} describing the cross-over from the linear and the nonlinear cell response (see text). (f) h_R viscous damping length. (g,h) Dissipation loss D_l computed from the difference of work integrals of the loading and unloading FICs (Eqs (2.69), (2.70) and (2.71)). The error bars in (a, b, c, d, e, f) were computed from the residuals of the least square minimisation method and the confidence intervals for each parameter estimated from the Jacobian matrix. The error bars in (g and h) were computed from the error of the mean from each 10 FIC subset.

or equivalently $h_{NL} = \eta_{\text{cell}}/\lambda$ decreases (Fig. 2.26(e)), as an indication that the cell increases its ridigity and its aptitude to local failures (plastic breaks) when increasing V_0.

This study is too preliminary to establish a clear classification between elastoplastic-like cells and viscoelastic-like cells and to make any conclusion concerning their phenotype or differentation state. In the next chapters, we will not have the opportunity to repeat the analysis that we have conducted here for different scan velocities, not only because of prohibitive time consuming statistical studies, but also because when performing many FIC recordings (10×8 to 10×15 curves) on each cell, there is a risk to anihilate or reinforce the mechanical phenotype of the cell. However, we will take advantage of the methodology that we have elaborated in this chapter to analyse and model FICs and their first derivatives.

Chapter 3

C2C12 myoblasts: from structural to mechanical properties

3.1 Structural properties of C2C12 myoblasts

The starting point of this project was the development of an experimental protocol to investigate the mechanical properties of living muscle cells. To carry out our single cell approach, we chose the mouse C2C12 myoblast cell line (Fig. 3.1). This cell line is a subclone produced by Blau et al. [Blau, 1983] of the mouse (*mus musculus*) C2 satellite cell line derived from a C3H mouse leg muscle cell line established by Yaffe and Saxel [Yaffe & Saxel, 1977]. The murine C2C12 cell line is relatively easy-to-manipulate and widely used as model for *in vitro* studies of muscle differentiation [Katagiri, 1994; Andrés & Walsh, 1996; Guttridge, 1999; Thomas, 2000; Burattini, 2004; Curci, 2008; Lee, 2009; Doherty, 2011], muscle hypertrophy and atrophy [Sharples & Stewart, 2011], and stem cell-based regenerative medicine [Menasché, 2001, 2003; Sim, 2004; Dib, 2005; Biagini, 2006; Durrani, 2010]. This cell line has also been used for mechanobiology investigations, thanks to its robustness, its ability to cope with different environments [Grover, 2012; Ramón-Azcón, 2013; Ostrovidov, 2014; Chen, 2015; Shin, 2015] and its mechanosensitive behaviour [Engler, 2004b; Palchesko, 2012; Al-Rekabi & Pelling, 2013; Ramón-Azcón, 2013; Ostrovidov, 2014; Bettadapur, 2016]. Although laboratory cell lines are altered as compared to cells *in vivo*, they have been and still are necessary and useful laboratory tools in biological research because of their potentially unlimited proliferative ability, their homogeneity, their lower cost and also for ethical reasons [Pan, 2009; Sharples & Stewart, 2011]. However, these biological models have some limitations; for example myoblast cell lines have limited differentiation capacity for long-term studies [Semsarian, 1999; Sharples & Stewart, 2011].

In this chapter, we first report on the general characteristics of C2C12 myoblast cells: their biological functions, their cell cycle and their morpho-structural features. Then, we discuss their *in vitro* behaviour such as their migration dynamics and their mechanosensitive adaptation to different culture substrates. We also describe the myogenesis process and the C2C12 myoblast differentiation. In a second step, we focus on C2C12 myoblast mechanical properties with special emphasis on the impact of different cytoskeleton perturbations on their mechanical responses. We report on some experimental results collected using different experimental setups: Differential Interference Contrast (DIC) microscopy, fluorescence labelling coupled with Confocal Microscopy, Scanning Surface Plasmon Phase Microscopy (SSPM) and Atomic Force Microscopy (AFM).

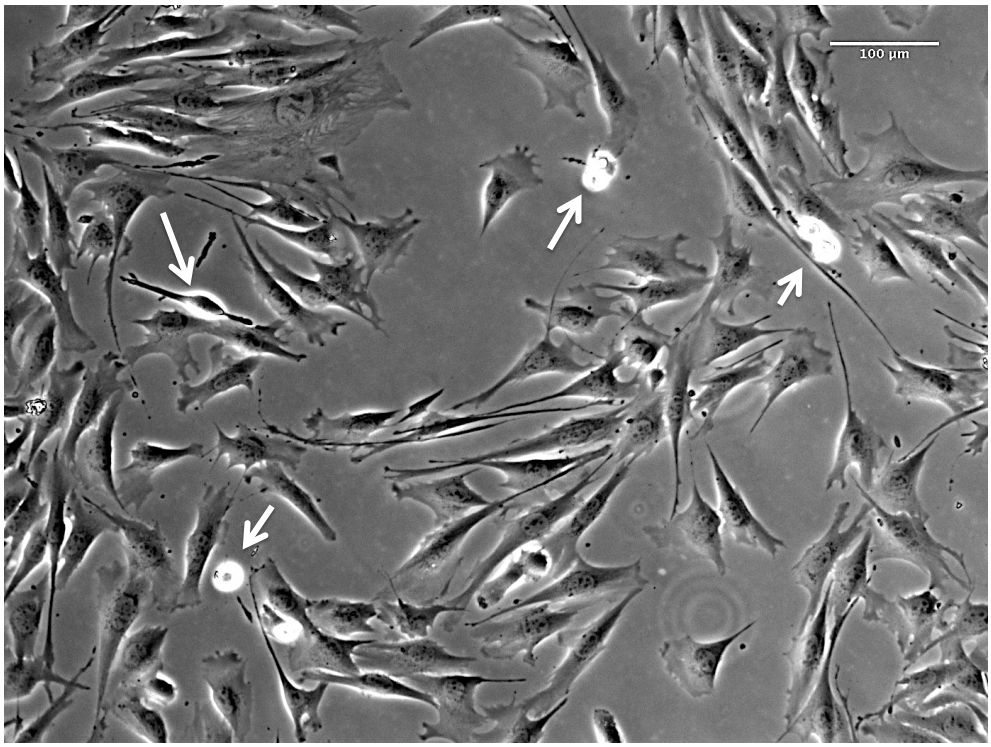

Figure 3.1: **C2C12 myoblasts on a collagen coated petri dish.** DIC image of C2C12 myoblasts adherent on a collagen coated petri dish. The arrows point to myoblast cells undergoing mitosis (at different stages). Scale bar: 100 μm.

3.1.1 Myoblasts and satellite cells

Myoblasts are mononucleated undifferentiated precursors of muscle fibers. In the vertebrate family, myoblasts are found during the entire organism lifetime from the embryonic stage to the adulthood, but they show different characteristics and specific biological functions at each stage of development. In embryos, myoblasts are generated from mesenchymal stem cells (MSCs), totipotent stem cells that can differentiate into adipocytes, chondrocytes, myocytes, fibrocytes and osteocytes. At the third week of embryonic development, myoblasts are located on the mesoderm, the middle germ layer that forms the body connective tissues (bone, cartilage, dermis, adipose tissue, blood, ...) and muscles (cardiac, skeletal and smooth) by a process known as myogenesis [Kiecker, 2016]. During the development and in the adulthood, myoblast renewal is preserved by quiescent myogenic stem cells called satellite cells. Satellite cells were discovered by Alexander Mauro who described these mononucleated cells as directly juxtaposed to frog myofibers [Mauro, 1961]. Since this discovery, and the hypothesized role of satellite cells in muscle growth and regeneration, a lot of progress has been made. Nowadays, we know that satellite cells are located in a niche between the basal lamina and the plasma membrane of myofibers, and that they have an important role in postnatal skeletal muscle adaptation, growth and regeneration [Zanou & Gailly, 2013]. In fact, although terminally differentiated multinucleate myofibers cannot undergo cell division, muscle tissues are able to reshape in response to biochemical and biophysical stimuli mainly thanks to satellite cell activity [Le Grand & Rudnicki, 2007; Sharples & Stewart, 2011]. When not activated, satellite cells are in a quiescent and transcriptionally inactive state (gap 0, G0 phase). Their morphology reflects their inactive state, displaying a

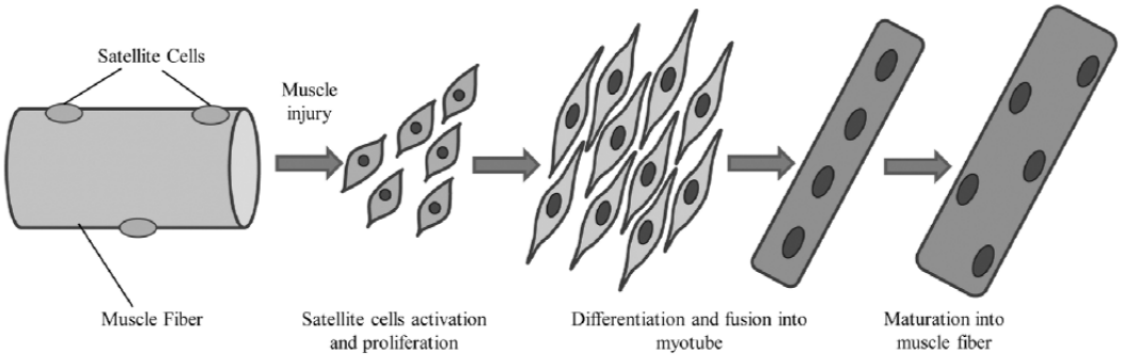

Figure 3.2: **Myogenesis and muscle regeneration after injury.** In the adult, myoblasts are located on the basal lamina of the myofibers as quiescent satellite cells. After muscle injury satellite cells are activated and myoblasts regenerate the affected muscle *via* myogenesis of new myofibers through subsequent steps: proliferation, alignment, fusion of myotubes and maturation of muscle fibers. Adapted from Journal of Physiology and Pharmacology [Ciecierska, 2013].

small nucleus with condensed chromatin [Schultz, 1978; Yin, 2013] and a rounded cell shape. In mouse, the number of satellite cells in muscles decrease from early development stage (30- 35 % of the muscle nuclei) to adulthood (2-7 %) [Allbrook, 1971; Schultz, 1974; Rudnicki, 2008]. In this quiescent state, myogenic proteins are not significantly expressed. Different experimental approaches (^{3}H thymidine labelling, electron microscopy, phase-contrast microscopy, ...) showed that, although satellite cells are quiescent in adult muscles, after myotrauma such as muscle injury, they become activated in order to provide new functional myotubes and thus to regenerate the affected myofibers (Fig. 3.2). When activated, satellite cells are released from beneath the basal lamina, they enter cell cycle, undergo mitosis and clonal expansion ensuring self-renewal. A sub-population of the activated satellite cells, the muscle precursor cells (MPCs), differentiate into functional myotubes with centrally located nuclei. These myotubes finally maturate into new muscle fibers with peripherally located nuclei [Konigsberg, 1963; Reznik, 1969; Yaffe, 1969; Moss & Leblond, 1970; Konigsberg, 1975; Mohun, 1992; Hawke & Garry, 2001; Charge & Rudnicki, 2004; Shinin, 2006; Le Grand & Rudnicki, 2007]. The equilibrium between activated satellite cells undergoing proliferation and/or differentiation is regulated by several myogenic regulatory factors (MRFs), such as transcription factors (Myf5, MyoD, MRF4) and myogenin (MYOG) [Buckingham, 2003; Kamli, 2014]. Activated satellite cells can migrate to injury sites from undamaged areas [Zanou & Gailly, 2013], as an indication that their locomotion ability is important for the achievement of their biological function. The satellite cell activation is therefore the first step in muscle regeneration. It requires the cooperation of different compartments such as the nervous, vascular and immune systems, as well as the muscle niche. In fact, it has been shown that satellite cells show reduced activation when subjected to mitogen stimulation in the case of intact myofibers [Bischoff, 1990; Yin, 2013], corroborating the role of microenviromental muscle niche on muscle regeneration [Trensz, 2015]. *In vivo*, this process depends on the extent of muscle injury, innervation, vasculature, nutrition, hormones and growth factors [Jirmanová & Thesleff, 1972; Hansen-Smith, 1979; D'Albis, 1987; McGeachie & Grounds, 1987; Phillips & Bennett, 1987; Mulvaney, 1988]. The regeneration of degenerated muscles, both in physiological (extensive exercise) or pathological (muscle injury) conditions, is therefore a well-

regulated complex process. It initiates with myofiber necrosis which stimulates inflammatory response, followed by myoblast differentiation and terminates with myofiber formation [Parise, 2008; Lepper, 2011; Murphy, 2011; Sambasivan, 2011]. C2C12 cells (Fig. 3.1) are immortalized myoblasts derived from mouse satellite cells that can switch from proliferation to differentiation according to the culture conditions. C2C12 myoblasts can differentiate into other cell types such as adipocytes and osteoblasts when stimulated with nuclear transcription factors and other molecular cues [Katagiri, 1994; Yu, 2006; Mancini, 2007]. When maintained in growth factor rich medium (growth medium, GM (see Chapter 5)), the C2C12 myoblasts remain in an undifferentiated proliferative and migratory state with a mesenchymal locomotion process. When maintained in a growth factor poor medium (differentiation medium, DM; (see Chapter 5)), confluent myoblasts undergo differentiation and fusion spontaneously, and become syncitia of multinucleate myotubes after a few days [Blau, 1983; Andrés & Walsh, 1996], producing characteristic muscle proteins. This differentiation process and C2C12 myotubes are discussed in details in Section 3.1.7.

3.1.2 Cell cycle

The C2C12 myoblast cell cycle, *i.e.* the events between one cell division and the next one, lasts 16 hours. For eukaryotes, the cell cycle is a complex process regulated by a specific program. It can be divided in two main phases: the interphase during which the cell is metabolically active and replicates the DNA, and the mitosis (M) which terminates with the division in two daughter cells [Cooper & Hausman, 2000; Nigg, 2001; O'Connor, 2008a; Bendris, 2015]. The interphase can be subdivided in three sub-phases: (i) the gap 1 phase (G1), during which the cell grows; (ii) the synthesis (S) phase when the DNA replication takes place, and (iii) the gap 2 (G2) phase during which the cell keeps growing while proteins necessary for the cell division are synthesized. During the interphase, that overall lasts $90-95$ % of the cell cycle time, cells grow and increase their size at a steady rate. As shown in Fig. 3.1, most of the myoblasts are adherent on the collagen coated petri dish substrate. However, the cells marked with a white arrow are detached or loosely attached on the substrate, since they exhibit a more rounded shape. These cells are undergoing mitosis and they are at different stages of this process. For C2C12 myoblasts, as for most adherent cells *in vivo* and *in vitro*, the mitosis process can be anticipate by mitotic cell rounding: cells become more rounded and loosely attached to the substrate (*in vitro*) or to other cells (*in vivo*) [Cramer & Mitchison, 1997; Gibson, 2006; Théry & Bornens, 2006]. Fig. 3.3 shows a mitotic cell rounding during 1 hour and 30 minutes of the upper left myoblast indicated by a white arrow in Fig. 3.1. The mitotic cell shape remodelling was observed for the first time in 1935 in mammalian fetal neural tube [Sauer, 1935]. Nowadays, it is well recognized that the spherical shape of a mitotic cell is the result of actin cytoskeleton remodelling and microtubule mitotic spindle formation that involve loss of actin stress fibers and focal adhesions [Yamakita, 1999; Suzuki & Takahashi, 2003], surface tension and hydrostatic pressure increase [Cramer & Mitchison, 1997; Stewart, 2011]. After cell rounding, myoblasts undergo mitosis (Fig. 3.4). During this process, the chromosomes are condensed and segregated before cell division in two daughter cells (*i.e.* cytokinesis). This process involves the complete breakage and the following reconstruction of cellular and nuclear membranes. Finally, as shown in Fig. 3.5, the two post-mitotic daughter cells spread and establish new adhesion foci with the substrate. Théry and Bornens [Théry & Bornens, 2006] showed that the daughter cells spread according to the adhesion pattern of their mother cell, recreating the pre-mitotic traction field *via* new adhesion

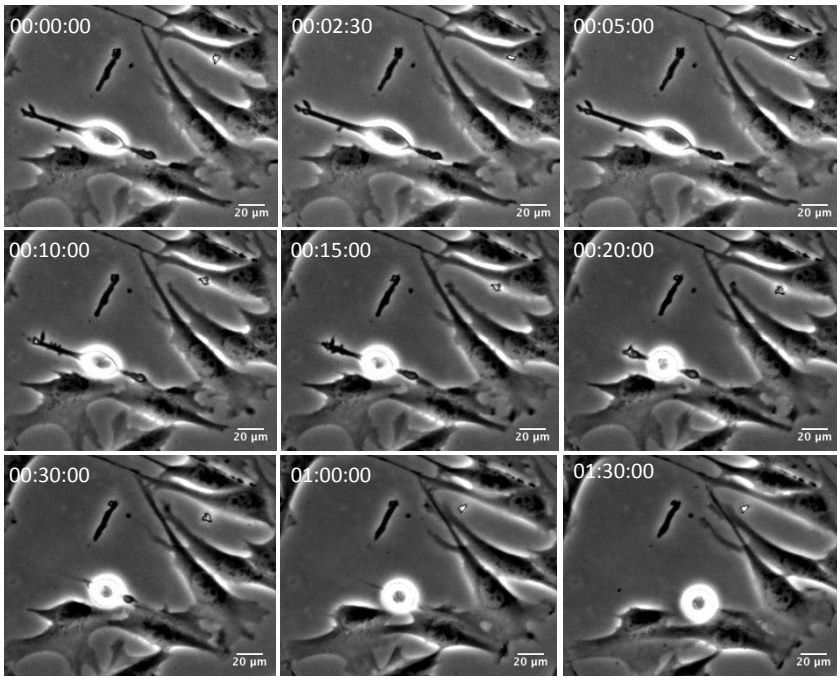

Figure 3.3: **Mitotic cell rounding of a C2C12 myoblast undergoing mitosis.** DIC images are taken from the same time-lapse video recording of C2C12 myoblasts on a collagen coated petri dish as in Fig. 3.1. The time is reported as hh:mm:ss. Scale bar: 20 μm.

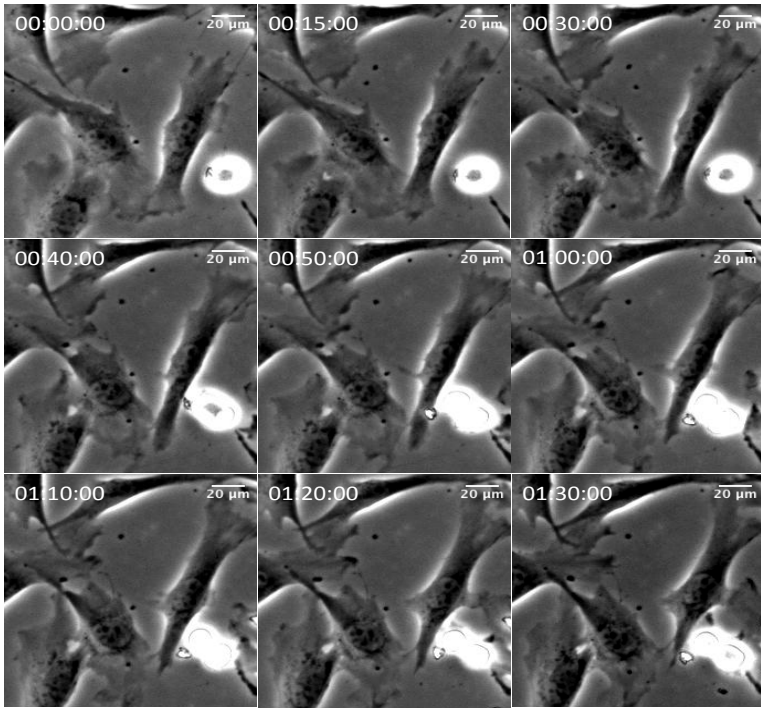

Figure 3.4: **Mitosis and cytokinesis of C2C12 myoblasts.** DIC images are taken from the time-lapse video recording dynamics of C2C12 myoblasts on a collagen coated petri dish (Fig. 3.1). The time is reported as hh:mm:ss. Scale bar: 20 μm

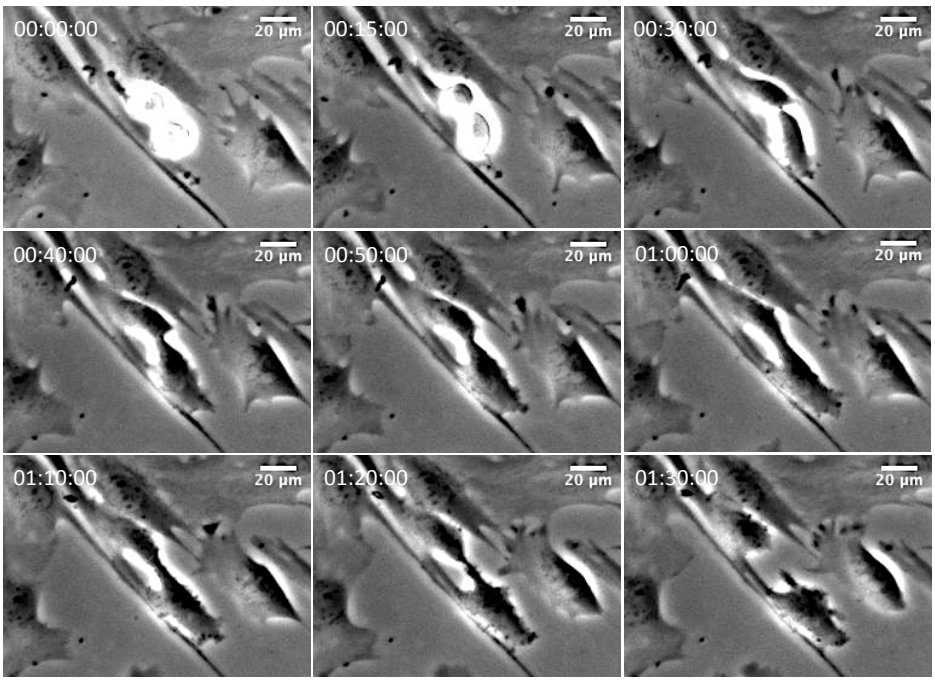

Figure 3.5: **Post-mitotic reattachment of C2C12 myoblast daughter cells.** DIC images are taken from the time-lapse video recording of C2C12 myoblasts on a collagen coated petri dish (Fig. 3.1). The time is reported as hh:mm:ss. Scale bar: 20 μm.

sites. This illustrates again the role of the mechanical forces in the regulation of critical myoblast events such as the cell mitosis. During the cell cycle, the cell mechanical properties change due, among others, to actin cytoskeleton rearrangements [Hiramoto, 1987; Kelly, 2011; Bailey, 2014]. The understanding of how the mechanical properties of myoblasts evolve during the cell cycle and more specifically during the interphase remains an interesting challenge. Mitotic myoblasts were easily excluded from our AFM experiments thanks to their peculiar rounded shape. In this chapter, collected data correspond to myoblasts during interphase.

3.1.3 Morphology

As observed through an optical microscope (Fig. 3.6), undifferentiated C2C12 myoblasts in routine culture conditions (GM and standard petri dish) appear as well adherent on the substrate with their characteristic fibroblast-like morphology [Burattini, 2004; Gundry, 2009]. According to their shape, two population of cells can be distinguished: (i) fusiform or spindle-shaped cells, as cell 1 in Fig. 3.6, and (ii) star-shaped cells, like cell 2 and cell 3. The star-shaped myoblasts are less elongated compared to fusiform cells. Indeed, while the width of all the cells in Fig. 3.6 is ~ 40 μm, their length varies between 120 μm for cell 1 and 55 μm for cell 3. C2C12 myoblast DIC images were analyzed with ImageJ to characterize in a quantitative way their morphology. The aspect ratio (A_R) parameter, which is the ratio between the cell maximum and minimum widths was also calculated. This parameter quantifies the degree of cell elongation. For example, A_R of cell 1 is 3 as compared to 1.4 for cell 3. Other quantitative morphological parameters will be discussed in more details in Section 3.1.5, together with the impact of different culture substrates on C2C12 myoblast morphology. Adherent C2C12 myoblasts exhibit a central

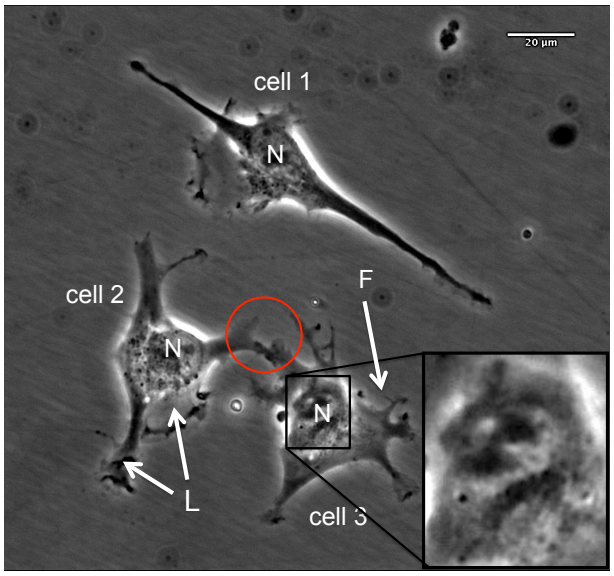

Figure 3.6: **Fusiform and star-shaped C2C12 myoblasts.** DIC microscopy image of adherent C2C12 myoblasts on a standard petri dish (SPD). Legend: filopodia (F), lamellipodia (L) and nucleus (N). Scale bar: 20 μm.

nucleus with one or more nucleoli that are visible as rounded dark grains not surrounded by a membrane (Fig. 3.6, subpanel) [Burattini, 2004]. In eukaryotic cells, the nucleolus is a nuclear compartment dense of genetic material and proteins. Nucleolus has several regulatory functions, including the well-known ribosomal biogenesis [Olson, 2000; Boisvert, 2007; Hernandez-Verdun, 2011]. The nucleolus size and arrangement are related to the ribosomal production and vary during the cell cycle [Hernandez-Verdun, 2011]: the ribosome production lasts during the entire interphase, increasing during G1 up to a maximum in G2, and it ends at the beginning of the mitosis [Gébrane-Younès, 1997]. Therefore, the presence of the nucleolus domains on myoblast nuclei confirms their engagement in the interphase. Although C2C12 cells grow typically as cell monolayers, Fig. 3.6 displays (inside the red circle) a typical cell-cell interaction between cells 2 and 3, as characterized by the overlapping of small cell peripheral regions. Note that rounded black spots appear concentrated around the nuclear area, likely corresponding to typical cytoplasm organelles of eukaryotic cells. Myoblasts also show lamellipodial plasma-membrane protrusions (Fig. 3.6, L), which are involved in the lamellipodial crawling migration and contain dense branched actin networks. Filopodial (Fig. 3.6, F) are also actin-rich protrusions utilized by the cells to probe their environment and to direct their movement [Blanchoin, 2014]. More details about the cytoskeleton of C2C12 myoblasts will be provided in Section 3.1.4.

3.1.4 Cytoskeleton organization

The general intracellular organization of an eukaryotic cell was presented in the Introduction (Chapter 1). In this section, we describe the cytoskeleton (CSK) of myoblasts, as characterized by fluorescence labelling coupled to confocal microscopy. We also provide some insights into the organization, the regulation and the function of the CSK filaments. The CSK deserves particular attention since it represents the cellular "musculoskeletal system". Its organization and dynamics are linked to cell mechanical properties and affect substantially several important cellular processes such as morphogenesis, reshaping, deformability, motility, division, adhesion and

connection with the extra cellular matrix (ECM) [Fletcher & Mullins, 2010; Wickstead & Gull, 2011; Blanchoin, 2014]. Thanks to this dynamical network, cells can detect external forces (*i.e.* mechanosensitivity), transmit external stresses to internal compartments and inversely couple the internal nucleus mechanics to the ECM (*i.e.* mechanotransduction) [Ingber, 2003b].

The CSK is a dynamical interconnected network of filamentous polymers, regulatory proteins, motor proteins and molecular complexes. Three types of filaments can be distinguished: (i) microtubules (MTs) made from proto-filaments of tubulin, (ii) intermediate filaments (IFs) polymerized from different protein monomers depending on the cell type, and (iii) microfilaments (MFs), compartments made from actin homo-polymers arranged in a double helix [Costa, 2014]. The three CSK filaments of C2C12 myoblasts and their characteristic organisations are shown

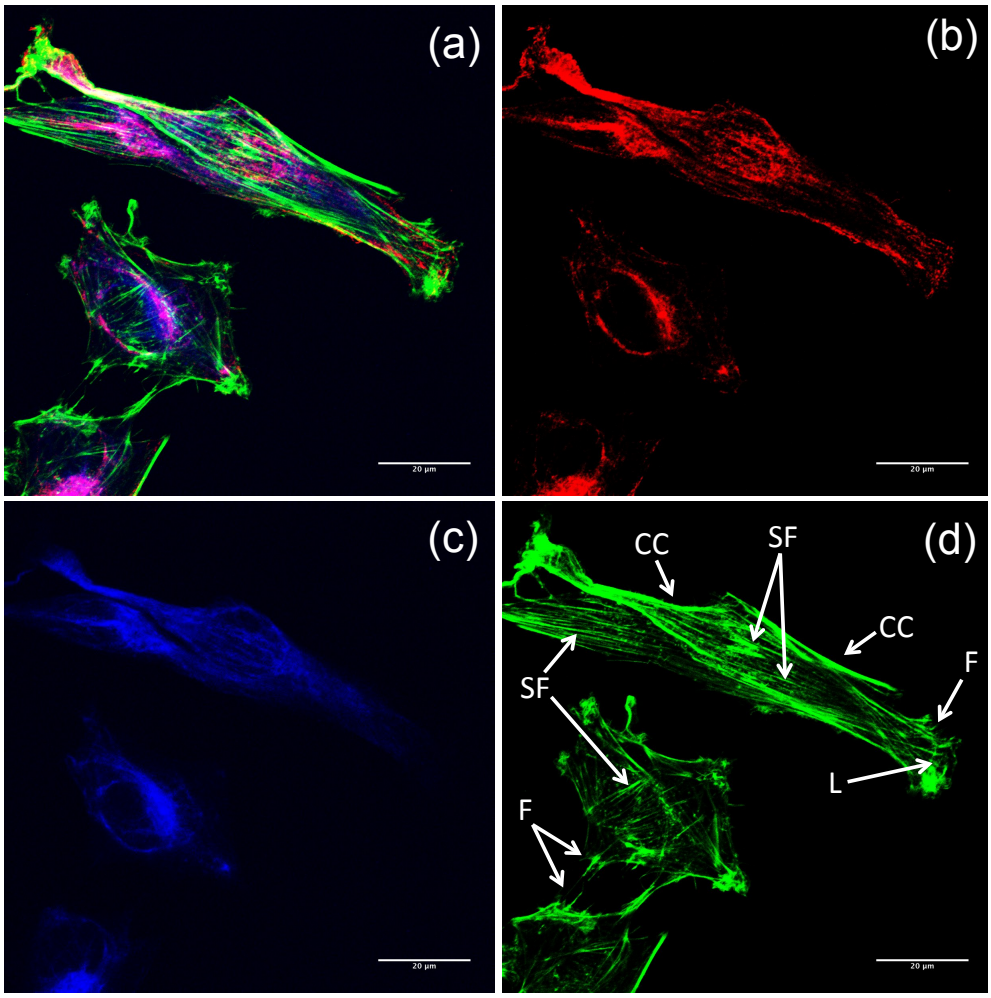

Figure 3.7: **Confocal microscopy images of fluorescence labelled cytoskeleton of elongated and star-shaped C2C12 myoblasts.** (b) Microtubules (anti-β-tubulin Cy3-conjugate, red), (c) intermediate filaments (anti-desmin and AMCA-conjugate secondary antibody, blue) and (d) microfilaments (phalloidin-Alexa Fluor 488, green). (a) Merged channels showing a partial colocation of β-tubulin and desmin (magenta, color corresponding to the sum of red and blue). CC = cell cortex, SF = stress fibers, L = lamellipodium and F = filopodium. Scale bar: 20 μm.

in Fig. 3.7(a), where microtubules (β-tubulin, red), intermediate filaments (desmin, blue) and

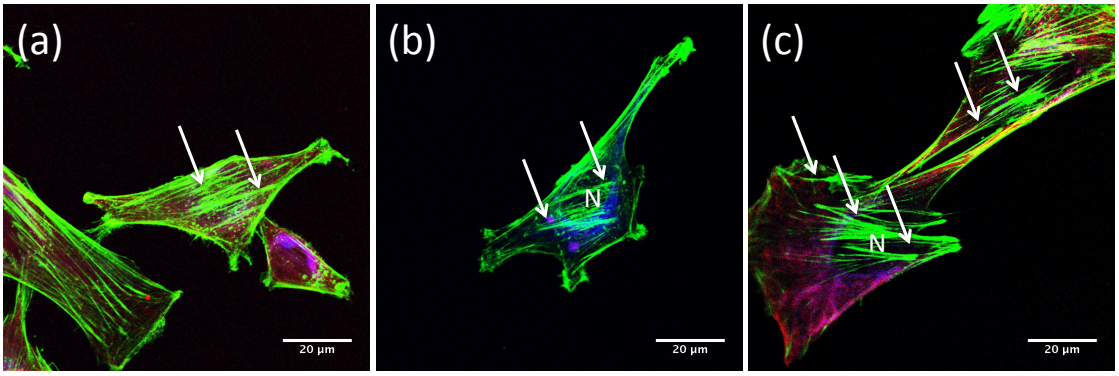

Figure 3.8: **Immuno-fluorescence confocal images of C2C12 myoblast cytoskeleton.** N= nucleus; white arrows point to stress fibers. Staining: F-actin (phalloidin-Alexa Fluor 488, green), desmin (anti-desmin and AMCA-conjugate secondary antibody, blue) and β-tubulin (anti-β-tubulin Cy3-conjugate, red). Scale bars: 20 μm.

microfilaments (F-actin, green) create three dense, interconnected networks with different organizations and localizations. For example, dense bundles of MFs (Fig. 3.7(d), green) are visible on the cell cortex while MTs and IFs accumulate on cytoplasmic epinuclear areas (Fig. 3.7(b), red and (c), blue). Small colocation regions of MTs and IFs (Fig. 3.7(a), magenta) are also visible.

3.1.4.a Microtubules

In eukaryotic cells MTs are hollow polarized cylindric filaments composed of α- and β-tubulin heterodimers. MTs are well-known in cell cycle studies since they participate to the scaffold of the mitotic spindle: the machinery which segregates chromosomes during mitosis. MTs play an important role in maintaining cell shape, in vesicle intracellular trafficking, and in the distribution of organelles such as nucleus and mitochondria together with the IFs [Lüders, 2016]. MTs represent also the cellular railroad tracks to transport vesicles in a centrifuge direction. Active transport of vesicles and organelles is achieved with the aid of ATP-driven molecular motors such as kinesin and dynein. MTs are also involved in cilia and flagella movements. MTs are characterized by peculiar instability dynamics: their polarization and stability are GTP dependent [Desai & Mitchison, 1997; Nogales & Wang, 2006] and they show stochastic periods of growth (polymerization) and shrinkage (depolymerization) [Mitchison & Kirschner, 1984; Sept, 2007]. In myoblasts, dynamical individual MT filaments are distributed radially from the centrosome, also called microtubule organizing center (MTOC), which indeed is their nucleation center [Musa, 2003; Mian, 2012; Lüders, 2016]. The radial cytoplasmic organization of the MTs around the nuclear area highlights the anisotropic MT-guided transport of organelles and vesicles [Keating & Borisy, 1999; Musa, 2003]. In Fig.3.7(b) we can observe the cytoplasmic distribution of β-tubulin, one of the two subunits that build the MTs but not the centrosome. Note that the two cells show different MT structures according to the dynamical nature of the MT network. Fig. 3.8(c) shows an example of MTs organization in C2C12 myoblasts with a more pronounced radial distribution.

3.1.4.b Intermediate filaments

Intermediate filaments (Fig. 3.7(c)) are non polarized copolymers. They are involved in the regulation of cell survival, signalling pathways, cell-cell adhesion connections and cell shape maintenance. They also play an essential role in MT and MF networks. In humans, about 70 genes encoding for IF proteins are known; among them only 3 encode for nuclear proteins while the other ones encode for those of the cytoplasm [Kim & Coulombe, 2007]. Several muscle IF proteins with different functions have been identified such as laminin, desmin, vimentin, nestin, synemin, syncolin and cytokeratin [Costa, 2014]. Fig. 3.7(c) displays the cytoplasmic localization of the IF protein desmin in C2C12 myoblasts; this protein accumulates in the epinuclear region with a cloud-like shape. Although the best way to visualize desmin is immunofluorescence, confocal microscopy displays IFs either as filaments or as fuzzy fluorescence zones, most likely due to their sub-resolution size [Costa, 2004b]. Desmin is a muscle-specific IF protein expressed exclusively in satellite cells, replicating myoblasts, differentiated muscle and endothelial cells [Lazarides & Hubbard, 1976; Small & Sobieszek, 1977; Lazarides, 1982; Kaufman & Foster, 1988; Allen, 1991]. Its distribution differs between muscle cell types [Costa, 2004b]. In undifferentiated myoblasts, desmin is known to be located close to the nuclear membrane [Tolstonog, 2002; Mermelstein, 2006; Costa, 2014], as shown in Figs. 3.7(c) and 3.8(b). The partial colocation of MTs and IFs is not surprising since these two type of CSK filaments share some cellular functions. For example in fibroblasts, IFs are found often in juxtaposition to MTs [Ball & Singer, 1981]. Moreover, IFs play a major role in the MT and MF network crosstalk *via* the plakin protein family [Helfand, 2004; Kim & Coulombe, 2007]. Mature IFs can establish dynamical connections with MTs *via* molecular motors such as dynein [Chang & Goldman, 2004].

3.1.4.c Microfilaments

The third and best characterized type of CSK filaments are the microfilaments (MFs), mainly composed of actin filaments. Among all the filaments and molecules which contribute to the structure and function of the CSK, the actin filaments are involved in many mechanical processes such as cellular reshaping, locomotion, substrate adhesion, phagocytosis and plasma membrane compartmentalization [Blanchoin, 2014]. Actin dynamics is the universally known driving force in eukaryotic cells that provides structural strength and protrusive power for the cell movement (lamellipodia, filopodia, micro-spikes) [Pollard & Borisy, 2003]. The special link between actin dynamics and cell mechanics pushed us to pay special attention to actin organization and dynamics. Actin filaments (filamentous actin or F-actin) are double-stranded helical filaments created *via* polymerization of a 42 kDa protein actin (monomeric actin or G-actin) [Holmes, 1990]. The first step of actin polymerization is the nucleation, namely the creation of a trimeric complex from ATP-G-actin (*i.e.* actin nucleus). Actin monomers need to be bound to ATP for their polymerization. Although ATP-G-actin concentration can be high in cells, this nucleation step is thermodynamically limiting actin polymerization. First actin dimers and trimers are unstable, and second actin nucleation necessitates the participation of nucleation proteins named actin-nucleating proteins [Rosenblatt, 1995; Blanchoin, 2014]. Therefore this step represents the first control point of actin dynamics. At least three families of actin-nucleating proteins do exist: (i) the actin-related protein-2/3 (Arp2/3) complex in cooperation with its nucleation promoting factors (NPFs), (ii) formins, and (iii) tandem-monomer-binding nucleators [Firat-Karalar & Welch, 2011]. Among them, the Arp2/3 complex nucleates new MFs starting from existing F-actins with a 70 °angle, thus creating a Y-branched network (Fig. 3.9). Formin dimers

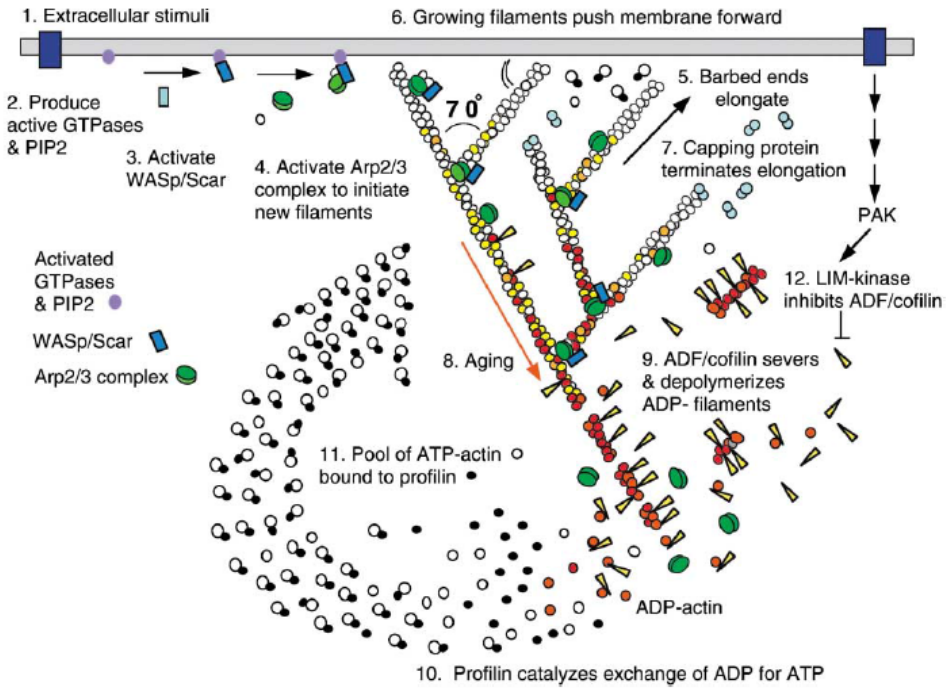

Figure 3.9: **Dendritic nucleation/array treadmilling model.** This model describes the actin dynamics and its regulation at lamellipodia protrusions of migratory cells. The different steps and the regulatory actors of actin polymerization and depolymerization are enumerated. This process involves several actin binding proteins and other regulatory complexes. Adapted from Cell [Pollard & Borisy, 2003].

construct unbranched F-actin and elongate them [Chesarone, 2010]. The third class of actin-nucleating proteins are termed tandem-monomer-binding nucleators because they have tandem G-actin-binding motifs that can assemble actin nuclei starting from ATP-G-actin. The activity of these actin nucleators has been recently elucidated in the regulation of actin nucleation [Firat-Karalar & Welch, 2011]. After nucleation, the actin nucleus is rapidly elongated when the actin concentration exceeds some critical concentration (~ 0.1 μM) [Wegner & Engel, 1975; Pollard, 2000]. Actin filaments are polarized, showing a more dynamical end called barbed end (+) and a less dynamical pointed end (-). The barbed end elongates 10 times faster than the pointed one [Pollard, 1986]. It is sufficient to say that an actin barbed end can elongate to 10 μm in less than 2 seconds to give an idea of the extremely dynamical nature of the actin network [Pollard, 2000]. The intrinsic polarity of actin filaments defines the cell polarity necessary for cell migration, as further discussed in Section 3.1.6. Actin filaments are constantly assembled and disassembled in cells in a highly dynamical manner. This dynamics implies not only an elongation but also a shortening process. The hydrolysis of ATP is followed by the depolymerization of actin filaments *via* the removal of ADP-G-actin monomers from F-actin [Melki, 1996; Blanchoin & Pollard, 2002; Blanchoin & Michelot, 2012; Blanchoin, 2014]. Actin dynamics is indeed very complex since it is strictly regulated in time and space by a considerable number of actin binding proteins (ABPs) and other molecules. The number of molecules identified as involved in the regulation of actin dynamics is constantly growing, and so does the number of studies in this field. It is possible to classify some of the ABPs according to their function [Borisy & Svitkina, 2000; Cooper & Schafer, 2000; Bear, 2002; Pinyol, 2007; Xue & Robinson, 2013]:

- triggering the signalling to promote actin nucleation (phosphatidylinositol 4,5-bisphosphate PIP2, Wiskott-Aldrich Syndrome protein WASp and the related protein SCAR);
- capping (Arp2/3 complex that, besides its nucleator action, can bind the pointed end promoting the nucleation at the other end; or capping proteins which block the filament elongation);
- crosslinking (α-actinin, fascin, filamin);
- severing (gelsolin, ADF/cofilin, profilin);
- sequestering subunits (thymosin β4);
- promoting dissociation from the pointed end (ADF/cofilin);
- regulating association at the barbed end (profilin);
- enhancing actin polymerization (vasodilator-stimulated phosphoprotein Ena/VASP).

These proteins work *in concerto* for the regulation of actin dynamics. A model of actin dynamics regulation was reported by Pollard and Borisy [Pollard & Borisy, 2003] (Dendritic Nucleation/Array Treadmilling Model shown in Fig. 3.9). Briefly, extracellular signal transmission *via* Rho-family GTPases and PIP2, and subsequent WASp/Scar activation, bring together activated Arp2/3 complex and ATP-G-actin, creating new actin branches on existing filaments. By elongation, the barbed end filaments are able to push forward the cell membrane. While capping proteins stop filament elongation, MFs age by bound ATP hydrolysis by γ phosphate dissociation catalyzed by the actin ATPase activity. This depolarization process is assisted by

ADF/cofilin proteins which also sever ADP-actin filaments. Conversely, the actin recycling process is promoted by profilin which "recharges" the ADP-G-actin by a phosphate. A negative control of the actin turnover is achieved by Rho-family GTPases through the activation of PAK and LIM kinases. Genetic defects and abnormal expression of actin-monomer binding proteins are often related to congenital and acquired human diseases confirming their critical role in actin dynamics regulation [Yamaguchi & Condeelis, 2007].

As MTs, microfilaments can also function as tracks for their molecular motors: the myosins. Molecular motors are proteins able to convert chemical energy (ATP-driven) in mechanical work. MF motor proteins belong to the myosin superfamily [Coluccio, 2007]. All myosins possess actin- and ATP-binding domains and their activity is also regulated by an ATP/ADP cycle [Hartman & Spudich, 2012]. In particular, the lower actin affinity for ATP-myosin is essential for myosin function. Among myosins, non-muscle myosin II (NM II) is the principal regulatory protein of the actin network: its strong binding to actin filaments is able to tense MFs, for example during cytokinesis [Vicente-Manzanares, 2009; Ma, 2012]. The cellular actomyosin contractile compartment is known to have an important role on the cell shape and motility [Buckley & Porter, 1967; Schloss, 1977; Goldman, 1979]. This dynamic apparatus, involving stress fibers, is responsible for linking the extra cellular environment to the cytoskeleton *via* focal adhesions (FAs). This explains that it plays an important role in mechanotransduction [Alenghat & Ingber, 2002; Bershadsky, 2006]. Nowadays, there is a consensus picture of the coordination of spatio-temporal cell dynamics by the actomyosin machinery and its versatile coupling to the extracellular environment *via* the recruitment of integrin adhesion complexes [Fletcher & Geissler, 2009]. Because of its tensional activity, NMMII is involved in the regulation of the cell mechanical properties. More details about the role of NMMII in CSK organization and cell mechanics will be provided later in this chapter.

Green phalloidin staining coupled to confocal microscopy (Fig. 3.7(d)) reveals the F-actin network organization of C2C12 myoblasts. As illustrated in Fig. 3.10, for adherent migrating cells, different actin structures are observed according to their intracellular localisations. Actin accumulates closer to the plasma membrane as compared to the other CSK filaments. The cell cortex visible at the cell periphery (Fig. 3.7, CC), is composed by a thin layer of cross-linked actin network that covers the intracellular side of the plasma membrane, and which is essential for shape maintenance and remodelling. Branched and cross-linked actin networks are present at the lamellipodia while parallel bundles of microfilaments sustain filopodia protrusions (Fig. 3.7, resp. L and F). The Arp2/3 branched actin dynamics [Goley & Welch, 2006], is not only involved in lamellipodia dynamics but also in vesicle and organelle transport, endocytosis and phagocytosis. Note that these types of movements are not motor protein driven but due to non-equilibrium actin self-assembly. The filopodia formed by parallel bundles act as antennae for probing the cell environment and thus direct the cell movement. This cortically actin distribution is lost during myogenesis since the actin network then spreads over the whole myotube cytoplasm (Section 3.1.7). Myoblasts exhibit the characteristic stress fibers (SFs) extended longitudinally through the cell body (ventral stress fibers, transverse arcs). These SFs are contractile bundles of antiparallel actin filaments cross-linked by actinin [De Almeida Ribeiro, 2014]; their contractility is conferred by the molecular motor myosin.The ventral stress fibers are most commonly found in mature cells and are believed to have a key role in cellular mechanosensing [Pellegrin & Mellor, 2007; Tojkander, 2012]. The cooperation of semi-flexible actin filaments and myosin permits the exertion of or resistance against forces [Blanchoin, 2014]. It has been suggested that ventral stress fiber could merge from one transverse arc bundle and two dorsal stress fibers in a tension-

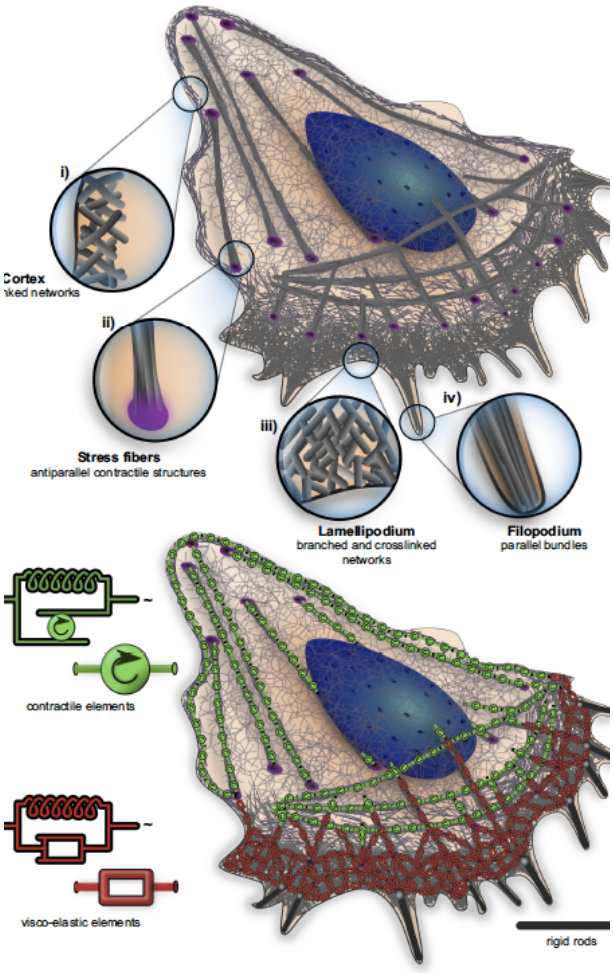

Figure 3.10: **Actin organization and its mechanics in adherent motile cells.** (Top) Graphical description of the different actin structures and their cellular locations. Grey = the actin filaments; purple = focal adhesions; blue = the nucleus; pink = the cytoplasm. (Bottom) Mechanical features of the above mentioned actin structures. Green circles are active springs representing the myosin activity. Red rectangles are viscous dashpots representing the extremely dynamic actin network at the leading edge. Adapted from Physiological Reviews [Blanchoin, 2014].

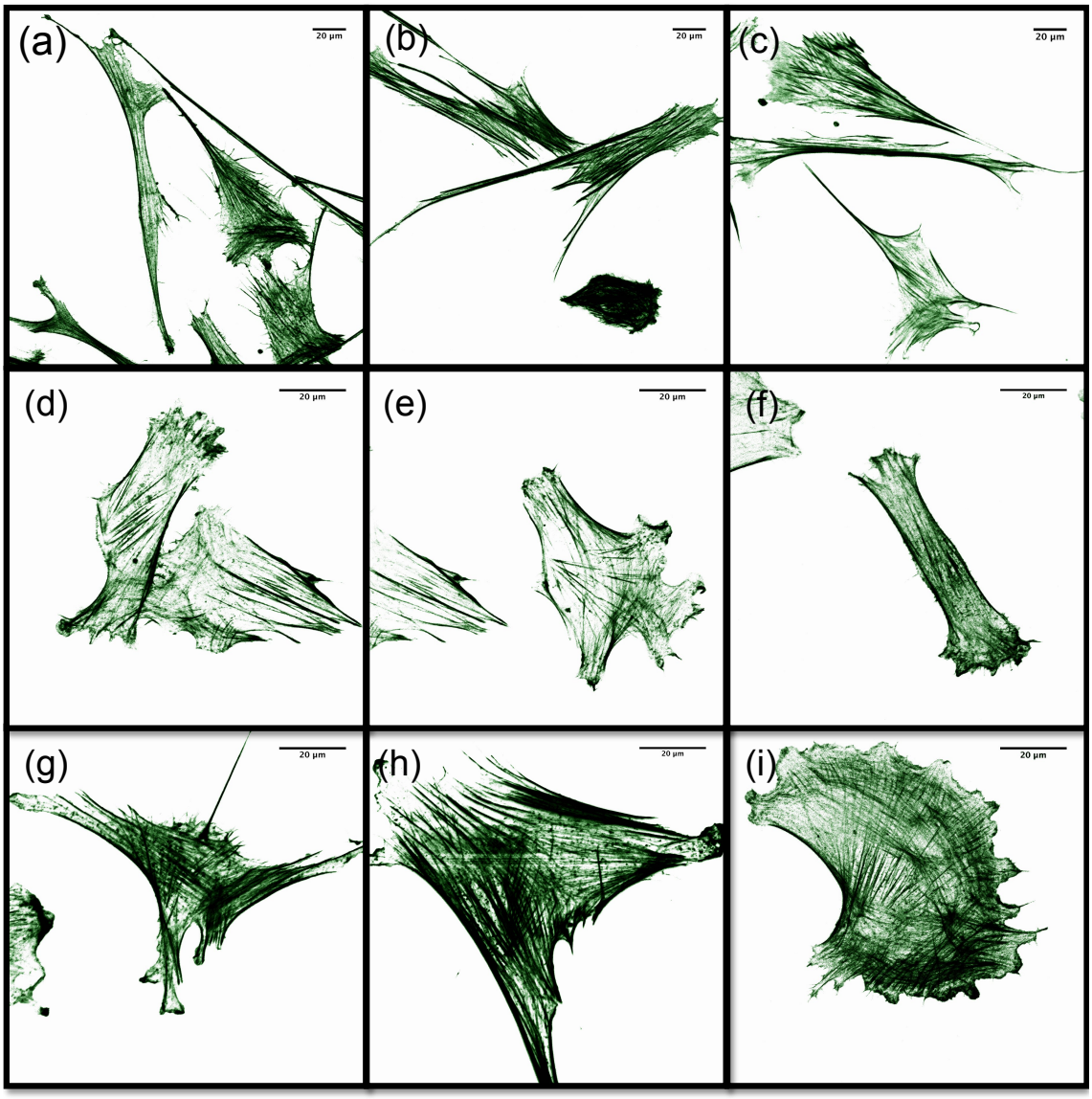

Figure 3.11: **Actin network of C2C12 myoblasts on collagen-coated petri dishes.** Confocal Microscopy images of C2C12 myoblast F-actin microfilaments stained with phalloidin-Alexa Fluor 488. The images were then treated with ImageJ by using the inverted " Thallium" LUT scale. Scale bars: 20 μm.

mediated manner. Ventral stress fibers include two additional subtypes: peripheral stress fibers that run along the long stable edges of a cell and actin cap stress fibers which are draped over the nucleus [Khatau, 2009]. This perinuclear cap is mostly important in this work, since it is also very sensitive to disruptions or weaknesses of the nuclear membrane (laminopathies) or disability of the force transmission in between the motoneurons and the underlying myotube nuclei in neuromuscular junctions. We will specifically focus on the mechanics of the perinuclear cap stress fibers in this manuscript.

SFs are also in charge of connecting the ECM with the CSK through the focal adhesions (FAs). Other examples of C2C12 myoblast CSK organization are shown in Figs. 3.8 and 3.11, where similar features are observable: SFs, cortical and branched actin. At the molecular level,

force generation occurs by harnessing chemical energy (ATP) into mechanical work. Local stresses (intrinsic to the cell or produced by surrounding forces) are necessary to construct polar and dynamic CSK filaments such as actin and microtubules. The molecular interactions between F-actin and non-muscle myosin II govern the generation of contractile forces over a wide range of length scales, from nanometers to several millimeters, from the contraction of subcellular compartments to the cooperative contraction of multicellular populations (non-muscle tissues in development). Our confocal microscopy observations of a well-organized actin network, with characteristic straight actin stress fibers close to the substrate and a highly branched network on the lamellipodia protrusions, confirm that a correct morphology is a guarantee of myoblast aptitude to mechanical contractility.

From *in vitro* studies, it emerges that actin filament are semi-flexible chains when longer than ~ 10 μm and rigid rods when shorter than this so-called persistence length (basically the maximum length below which the pure polymer does not bend) [Harasim, 2013; Blanchoin, 2014]. According to these findings, actin filaments are almost straight structures because of the limited size of the cells, but they can buckle under pN order forces. Moreover, the length of the filament influences the force necessary for bending: the shorter the filaments, the higher the load. The persistence length of other biological polymers was experimentally estimated; for example the persistence length of MTs is ~ 1 mm. However, the situation is somehow different *in vivo* because of the action of regulatory and motor proteins. If there is no doubt that *in vitro* experiments are really interesting to unravel some quantitative characterization of biological polymers such as CSK filaments, they are unfortunately far from been comparable to the real *in vivo* environment of muscle cells.

3.1.5 Impact of the culture dish surface properties on C2C12 myoblasts

External mechanical forces are known to affect several dynamical biological processes, including cell morphology, adhesion, locomotion and protein expression [Geiger & Bershadsky, 2002; Georges & Janmey, 2005]. External mechanical stresses, such as fluid shear stress, pressure, elongation stress are recognized by living cells throughout the process called mechanosensing. Indeed, living cells are able to sense and respond to different mechanical stimuli, and to trigger specific signalling pathways in the same manner as biochemical cues [Teixeira, 2006]. The ECM and environment properties can deeply affect cell structure, dynamics, function and differentiation. In the same way, the physical and chemical properties of the adhesion surface can impact the cell behaviour [Bischofs & Schwarz, 2003]. As discussed in Section 3.1.4, one of the main target of such mechanical stimuli is the CSK [Helmke & Davies, 2002; Georges & Janmey, 2005]. There is growing evidence that mechanosensing involves integrin-based contacts between the cell and the ECM facing the focal adhesions (FAs). FAs represent the physical contact points between the cell and its environment; they allow the external mechanical information to enter the cell and to be transmitted into the cell machinery. Although this phenomenon is not completely described at the molecular level, it has been shown that muscle, endothelial and nervous cells, as well as many other types of cells, can detect and react to substrate rigidity [Wang, 2000; Deroanne, 2001]. The surface topography can impact cell morphology, alignment, orientation, migration and adhesion [Curtis & Wilkinson, 1997; Johansson, 2006; Charest, 2007]. The substrate elasticity was also shown to regulate adhesion structures, cell locomotion [Pelham & Wang, 1997], cell spreading [Engler, 2004a; Georges & Janmey, 2005], myogenic differentiation [Engler, 2004b] and normal cell fate without having any effect on oncogene transformed

cells [Stoker, 1968; Wang, 2000]. In general, the cell response to the extracellular microenvironment can be classified in short-time adaptation (*e.g.* cell spreading, morphology, adhesion and motility) and long-time response (*e.g.* cell proliferation, differentiation and protein synthesis) [Engler, 2007]. The most important actor of this response is the actomyosin machinery and its adhesion complexes [Discher, 2005]. This network allows the transmission of the contractile forces to other cell compartments such as the cell nucleus, possibly leading to the modulation of expression level of certain genes with potential implications on development, differentiation, disease, and regeneration [Deroanne, 2001].

In this section, we describe and quantify the short time morphological adaptation of living C2C12 myoblasts adherent on different culture substrates (*i.e.* gold coated micro-slides, standard and collagen coated petri dishes) using DIC imaging (Fig. 3.12). It should be noticed that not all the cell types respond in the same manner to the same stiffness of adhesion substrates [Yeung, 2005; Georges & Janmey, 2005]. The specificity of the cell response to the ECM environment reflects the variability of the cell behaviour and of the tissue mechanical properties *in vivo*. Some types of cells (*e.g.* neutrophils) appear to be insensitive to changes in substrate rigidity. Neurons instead spread further their axons and better survive on soft materials that correspond to necessary conditions for synapse formation during development and regeneration [Flanagan, 2002; Yeung, 2005]. Mesenchymal stem cells (MSCs) can differentiate to myocytes, neurons or osteoblasts when the culture substrate stiffness is close to the *in vivo* tissue rigidity [Engler, 2006]. Cells from solid tissues can survive *in vitro* if adhering on appropriate elastic matrix [Engler, 2004a; Rajagopalan, 2004]. It was shown that both the chemical and physical properties (*e.g.* stiffness, roughness) of the surface influence the adhesion, proliferation, signalling and differentiation of myoblasts [Engler, 2004b; Nemir & West, 2010; Hu, 2011; Romanazzo, 2012; Ostrovidov, 2014]. For adherent mechanosensitive cells such as C2C12 myoblasts, the cell-surface interface has a critical impact not only on the cell response to different stimuli, but also on the development, differentiation, disease, and regeneration [Discher, 2005]. Since adherent cells are anchored on a surface, by pulling on it they are capable to probe surface elasticity [Discher, 2005]. For example, adherent fibroblasts are mechanosensitive to the surrounding environment stiffness and react by up-regulating FAs and SFs *via* Rho-signalling when adhering on stiff substrates. For the majority of tested cells requiring anchoring on a surface, softer substrates lead to higher cell motility while stiffer substrates normally produce greater spreading and cell contractility [Yeung, 2005; Georges & Janmey, 2005]. Collagen gel coated surfaces are an exception in this context since, although classified as soft surfaces, they lead to maximal cell spreading as reported for aortic smooth muscle cells [Engler, 2004a]. C2C12 myoblasts were shown to have a mechanosensitive response to substrate rigidity through a modulation of their myogenic differentiation [Engler, 2004b; Palchesko, 2012; Bettadapur, 2016; Ramón-Azcón, 2013; Ostrovidov, 2014]. Also myotubes increase their striation on muscle-like stiffness substrates ($\sim$ 12 kPa) [Engler, 2004b]. Al-Rekabi and Pelling [Al-Rekabi & Pelling, 2013] showed that C2C12 myoblasts respond with increased cellular traction dynamics when pressed by AFM (10 nN force load on the nucleus). The survey of the impact of different culture surfaces on C2C12 myoblasts by DIC microscopy (Figs. 3.12 and 3.13) reveals that if this cell line is able to adhere correctly on the three tested surfaces, some variability in cell shape is observed. For example, the cell spreading area seems greater for cells on CCPD than on other surfaces. Filopodial protrusions and cell-cell contacts are more frequent on collagen coated petri dishes as compared to standard petri dishes (Fig. 3.13).

From DIC images of living adherents C2C12 myoblasts on gold coated micro-slides (gold),

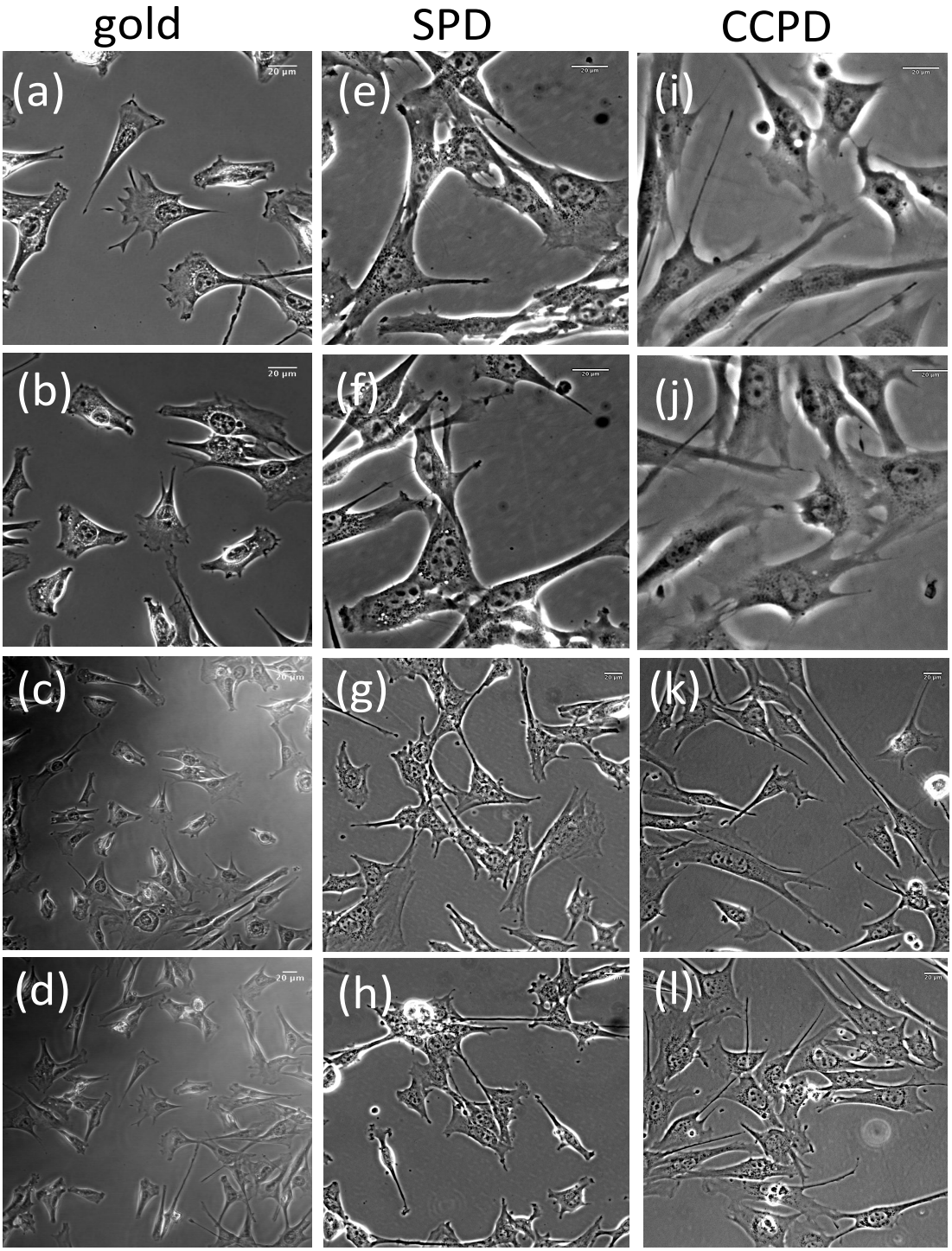

Figure 3.12: **Comparison of C2C12 myoblast morphology on different culture substrates.** DIC images of adherent C2C12 myoblasts on (a-d) gold coated micro-slides, (e-h) standard petri dishes (SPD) and (i-l) collagen coated petri dishes (CCPD). Scale bars: 20 μm. It should be noticed that the magnification is not the same for all the images.

standard (SPD) and collagen coated petri dishes (CCPD), we used ImageJ and Matlab to estimate morphological parameters: the length (longest side) and the width (smallest side) of the cell and of its nucleus. The results reported in Fig. 3.14(a-c) show a significant increase of

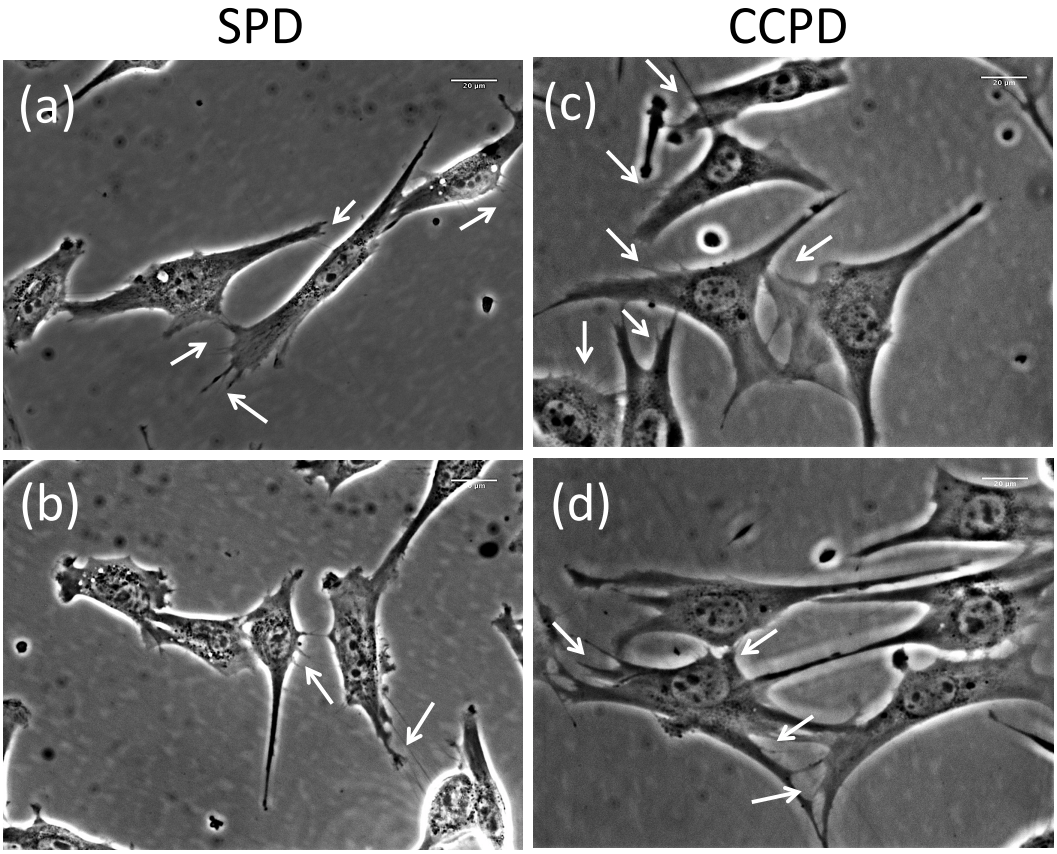

Figure 3.13: **Comparison of C2C12 myoblast filipodia between standard and collagen coated petri dishes.** (a) and (b) Adherent C2C12 myoblasts on standard petri dish (SPD). (c) and (d) C2C12 myoblasts growing on collagen coated petri dish (CCPD). The arrows point at filopodial protrusions. Scale bars: 20 μm

C2C12 myoblast length, width and area when grown on CCPD compared to the other surfaces. The same conclusion can be drawn for the C2C12 myoblast nucleus in Fig. 3.14(d-f). Let us point out that these results are in agreement with those previously reported in the literature ([Engler, 2004a]). The smallest morphological parameters were obtained with cells adherent on gold-coated surfaces. For the length and width estimates, one can compute their ratio also called cell aspect ratio (resp. the nucleus aspect ratio) which is the degree of cell elongation: the greater the ratio, the more elongated the cell (resp. nucleus). An aspect ratio of 1 characterizes a circular shape. Interestingly, Fig. 3.15(a) shows that there is no significant difference between the cell aspect ratio distributions obtained for the three cell populations. This means that, although the cell morphological parameters are different for CCPD cells, their shape is still similar to the other cells. This is no longer true for the cell nucleus that looks more rounded in gold coated surfaces (Fig. 3.15(b)). Moreover, when computing the area ratio defined as the ratio of the cell and nucleus, we got a greater area ratio of CCPD myoblasts, as an indication of a larger cytoplasmic area not occupied by the nucleus in these conditions.

To conclude, when performing *in vitro* experiments in well-defined culture conditions (*e.g.* temperature and pH), the culture dish surface properties are an important factor to control, especially when the cells under study are mechanosensitive [Engler, 2007]. The impact of the

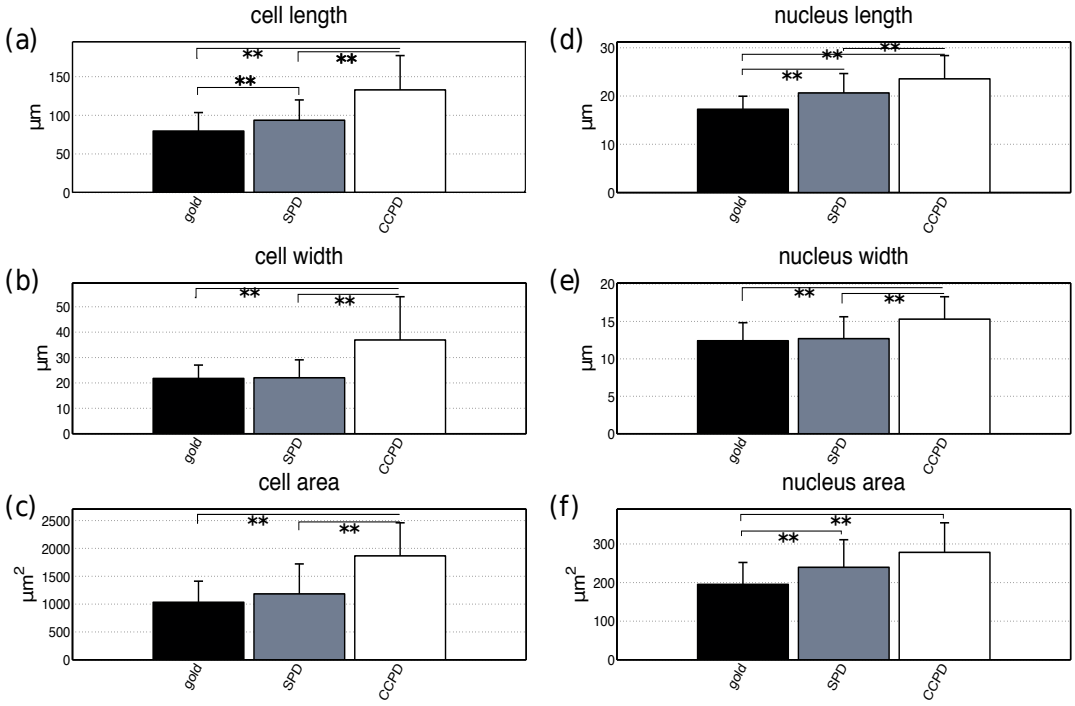

Figure 3.14: **Morphological parameters of C2C12 myoblasts on different substrate surfaces.** (a) Length; (b) width; (c) area of C2C12 cells. (d) Length, (e) width, (f) area of the cell nucleus. C2C12 cells were let to adhere on gold coated micro slides (black), standard petri dishes (grey) and collagen coated petri dishes (white). Values were measured with ImageJ on 10 DIC images. The data are reported as mean ± SD over n= 30 cells for each condition. ** marks for a significant difference between data distributions (p-value: $p \leqslant 0.05$).

ECM properties on the cell behaviour should also be taken into account for biomedical and bioengineering applications. For example, the knowledge of the mechanical properties of biological materials should be exploited in producing biomimetic materials. In this work we chose type I collagen as adhesion molecules for AFM experiments because this protein is one of the major insoluble fibrous protein found in the *in vivo* ECM. We have just seen in Figs. 3.13, 3.14 and 3.15 that C2C12 myoblast cells are able to sense collagen I coated surfaces and to react by increasing their length, width and area. A similar increase of the nucleus area is observed but to a lesser extent, indicating some relative increase of the cytoplasm area in these conditions.

3.1.6 Migration

Movement is probably one of the most fascinating property of living cells and organisms. Cell migration is such a critical process that its quality can determine the fate between life and death. For example, cell locomotion is necessary for the implantation of a fertilized ovum and for the following embryonic development [Gilbert, 2003]. In adult body, cell migration is associated with several physiological events such as the immune response of white blood cells, growth, maintenance and renewal of tissues (*e.g.* skin and intestine) [Ridley, 2003]. Also, cell locomotion is involved in pathological processes like chronic inflammatory and vascular diseases, osteoporosis, mental retardation and cancer [Ridley, 2003]. Over the past few decades, cell migration has been

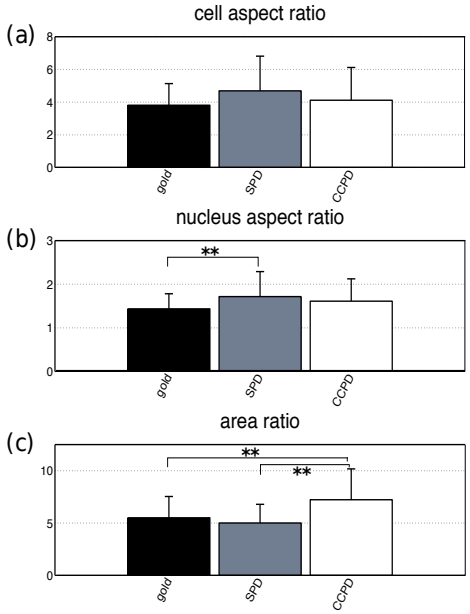

Figure 3.15: **Cell and nucleus aspect ratio of C2C12 myoblasts on different substrate surfaces.** Aspect ratio of the cell (a) and nucleus (b) of C2C12 myoblasts grown on gold coated micro slides (black), standard petri dishes (grey) and collagen coated petri dishes (white). Values were measured with ImageJ on 10 DIC images. The data are reported as mean ± SD over n= 30 cells for each condition. ** marks for a significant difference between data distributions ($p \leqslant 0.05$).

a hot-topic in biomedical and biomechanical research aiming at improving our understanding of these complex processes with the perspective of finding new therapeutic strategies [Zigmond, 1989; Wilkinson, 1996; Ridley, 2011; Ladoux & Nicolas, 2012]. Mesenchymal migration used by fibroblasts and more generally cells of the mesenchymal lineage is characterized by elongated cell shapes with long membrane protrusions and strong adhesion sites. It differs from amoeboid migration, more frequently observed in leukocytes vertebrate cells (besides the D. discoideum amoeboid), where the cells are rounded in shape and lack strong adhesive interaction. Both mesenchymal and amoeboidal migrations are characterized by a series of cyclically repeated steps in order to produce cell movement [Lodish, 2000; Ridley, 2011; Ladoux & Nicolas, 2012]. All the steps of mesenchymal migration process have been deciphered. They involve mainly contractile forces, actin network and focal adhesion dynamics. The cell polarization is a prerequisite for cell migration. Polarity concerns both the morpho-structural compartments as well as the molecular processes. In other words, the shape and the biomolecular events are not the same at the front and at the back of polarized cells [Ridley, 2003]. The cell polarization involves the extension of lamellipodial protrusions from the cell border facing the movement direction, which is the leading edge. The formation of this lamellipodial protrusion is coordinated by the polymerization of actin filaments that act as intracellular pushing components (Section 3.1.4). On this leading edge, new adhesion sites of the lamellipodium with the substrate are permanently generated, driven by integrin transmembrane receptor clustering. Then the cell body is pulled forward by the contractile forces of stress fibers (*i.e.* actomyosin forces) accompanied by

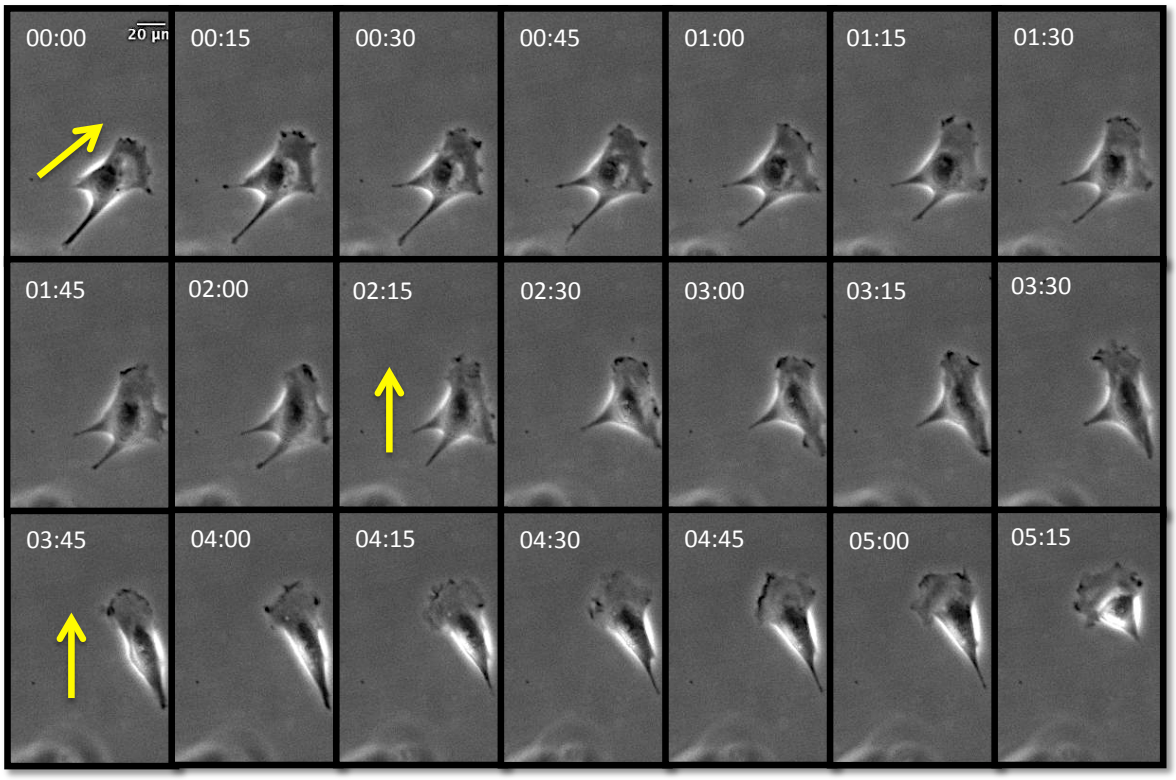

Figure 3.16: **Isolated C2C12 myoblast migrating on a gold surface.** The yellow arrows indicate the direction of the cell migration. Three different directions are recognisable during 5 hours time-lapse video recording. The time is reported as hh:mm. Scale bar: 20 μm.

a retrograde cytosol F-actin flow. On the backward side of the cell (opposite to the movement direction), the old FAs are disassembled allowing the back of the cell body to retract [Ladoux & Nicolas, 2012]. This multistep process is repeated contributing to the cell body progression in the direction pointed by the lamellipodia protrusion. Globally this 2D locomotion can be imagined as a cell walking on a substrate. Spatial and temporal regulation is achieved by complex signalling pathways involving feedbacks, as illustrated in Fig. 3.9. Although this process can be described by a series of general steps, different cells can migrate in different ways and the same cell can modify its migration depending on the microenviromental conditions (*e.g.* from *in vivo* to *in vitro*) [Ridley, 2003]. The impact of chemical and physical cues on the morphology and the spreading of cells has already been discussed. In the same manner, external stimuli such as biochemical cues (*e.g.* chemokines) [Swaney, 2010; Phillipson & Kubes, 2011] and the chemical properties of the adhesion substrate [Maheshwari, 2000; Peyton & Putnam, 2005] impact cell motility, adhesion and contractility [Discher, 2005]. Cell migration and adhesion are modulated by the mechanical properties of the ECM, its topography [Curtis & Wilkinson, 1997; Berry, 2004; Dalby, 2009; Ghibaudo, 2009; Le Digabel, 2010] and its rigidity [Lo, 2000; Peyton & Putnam, 2005; Discher, 2005; Zaman, 2006; Ghassemi, 2012]. It has been shown that cells migrate faster on collagen coated surfaces if they exercise less tension. Lo et al. [Lo, 2000] have reported evidence that 3T3 fibroblasts can regulate their migration by probing the substrate stiffness (durotaxis) in the same manner as cells do for chemical gradients (chemotaxis). In particular, fibroblasts direct their movement toward stiffer substrate zones through the regulation of the lamellipodia dynamics. Cancer cells can also adapt their migration behaviour to environmental

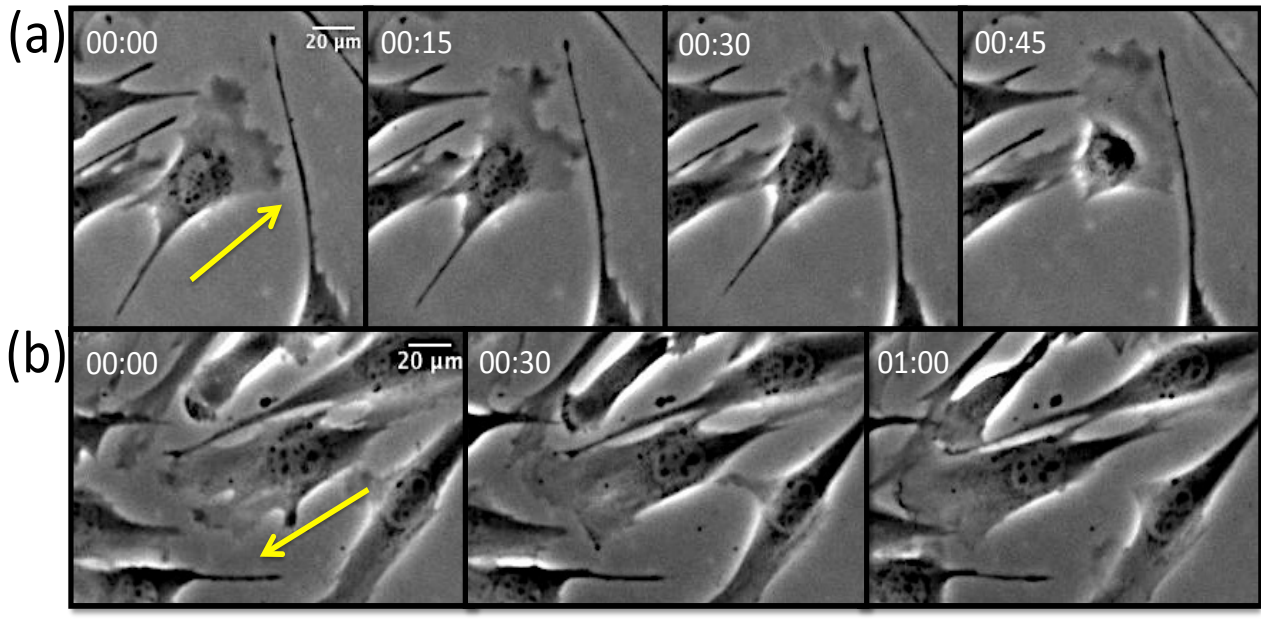

Figure 3.17: **C2C12 myoblasts migrating on collagen coated petri dishes.** DIC images taken from the time-lapse video recording: (a) a myoblast moving toward the upper-right direction; (b) another myoblast migrating toward the lower-left direction. Both cells adopt a mesenchymal migration mode. The yellow arrows indicate the direction of the cell movement. The time is reported as hh:mm. Scale bar: 20 μm.

modifications [Knight, 2000; Friedl & Wolf, 2003]. An example of C2C12 myoblasts crawling on gold surface is shown in Fig. 3.16. A similar illustration of C2C12 migration on a CCPD is shown in Fig. 3.17. In both cases the C2C12 myoblasts are moving by mesenchymal migration *via* lamellipodia protrusions developing on the leading edge in the movement direction. Using these DIC time-lapse videos, we estimated the migration velocity of C2C12 myoblasts in both conditions. We recorded 1 image every 30 seconds using a low magnification objective (0.648 μm/pixel size) mounted on an inverted Axiovert 135 microscope. The video lasts 1 h 30 min for myoblasts on CCPD and 8 h for cells on gold micro slides. For each substrate, we estimated the myoblast locomotion speed by measuring the distance covered by 10 cells (tracking their nucleus center). Myoblasts migrate at about 3 nm/sec, *i.e.* 0.18 μm/min and thus $\sim$ 10 μm/h. In particular, myoblasts seem to migrate slightly faster when adhering on collagen (3.2 $\pm$ 1.2 nm/sec) as compared to those moving on a gold surface (2.3 $\pm$ 1.2 nm/sec). These results are in agreement with previous studies of cell migration rate on softer substrates. We also recorded C2C12 myoblast migration and adhesion dynamics through Scanning Surface Plasmon Phase Microscope (SSPM) [Berguiga, 2007, 2011]. SSPMs, as all evanescent field microscopes, are based on reflectance field measurements and are better suited to follow the dynamics of cell adhesion on gold surfaces without need of staining the living samples. This non-intrusive optical microscopy was used to capture and quantify the evolution of myoblast adhesion and migration during very long periods (several days). Time-lapse videos of 50 hours were recorded during which C2C12 myoblast adhesion and motility dynamics was captured in real time [Berguiga, 2016]. Fig. 3.18 shows a set of SSPM images of myoblasts where we can distinguish sharp and

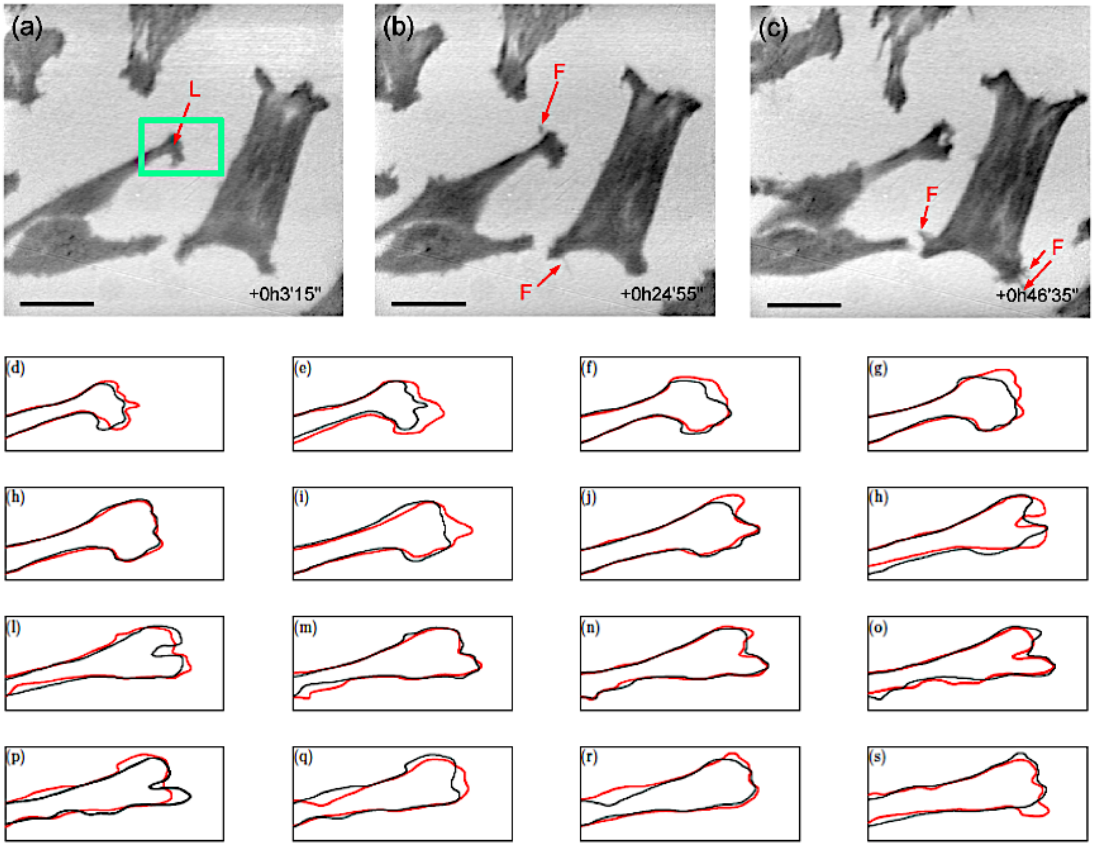

Figure 3.18: **Adherent living C2C12 myoblast cell protrusion dynamics probed by SSPM.** (a-c) Global images of the scanned region (100 x 100 μm^2) at different times. At the leading edges of the two central cells, an intense lamellipodial or filopodial activity is outlined with read arrows. (d-s) Zoom (17 μm x 22 μm) on the cell area marked in green in (a) showing two successive cell contours from images separated by 10 minutes, the oldest (respectively newest) one being plotted in black (respectively red). Scale bars: 20 μm; intensity scale = [-0.02; 0.08].

elongated filopodia, extended lamellipodia and nuclei. With this method we could trace the temporal deformation of cell protrusions (lamellipodia) during their migration on gold surfaces [Streppa, 2016]. Two important information came out from this preliminary study: (i) the velocity of the leading edge contour is not constant in time, and we can observe situations where the leading edge is moving back, (ii) the distribution of velocities along the leading edge contour is not an invariant of the dynamics, as expected for Laplacian field driven interfaces [Argoul, 1997].

3.1.7 Myoblast differentiation and myotube properties

As introduced in Section 3.1.1, C2C12 myoblasts undergo myogenic differentiation when maintained in growth factor poor medium, such as in low-serum conditions. Their differentiation ability ranked this cell line as one of the mostly used biological model for *in vitro* studies of muscle development and differentiation [Yaffe, 1969; Katagiri, 1994; Andrés & Walsh, 1996; Guttridge, 1999; Thomas, 2000; Burattini, 2004; Curci, 2008; Lee, 2009; Doherty, 2011]. Once 80 % cell confluence is reached, C2C12 myoblast myogenic differentiation can be initiated by

replacing the growth medium (GM) with the differentiation medium (DM) (Chapter 5). We monitored their differentiation process on collagen coated petri dish by DIC microscopy every 24 hours, from 1 hour before changing the medium until 5 days after differentiation induction. Before inducing the differentiation (Fig. 3.19(a,g,m)), C2C12 myoblasts appeared not confluent, keeping their previously described characteristic morphology. 24 hours after replacing GM by DM (Fig. 3.19(b,h,n)), myoblasts could complete one full cell cycle and the number of cells had doubled. At the lower objective magnification, cells then appeared confluent. Besides the increased number of cells, we could identify some cells which were still undergoing cell rounding and mitosis. It is possible that some myoblasts keep on proliferating even in these conditions. This *in vitro* phenomenon reflects the *in vivo* self-renewal ability of myoblasts. In particular, myoblasts undergoing mitosis, and thus not committed to differentiation, were also found during the entire observation period (120 hours). As previously reported [Ceruti, 2000; Querfurth, 2001; Burattini, 2004], besides mitosis, some apoptotic behaviour can be observed in muscle systems, as regulatory events for maintaining an appropriate cell number. The second day of differentiation (Fig. 3.19(c,i,o)), C2C12 cells exhibited a more elongated shape and a more aligned organization. The third day, cells were still reshaping and displayed narrower cell bodies. During the following 24 hours, myoblasts fused their cell membranes and created multinucleated elongated cells: the myotubes (Fig. 3.19(e,k,q)). The fifth day of differentiation, myotubes had maturated through the fusion of other myoblasts since they showed a higher number of centrally located nuclei (Fig. 3.19(f,l,r)). Note that giant cells were observable during the entire process (data not shown) as non-elongated, almost rounded very large cells, often with a polyploid nucleus. Their presence is known to be associated with cell differentiation but their specific role is still not fully understood [Hieter & Griffiths, 1999; Leitch, 2000; McGann, 2001; Burattini, 2004]. Membrane blebbing often appeared, especially during time-lapse DIC recording (data not shown). It has been hypothesized that membrane ruffling or blebbing could be correlated with primitive contraction because, at this stage, myotubes show an important increase in voltage-gated Ca^{2+} channel density on their plasma membrane [Burattini, 2004]. However, this hypothesis is still very speculative since co-culture of myotubes with motoneurons is necessary for a complete contraction. In order to quantify the degree of myotube formation, we calculated the fusion index defined as the percentage of nuclei contained in myotubes as compared to the total number of nuclei in each image [Lee, 2013; Kamli, 2014]. On the fifth differentiation day on CCPDs, the mean fusion index reaches 78 % (estimated from 5 images of similar magnification chosen at random).

Quantitative evaluation of these morphological modifications during differentiation was performed by using the same protocol as in Section 3.1.5. The results are shown in Figs. 3.20 and. 3.21. The length of C2C12 cells increases slightly 48 and 72 hours after the differentiation induction before rising sharply the two following days (Fig 3.20(a)). These results are in agreement with the images shown in Fig 3.19 where very elongated myotubes start being visible the fourth day. The cell width instead decreases constantly during the differentiation process reflecting the observed cell narrowing (Fig 3.20(b)). The cell area remains unchanged the 3 first days, before almost doubling the last two days (Fig 3.20(c)). Thus, it is only the fourth and fifth days that elongated myotubes with different morphology appeared. Concerning the nuclei, their morphological parameters remain roughly unchanged until the fourth day, where all the values decrease (Fig 3.20(d-f)). These results indicate that myotubes have smaller nuclei as compared to myoblasts. Consistently, the cell aspect ratios (Fig. 3.21(a)) increase significantly the last two days, confirming that myotubes are more elongated than myoblasts. Less evident

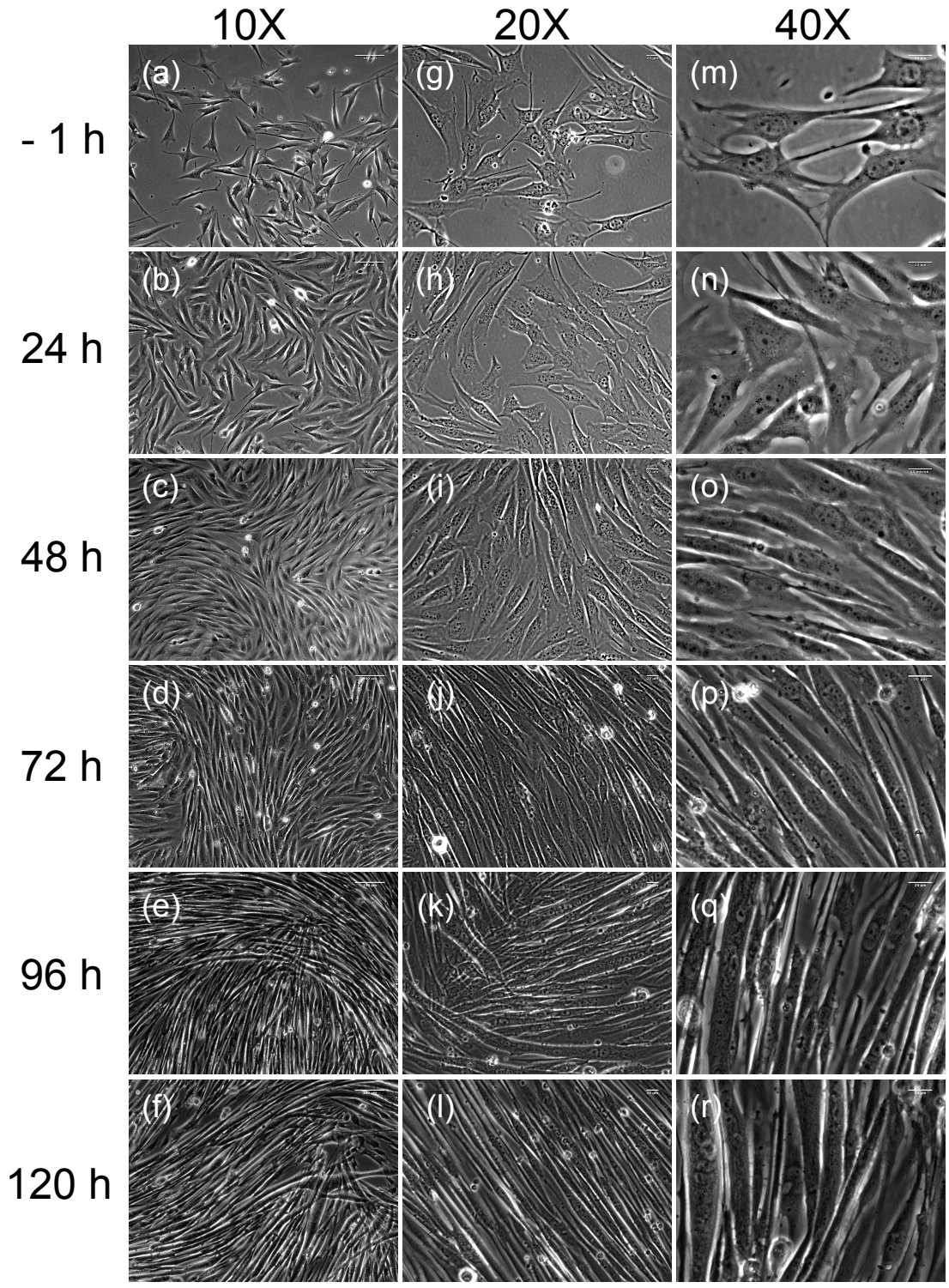

Figure 3.19: **C2C12 myogenic differentiation process.** DIC microscopy images captured with the (a-f) low, (g-l) middle and (m-r) large objective magnification. The observations were performed every 24 hours, starting 1 hour before changing the medium ((a), (g) and (m)) until the fifth day of differentiation ((f),(l) and (r)). Cell were grown on collagen-coated petri dishes. Scale bars: (a-f) 100 μm; (g-r) 20 μm.

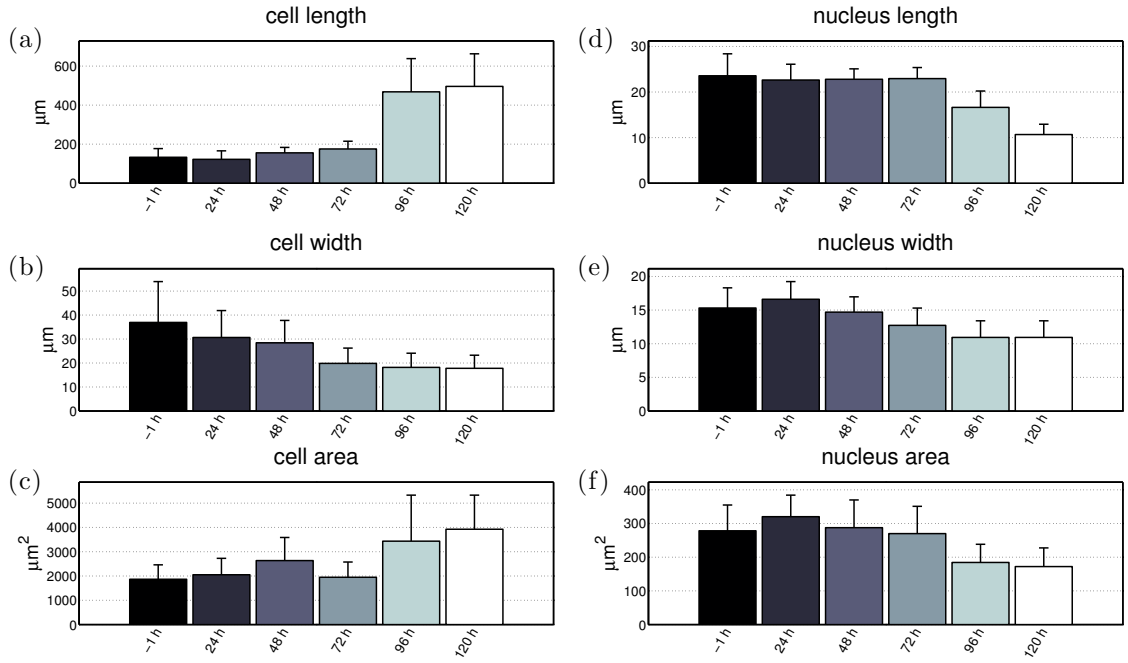

Figure 3.20: **Morphological parameter evolution during C2C12 myoblasts differentiation.** (a) Length; (b) width; (c) area of C2C12 cells adhering on collagen coated petri dishes. (d) Length, (e) width, (f) area of the nuclei of the same cells. Values were measured with ImageJ from at least 10 DIC images. The data are reported as mean ± SD over n= 30 cells for each day.

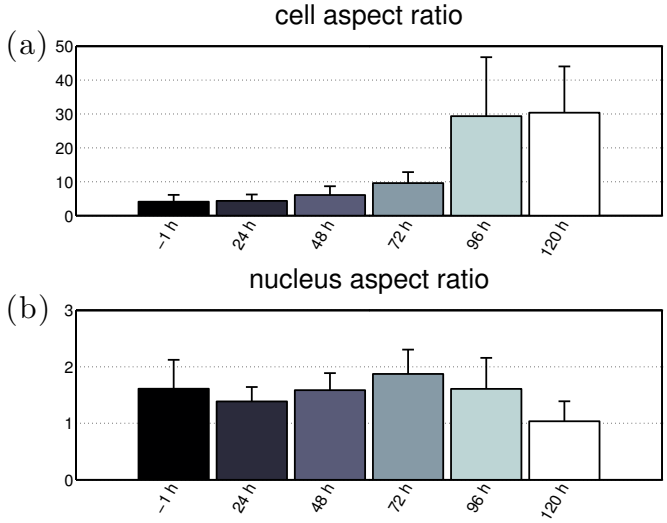

Figure 3.21: **Cell and nucleus aspect ratio evolution during differentiation.** Aspect ratio of the cell (a) and of the nucleus (b) at different stages during C2C12 myoblast differentiation. Values were measured with ImageJ from at least 10 DIC images. The data are reported as mean ± SD over n= 30 cells for each day.

conclusions can be drawn from the evolution of the nucleus aspect ratio (Fig. 3.21(b)). 120 hours after switching to DM, the mean nuclear aspect ratio reaches 1, meaning that myotubes have almost rounded nuclei. Let us point out that these observations of C2C12 cell differentiation are in agreement with the well-known steps of this process previously reported in the literature: myogenic committed cells exit from the cell cycle, elongate, align, fuse their plasma membrane becoming multinucleate myotubes with centrally located nuclei and finally maturate in myofibrils with laterally located nuclei. We also tried to differentiate the C2C12 cell line on glass bottom and on standard petri dishes. The C2C12 cell line was unable to differentiate on glass surfaces. On standard petri dishes, although the differentiation was achieved and multinucleate myotubes appeared on the fifth day, they exhibited a more variable morphology, less parallel patterns with larger fraction of myotubes detached from the surface. In these conditions, the fusion index decreased to 55 %, indicating less fusion capability. Note that this value is in agreement with previously experimental estimations [Yoshida, 1998; Burattini, 2004]. The parallel alignment of myofibers is critical *in vivo* for generating high contractile forces in muscle [Okano, 1997]. Myogenesis is known to be impacted by the substrate properties. In particular, during differentiation, C2C12 myoblasts spontaneously contract, causing their detachment from non flexible substrates [Cooper, 2004; Engler, 2004b]. Moreover, Bhana et al. [Bhana, 2010] showed that C2C12 myotubes can contract spontaneously after four days in DM on soft but not on stiff substrates. Therefore, to obtain a more homogeneous and resistant population of myotubes, we used collagen coated petri dishes as adhesion surface for the study of myotube mechanical properties.

Indeed, not only the morphology but the intracellular structure also changes dramatically during differentiation, leading to a very different CSK organization than in myoblasts. During myogenesis, the three CSK filaments, the adhesion structures and the intracellular organization change significantly [Musa, 2003; Mian, 2012]. The most remarkable event during differentiation is the membrane fusion which causes a breakdown of the cell membrane and some important rearrangement of the CSK. At the beginning, fusion concerns mononucleated myoblasts; then myoblast-myotube and myotube-myotube fusions start occurring [Horsley, 2003; Musa, 2003]. Using time-lapse imaging and fluoresce staining, Nowak et al. [Nowak, 2009] evidenced the following specific events that take place before and during myoblast fusion: (i) evolution to an elongated bipolar shape of fusing myoblasts, (ii) alteration of their membrane organization, and (iii) lamellipodia and filipodia dynamic modifications when forming myotubes. The fusing myoblasts acquire a bipolar elongated shape before undergoing plasma membrane fusion. Such a re-organization of the cell morphology requires not only non-muscle myosin II and actin dynamics but also cadherins, integrins and DOCK1 (dedicator of cytokinesis protein 1, previously known as DOCK180), all *via* the activation of Rac1 [Swailes, 2006; Laurin, 2008; Peckham, 2008]. The typical bipolar-shaped cells committed to membrane fusion and thus to myogenic differentiation are indicated by an arrowhead in Fig. 3.22. Cell-cell interactions *via* gap junctions and small pores were observed on plasma membranes prior to fusion [Kalderon & Gilula, 1979; Doberstein, 1997; Nowak, 2009]. Nowak et al. [Nowak, 2009] also showed that the second day of differentiation, filipodia and lamellipodia protrusions were no longer observable perpendicularly to the main axis of elongated cells; instead filipodial dynamics, as protraction and retraction, were found on their short sides. The reorganisation of the cell shape, the filipodia and lamellipodia dynamics are events known to be correlated to actin dynamics. Moreover, genetic studies have demonstrated the important role of actin on myoblast membrane fusion, in particular of the genes related to Arp2/3 complex and actin remodelling [Kesper, 2007; Schäfer, 2007; Berger,

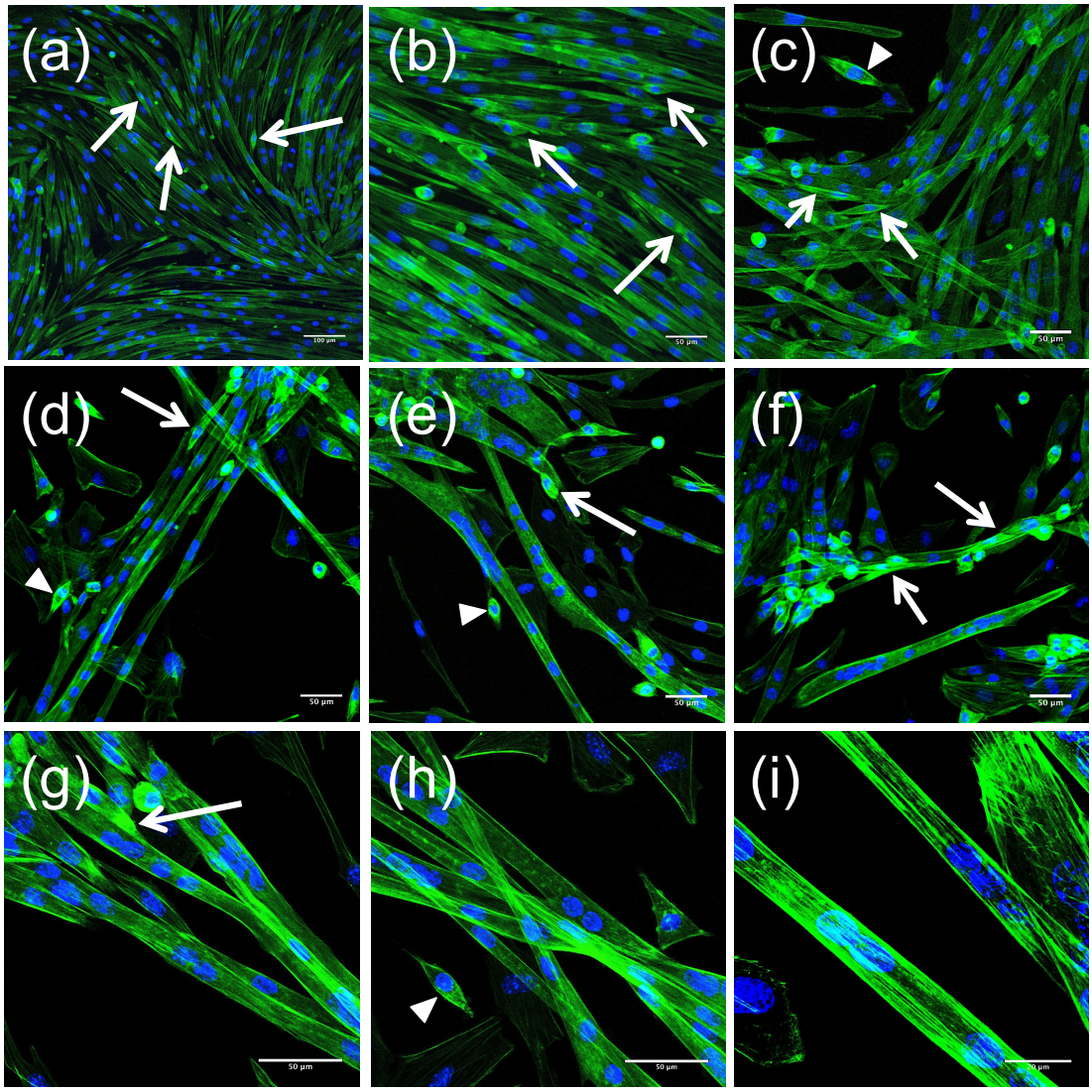

Figure 3.22: **Fluorescence staining of F-actin and nuclei on C2C12 myotubes.** Confocal microscopy imaging of microfilaments (green) and nuclei (blue) of C2C12 myotubes, the fifth day after differentiation induction. White arrows indicate events of cell fusion on forming myotubes; arrowheads indicate the typical bipolar shape of myogenic committed myoblasts. Staining: F-actin (phalloidin-Alexa Fluor 488, green) and nuclei (DAPI, blue). Scale bars: (a) 100 μm, (b-h) 50 μm, and (i) 20 μm.

2008]. For example, the pleckstrin homology (PH) domain-containing protein casein kinase 2 interacting protein-1 (CKIP-1) is known to regulate myoblast fusion in C2C12 myoblasts by coordination of the Arp2/3 complex activity. In fact it has been shown that in C2C12 myoblasts, CKIP-1 ectopic expression increases their cell fusion [Safi, 2004] while CKIP-1 expression inhibition depletion significantly impairs this process [Safi, 2004; Baas, 2012]. The critical role of actin has also been proved by its pharmacological inhibition which causes lower fusion index and abnormal shapes [Nowak, 2009]. Highly dynamic accumulation of actin was observed in Drosophila in fusion areas termed actin *foci* [Richardson, 2007]. It is now well admitted that

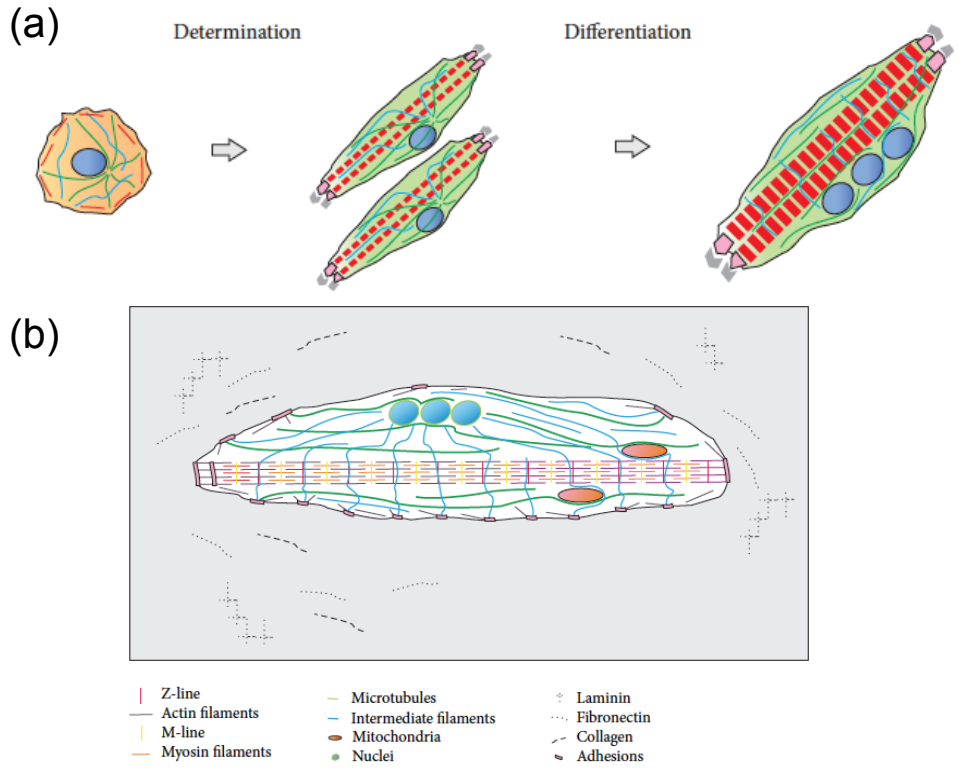

Figure 3.23: **CSK rearrangement during myogenesis and myotube intracellular organization.** (a) Schematic representation of the CSK evolution during myogenesis: mononucleated myoblasts show cortical actin filaments (red), cytoplasmic intermediate filaments (blue) and radial microtubules (green); after mitosis, cell daughters become bipolar cells that align and start creating myofibrils (red) and polar adhesions (pink); after myoblast fusion, multinucleate myotubes exhibit strong myofibrils, IFs around the Z-line and longitudinal MTs without centrosomes. (b) Organization of the major CSK compartments of a myofiber. Adapted from ISRN Developmental Biology [Costa, 2014].

actin is a major actor in myoblast fusion and that this role is conserved across different species [Kesper, 2007; Schäfer, 2007; Berger, 2008; O'Connor, 2008b; Nowak, 2009].

It should be noticed that together with actin, the two other types of CSK filaments, namely MTs and IFs, are also involved in myoblast fusion and myogenesis. Fusion events between bipolar myoblasts and forming myotubes are marked by white arrows in Fig. 3.22. Denser actin arrangements on fusing bipolar myoblasts are recognisable as compared to non myogenic committed triangular and enlarged myoblasts. Because of the fusion, myotubes with 3 or more nuclei appear; in the hours following the first fusion, nascent myotubes keep incorporating mononucleated precursors thus increasing their number of nuclei. At late differentiation stage, myotubes have more (several) nuclei, either clustered, or disseminated longitudinally. From our observations after 5 days of culture in DM, most of the nuclei are centrally located but laterally located nuclei are sometimes visible. The distribution of myotube nuclei can be studied from fluorescence microscopy images (Fig. 3.22), with nucleus DAPI staining. Besides the multinucleate nature of myotubes, protein synthesis also switches from housekeeping isoform to muscle-specific protein production. During differentiation, CSK compartments remodel in order to create a highly specialised CSK capable of contraction as sketched in Fig. 3.23. MTs are

also involved in myogenesis for the replacement of nuclei, myofibrillogenesis, adhesion, fusion and alignment [Kaufmann, 1999; Pizon, 2005; Khairallah, 2012; Costa, 2014]. In differentiated myotubes, MTs are longitudinally organized as less dynamical [Gundersen, 1989] linear arrays along the long axis of the cells [Tassin, 1985] (Fig 3.23). Some microtubule binding proteins (MAP4, EB1 and EB3) involved in MT elongation and stabilisation were identified [Mangan & Olmsted, 1996; Straube & Merdes, 2007; Whipple, 2010]. IFs are abundantly distributed over the entire cell body as shown in blue in Fig 3.23(b). In particular, the IF network contributes to mechanochemical connections between nuclei, mitochondria network, plasmatic membrane, intercellular adhesion structures and the contractile myofibrils through the Z-lines [Lazarides, 1980; Capetanaki, 2007; Costa, 2014]. As one of the most abundant muscle IF protein, desmin has a critical role in the fusion during C2C12 myogenesis [Li, 1994] and in muscle pathology. Molecular biology studies have identified a class of diseases affecting skeletal and cardiac muscles related to desmin mutations called desminophaties [Goldfarb, 2004; Costa, 2004b]. However, in differentiated striate muscles the role of desmin is still not fully understood [Costa, 2004b].

Actin filaments, the third type of CSK filaments, experience probably the most amazing reorganization. From a cortical actin distribution of stress-fibers in myoblasts (Section 3.1.4), in myotubes (and particularly in myofibrils) most of the actin is found in the cytoplasm or close to adhesion regions of the sarcolemma (Fig 3.23(b)). Contractile sarcomeres are the basic-unit of myofibrils; they are the main muscle specific structures created *de novo* during myogenesis. Indeed, the smallest building block of the muscle sarcomere is the actin-myosin unit. If the configuration of these building blocks in muscle-specific proteins is well-known, as well as all the molecular events that lead to contraction, their assemblage during myogenesis is still not completely understood. Sanger et al. [Sanger, 2002] elaborated on an immature myofibril arrangement at intermediate differentiation stages, that finally evolves in a fully organised sarcomere in mature myofibrils. Van der Ven et al. [Van Der Ven, 1999] described some stress fiber-like structures containing protein filaments like titin as primitive form of sarcomeres. More recently, the participation of integrin-dependent FAs interacting with the ECM has been suggested [Sparrow & Schöck, 2009]. Interestingly, the mature sarcomere organization has been well-described. The sarcomeric actin isoform, which switches during myogenesis from the α-cardiac actin isoform (expressed in myoblasts) to the α-skeletal actin (expressed in myotubes) [Mizuno, 2009], is at the heart of this organization. Indeed, it is the sliding of the ATPase myosin (the muscle-specific isoform myosin II) on actin that creates the muscle contraction at the molecular level. It should be noticed that sarcomeric myosin II has several variants according to the muscle type (*e.g* cardiac myosin II, and fast and slow skeletal myosin II) that differ from the non-muscle myosin II previously discussed for myoblasts; they indeed correspond to two different isoforms [Costa, 2014]. Actin dynamics is regulated by several actin binding proteins (ABPs), but the sarcomeric actin turnover is slower and its regulation is completely different as compared to non sarcomeric actin. For instance, in sarcomeres there are several proteins that specifically regulate actin length (*i.e.* CapZ, tropomodulin and nebulin) [Costa, 2014]. Moreover, actin filaments of the sarcomeres are bound to other muscle-specific proteins, such as tropomyosin and troponin, that regulate their solidity and the interaction with myosin. When Ca^{2+} is released from the sarcoplasmic reticulum, it binds the calcium-binding subunit of troponin that causes a change of its conformation, which in turn leads to the displacement of tropomyosin from its myosin-binding domain. In these conditions, myosin slides on actin using ATP and generates muscle contraction. From the F-actin phalloidin staining shown in Fig. 3.22, the typical sarcomeric striated organization is not detectable. However, the accumulation of

F-actin in the entire cytoplasm is evident. This is probably due to the low image resolution and the use of phalloidin. Indeed, this molecule binds F-actin while in order to observe the striated organization it would be best to mark α-actinin of the Z-line. Burattini et al. [Burattini, 2004] partly solved this problem using Transmission Electron Microscopy (TEM) since characteristic sarcomeres with thin and thicker filaments were recognized in C2C12 myotubes.

3.2 Mechanical properties of muscle cells: a literature survey

In this section we review different experimental studies devoted to the mechanical properties of single cells and muscle tissues. We also discuss the impact of CSK perturbations (ATP depletion and blebbistatin) which have been used in our AFM experiments.

3.2.1 Single cell mechanical studies

Single cell biomolecular and biochemical studies have proven to be decisive steps for a better understanding of tissular and organic processes. The early stages of disease pathogenesis take place at single cell level and they systematically involve cell mechanics. Thus, single cell approaches have been widely developed in the past two decades to evaluate the mechanical properties of cells and their interplay with the extracellular environment, both in physiological and pathological conditions [Rodriguez, 2013]. For years, the interest of the scientific community in cell mechanics has been steadily growing. In fact, among the 12 724 publications available in Web of Science database under the keyword "cell mechanics", 9129 were published during the past decade. The majority of cell mechanics studies involve techniques and instruments adapted from physics experiments. Actually, there exists a wide variety of experimental approaches implying mechanical, optical, acoustic methods at the single cell level. Among them, we selected in Table 3.1 some recent papers reporting on mammalian cell mechanics. We preferentially concentrated on AFM experimental studies [Lekka, 1999; Kuznetsova, 2007; Kirmizis & Logothetidis, 2010; Rodriguez, 2013] and we compared the estimated values of the Young's modulus (E). In one case (marked with ($\star$) in Table 3.1), we calculated E from the reported shear modulus (G) through Eq. (2.42) and assuming a Poisson's ratio ν=0.5.

The typical range for the Young modulus of living cells varies from a few hundreds of Pa to hundreds of kPa. For fixed cells, the measured Young's modulus can attain values between 0.1 and a few MPa (*e.g.* endothelial cells fixed with glutaraldehyde [Arce, 2008; Birukova, 2009]). The measured stiffness of living cells is therefore lower than the one of CSK filaments (isolated or in bundles) or protein complexes, that can reach values up to GPa. The values of E reported in Table 3.1 vary between 300 Pa for weakly adherent human osteoblasts to 700 kPa for fixed astrocytes. This variability is due to several factors. First of all, it has been shown that cell stiffness is cell-type dependent. For example, fibroblasts are softer than skeletal muscle or bone cells. Moreover, the Young's modulus of muscle cells increases in the following order: myoblasts (the softest), smooth, skeletal and cardiac muscles (the stiffest) (Table 3.1). This variability reflects the adaptability and the variety of *in vivo* cellular functions. In fact, while myoblasts need high motility to fulfill their tasks, cardiac muscle cells require high resistance against mechanical stress. Secondly, the context or confinement of a living cell has a precise impact on the measured elastic modulus. Simon et al. [Simon, 2003] reported much lower stiffness of weakly adherent human osteoblasts (E = 0.3 kPa) than strongly adherent osteoblasts (E = 200 kPa). It has often been observed that rounded detached cells behave as softer liquid-like cells [Darling,

cell type	technique	c. region	E (kPa)	reference
human osteoblasts				
HBMSCs (weak adherent)	AFM	n.s.	0.3	[Simon, 2003]
HBMSCs (strong adherent)	AFM	n.s.	200	[Simon, 2003]
rat cerebrum astrocytes				
living	AFM	nucleus	2 - 3	[Yamane, 2000]
living	AFM	F-actin	10 - 20	[Yamane, 2000]
fixed	AFM	map	200 - 700	[Yamane, 2000]
human platelets				
activated	AFM	map	1 - 50*	[Radmacher, 1996]
human cervix cell lines				
End1/E6E7 (normal)	AFM	central	$\sim$ 5.50	[Hayashi & Iwata, 2015]
Hela (cancerous)	AFM	central	$\sim$ 2.48	[Hayashi & Iwata, 2015]
human breast cell lines				
MCF-10A (non-malignant)	AFM	central	$\sim$ 0.8	[Li, 2008]
MCF-7 (malignant)	AFM	central	$\sim$ 0.4	[Li, 2008]
mouse ovarian tumor-initiating cells				
TICs (early stage)	AFM	nuclear	0.607 - 1.721	[Babahosseini, 2014]
TICs (late stage)	AFM	nuclear	0.389 - 0.813	[Babahosseini, 2014]
human lymphocytes				
control	AFM	n.s.	2.54 - 3.26	[Zheng, 2015]
chronic lymphocytic leukemia (CLL)	AFM	n.s	5.02 - 5.78	[Zheng, 2015]
fibroblasts				
mouse 3T3 (non-polarized)	AFM	nuclear	0.89 - 1.17	[Harn, 2015]
mouse 3T3 (polarized)	AFM	nuclear	0.51 - 0.89	[Harn, 2015]
mouse 3T3	OS	whole cell	0.62 - 0.71 ($\star$)	[Ananthakrishnan, 2006]
mouse 3T3	AFM	non nuclear	$\sim$ 20	[Chaki, 2013]
muscle cells				
mouse C2C12 myoblasts	C	whole cell	0.82 - 1.46	[Peeters, 2005]
mouse C2C12 myoblasts	AFM	several	0.72 - 12.8 kPa	□
mouse C2C12 myotubes	AFM	non nuclear	5 - 49.3	◊
rat aortic smooth muscle	MS	whole cell	2.1 - 12.9**	[Nagayama, 2006]
chicken myocytes	AFM	lamellipodia excluding SFs	5 - 30	[Hofmann, 1997]
rat myocyte	AFM	n.s.	34.4 - 35.8	[Lieber, 2004]
rat myocyte (aging)	AFM	n.s.	41.5 - 43.5	[Lieber, 2004]
rabbit myocytes	AFM	non nuclear	89.6 - 111	[Mathur, 2001]
chicken myocytes	AFM	lamellipodial SFs	100 - 200	[Hofmann, 1997]

AFM = atomic force microscopy
PT = particle tracking
OS = optical stretch
MS = mechanical strech
C = compression
*=depending on the cell region (pseudo nucleus = softer)
** = depending on the sample preparation
($\star$) = E calculated from G
n.s. = non specified
□ = [Collinsworth, 2002; Sbrana, 2008; Takemoto, 2012; Al-Rekabi & Pelling, 2013; Sun, 2014; Li, 2016]
◊ = [Mathur, 2001; Collinsworth, 2002; Zhang, 2004]

Table 3.1: **Review of the measured elastic modulus on single mammalian cells.** Single cell mechanics studies performed on several types of cells in different conditions (*e.g.* normal and pathological). The stiffness is estimated from the measured Young's modulus (E). The probed cell region (c. region) is also provided.

2008; Chen, 2014]. These findings indicate that cell mechanical properties are dynamic and that they depend on the CSK conformation.

The estimated cell elasticity also varies according to the cell source and the sample preparation protocol. In fact, the stiffness of rat aortic smooth muscle cells was found larger ($E = 11.0 \pm 1.9$ kPa) for freshly isolated cells (FSMCs) than for cultured cells (CSMCs) ($E = 2.6 \pm 0.5$ kPa) [Nagayama, 2006]. Nagayama et al. also reported that disruption of F-actin network by cytochalasin D treatment increases the CSMCs deformability ($E = 1.5 \pm 0.2$ kPa). This is a typical example of CSK-perturbed cell study. Indeed, since the CSK dynamics and especially the actin network, have a major role in the regulation of cell mechanics, their perturbation is generally associated with a variation of the cell stiffness.

Concerning AFM experiments, we have shown in Chapter 2 that the mechanical response to stress of myoblasts and myotubes changes with the cantilever scan velocity. The geometry of the cantilever tip has also a remarkable impact on the estimated Young's modulus [Chen, 2014]. For instance sharper tips (conical, pyramidal, single needle) lead to higher estimates of the Young's modulus than spherical tips [Rico, 2005; Vargas-Pinto, 2013; Chen, 2014], mostly because the gradient of shear forces at the tip apex is steeper in the first case. For example, osteoblasts behave stiffer when probed with a pyramidal tip ($E \sim 14$ kPa) [Charras & Horton, 2002a]) or a spherical tip ($E \sim 3.18$ kPa) [Charras & Horton, 2002b]). Sharp indenters, such as conical or pyramidal tips, are better suited to probe local (nanoscale) mechanical properties, but they are more prone to local perturbations or disruptions of the CSK network. Spherical tips are instead used to estimate more global cell mechanical properties [Chen, 2014]. Using sharp indenters, the spatial heterogeneity of mechanical properties of specific cell compartments (*i.e* elasticity maps) was evidenced [Hoh & Schoenenberger, 1994; Rotsch, 1999]. Very local measurements on single filaments were also performed with sharp indenters. Hofmann et al. [Hofmann, 1997] measured the *in situ* SF elasticity of chicken myocytes ($E = 100 - 200$ kPa) and Yamane et al. [Yamane, 2000] those of F-actin filaments of astrocytes ($E = 10 - 20$ kPa). Sharp indenters are mandatory for resolving the spatial mechanical inhomogeneity of cell CKS and its dependence on the experimental context and the cell type. On the one hand, it has been reported that peripheral regions of primary human umbilical vein endothelial cells (HUVEC), HeLa S3 cells and chicken cardiocytes are stiffer than their nuclear domains [Mathur, 2000; Yokokawa, 2008; Vargas-Pinto, 2013; Schaefer, 2014]. On the other hand, the nuclear regions have been described significantly stiffer than the peripheral regions in human-derived cancer cells (A549, U251), adult stem cells (MSCs), fibroblast-like valve interstitial cells (VICs), leukocytes and also in HUVEC [Dong, 1990; Hofmann, 1997; Harada, 2014; Liu, 2014]. Besides these contrasting results, the majority of the reported experimental data reveals a spatial heterogeneity of the local cell mechanical properties. But since peripheral regions of adherent cells are generally thin, model variants (including higher order nonlinear terms) have been proposed to include the effect of the underlying solid substrate on the FICs [Gavara & Chadwick, 2012]. Interestingly, Yu et al. [Yu, 2015] showed the higher cortical stiffness of the lung adenocarcinoma cell nuclear regions as compared to their non-nuclear areas by AFM indentations. They also reported for the same cells, some increase of the viscoelasticity with the distance to the nucleus using intracellular particle tracking (PT) micro-rheology. Although these results may appear contradictory, they may be the consequence of using different mechanical probes: AFM nano indentations ($h \sim 500$ nm) are actively driven by the operator, they measure mainly the elastic modulus (or more generally the viscoelasticity) of the cell cortex, while PT experiments are driven by thermal fluctuations (without any action of the operator) and measure the intracellular viscoelasticity. It is therefore very important, when comparing different experimental studies on single living cells, to carefully take into account both the experimental constraints and the cell type and origin.

Mechanical properties of single cells change with their pathological state and their microenvironment. It is widely accepted that the mechanical properties of the cell environment play an import role in the pathogenesis of several diseases [Ingber, 2003a; Rodriguez, 2013], such as atherosclerosis [Gimbrone, 2000], asthma [Affonce & Lutchen, 2006], osteoporosis [Klein-Nulend, 2003], glaucoma [Tan, 2006], muscle dystrophy and cardiac myopathy [Kumar, 2004; Heydemann & McNally, 2007]. Moreover, it has been widely shown that the mechanical properties of cells are altered in human diseases, such as cancer [Rosenbluth, 2006; Li, 2008; Babahosseini, 2014; Hayashi & Iwata, 2015; Zheng, 2015]. Some types of cancer cells (*e.g.* malignant human breast cell lines, cancerous human cervix cell lines, lung and pancreas cancer cells) are softer than their normal counterparts [Cross, 2007; Li, 2008; Hayashi & Iwata, 2015]. In many cancer types, high deformability of malignant cells seems to be correlated to their invasiveness, and thus to their metastatic potential. Some type of cancers are characterized by a reduced level of lamins A and nesprins, which leads to softer nucleus and easier cell squeezing through different tissues [Friedl, 2011]. In this context, the Young's modulus can be considered as a trustable bio-marker of metastasis risk [Luo, 2016]. On the contrary, mouse ovarian tumor-initiating cells (late stage TICs), lymphocytes in chronic lymphocytic leukaemia (CLL) and immature hematopoietic cells in myelogenous leukemia (CML) are stiffer than their earlier stage (TICs) or healthy counterparts [Babahosseini, 2014; Zheng, 2015; Laperrousaz, 2016a]. These opposite results may be explained by the profound differences of these cancer cells and their microenvironments. For example, breast cancer cell softening improves their tissue invasiveness, while stiffening of lymphocytes allow them to better resist to mechanical constraints exerted within the bone marrow. Some correlation between cell migration, Young's modulus and metastatic potential in several cancer types has been found. However, this correlation is lost for cells with chemically or genetically modified motility [Luo, 2016]. High motility has also been observed for soft cells in non pathological conditions [Mihai, 2012; Zou, 2013; Zhang, 2014; Harn, 2015]. For all these reasons, the knowledge of the specific cell type together with the experimental and analytical conditions is primordial to correctly interpret the cell mechanic experimental data.

3.2.2 The role of ATP in single cell mechanics and CSK active processes

3.2.2.a ATP as a versatile source of energy for living organisms

Adenosine 5' triphosphate (ATP) is a vital molecule for most living organisms on Earth. Due to its chemical structure (phosphates coupled to an adenine), ATP carries the chemical energy through the cells, participates in several enzymatic reactions as co-substrate and has a central role in cell metabolic functions (catabolism and anabolism) [Devin & Rigoulet, 2007; Bonora, 2012; Nelson, 2013]. In aerobic cells, ATP is synthesized by two different processes [Nelson, 2013]: (i) a substrate-level phosphorylation catalyzed by phosphotransferase during glycolysis (2 moles of ATP produced from 1 mole of glucose), and (ii) a mitochondrial oxidative phosphorylation (OXPHOS), which requires electron transfer by the electron transport chain (ETC) to trigger the ATP synthase activity (up to 36 ATP moles per mole of glucose) [Oster & Wang, 2003; Jonckheere, 2012; Young, 2013]. In normal aerobic cells, the ATP production is unbalanced toward the more efficient OXPHOS. However, high proliferative continuously cultured cell lines fed with high levels of glucose, as C2C12 myoblasts, use a combination of oxidative and glycolytic energy metabolisms [Mandel, 1986; Lunt & Vander Heiden, 2011; Young, 2013]. This paradoxical metabolism is similar to the upregulated aerobic glycolysis in cancer cells (Warburg effect) [Ferreira, 2010; Yu, 2016]. Thus, to block completely the ATP production

in C2C12 myoblasts, we inhibited both the ETC complex III (antimycin A, AMA) [Nakayama, 1956; Pham, 2000; Ma, 2011; Rakhmatullina, 2015] and the glycolysis (2-deoxy-D-glucose, 2-DG) [Bright, 1995; Pelicano, 2006; Fokt, 2009] (see also the Materials and Methods in Chapter 5). Inside our ATP depletion buffer, the cellular ATP concentration dropped down to $\sim 7\%$ of its initial value after 15 minutes and then continued to decline at a slower rate [Theander, 2002].

The energy is released from ATP by hydrolysis of its phosphate bonds. The partial hydrolysis of ATP by cleavage of the bond between its γ phosphate group (*i.e.* the terminal phosphoanhydride) produces one molecule of adenosine diphosphate (ADP) and a phosphate group (Pi). In standard conditions, ATP + $H_2O \rightarrow$ ADP + Pi + H leads to a drop $\Delta G = -30.5$ kJ/mol of the Gibbs free energy [Frey & Arabshahi, 1995; Nelson, 2013]. The actual Gibbs energy delivered by ATP hydrolysis in living cells is higher (*e.g.* $\Delta G = -52$ kJ/mol in human erythrocytes, [Nelson, 2013]) because of different concentrations of ATP, ADP and Pi in living cells as compared to standard conditions, and the chelation of ATP^{4-} by Mg^{2+} ions ($Mg\ ATP^{2-}$). Therefore, ATP hydrolysis is highly exergonic and thermodynamically favoured in living cells, as well as its further hydrolysis in adenosine monophosphate (AMP). But intracellular ATP levels are maintained at much higher values than expected from thermodynamic laws [Berg, 2002] because $Mg\ ATP^{2-}$ is kinetically stable at pH 7 due to a high activation energy of ATP hydrolysis. For a rapid cleavage of ATP phosphate bonds, the enzymatic catalysis by ATPase is required [Berg, 2002; Nelson, 2013].

ATP is fundamental for cellular function maintenance (homeostasis). ATP is involved in many essential biological processes, such as the synthesis of macromolecules from their precursors, the expression and replication of the genetic material, the thermogenesis, the active transport across the cell membrane [Grabe, 2000; Shilton, 2015], the regulation of cell signalling by phosphorylation, the non-equilibrium cytoskeleton dynamics [Mizuno, 2007], cell movement [Pollard & Borisy, 2003], cell division, the regulation of growth, development and differentiation [Martinello, 2011], the cell survival [Hoebertz, 2002], purinergic signalling mechanisms [Praetorius & Leipziger, 2009; Corriden & Insel, 2010; Martinello, 2011; Burnstock & Verkhratsky, 2012; Burnstock, 2013] and the elimination of waste products and misassembled proteins [Ambro, 2012; Amm, 2014]. In skeletal muscles, ATP has a critical role in myogenesis, regeneration and muscle contraction-relaxation[Kolb & Wakelam, 1983; Lu & Smith, 1991; Martinello, 2011; Burnstock & Verkhratsky, 2012]. ATP is continuously hydrolyzed and regenerated; its half-life time varies from seconds to minutes depending on the cell type and the metabolic activity. Each human being consumes daily an amount of ATP that is approximately equal to his body weight to sustain his energy needs [Törnroth-Horsefield & Neutze, 2008].

3.2.2.b Impact of ATP depletion on single cell mechanics

At a single cell level, ATP depletion has dramatic consequences comparable to hypoxia (ischemia), leading to cell death by necrosis [Edinger & Thompson, 2004]. A 5-10 % decrease of cellular ATP concentration causes a series of widespread consequences on different cellular compartments [Kumar, 2014]. All the ATP dependent processes are slowed down, the activity of the Na^+/K^+ ATPase pump also decreases resulting in intracellular Na^+ accumulation and K^+ diffusion outside of the cell. This non physiologic condition, characterized by an increase of intracellular Na^+, causes cell swelling by water import and dilation of the endoplasmic reticulum by passive osmotic process. Failure of the Ca^{2+} exporter pump leads to intracellular excess of calcium with damaging effects on numerous cellular components. The protein synthetic

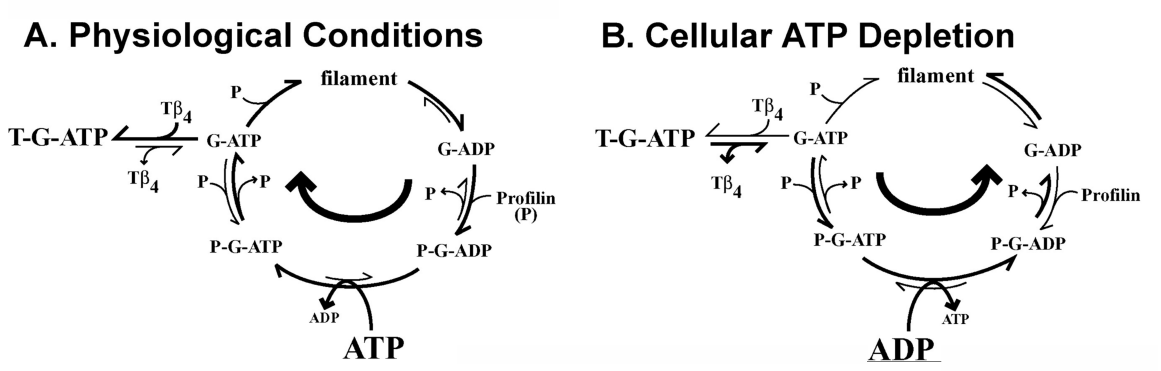

Figure 3.24: **Model of F-actin regulation in normal and ATP depleted conditions.** (a) In normal conditions, the ATP-G-actin concentration is higher than ADP-G-actin; profilin (P) catalyses the formation of ATP-G-actin which can be severed by the protein thymosin (Tβ4) and accumulates in the sequestered pool. (b) In ATP depletion conditions, the higher level of ADP-G-actin and its lower affinity for thymosin, reverses the actin diagram flux leading to F-actin aggregate formation. Adapted from Journal of Biological Chemistry [Atkinson, 2004].

apparatus is also altered by a depletion of ATP. Ribosomes detach from the rough endoplasmic reticulum (RER), polysomes dissociate in monosomes with a consequent reduction in protein synthesis and an irreversible injury of mitochondrial and lysosomal membranes causing cell necrosis [Kumar, 2014].

Before these critical long-term systemic effects leading to the loss of cell homeostasis and ultimately to cell death, ATP depletion has short-term effects on the cell CSK. ATP depletion in Madin-Darby canine kidney (MDCK) cells was shown to decrease the so-called "gate function" (the regulation of the transport between cells by trans-epithelial resistance (TER)) and to disrupt the tight junctions (TJ) [Mandel, 1993; Tsukamoto & Nigam, 1997] while the "fence function" (the asymmetrical composition of the apical and basolateral cell membrane) remained unchanged [Mandel, 1993]. Bacallao et al. [Bacallao, 1994] confirmed these findings in two renal cell lines (MDCK and JTC) and showed that ATP depletion affects dramatically the actin network during the early hours after drug administration. They reported F-actin depolymerization after 30 minutes of ATP depletion, before apical actin ring loss, and the formation of actin aggregates in the perinuclear regions after 60 minutes [Bacallao, 1994]. Disruption of the well-organized F-actin network (stress fibers and actin cortex) and secondary formation of ectopic actin aggregates (especially in perinuclear regions) was observed in different cell lines after ATP depletion [Bershadsky, 1980; Glascott, 1987; Molitoris, 1991; Herget-Rosenthal, 2001; Jahraus, 2001; Shelden, 2002; Atkinson, 2004] and in injured cells after ischemic events [Hinshaw, 1988; Sutton & Molitoris, 1998; Kwon, 2002]. Atkinson et al. [Atkinson, 2004] (Fig. 3.24) proposed that the decrease of ATP-G-actin over ADP-G-actin ratio (increased ADP-G-actin with ATP depletion) and the lower affinity of ADP-G-actin for the actin monomer severing protein thymosin, could imbalance the dynamical microfilament assembly/disassembly machinery, leading to F-actin aggregate formation.

In normal conditions, F-actin polymerization is counterbalanced by two major sequestering proteins, thymosin (Tβ4) and profilin, that maintain a pool of monomeric actin (ATP-G-actin/ADP-G-actin). Tβ4 prevents G-actin from joining either end of an existing actin filament, and isolated profilin precludes G-actin nucleation or pointed-end filament elongation. Contrast-

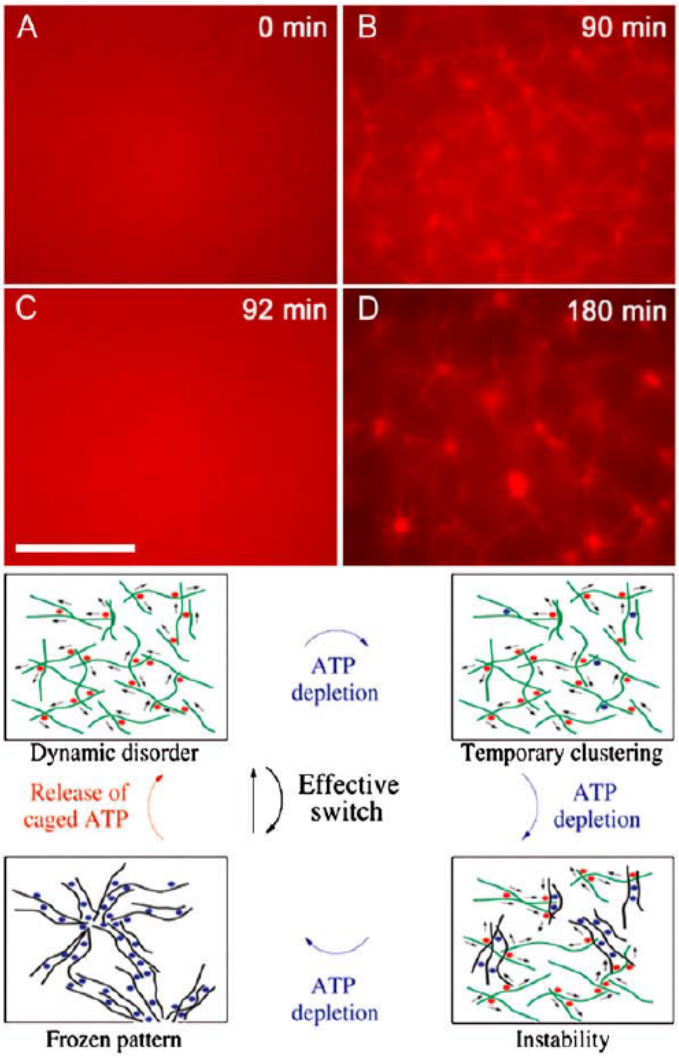

Figure 3.25: *In vitro* **actomyosin reversible reorganization in presence and absence of ATP.** (Top pictures) Fluorescence staining (rhodamine-phalloidin) of actin (2.4 μM) in solution with myosin ($\sim$ 50 minifilaments per actin filament): (A) In the presence of ATP the actomyosin network is disordered (randomised by the motors); (B) Self-assembly of "frozen" actomyosin structures is observed when initial ATP is exhausted (90 min); (C) After reintroduction of ATP, self-assembly structures are disrupted in 2-3 minutes and the system returns to a disordered state; (D) Self-assembly is again observed when reintroduced ATP is exhausted (180 min). (Bottom diagrams) Schematic for the instability-driven switch between dynamic disorder ("randomised") and ordered ("frozen") actomyosin architectures. Green lines= free actin filaments; black lines= actin filaments incorporated into an actomyosin cluster; red circles = active myosin II mini filaments; blue circles = inactive myosin II minifilaments. (Scale bars: 20 μm.) Adapted from Biophysical Journal [Smith, 2007].

ingly, profilin actively participates in barbed-end filament elongation. The two major reported consequences of ATP lack at the CSK level in different cell lines are (i) the early disorganization of the actin network, especially disruption of SFs, and (ii) the subsequent spontaneous formation of F-actin aggregates in the cytoplasm. The reconstitution of F-actin networks from purified proteins has been a powerful approach for understanding the physics of cytoskeletal networks. It has been shown *in vitro* that when myosin II motors are incorporated into an actin network, they generate internal stresses that may stiffen the network [Mizuno, 2007]; the architecture of the actin network and its cross linking proteins determines to which extent actomyosin contracts the network. Purified actin gels reconstituted with myosin in the presence of ATP produced disordered (randomised) actomyosin networks (Fig. 3.25(A,C)) [Smith, 2007]. Whereas in the absence of ATP, self-assembly of F-actin via ADP-NM II cross-linking, gave an ordered ("frozen") actomyosin network (Fig. 3.25(B,D))[Smith, 2007]. A complete ATP depletion can cause a 100-fold increase in the elastic stiffness of the actomyosin network [Smith, 2007]. It has been reported that ATP depletion did not compromise the MT network organization in MCDK cells [Bacallao, 1994], and could even stabilise it in fibroblasts [Bershadsky & Gelfand, 1983]. More generally, ATP depleted cells loose their typical intracellular actin organization but they retain their morphology (like if they were frozen) [Glascott, 1987; Bacallao, 1994; Tsukamoto & Nigam, 1997].

ATP depletion perturbation has been widely used in cell microrheology studies to distinguish ATP-driven (or active) from Brownian passive fluctuations and their impact on cell mechanics [Hoffman, 2006]. For example, different biophysical techniques have been largely applied to observe the impact of ATP depletion in red blood cell (RBC) mechanics [Weed, 1969; Meiselman, 1978; Betz, 2009]; however, contrasting results have been reported [Tomaiuolo, 2014]. ATP free solutions (also called rigor solutions) have been also utilized for cell mechanic experiments on differentiated muscle cells. The ATP decrease and the subsequent ADP increase immobilise the sarcomeric myosin II on actin filaments. Muscle fibers in rigor conditions appear remarkably stiffer than active or relaxed fibers [Yoshikawa, 1999; Akiyama, 2006; Ogneva, 2010], similarly to muscle rigor mortis of cadavers. Van Citters et al. [Van Citters, 2006] showed that ATP depletion in cultured epithelial cells affects their actin network, but in a less severe manner than blebbistatin. They also reported that ATP depleted cells appeared 4-fold softer at short time lags by internal laser tracking microrheology (LTM) (inner cell body). However, they did not detect significant variations in stiffness by external LTM and two-point microrheology (TPM). Loss of active motion was observed in ATP-depleted cells several times [Van Citters, 2006; Massiera, 2007]. Using micro-indentation, Embry et al. [Embry, 2016] reported a decrease of renal glomeruli Young's modulus from 2.1 kPa to 1.5 kPa upon reduction in ATP synthesis, as a possible signature of the disorganisation of podocyte cytoskeletons. Using membrane tethers together with optical tweezers, Titushkin et al. [Titushkin & Cho, 2007] showed the ATP contribution in CSK-membrane interaction (through ATPase linker proteins) produced an increase of the tether lengths in osteoblasts, without noticeable changes in cell morphology or cytoskeleton structure. Altogether, these findings indicate that ATP depletion has contrasted effects on active cell rheology since it varies with the type of cell and the tested compartment. The majority of the probed single cells appear softer in ATP depletion conditions whereas differentiated muscle cells exhibit a rigor behaviour characterised by increased stiffness when deprived of ATP.

3.2.3 Enlightening the major role of NMMII through its inhibition by blebbistatin

Blebbistatin is a small molecule which can cross spontaneously the cell membrane to find its target inside the cytosol. His name was given by its cell blebbing inhibition function [Limouze, 2004; Allingham, 2005; Liu, 2015]. Blebbistatin inhibits the NMMII motor activity by slowing down the phosphate release after ATP hydrolysis, thus blocking NMMII in a weak actin-binding state and disassembling the stress fibers and the focal adhesions [Shutova, 2012]. Blebbistatin strongly impairs NMMII and striated muscle myosin II isoforms, and has a much weaker and species activity against smooth muscle myosin II. The fact that the contractile bundles of actomyosin that form the stress fibers (SFs) (Section 3.1.4) can no longer maturate in the presence of blebblistatin limits dramatically the ability of adherent cells to tense or to stretch on stiff substrates.

Blebbistatin blocks the NMMII heads and their ATPase activity, giving actomyosin complexes with low actin affinity (or detached state) and blocking its molecular motor function [Straight, 2003; Kovács, 2004]. It has been shown that blebbistatin inhibits cell spreading, invasion and locomotion of pancreatic adenocarcinoma cells [Duxbury, 2004]. In amoeboid-like migrating cells as leukocytes and walker 256 carcinosarcoma cells, cell migration is inhibited by blebbistatin [Lämmermann, 2008; Bergert, 2012; Sroka, 2016]. In particular for leukocytes, NMMII is necessary for translocation of the nucleus during locomotion [Lämmermann, 2008], and actomyosin activity is required together with Rho signalling for blebbing locomotion of rounded cells [Sanz-Moreno & Marshall, 2010]. Engler et al. [Engler, 2006] reported that blebbistatin compromises the lineage specification of mesenchymal stem cells (MSCs) normally induced by different matrix elasticities. These results confirm the role of NMMII in substrate sensing which is necessary for the specification of stem cells. In fibroblasts, NMMII inhibition causes alterations of the nuclear shape because of the impairment of the perinuclear dome-like actin cap [Khatau, 2009]. Griffin et al. [Griffin, 2004] showed that blebbistatin treatment in C2C12 myotubes slowed down their relaxation after mechanical detachment of prestressed cell from their substrate, providing evidence for NMMII involvement in production of cellular tension. It has been shown that NMMIIA isoform is required for the differentiation of mouse myoblasts by the formation of a dense cortical actin wall [Duan & Gallagher, 2009]. Optical tweezer measurements revealed a perturbation of both elastic and loss moduli of C2 myoblasts after NMMII inhibition [Balland, 2005]. In particular, the actin network of treated cells appeared less stiff and exhibits less energy dissipation compared to normal cells.

In C2C12 myoblasts, blebbistatin treatment caused a reversible and reproducible morphological alteration (shape rounding) [Al-Rekabi & Pelling, 2013; Inoue, 2015], a decrease of the cell area in close contact with the substrate [Modulevsky, 2012], a disruption of stress fibers [Van Citters, 2006; Modulevsky, 2012; Al-Rekabi & Pelling, 2013], a decrease in size or complete loss of focal adhesions (the vinculin distribution lost its typical punctate morphology, the integrin distribution over the cell contact area remained unchanged) [Modulevsky, 2012; Al-Rekabi & Pelling, 2013], a slight decrease (-23 %) of substrate adhesion [Modulevsky, 2012], a lower CSK tension [Wang, 2014] although the MT network remained unchanged [Modulevsky, 2012]. Inability of cell reshaping in response to substrates with different stiffness was also reported for C2C12 myoblasts after blebbistatin addition [Inoue, 2015]. Al-Rekabi and Pelling [Al-Rekabi & Pelling, 2013] showed that C2C12 myoblasts treated with blebbistatin had impaired mechanotransduction responses. While normal C2C12 myoblasts responded transiently with increased

traction forces when stimulated by AFM indentation (10 nN) on the nucleus, this ability was lost in treated myoblasts. Sbrana et. al [Sbrana, 2008] measured by AFM a decrease of the stiffness of blebbistatin and sphingosine 1-phosphate (S1P) treated C2C12 myoblasts (E $\sim$ 0.6 kPa) as compared to untreated cells (E $\sim$ 1 kPa), while their normalized hysteresis (equivalent to D_l (Eq. (2.69)) was increased from 0.4 to 0.6. Given that SP1 enhanced SFs formation, they concluded that SFs alone cannot ensure normal cell stiffness and viscosity without correct NMMII activity. This body of evidence demonstrates that NMMII is necessary for shape maintainance and remodelling, mechanosensing, CSK tension, cell adhesion and motility. Therefore, we expect to observe a perturbation of the mechanical properties of blebbistatin treated C2C12 myoblasts, and in particular a decrease of their elastic modulus and of their energy dissipation loss [Balland, 2005].

3.2.4 Viscoelasticity of C2C12 myoblasts: Young modulus estimations with AFM

The viscoelastic properties of C2C12 myoblasts have been studied with AFM indentation many times in the past few years. In the studies reported in Table 3.2, FICs were recorded either by indenting the cell several times at the same location or by constructing elasticity spatial maps. The AFM experimental conditions comprised cantilevers with sharp or spherical tips and spring constants varying between 0.01 and 0.12 N/m. The tested scan velocity range covered velocities between 0.5 and 12 μm/s. The Hertz model or its Sneddon's extension were used to analyze FICs according to the tip shape, whereas the Maxwell model was applied for stress-relaxation curve analysis (Section 2.3). Although living C2C12 myoblasts did not strictly obey a linear elastic model, for small indentation depth (less than 500 nm), they were assumed to behave as a purely elastic, isotropic, homogeneous and semi-infinite material. Nowadays, it is well recognized that cells are not purely elastic but behave as viscoelastic, elasto-plastic or visco-plastic materials, as confirmed by the generally encountered separation of the loading and the unloading indentation curves. However, among the studies reported in Table 3.2, only three of them reported viscosity estimations of myoblasts: Collinsworth et al. [Collinsworth, 2002] and Sbrana et al. [Sbrana, 2008] measured the normalized hysteresis of FICs (equivalent to our D_l (Eq. (2.69))), while [Li, 2016] estimated two relaxation times (*e.g.* for conical tip $\tau_1 = 0.045$ s and $\tau_2 = 0.58$ s) by analysing AFM stress-relaxation curves with a second-order generalized Maxwell viscoelastic model. Since for Maxwell model the relaxation time $\tau_R = \eta/E$ (Section 2.3.3.a), and from their reported Young's modulus (*e.g.* for conical tip $E \sim 3$ kPa), we estimated two viscosity coefficients η_1 and η_2, for each condition, that are reported in Table 3.2. Note that the values of D_l are similar to those we estimated in Figure 2.26 for the same scan velocity value V_0.

The C2C12 myoblast Young's modulus estimated with AFM indentation varies between 0.72 and 12.8 kPa. As previously discussed, this variability is probably due to different experimental and analytical conditions. Conical sharp indenters lead to higher values of E [Li, 2016]. From our experimental studies of AFM indentation of myoblasts with increasing scan velocity (Chapter 2), we observed that both the linear (E_{cell}, Fig. 2.26(a)) and non-linear (λ, Fig. 2.26(c)) coefficients describing the mechanical properties of myoblasts increase as a function of V_0. However, from the data reported in Table 3.2, this correlation is not immediate because the data are disparate. It should be noticed that other non reported sample conditions may influence the AFM results (*e.g* culture substrate, temperature, medium, ...). Sbrana et al. [Sbrana, 2008] collected elasticity

AFM setup				**FIC analysis**		**region**	E**(kPa)**	**viscosity parameters**	**reference**
k**(N/m)**	**tip**	V_0 **(μm/s)**	**F(nN)**	**h**	**model**				
~ 0.045	△	0.5	n.s.	< 15 %	S	central	11.5 ± 1.3	$D_l \sim 0.18$	[Collinsworth, 2002]
0.109	◯	~ 1	20	400 nm	H	non-nuclear	~ 1	$D_l = 0.4$	[Sbrana, 2008]
0.01	△	7.5	n.s.	n.s.	S	nuclear	11 ± 1	–	[Takemoto, 2012]
0.069	n.s.	n.s.	n.s.	n.s.	H	nuclear	~ 7	–	[Al-Rekabi & Pelling, 2013]
0.12	◯	2	3	n.s.	H	n.s.	~ 3	–	[Sun, 2014]
0.03	△	12	5	n.s.	S	central	2.97 ± 0.19	$\eta_1 = 134.3$ Pa.s $\eta_2 = 1714.8$ Pa.s	[Li, 2016]
					M				
0.12	◯	12	20	n.s.	H	central	0.77 ± 0.05	$\eta_1 = 33.7$ Pa.s $\eta_2 = 432.4$ Pa.s	[Li, 2016]
					M				

k = cantilever spring constant
V_0 = scan speed
h = indentation length
% = percentage of the cell thickness

△ = sharp tip
◯ = spherical tip
n.s. = not specified

S = Sneddon
H = Hertz
M = Maxwell

Table 3.2: **Review of AFM indentation experiments on C2C12 myoblasts**. AFM experimental conditions and analytical models used to estimate the Young's modulus (E) of C2C12 myoblasts. It should be noticed that some (non reported) sample conditions (*e.g.* culture substrate, medium, temperature, ...) were different.

maps on living C2C12 myoblasts cultured on glass substrates. One of these maps showed that the myoblast nuclear region (assuming that the nucleus is located in the highest region of the cell) is softer than its peripheral zones (results reported in arbitrary units). Focusing on C2C12 myoblast peripheral regions, they found a correlation between higher local stiffness and corrugation zones of the cell membrane. They also showed that SFs activate the stretch activated channels (SACs) of C2C12 myoblasts thanks to tensional activity of non muscle myosin II (NMMII) [Sbrana, 2008], suggesting that the activity of this molecular motor is required in this cell line for achieving suitable stiffness, hysteresis and membrane stretching. Takemoto et al. [Takemoto, 2012] observed an increase of the C2C12 myoblast Young's modulus after single step-like elongation, which was interpreted by the activation of the non-muscle myosin II. Sun *et al.* [Sun, 2014] reported that oxidative stress (H_2O_2) that causes a lower expression of actin, FAs and of protein cross-linkers of the cell membrane with the CSK network, leads to a reversible lowering of the cell stiffness. Li et al. [Li, 2016] reported that the anticancer drug methotrexate reduces the elasticity of C2C12 myoblasts, their relaxation time, and modifies their morphology. Passive microrheology study performed with AFM [Martinez-Torres, 2016] showed that the cortical region of C2C12 myoblasts is more elastic-like (solid), as compared to deeper regions (closer to the nucleus) which are more viscous-like (liquid). Using a flat and large area compression device on single adherent C2C12 myoblasts and a Neo-Hookean model, Peeters et al. [Peeters, 2005] estimated their Young's modulus $E = 1.14 \pm 0.32$ kPa and observed cell bulging and membrane rupture beyond an applied force of 8.7 ± 2.5 μN and an axial strain of 72 ± 4 %, leading to an irreversible cell bursting.

3.2.5 Viscoelasticity of myotubes and muscle tissues: AFM studies

AFM setup				FIC analysis		cell info		E (kPa)	reference
k (N/m)	tip	V_0 (μm/s)	F (nN)	h	model	diff. day	region		
C2C12 myotubes									
0.03 - 0.05	△	< 0.25	n.s.	< 10 %	BCS/S	2nd	non-nuclear	24.7 ± 3.5	[Mathur, 2001]
0.03 - 0.06	△	0.5	n.s	< 15 %	S	3th	central	∼ 14	[Collinsworth, 2002]
0.03 - 0.06	△	0.5	n.s	< 15 %	S	4th	central	∼ 21	[Collinsworth, 2002]
0.03 - 0.06	△	0.5	n.s	< 15 %	S	5th	central	∼ 13.5	[Collinsworth, 2002]
0.03 - 0.06	△	0.5	n.s	< 15 %	S	6th	central	∼ 18	[Collinsworth, 2002]
0.03 - 0.06	△	0.5	n.s	< 15 %	S	7th	central	∼ 13	[Collinsworth, 2002]
0.03 - 0.06	△	0.5	n.s	< 15 %	S	8th	central	45.3 ± 4.0	[Collinsworth, 2002]
0.03 - 0.06	△	0.5	n.s	< 15 %	S	10th	central	∼ 36	[Collinsworth, 2002]
0.03 - 0.05	△	n.s.	n.s.	n.s.	S	1st	n.s	∼ 5	[Zhang, 2004]
0.03 - 0.05	△	n.s.	n.s.	n.s.	S	2nd	n.s	∼ 6.5	[Zhang, 2004]
0.03 - 0.05	△	n.s.	n.s.	n.s.	S	3th	n.s	∼ 8.5	[Zhang, 2004]
0.03 - 0.05	△	n.s.	n.s.	n.s.	S	4th	n.s	∼ 10.5	[Zhang, 2004]
myofibers and muscles						**sample type**	**region**		
0.02	○	1	n.s.	25 - 60 nm	H	rabbit myofibrils	several	8 - 102.1 *	[Yoshikawa, 1999]
0.06	△	n.s.	n.s.	n.s.	H	mouse EDL muscle	several	12 ± 4	[Engler, 2004b]
0.02 - 0.03	△	1 - 3	1	up to 1 μm	P	mouse FDB myofibers	several	61± 5	[Defranchi, 2005]
0.02	○	n.s	n.s	25 - 30 nm	H	rabbit skeletal myofibrils	overlap regions	5 - 61*	[Akiyama, 2006]
0.05 - 0.12	○	n.s.	n.s.	150 nm	H	rat soleus myofibers	several	19 - 301 *	[Ogneva, 2010]

k = cantilever spring constant
V_0 = scan speed
△ = sharp tip
○ = spherical tip
h = indentation length
% = percentage of the cell thickness
n.s. = not specified

S = Sneddon model
H = Hertz model
BCS = blunt cone–spherical cap model
P= according to [Pharr, 1992]
EDL = extensor digitorum longus
FDB =flexor digitorum brevis
* = depending on the sample conditions (*e.g.* relaxed/active/rigor) and locations

Table 3.3: **Review of AFM indentation experiments on C2C12 myotubes, mammalian myofibers and muscles.** The upper part focuses on C2C12 myotubes at different stages of differentiation. The bottom part concentrates on fully differentiated mammalian muscle tissues. AFM experimental conditions and analytical models used to estimate the Young's modulus (E) are reported. It should be noticed that some non reported sample conditions (culture substrate, medium, temperature, etc.) were also different.

Similarly to C2C12 myoblasts, C2C12 myotubes have also been characterised at different stages of differentiation with AFM (Table 3.3). Some data about muscle tissues, fully differentiated muscle cells (myofibers), and contractile units of muscle fibres (myofibrils) are also reported in Table 3.3. We found three publications [Mathur, 2001; Collinsworth, 2002; Zhang, 2004] where C2C12 myotube Young's modulus was measured by AFM during differentiation, using sharp conical tips and cantilever spring constant between 0.03 and 0.06 N/m. Sneddon's variations of the Herz model was used in most cases. Indentation depths (h) were limited to a small fraction (10 - 15%) of the cell thickness to stay within the linear regime and to minimise the impact of the underlying substrate stiffness on the FICs. Globally, the reported Young's modulus of C2C12 myotubes varies between 5 and 49.3 kPa during 10 days of differentiation. Globally, C2C12 myotubes behave stiffer under fixed velocity deformation as compared to C2C12 myoblasts (Table 3.2); their stiffness increases with differentiation and fully differentiated my-

ofibers and isolated myofibrils seem to be stiffer than isolated myotubes. However, this stiffness is strongly dependent on the sample conditions and the probed sarcomeric region; for instance relaxed myofibrils were found softer than active and rigor (ATP depleted) ones [Yoshikawa, 1999; Nyland & Maughan, 2000; Akiyama, 2006; Ogneva, 2010]. Surprisingly, mouse EDL muscle elasticity was reported closer to myoblast and myotubes (E $\sim$ 12 kPa) [Engler, 2004b] than to fully differentiated myofibers. The higher variability of fully differentiated muscle cell elasticity must therefore be considered cautiously.

Mathur et al. [Mathur, 2001] measured a higher Young's modulus for C2C12 myotubes on the 2nd differentiation day ($E = 24.7 \pm 3.5$ kPa) as compared to endothelial cells ($E = 1.4 - 6.8$ kPa), but lower than cardiac cells ($E = 100.3 \pm 10.7$ kPa). Monitoring myoblast elasticity (E) during their differentiation, Collinsworth et al. [Collinsworth, 2002] did not find significant difference until the 8th day, where it increased sharply. Using the same approach, Zhang et al. [Zhang, 2004] found a more gradual increase throughout four days of differentiation (two-fold increase on the fourth day). In the three AFM studies on myotubes reported in Table 3.3, particular attention was also payed to their viscosity. Mathur et al. [Mathur, 2001] reported that the FIC hysteresis (ascribed to viscous dissipation) observed on the 2nd differentiation day increases significantly for speeds above 0.25 μm/s. They also reported that this viscous dissipation was lower for skeletal muscle cells ($\sim$ 30 % of energy input, $D_l \sim 0.3$) than for endothelial and cardiac muscle cells ($\sim$ 70 % of energy input, $D_l \sim 0.7$). By contrast, Collinsworth et al. [Collinsworth, 2002] did not find significant differences in the normalized FIC hysteresis (equivalent to D_l) of C2C12 cells during the differentiation process, from the first to the tenth day of differentiation ($D_l = 0.11 - 0.24$). This was also confirmed by Zhang et al. [Zhang, 2004] during the 4 first days of C2C12 myogenic differentiation ($D_l = 0.15 - 0.2$).

3.3 Revisiting the interpretation of FICs collected on single living cells: application to myoblasts

In this section, we report the mechanical characterization of normal C2C12 myoblasts and myotubes with fixed scan velocity AFM indentation technique. We concentrate more particularly on the mechanics of perinuclear regions, where the actin cap stress fibers play the role of a tensed and contractile sheet of α-actinin cross-linked actomyosin fibers which not only protect and sustain the nucleus but also transmit the mechanical forces from the ECM to the nucleus [Khatau, 2009]. The softness or rigidity of this cap is also intimately related to that of the other contractile stress fibers such as the ventral SFs and transverse arcs. The ability of this perinuclear zone to sustain rather large scale deformations without rupture will be a strong indication of the ductility of the cells and of their potential for recovering their original shape after deformation. In the opposite case, when this perinuclear zone will fracture around cross-linked and more rigid domains, this recovery will be more difficult as more mechanical work will likely be dissipated. It is therefore important to focus on local events occurring during the force indentation curves. Here we extend the wavelet-based analyzing method introduced in Chapter 2 to detect and quantify the local rupture events which occur during indentation (their nature, their chronology or repeatability upon multiple indentations) to elaborate a non stationary approach of living cell indentation experiments. Comparing normal myoblasts and myotubes, together with myoblasts with CSK alterations (ATP depletion, injection of blebbistatin, cell fixation) will be also helpful to interpret the experiments devoted to human myoblasts with or

without the Duchenne muscular dystrophy (Chapter 4).

3.3.1 Deciphering the temporal signature of living cell adaptation to local stress from AFM FICs

Chapter 2 was limited to a global FIC analysis with the assumption of homogeneous and permanent mechanical properties of the cells during indentation. We did not consider local features of the FICs, because our initial goal was to provide a simple picture that could distinguish myoblast and myotube mechanical properties, based on simple homogeneous viscoelastic models.

3.3.1.a Evidencing local rupture events in FICs recorded on myoblasts and myotubes

Focusing on local FIC fluctuations, their distribution and their intensity will bring us additional parameters to characterise the mechanical compliance of perinuclear stress fibers and to understand their protective and compressive role on the interphase nucleus. We selected 6 different myoblasts in Figs 3.26, 3.27 and 3.28 and we plotted in red (resp. green) lines the loading (resp. unloading) FICs. The black lines correspond to the mean of the loading curves, they provide a general trend of the FICs (which was characterised in Chapter 2), but they hide large amplitude fluctuations which are not due to external noise (acoustic or hydrodynamic). Comparing the force derivatives of myoblasts 1 and 2 in Fig. 3.26(b) and (d) and their corresponding transmission microscopy images is rather puzzling. Cell 1 appears to be much stiffer and closer to an elastic material (beyond $h = 1$ μm the force derivative can be fitted by a straight line) (Fig. 3.26(b)), whereas the force derivative of cell 2 saturates beyond $h = 1$ μm (Fig. 3.26(c)). This difference could not be guessed from their typical adherent and spread morphology. The two FICs recorded from myoblasts 3 and 4 are quite similar to those of myoblasts 2 and 1 respectively (Fig. 3.27). Again, the temporal response to strain of myoblast 4 could be better approximated by an elastic response (or quasi-elastic) but myoblast 3 response is different because we can distinguish three regimes, a slow quasilinear increase of the force derivative (elastic regime) for $h \lesssim 1$ μm, a steeper increase beyond 1.5 μm which aborts after 2 μm. The myoblast 3 behaves as much softer at deeper indentations, suggesting that its perinuclear actin cap breaks locally to give way to the invading cantilever tip. Note that we took a larger wavelet size to compute the first, second and third derivatives of the forces for a better discrimination of the superimposed force curves in Figs 3.26, 3.27 and 3.28. We will use a smaller wavelet size $2\sqrt{2}s_g^{(0)} = 2\sqrt{2}s_g^{(1)} = 2\sqrt{2}s_g^{(2)} = 2\sqrt{2}s_g^{(3)} = 9$ nm to detect the local maxima (or minima) of the force derivatives in the forthcoming paragraphs.

FICs collected from myoblasts 5 and 6 display an important variability from one load-unload scan to the next one (Fig. 3.28). Not only these FICs include clear disruptions that interrupt the force increase (sudden falls of F, corresponding to a drop down of the first derivative and a sharp maxima of the third derivative), but these events are intermittent in time and do not occur at the same indentation depth. Using a three-dimensional plot of the FICs of the myoblasts 5 and 6 and of their difference with their averaged FIC (over 30 FICs), we show in Figs 3.29 and 3.30 that the disruption events do not systematically occur at the first indentation but that they rather build progressively and can also disappear temporarily to show up again after a finite set of load-unload loops (Fig. 3.29) or definitely during the course of the experiment (Fig. 3.30). With myoblast 6, the first disruption event shifts and increases progressively, suggesting that

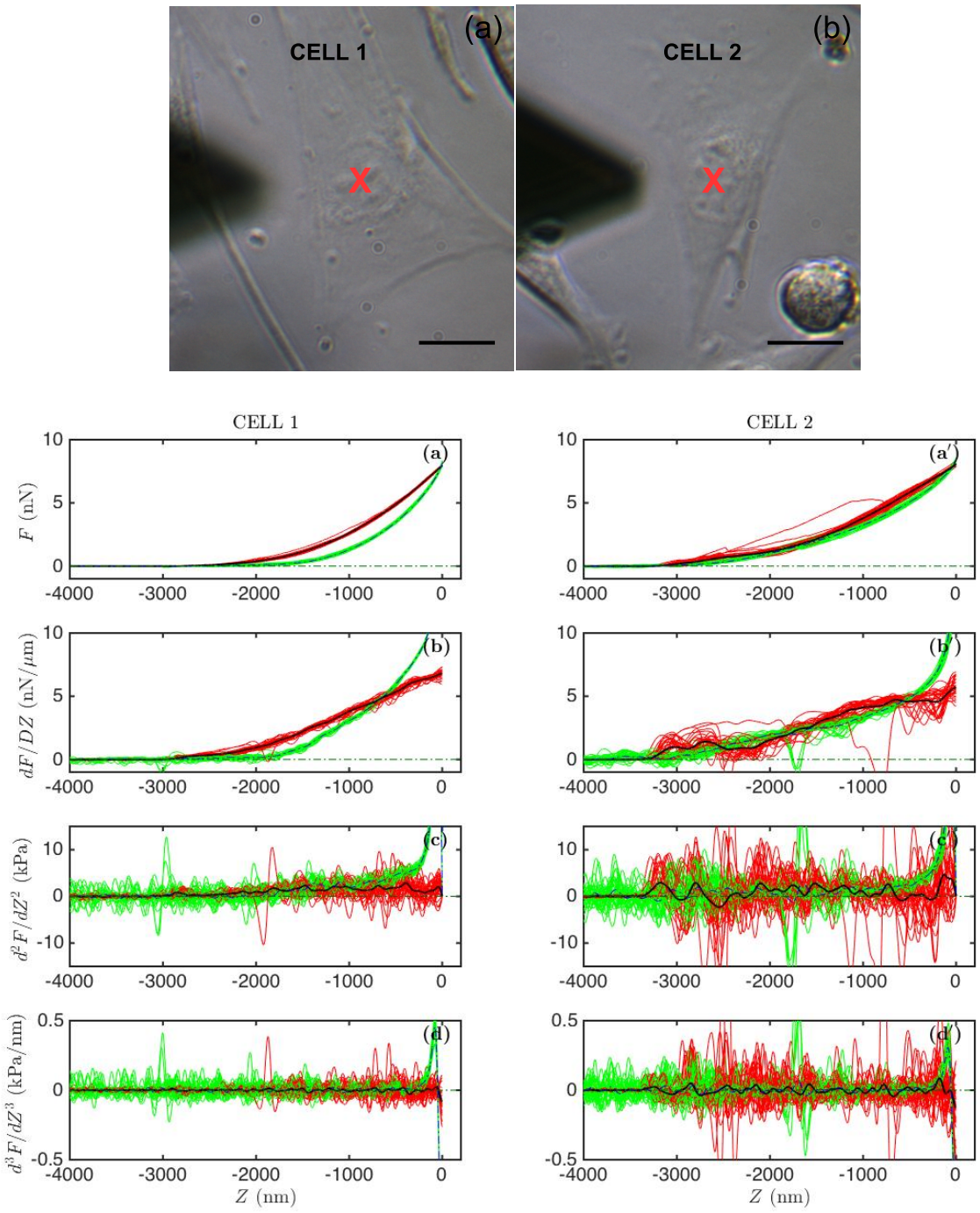

Figure 3.26: **FICs collected from two myoblasts (1 and 2).** Top panels: transmission microscopy images of the two myoblasts 1 and 2. The points of indentation are marked by a red cross. Scale bar: 20μm. (a,a') FIC series (30 curves for each cell) were recorded at a scan velocity $V_0 = 1\mu$ m/s and filtered from the raw FICs using a Gaussian wavelet of width $2\sqrt{2}s_g^{(0)} = 9$ nm (Eq. (5.10)). (b,b') FIC derivatives computed from the raw FICs using a Gaussian derivative wavelet of width $2\sqrt{2}s_g^{(1)} = 110$ nm (Eq. (5.11)). (c,c') Second-order derivatives computed from the raw FICs with a second derivative of a Gaussian wavelet of width $2\sqrt{2}s_g^{(2)} = 110$ nm (Eq. (5.12)). (d,d') Third-order derivatives computed from the raw FICs with a third derivative of a Gaussian wavelet of width $2\sqrt{2}s_g^{(3)} = 110$ nm (Eq. (5.13)). See Materials and methods, Section 5.4.4. Loading (resp. unloading) FICs are plotted in red (resp. green). The black curves correspond to the mean of the loading FICs and FIC derivatives.

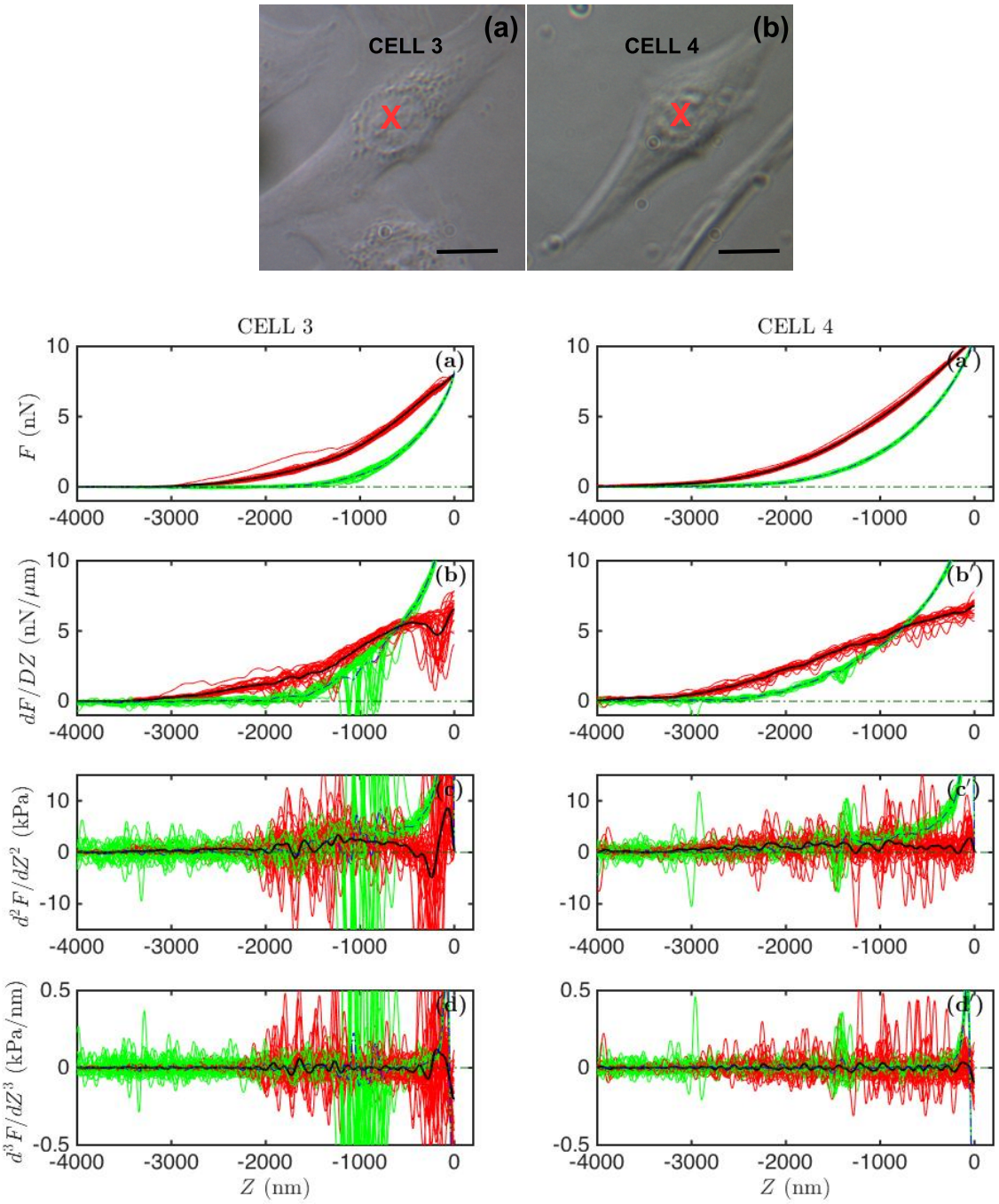

Figure 3.27: **FICs collected from two myoblasts (3 and 4).** Top panels: transmission microscopy images of the two myoblasts 3 and 4. The points of indentation are marked by a red cross. Scale bar: 20μm. (a,a') FIC series (30 curves for each cell) were recorded at a scan velocity $V_0 = 1\mu$ m/s and filtered from the raw FICs using a Gaussian wavelet of width $2\sqrt{2}s_g^{(0)} = 9$ nm (Eq. (5.10)). (b,b') FIC derivatives computed from the raw FICs using a Gaussian derivative wavelet of width $2\sqrt{2}s_g^{(1)} = 110$ nm (Eq. (5.11)). (c,c') Second-order derivatives computed from the raw FICs with a second derivative of a Gaussian wavelet of width $2\sqrt{2}s_g^{(2)} = 110$ nm (Eq. (5.12)). (d,d') Third-order derivatives computed from the raw FICs with a third derivative of a Gaussian wavelet of width $2\sqrt{2}s_g^{(3)} = 110$ nm (Eq. (5.13)). See Materials and methods, Section 5.4.4. Loading (resp. unloading) FICs are plotted in red (resp. green). The black curves correspond to the mean of the loading FICs and FIC derivatives.

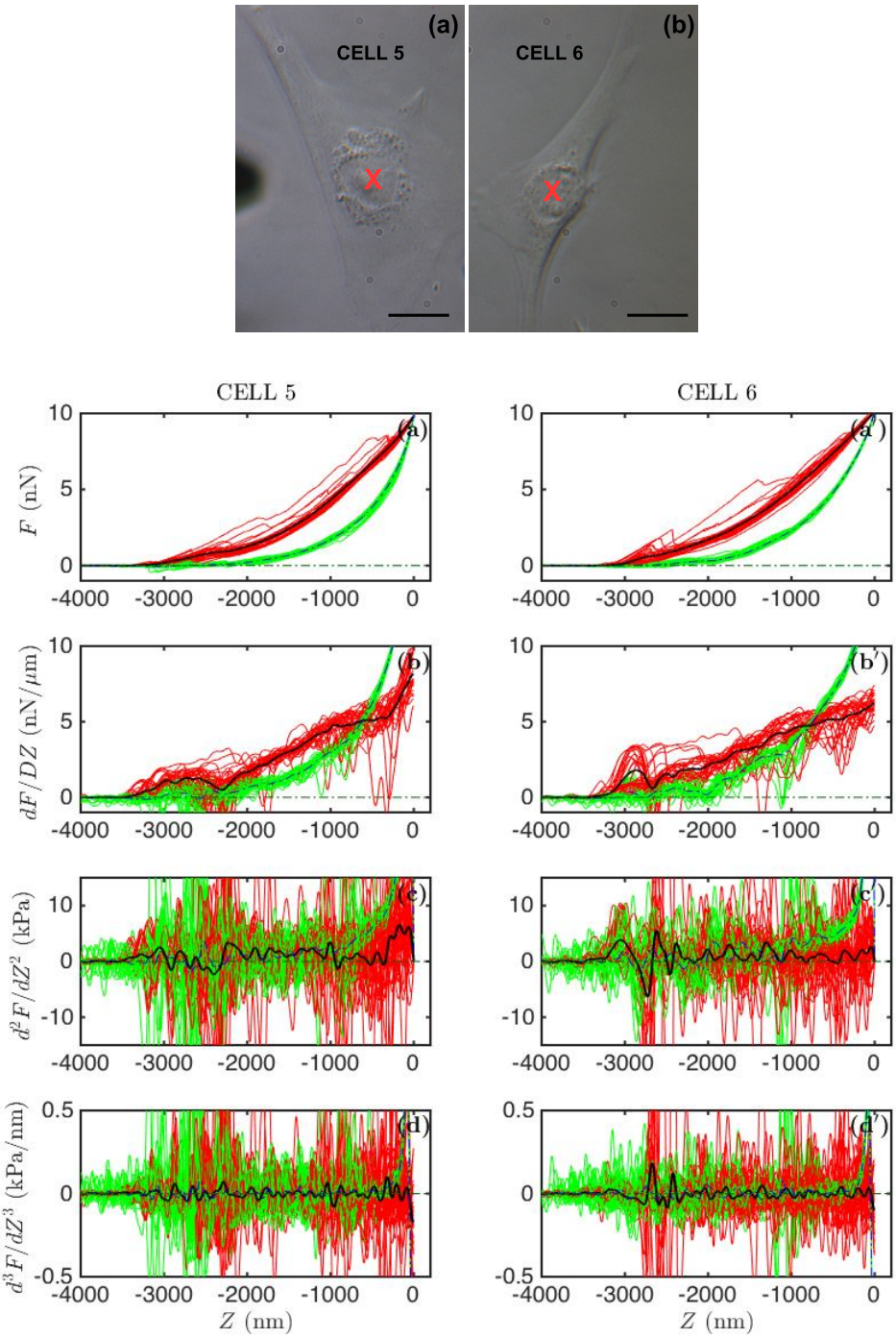

Figure 3.28: **FICs collected from two myoblasts (5 and 6).** Top panels: transmission microscopy images of the two myoblasts 5 and 6. The points of indentation are marked by a red cross. Scale bar: 20μm. (a,a') FIC series (30 curves for each cell) were recorded at a scan velocity $V_0 = 1\mu$ m/s and filtered from the raw FICs using a Gaussian wavelet of width $2\sqrt{2}s_g^{(0)} = 9$ nm (Eq. (5.10)). (b,b') FIC derivatives computed from the raw FICs using a Gaussian derivative wavelet of width $2\sqrt{2}s_g^{(1)} = 110$ nm (Eq. (5.11)). (c,c') Second-order derivatives computed from the raw FICs with a second derivative of a Gaussian wavelet of width $2\sqrt{2}s_g^{(2)} = 110$ nm (Eq. (5.12)). (d,d') Third-order derivatives computed from the raw FICs with a third derivative of a Gaussian wavelet of width $2\sqrt{2}s_g^{(3)} = 110$ nm (Eq. (5.13)). See Materials and methods, Section 5.4.4. Loading (resp. unloading) FICs are plotted in red (resp. green). The black curves correspond to the mean of the loading FICs and FIC derivatives.

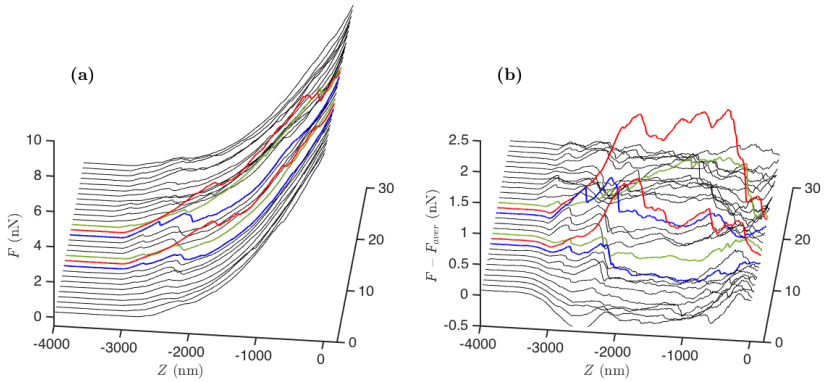

Figure 3.29: **Tracking the disruption events from a series of FICs collected on myoblast 5 (Fig. 3.28)**. (a) FICs plotted in a 3D representation with their recording index. (b) Difference of the FICs from the averaged FIC to emphasize the disruption events. The red curve highlights the mostly disrupted FIC, the blue and green curves correspond to the neighbouring FICs.

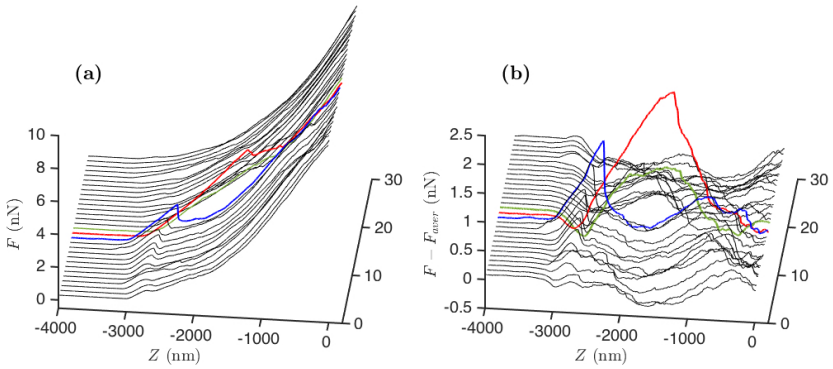

Figure 3.30: **Tracking the disruption events from a series of FICs collected on myoblast 6 (Fig. 3.28)**. (a) FICs plotted in a 3D representation with their recording index. (b) Difference of the FICs from the averaged FIC to emphasize the disruption events. The red curve highlights the mostly disrupted FIC, the blue and green curves correspond to the neighbouring FICs.

the cantilever tip invades tighter and tenser shells (red curve in Fig. 3.30). This sharpening of the FIC ends up fracturing sharply and leaving the passage to the cantilever for the next load-unload scan (green curve in Fig. 3.30). The fact that such FIC disruption events may be reinforced or weakened after a finite set of load-unload scans is an indication that the successive cantilever tip penetrations inside the cell are opening a space that the cell cannot restore in time between two scans.

We selected four myotubes and their FICs are shown in Fig. 3.31 and 3.32 for comparison with myoblasts 1 to 6. We note that disruption events appear also in these FICs that again reveal a strong variability of the cell response to fixed velocity strain. Myotubes 1 and 2 were chosen large enough to represent the fusion of several myoblasts, their FIC derivatives clearly saturate at larger deformations, remembering the FICs of myoblasts 2, 3, 5, 6 and what we have observed in Chapter 2 on the two tested myotubes with different scan velocities (Figs 2.24 and 2.25). The myotube 2 (Fig. 3.32) is much softer than myotube 1 (Fig. 3.31), since for the same force set point (8 nN at the end of the FIC) the cantilever can penetrate deeper inside, and the FIC derivative saturation occurs earlier. However, it must be noted that a much stiffer response

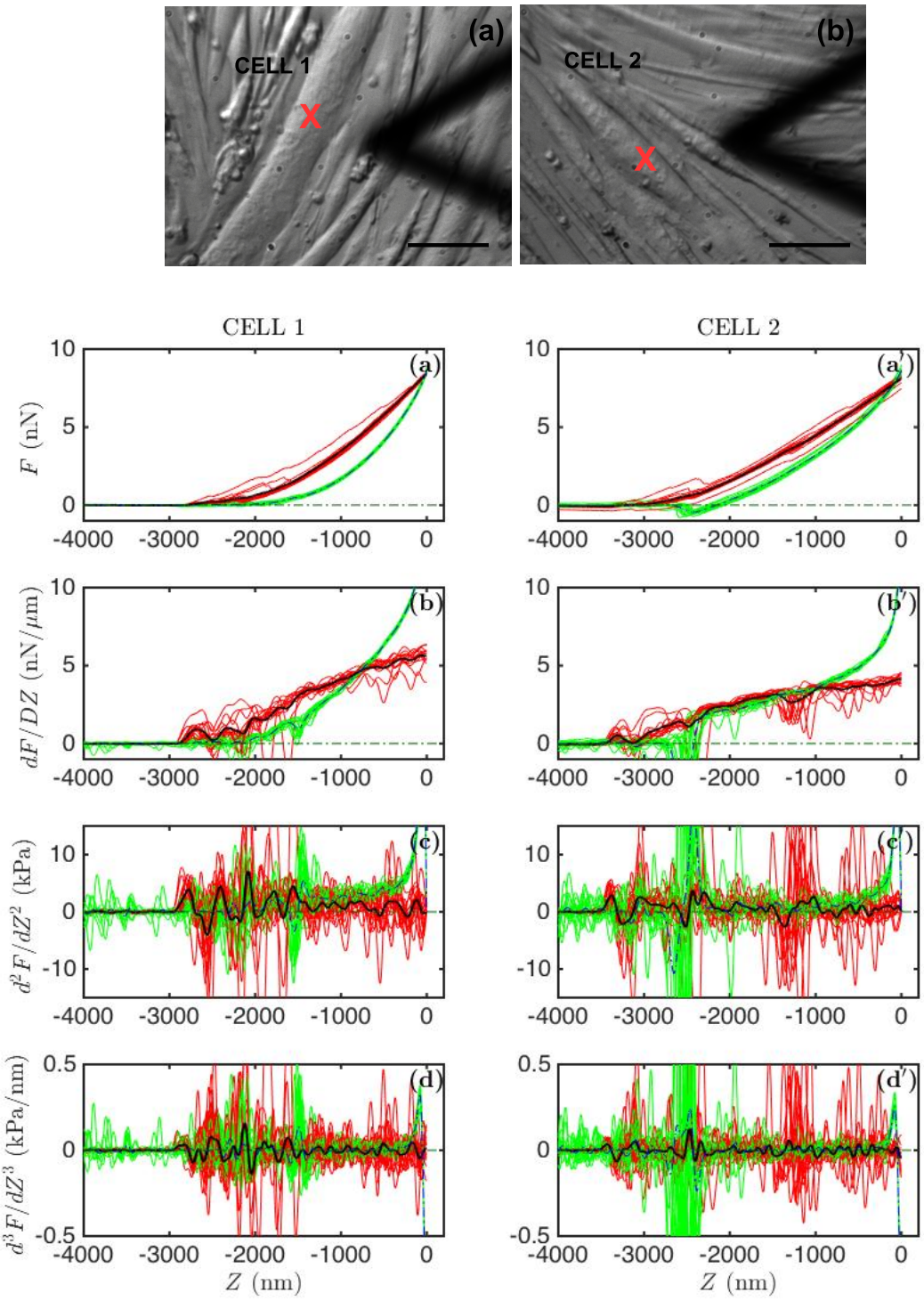

Figure 3.31: **FICs collected from two myotubes (1 and 2).** Top panels: transmission microscopy images of the two myotubes 1 and 2. The points of indentation are marked by a red cross. Scale bar: 40μm. (a,a') FIC series (30 curves for each cell) were recorded at a scan velocity $V_0 = 1\mu$ m/s and filtered from the raw FICs using a Gaussian wavelet of width $2\sqrt{2}s_g^{(0)} = 9$ nm (Eq. (5.10)). (b,b') FIC derivatives computed from the raw FICs using a Gaussian derivative wavelet of width $2\sqrt{2}s_g^{(1)} = 110$ nm (Eq. (5.11)). (c,c') Second-order derivatives computed from the raw FICs with a second derivative of a Gaussian wavelet of width $2\sqrt{2}s_g^{(2)} = 110$ nm (Eq. (5.12)). (d,d') Third-order derivatives computed from the raw FICs with a third derivative of a Gaussian wavelet of width $2\sqrt{2}s_g^{(3)} = 110$ nm (Eq. (5.13)). See Materials and methods, Section 5.4.4. Loading (resp. unloading) FICs are plotted in red (resp. green). The black curves correspond to the mean of the loading FICs and FIC derivatives.

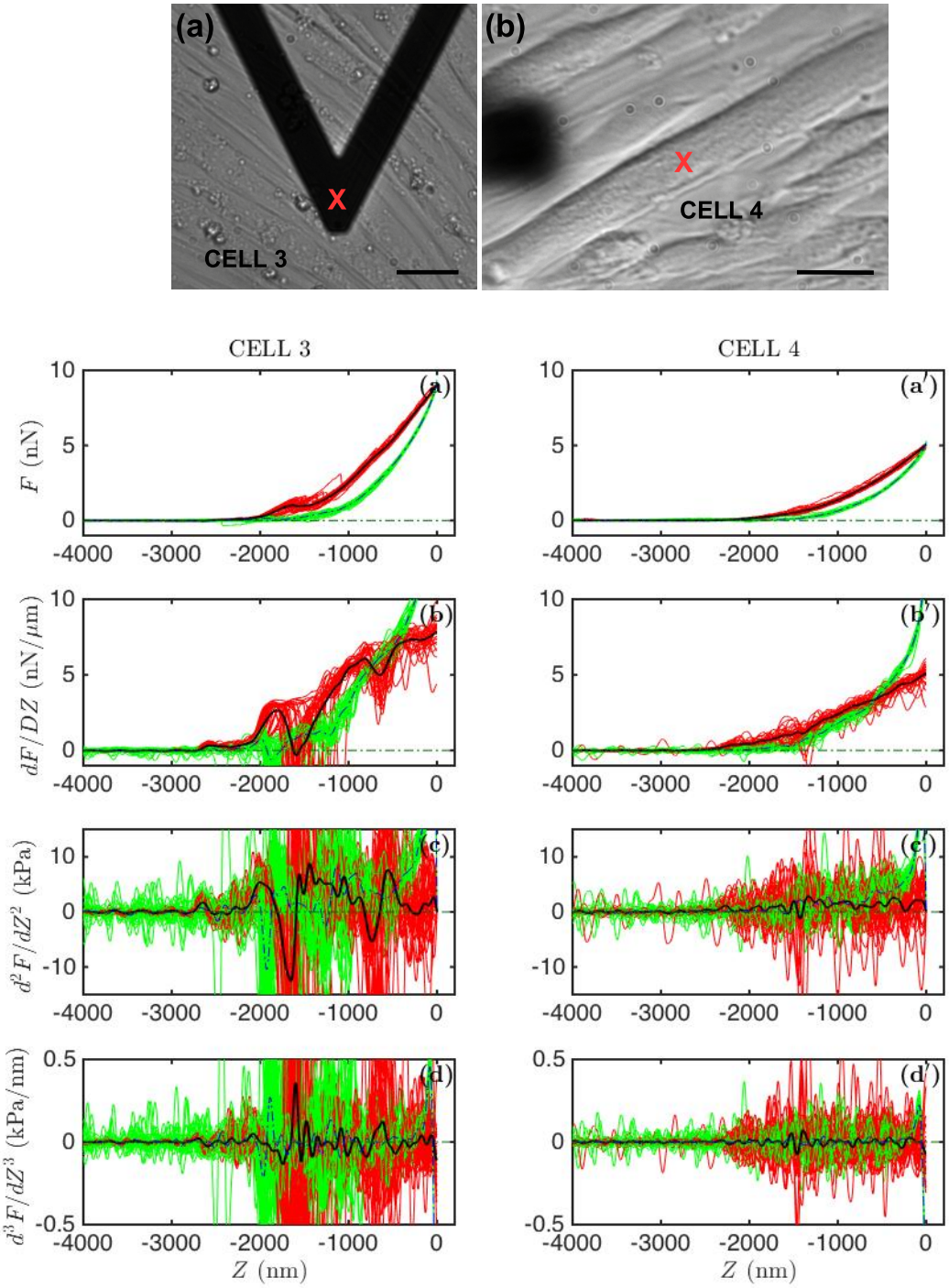

Figure 3.32: **FICs collected from two myotubes (3 and 4).** Top panels: transmission microscopy images of the two myotubes 3 and 4. The points of indentation are marked by a red cross. Scale bar: 40μm. (a,a') FIC series (30 curves for each cell) were recorded at a scan velocity $V_0 = 1\mu$ m/s and filtered from the raw FICs using a Gaussian wavelet of width $2\sqrt{2}s_g^{(0)} = 9$ nm (Eq. (5.10)). (b,b') FIC derivatives computed from the raw FICs using a Gaussian derivative wavelet of width $2\sqrt{2}s_g^{(1)} = 110$ nm (Eq. (5.11)). (c,c') Second-order derivatives computed from the raw FICs with a second derivative of a Gaussian wavelet of width $2\sqrt{2}s_g^{(2)} = 110$ nm (Eq. (5.12)). (d,d') Third-order derivatives computed from the raw FICs with a third derivative of a Gaussian wavelet of width $2\sqrt{2}s_g^{(3)} = 110$ nm (Eq. (5.13)). See Materials and methods, Section 5.4.4. Loading (resp. unloading) FICs are plotted in red (resp. green). The black curves correspond to the mean of the loading FICs and FIC derivatives.

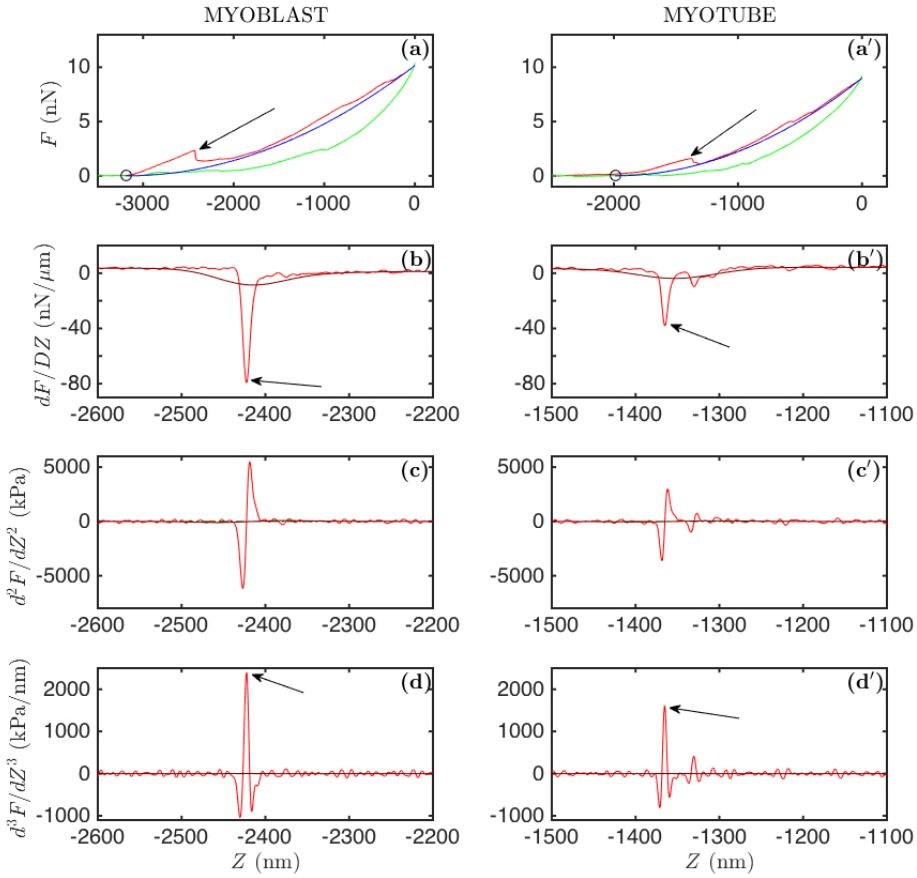

Figure 3.33: **FIC derivatives highlight the disruption events encountered during cell indentation.** (a,a') The two FICs were recorded at a scan velocity $V_0 = 1\mu$ m/s on a myoblast (a) and a myotube (a') and filtered from the raw FICs using a Gaussian wavelet of width $2\sqrt{2}s_g^{(0)} = 9$ nm (Eq. (5.10)). Red curve: loading curve, green curve: unloading curve; blue curve: a parabola envelope going through the initial FIC contact point and the final set point. (b,b') First-order derivatives of the raw FICs computed using a Gaussian derivative wavelet of width $2\sqrt{2}s_g^{(1)} = 9$ nm (Eq. (5.11)). (c,c') Second-order derivatives of the raw FICs computed with a second derivative of a Gaussian wavelet of width $2\sqrt{2}s_g^{(2)} = 9$ nm (Eq. (5.12)). (d,d') Third-order derivatives computed from the raw FICs with a third derivative of a Gaussian wavelet of width $2\sqrt{2}s_g^{(3)} = 9$ nm (Eq. (5.13)). For comparison are shown (magenta curves) the different FIC derivatives computed with a larger wavelet size $2\sqrt{2}s_g^{(1)} = 2\sqrt{2}s_g^{(2)} = 2\sqrt{2}s_g^{(3)} = 110$ nm as previously used for a visual inspection of the FICs in Figs 3.26, 3.27, 3.28, 3.31 and 3.32.

to strain can be observed in myotubes like myotubes 3 and 4 (Fig. 3.32) where the FICs include less or more localised disruption events.

3.3.1.b Refined time-frequency analysis for tracking FIC disruption events

These series of FICs collected on myoblasts and myotubes put into light the risk of using the average of FICs for characterising the corresponding cell mechanical properties. Averaging over successive load-unload scans may significantly modify the shape of the stress-to-strain curve and may lead to misleading conclusions. Clearly from one indentation to the next one, the cell CSK

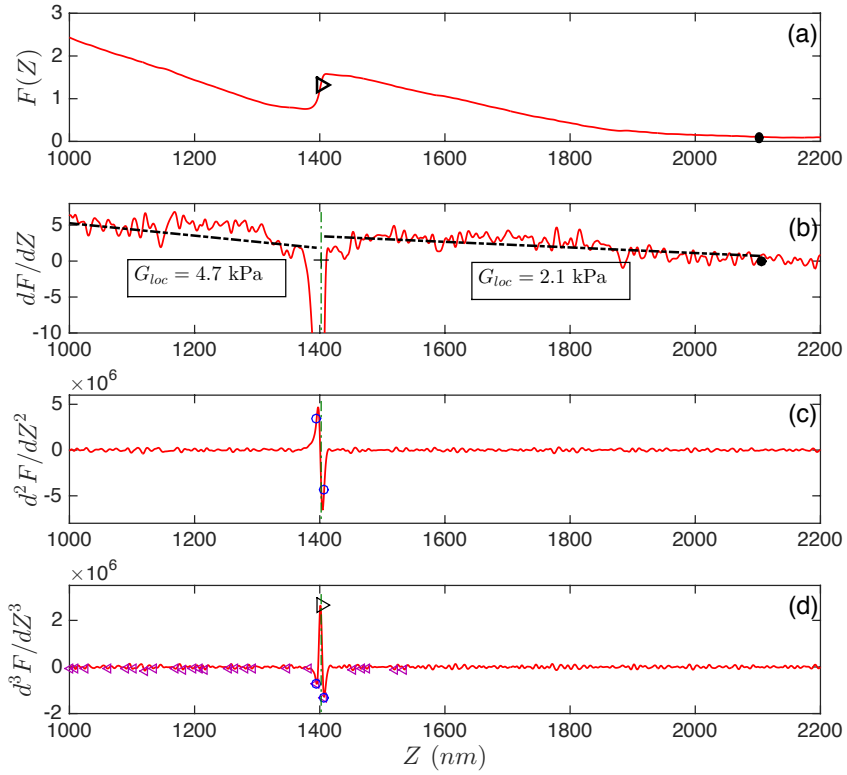

Figure 3.34: **FIC disruption event detection method.** (a) FIC filtered from the raw FIC with a Gaussian wavelet of width $2\sqrt{2}s_g^{(0)} = 9$ nm (Eq. (5.10)). (b) Derivative of the FIC computed with a first-order derivative of a Gaussian wavelet of width $2\sqrt{2}s_g^{(1)} = 9$ nm (Eq. (5.11)). The local slopes of dF/dZ before (right) and after (left) the disruption events provide some estimation of the local shear relaxation modulus G_{loc}. (c) Second-order derivative of the FIC computed with a second-ordre derivative of a Gaussian wavelet of width $2\sqrt{2}s_g^{(2)} = 9$ nm (Eq. (5.12)). (d) Third-order derivative of the FIC computed with a third-order derivative of a Gaussian wavelet of width $2\sqrt{2}s_g^{(3)} = 9$ nm (Eq. (5.13)). Note that the orientation of the Z axis has been inverted in this figure, the scan is therefore operated from the right part to the left part of the FICs. The contact point and the position of the FIC disruption event are marked by a black dot and a triangle respectively. The local minima of d^3F/dZ^3 are marked with blue circles. The small pink triangles correspond to secondary minima of d^3F/dZ^3 which are used as secondary bounds that assist the estimation of the local shear modulus G_{loc}.

may not completely recover from the deformation and we have therefore recorded a complex history of its deformation that incorporates passive and active processes. This alteration of the averaged curves is further amplified when taking their derivatives since the disruption events do not occur at the same indentation depth. We need therefore to perform a wavelet-based analysis on each FIC, as illustrated in Fig. 3.33.

The background FIC (neglecting the disruption events) can be characterized by a global shear relaxation modulus $\langle G \rangle$. If the cell was a purely elastic ball, we could extract a global shear relaxation modulus $\langle G \rangle$ from each FIC, using Eq. (2.43). $\langle G \rangle$ can be estimated as the prefactor of the parabola that crosses both the contact point and the final set point of the FIC

(blue curves in Fig. 3.33(a,a')):

$$\langle G \rangle = \frac{\pi(1-\nu)}{4\tan\alpha} \frac{(F_{\text{setpoint}} - F_c)}{(Z_{\text{setpoint}} - Z_c)^2} \,. \tag{3.1}$$

This remains a drastic approximation of the mechanical response of the cell under strain, and it may become worse when several disruption events occur during the indentation, however it will be used as a global marker for a global cell Young modulus with $\langle E \rangle = 3\langle G \rangle$.

On the two FICs shown in Fig. 3.33(a) and (a'), we note a major disruption event that occurs at ~ 700 nm after contact of the cantilever tip with the cell (marked with a black circle). The first (resp. second and third) derivative of these two FICs was computed with a first (resp. second and third) derivative of a Gaussian wavelet having the same width as the one used for the FICs in Fig. 3.33(a,a'): $2\sqrt{2}s_g^{(0)} = 2\sqrt{2}s_g^{(1)} = 2\sqrt{2}s_g^{(2)} = 2\sqrt{2}s_g^{(3)} = 9$ nm. When zooming on the major FIC disruption event in Figs 3.33(b-d) and (b'-d'), we show that this disruption event corresponds to a sharp local minima of the first-order derivative, a fast crossing through zero of the second-order order derivative and a sharp maxima of the third-order derivative. We used the third-order derivative of the FICs to threshold the intensity of the local disruption events above the background noise: $d^3F/dZ^3 > 0.1$ MPa/nm (Fig. 3.34(d)). The amplitude of this third-order derivative is a direct estimation of the curvature of the force derivative (Fig. 3.34(b)) and therefore of the abruptness of the disruption of the FIC. From the two minima of the third-order derivative (right and left) of the FIC (blue circles in Fig. 3.34(d)), we defined the upper and lower bounds of the Z intervals from which we computed the local shear modulus (G_{loc}) before and after the disruption event as the slope of the first-order derivative of the FIC (Fig. 3.34(b)). In the example reported in Fig. 3.34, we note that the slope of the force derivative increases after the disruption event, meaning that the stiffness of the cell compartment sensed after the FIC disruption is about twice larger than the stiffness before this event. This apparent reinforcement of the cell after FIC disruption is not generic, since the opposite trend may also occur. However, we have observed that cells that manifest FIC disruption events (rough FICs) have statistically higher local shear modulus values than those with no (or very weak) FIC disruption event (smooth FICs).

3.3.1.c Comparing the global shear relaxation modulus $\langle G \rangle$ and the dissipation loss D_l of FICs without and with disruption events

We first analyzed the global response to strain of C2C12 myoblasts, from a set of 1383 FICs recorded on 54 myoblasts (Fig. 3.35). The statistical distributions of the global shear modulus $\langle G \rangle$ and of the dissipative loss D_l were computed separately for FIC subsets without disruption event ($N_{peak} = 0$) and with disruption events ($N_{peak} > 0$). The means of the global shear modulus distributions of these two subsets are respectively $\overline{\langle G \rangle}_{[N_{peak}=0]} = 1.57 \pm 0.25$ kPa and $\overline{\langle G \rangle}_{[N_{peak}>0]} = 1.26 \pm 0.1$ kPa, showing that the mean shear modulus computed from FICs without disruption events is only slightly larger than with disruption events. The comparison of the distributions of $\langle G \rangle$ in Fig. 3.35(a) and (c)) is more instructive since the distribution of $\langle G \rangle$ values has a longer tail for undisrupted FICs than for disrupted FICs, corresponding to much higher apparent stiffness. However, the subset of FICs with disruption events are enriched in $\langle G \rangle$ values in the interval 1.5-2.5 kPa. The distributions of the dissipation loss D_l for these two subsets of FICs reveal a noticeable increase of D_l for disrupted (versus undisrupted) FICs ($\overline{D_l}_{\ [N_{peak}=0]} = 0.39 \pm 0.02$ and $\overline{D_l}_{\ [N_{peak}>0]} = 0.45 \pm 0.02$), which comforts the intuitive idea that

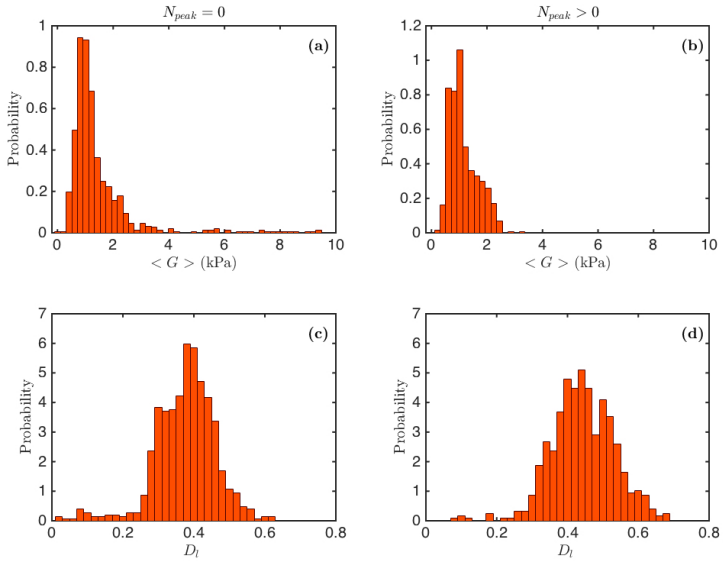

Figure 3.35: **Statistical distributions of $\langle G \rangle$ and D_l captured from 54 myoblasts (1383 FICs), distinguishing non-disrupted FICs ($N_{peak} = 0$ - 745 FICs) from disrupted FICs ($N_{peak} > 0$ - 638 FICs).** The myoblasts were adherent on collagen coated petri dishes and maintained in GM buffer at room temperature during the AFM recording (Materials and methods - Chapter 5). $\overline{\langle G \rangle}_{[N_{peak}=0]} = 1.57 \pm 0.25$ kPa and $\overline{\langle G \rangle}_{[N_{peak}>0]} = 1.26 \pm 0.1$ kPa, $\overline{D_l}_{\ [N_{peak}=0]} = 0.39 \pm 0.02$ and $\overline{D_l}_{\ [N_{peak}>0]} = 0.45 \pm 0.02$.

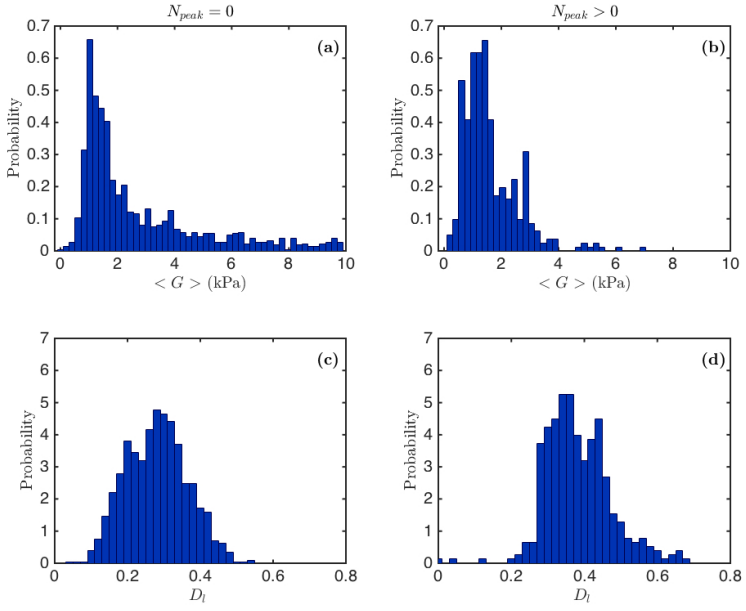

Figure 3.36: **Statistical distributions of $\langle G \rangle$ and D_l captured from 56 myotubes (1530 FICs), distinguishing non-disrupted FICs ($N_{peak} = 0$ - 1133 FICs) from disrupted FICs ($N_{peak} > 0$ - 397 FICs).** The myotubes were adherent on collagen coated petri dishes and maintained in GM buffer at room temperature during the AFM recording (Materials and methods - Chapter 5). $\overline{\langle G \rangle}_{[N_{peak}=0]} = 3.1 \pm 0.4$ kPa and $\overline{\langle G \rangle}_{[N_{peak}>0]} = 1.7 \pm 0.3$ kPa, $\overline{D_l}_{\ [N_{peak}=0]} = 0.28 \pm 0.01$ and $\overline{D_l}_{\ [N_{peak}>0]} = 0.38 \pm 0.03$.

if these disruption events are related to local ruptures of a component of the CSK network, the mechanical work required for these ruptures will unlikely be recovered upon unloading the AFM tip from the cell. The percentage of disrupted FICs ($R_D \sim 46.1\%$) gives the propensity of a type of cell to undergo rupture events when indented with a sharp indenter on micron-size distances. In the case of C2C12 myoblasts there is about 50% chance that a cell shows disrupting events upon deformation.

We repeated the same histogram reconstruction from FICs recorded on myotubes (Fig. 3.36) and we obtained larger mean global shear moduli $\overline{\langle G \rangle}_{[N_{peak}=0]} = 3.1 \pm 0.4$ kPa and $\overline{\langle G \rangle}_{[N_{peak}>0]} = 1.7 \pm 0.3$ kPa respectively. These values are somewhat misleading since the histograms of $\langle G \rangle$ values are not Gaussian; in particular the histogram for $\langle G \rangle_{[N_{peak}=0]}$ has a very long tail (much longer than the one for the myoblasts) that extends to shear modulus values as large as 10 kPa (Fig. 3.36(a)). The proportion of FICs with $\langle G \rangle \sim 1$ kPa (corresponding to the maximum of the distribution) is less than half of the total number of undisrupted FICs. Surprisingly, the histogram of $\langle G \rangle_{[N_{peak}>0]}$ values for myotubes (Fig. 3.36(b)) has strong similarities with the one previously obtained for myoblasts; the long tail corresponding to larger $\langle G \rangle$ values (Fig. 3.36(a)) has disappeared and as for the myoblasts there is an enrichment of disrupted FICs $\langle G \rangle$ values in the interval 1.5-2.5 kPa. The distributions of D_l (Fig. 3.36(c) and (d)) also show that the disrupted FICs have a higher dissipative loss, suggesting as before that when disruption events accumulate the cell is unlikely to recover the mechanical work that was a injected during the indentation ($\overline{D_l}_{\ [N_{peak}=0]} = 0.28 \pm 0.01$ and $\overline{D_l}_{\ [N_{peak}>0]} = 0.38 \pm 0.03$). The comparison of the $\langle G \rangle$ histograms from myoblasts and myotubes is quite amazing because it is only on the long tail distribution of $\langle G \rangle$ (> 2 kPa) that we can distinguish myoblast from myotube mechanical elastic properties. These two types of cells keep common CSK structural properties in their ability to sustain temporally the deformation and break suddenly (disruption event) with a percentage of FICs with disruption events which is significantly larger for myoblasts ($R_D = 46.1\%$) than for myotubes ($R_D = 26\%$) (Table 3.4). This phenomenon could be interpreted by a local viscoplasticity of the CSK network of these cells, corresponding to perinuclear actin stress fibers (all these FICs were recorded above the nucleus). In Chapter 2, we tried to make a clear separation between elastoplastic responses illustrated by two myoblasts and viscoelastic responses illustrated by two myotubes; this was a too strong simplification. Actually, those of the cells which responded to a fixed velocity indentation with disrupted events adopted a "visco-plastic" behaviour leading finally to a local failure of the actomyosin cross-linked network. The observed systematic increase of $\overline{D_l}_{\ [N_{peak}>0]}$ as compared to $\overline{D_l}_{\ [N_{peak}=0]}$, comforts this point of view.

At that point, one may wonder to which extent the myosin motors assist the actin stress fiber network adaptation during indentation. In other words, is the observed visco-plasticity a passive or active property of the CSK actin network? Depleting the source of ATP was one of the important test that could help us answering this question. The corresponding histograms for $\langle G \rangle$ and D_l are shown in Fig. 3.37. The histogram of $\langle G \rangle_{[N_{peak}=0]}$ values (Fig. 3.37(a)) is quite similar to the one obtained from unperturbed myoblasts (Fig. 3.35(a)). Conversely the histograms of $\langle G \rangle_{[N_{peak}>0]}$ (Figs 3.37(b) and 3.35(b)) can be distinguished by a shift of the histogram for ATP depleted cell to lower $\langle G \rangle$ values, suggesting that the activity of the myosin motors is likely to increase the tension of the perinuclear stress fiber network. But this difference could not be detected from the mean values of $\langle G \rangle$ only. Again, it was important to compare the histograms. Another interesting feature is given by the histograms of D_l. We also observed a shift of this histogram to higher D_l values for FICs with disrupted events (Fig. 3.37(d)),

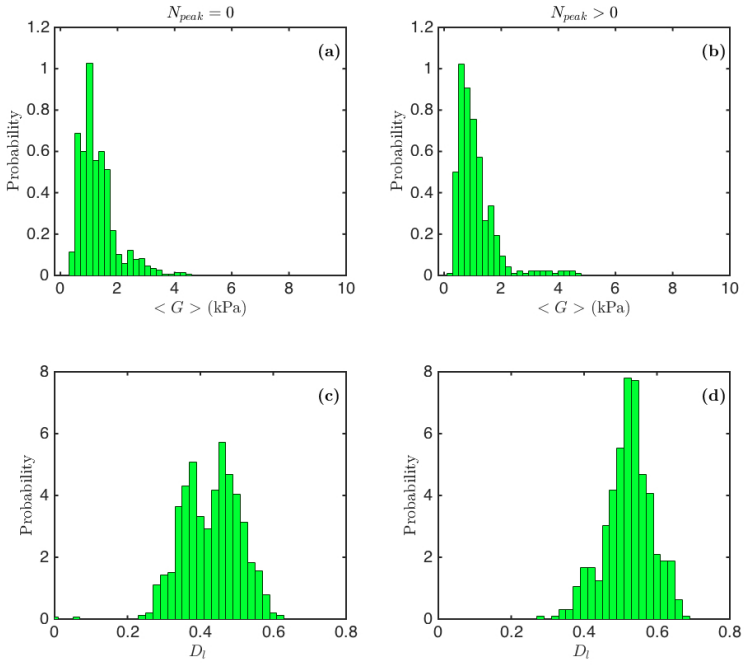

Figure 3.37: **Statistical distributions of $\langle G \rangle$ and D_l captured from 56 "ATP depleted" myoblasts (1248 FICs), distinguishing non-disrupted FICs ($N_{peak} = 0$ - 768 FICs) from disrupted FICs ($N_{peak} > 0$ - 480 FICs).** The myoblasts were adherent on collagen coated petri dishes and maintained in ATP depletion buffer at room temperature for 30 minutes before AFM FIC capture. (Materials and methods - Chapter 5). $\overline{\langle G \rangle}_{[N_{peak}=0]} = 1.4 \pm 0.2$ kPa and $\overline{\langle G \rangle}_{[N_{peak}>0]} = 1.2 \pm 0.2$ kPa, $\overline{D_l}_{\ [N_{peak}=0]} = 0.44 \pm 0.02$ and $\overline{D_l}_{\ [N_{peak}>0]} = 0.53 \pm 0.02$.

pointing the inability of these cells to recover the mechanical work that was injected by the AFM cantilever during their deformation. The histogram of $D_{l\ [N_{peak}=0]}$ values (Fig. 3.37(c)) is also very interesting because it seems to indicate that there could be two groups of FICs where the deformation energy recovery would be different. The FICs corresponding to the rightmost peak of the distribution of $D_{l\ [N_{peak}=0]}$ might correspond to a different stage of transformation of the CKS upon ATP depletion, that could be a precursor of the distribution of $D_{l\ [N_{peak}>0]}$ for disrupted FICs (3.37(d)). This drift of $D_{l\ [N_{peak}>0]}$ to very large values for disrupted FICs is quite puzzling and difficult to explain from the mean of $\langle G \rangle$ values and a further local analysis of the amplitude of FIC disruption events will be necessary to elaborate an explanation. The means of $\langle G \rangle$ and D_l for the cells belonging to the C2C12 myoblast group are reported in Table 3.4, the case of blebbistatin and fixed cells are also listed and will be discussed in the next paragraphs.

3.3.1.d Reconstruction of histograms from local rupture event characteristic features

To assist the interpretation of the global shear relaxation modulus and dissipative loss histograms reported in Section 3.3.1.c, we sorted out those with disruption events and we reconstructed the histograms from the local quantities that describe the disruption events (G_{loc},

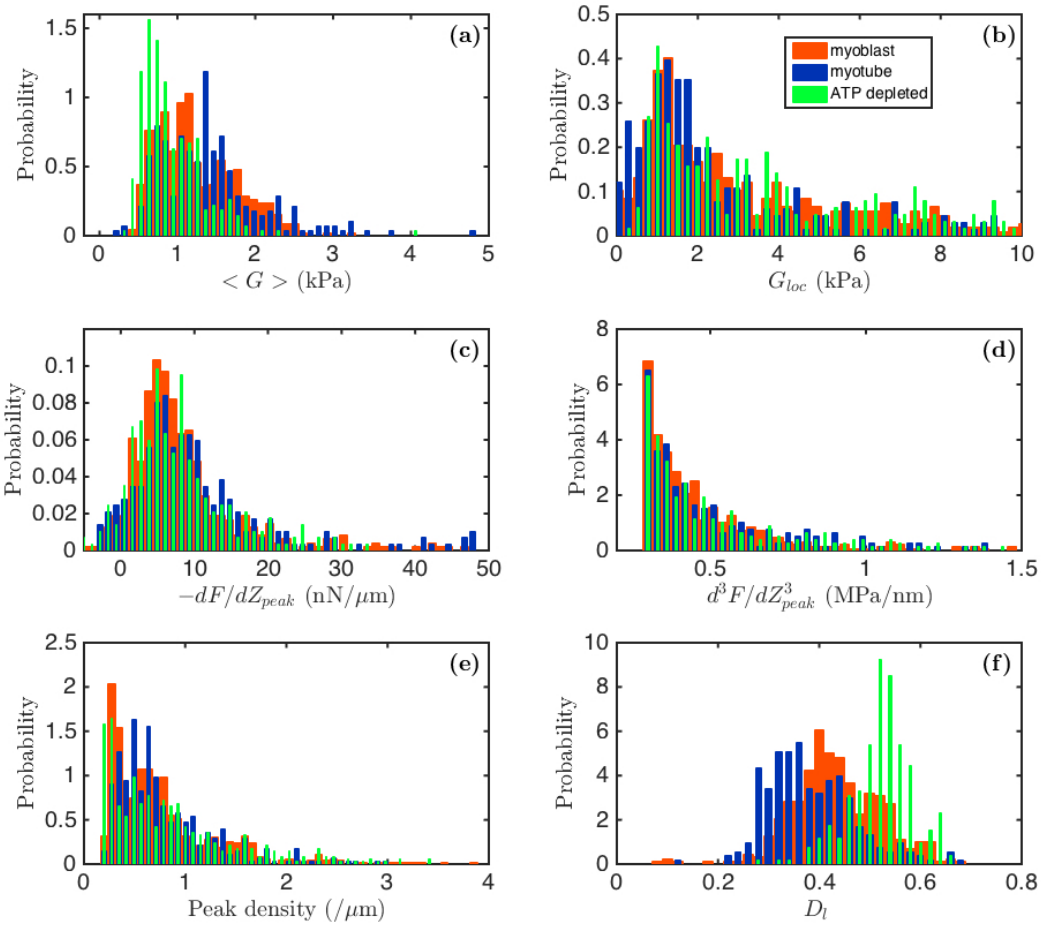

Figure 3.38: **Statistical distributions of global and local features computed from disrupted FICs ($N_{peak} > 0$) sorted out from FICs collected from myoblasts (red), myotubes (blue) and ATP depleted (green) myoblasts.** (a) $\langle G \rangle_{[N_{peak}>0]}$. (b) G_{loc} (defined in Fig. 3.34). (c) $-dF/dZ_{peak}$. (d) $\Gamma_{peak} = d^3F/dZ^3_{peak}$. (e) Peak density $\Lambda_{peak} = N_{peak}/|Z_{setpoint} - Z_c|$. (f) $D_{l\ [N_{peak}=0]}$.

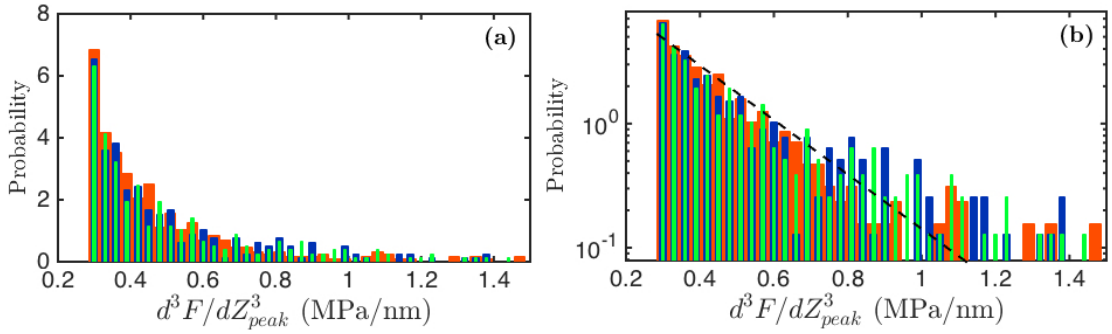

Figure 3.39: **Statistical distributions of $\Gamma_{peak} = d^3F/dZ^3_{peak}$ collected from myoblast (red), myotube (blue) and ATP depleted (green) myoblast FICs, represented in lin-lin (a) and lin-log (b) scales.**

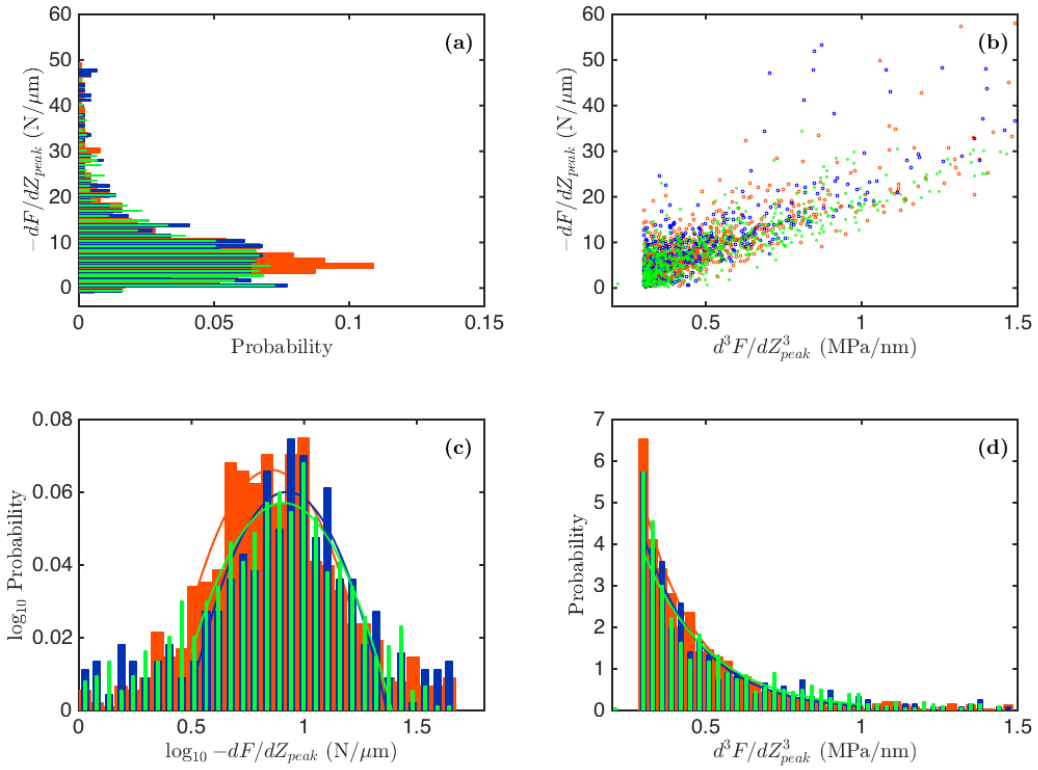

Figure 3.40: **Statistical distributions of $-dF/dZ_{peak}$ and $\Gamma_{peak} = d^3F/dZ^3_{peak}$ collected from myoblast (red), myotube (blue) and ATP depleted (green) myoblast FICs.** (a) $-dF/dZ_{peak}$. (b) Scatter point plot of $-dF/dZ_{peak}$ versus $\Gamma_{peak} = d^3F/dZ^3_{peak}$. (c) Log-normal distribution of $\log_{10}(-dF/dZ_{peak})$ and its parametrization with parabola functions. (d) Exponential distribution of $\Gamma_{peak} = d^3F/dZ^3_{peak}$.

type	N cells	N FICs	R_D	$\overline{\langle G \rangle}_{[N_{peak}=0]}$	$\overline{\langle G \rangle}_{[N_{peak}>0]}$	$\overline{D_l}_{\ [N_{peak}=0]}$	$\overline{D_l}_{\ [N_{peak}>0]}$
myoblast	54	1383	46.1	1.57 ± 0.25 kPa	1.26 ± 0.1 kPa	0.39 ± 0.02	0.45 ± 0.02
myotube	56	1530	26.0	3.1 ± 0.4 kPa	1.7 ± 0.3 kPa	0.28 ± 0.01	0.38 ± 0.03
ATP depl	56	1248	38.5	1.4 ± 0.2 kPa	1.2 ± 0.2 kPa	0.44 ± 0.02	0.53 ± 0.02
blebbist.	23	534	4.9	0.95 ± 0.1 kPa	1.1 ± 0.5 kPa	0.28 ± 0.06	0.4 ± 0.1
fixed	12	300	21	5.9 ± 0.6 kPa	5.7 ± 0.8 kPa	0.17 ± 0.04	0.23 ± 0.05

Table 3.4: **Compilation of the means of the global quantities $\langle G \rangle$ and D_l for C2C12 myoblast cells.** FICs without ($N_{peak} = 0$) and with ($N_{peak} > 0$) disrupted events are compared. R_D is the percentage of FICs with disruption events. Five types of cells are reported: normal C2C12 myoblasts, myotubes differentiated from C2C12 myoblasts, ATP depleted C2C12 myoblasts, blebbistatin treated C2C12 myoblasts and fixed C2C12 myoblasts. The global Young modulus is given by $\langle E \rangle = 3\langle G \rangle$ (with the Poisson coefficient $\nu = 0.5$).

dF/dZ, d^3F/dZ^3, density of peaks). In Fig. 3.38 are summarized the results of the FIC analysis for three sets of cells: myoblasts, myotubes and ATP depleted myoblasts. The left shift of the histogram of $\langle G \rangle_{[N_{peak}>0]}$ for ATP depleted myoblasts is highlighted in Fig. 3.38(a). The superimposition of the histograms of G_{loc} reveals two important points: (i) the distribution of G_{loc} for myotubes presents an enrichment of low (< 1 kPa) local shear modulus values, corresponding to softer cells (similar to those characterised in Chapter 2 where $E \sim 4$ kPa ($G \sim 1.3$ kPa) for $V_0 = 1$ μ/s); (ii) the G_{loc} distribution for normal C2C12 myoblasts shows a long tail for $G_{loc} > 2$kPa, meaning that in that case the stiffer myoblast cells have the propensity to higher rupture events than myotubes. The histogram of G_{loc} for ATP depleted cells is very interesting since it shows that despite the fact that the global $\langle G \rangle [N_{peak} > 0]$ values are smaller than those of myoblasts and myotubes on disrupted FICs, there is a significant proportion of FICs with local shear moduli G_{loc} above 3 kPa. Even if globally, the FICs of ATP depleted myoblasts that display disruption events can be interpreted as softer than normal myoblasts, the local shear moduli detected just before and after the disruption events lead to a different conclusion, namely that the internal stress fibers may behave locally as more rigid in ATP depleted cells than in normal cells.

The histograms of the values of the first-order derivative dF/dZ of the FICs, detected at the FIC disruption points (Fig. 3.38(c)), are more difficult to distinguish in these three cell types. dF/dZ gives the gradient of the force at the rupture (the negative slope at which the force drops upon disruption); it remains smaller than the nominative stiffness of the AFM cantilever $\sim 0.06 - 0.1$ N/m $= 60 - 100$ nN/μm. This slope estimation is also limited by the width of the analysing wavelet ($2\sqrt{2}s_g^{(1)} = 9$ nm). Typically a slope of 10 nN/μm over a distance of 9 nm, would give a force drop of $10*9*10^{-3} \sim 0.1$ nN. The force disruption event that we have shown in Fig. 3.33 for illustration is an extreme case that occurs rarely (tail of the distributions). Indeed the histograms of $-dF/dZ_{peak}$ have a single humped shape around 5 nN/μm (Fig. 3.38(c)). Conversely, the distributions of $\Gamma_{peak} = d^3F/dZ^3$ values do not show a hump-like shape, but

rather an exponential decay (Figs 3.38(d) and 3.39). This exponential decreasing distribution of Γ_{peak} means that large amplitude peaks (corresponding to high curvature of the force derivative) have a probability that decreases exponentially with a characteristic amplitude $\tau_\Gamma \sim 0.2\,\mathrm{MPa/nm}$ (the parametrization of these curves is illustrated in Fig. 3.40(d)). τ_Γ corresponds also to a characteristic slope of the second order derivative of the FIC, which expresses how fast the FIC can switch from a negative curvature (just before the disruption d^2F/dZ^2 is negative, locally the CSK can no longer sustain the deformation and breaks locally) to a positive curvature (just after the disruption event d^2F/dZ^2 is positive, which corresponds to much stiffer zones that counteract the cantilever penetration into the cell) (Fig. 3.34(c)). Since the two quantities dF/dZ and d^3F/dZ^3 are extracted from the same FICs, one may be interested to know if they are correlated. Plotting the first derivative of F versus the third derivative of F in Fig. 3.40(b) (lin-lin representation), we note, as expected, that the larger negative slopes of F ($-dF/dZ$) correspond to the larger peak amplitudes in d^3F/dZ^3. Interestingly, at low negative slopes $-dF/dZ$ and low peak amplitudes of d^3F/dZ^3, corresponding to the hump of the distribution of $-dF/dZ$ (visible on the histogram of $-dF/dZ$ turned by 90° in Fig. 3.40(a)), the two histograms of $-dF/dZ$ and $\Gamma_{peak} = d^3F/dZ^3$ differ notably. In particular, reconstructing the histogram of $-dF/dZ$ in log-log representation (Fig. 3.40(c)) puts into light the fact that the histograms of $-dF/dZ$ for the three sets of cells (myoblasts, myotubes, and ATP depleted myoblasts) are well approximated by a log-normal distribution [Limpert, 2001] in the interval $\log_{10} -dF/dZ \in [0.6 : 1.4]$. This log-log representation offers a better distinction of the distributions of $-dF/dZ$; for instance we see clearly that the center of the lognormal distribution of $-dF/dZ$ for the myoblasts (in red) is shifted to lower $-dF/dZ$ values and that the distributions for the myotubes and the ATP depleted myoblasts are superimposed.

When comparing the distributions of the dissipative loss D_l in Fig. 3.38(f), we confirm the fact that for the ATP depleted myoblasts, the recovery of mechanical energy expanditure is harder during unloading scan. This important shift of the D_l histogram points out the importance of active processes driven by ATP (NMMII) for the cells to recover from the deformation. It also suggests that the myotubes have a more efficient way to recover the deformation than the myoblasts. The values of the means of D_l are listed in Table 3.4: $\overline{D_l}_{\,[N_{peak}>0]} = 0.45 \pm 0.02$ for the myoblasts, $\overline{D_l}_{\,[N_{peak}>0]} = 0.38 \pm 0.03$ for the myotubes and $\overline{D_l}_{\,[N_{peak}>0]} = 0.53 \pm 0.02$ for the ATP depleted myoblasts. A full confirmation of this mechanical observations would require performing fluorescence microscopy characterization (3D confocal microscopy at high resolution of both myosin, actin stress fibers and their focal adhesions) of the perinuclear actin network from living cells (unfixed). Unfortunately, such a study could not be performed during this PhD thesis.

Finally, we compare in Fig. 3.38(e) the distributions of peak (disruption event) density $\Lambda_{peak} = N_{peak}/|Z_{setpoint} - Z_c|$ for the three sets of cells. Again, these distributions are asymmetric, with a long tail at larger peak density values. The mean of these distributions are respectively: $\overline{\Lambda}_{peak} = 0.82 \pm 0.12$ $/\mu$m for the myoblasts, $\overline{\Lambda}_{peak} = 1.13 \pm 0.38$ $/\mu$m for the myotubes and $\overline{\Lambda}_{peak} = 2.6 \pm 1.9$ $/\mu$m for the ATP depleted myoblasts. The error of the mean of these quantities is quite large, given that these distributions are asymmetric and have quite long tails. However, the increase of $\overline{\Lambda}_{peak}$ for the ATP depleted myoblasts is significative and suggests that depleting the intracellular ATP does not seem to disassemble totally the cross-linked perinuclear actin network, but more likely disorganize this network of straight and long actin filaments crossing over the whole cell body into interconnected small aggregates of shorter actin filaments. This actin filament CSK reorganization was confirmed by fluorescence microscopy

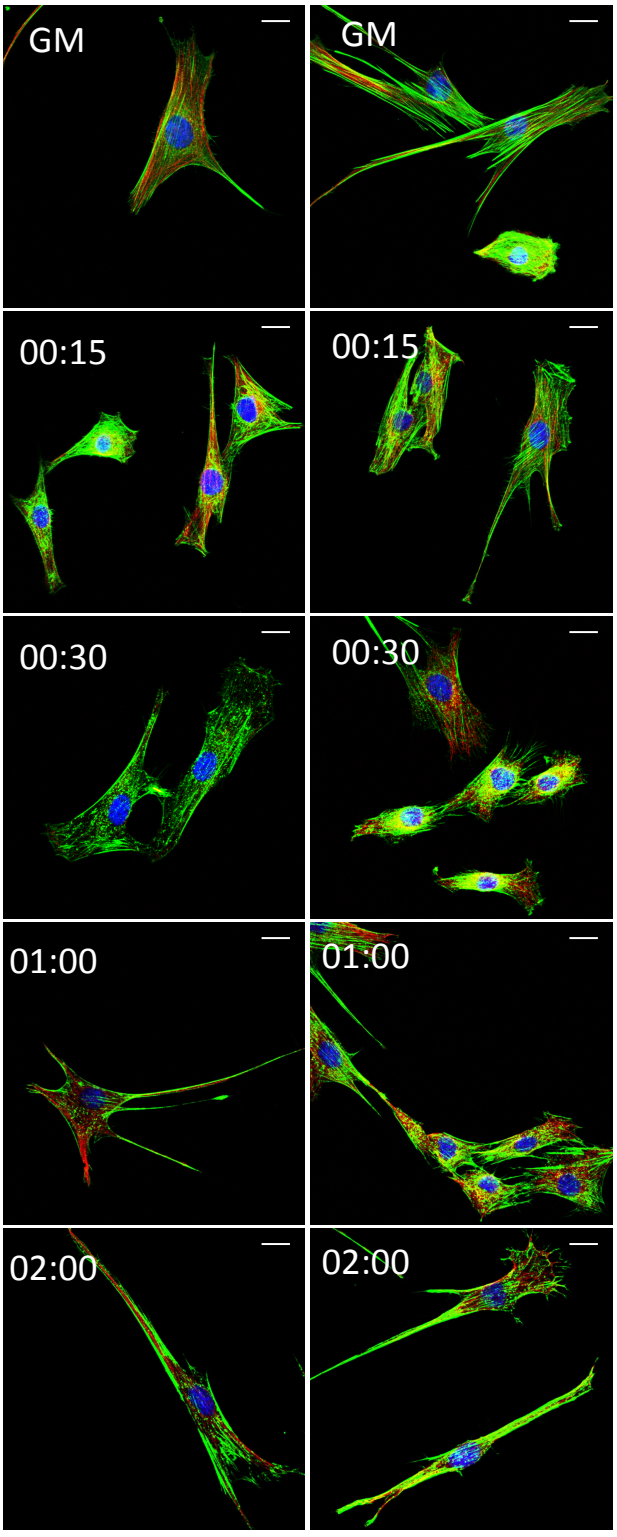

Figure 3.41: **Immuno-fluorescence confocal images of ATP depleted C2C12 myoblasts.** C2C12 myoblasts on CCPD were stained at different times after being immersed in the ATP depletion buffer. The samples were kept at room temperature during the treatment. Staining: F-actin (phalloidin-Alexa Fluor 488, green), β-tubulin (anti-β-tubulin Cy3-conjugate, red) and nucleus (DAPI, blue). The time is reported as hh:mm. Scale bars: 20 μm.

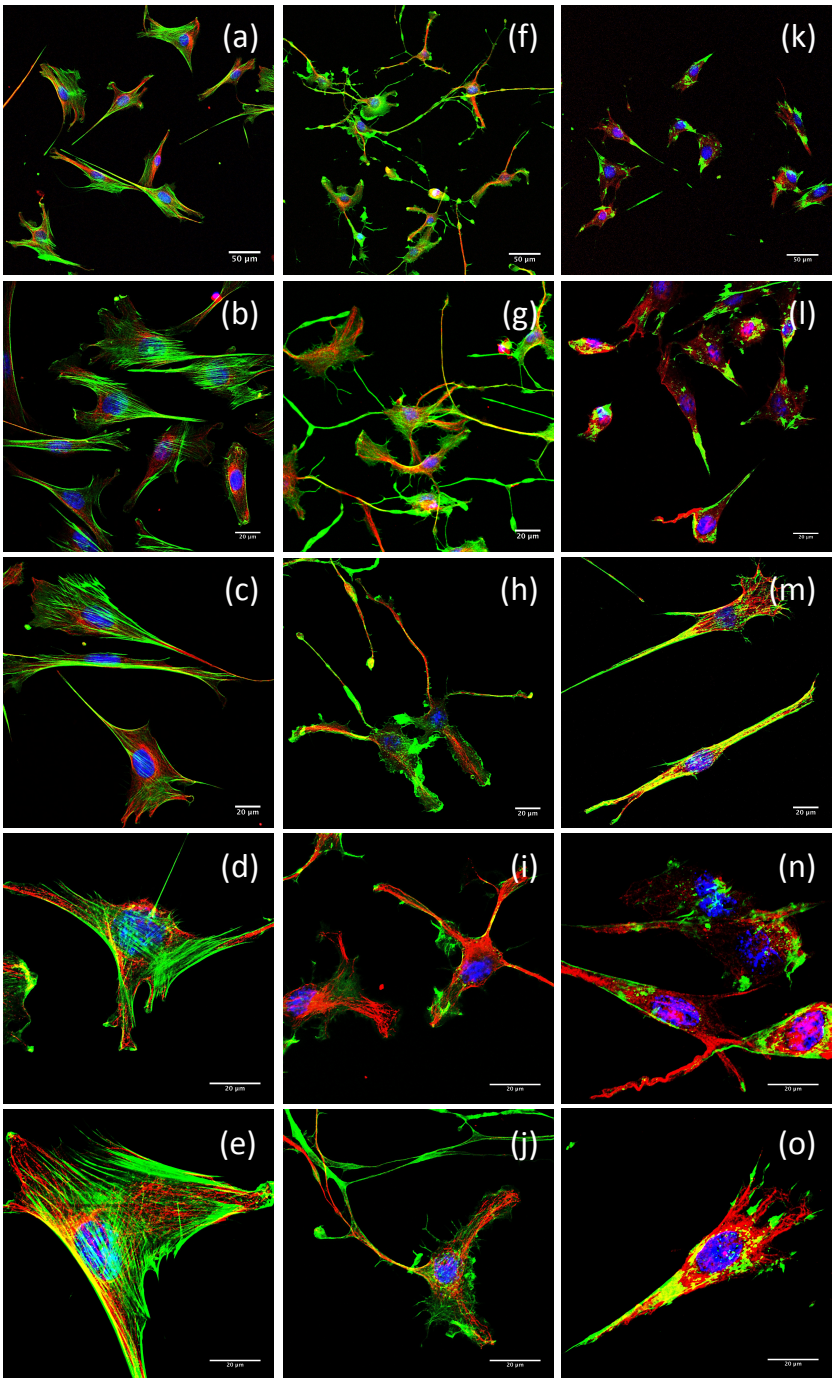

Figure 3.42: **Immuno-fluorescence confocal images of normal, blebbistatin treated and ATP depleted C2C12 myoblasts.** C2C12 myoblasts on CCPD were stained after 2h in (a-e) normal GM, (f-j) GM with blebbistatin, and (k-o) in the ATP depletion buffer. The samples were kept at room temperature during the treatments, similar to the AFM experimental conditions. Staining: F-actin (phalloidin-Alexa Fluor 488, green), β-tubulin (anti-β-tubulin Cy3-conjugate, red) and nucleus (DAPI, blue). Scale bars: (a, f, k) 50 μm, all the other images 20 μm.

imaging of fixed myoblasts in Fig. 3.41.

ATP depletion shifts the balance ATP-NMMII/ADP-NMMII in favour of ADP-NMMII, blocks the motility of the myosin motors on actin filaments, shortens the perinuclear actin stress fibers and limits their connection to distant focal adhesions (in the front and the rear of the cell). Fluorescence staining of actin filaments from fixed myoblasts at different stages of ATP depletion (Fig. 3.41) shows that the cells do not detach from their substrate, and that they also keep their elongated shapes (flat lamellipodia and filopodia). The other ventral and peripheral (basal) actin stress fibers do not seem to be much affected by ATP depletion. It has been shown by fluorescence recovery after photobleaching of cells transfected by EGFP-actin that the exchange dynamics between F-actin from the perinuclear stress fibers and monomeric G-actin in the cytoplasm is much faster than actin exchange dynamics from basal stress fibers [Khatau, 2010; Kim, 2012]. The sequestering of actin filaments is performed by two major proteins, thymosin (Tβ4) and profilin. In the absence of ATP, the self-assembly of F-actin via ADP-NMMII cross-linking gives a different actomyosin network, less motile and compliant to deformation (Fig. 3.25(B,D)) [Smith, 2007]. It has also been shown that a complete ATP depletion can cause a 100-fold increase in the elastic stiffness of the actomyosin network [Smith, 2007]. Our AFM experiments with sharp conical indenters imposed the shearing of the cells above the perinuclear area; they did not corroborate such an increase of cell stiffness (global shear relaxation modulus $\langle G \rangle$). However we observed the increase of the local shear relaxation moduli collected before and after the FICs disruption events. It is therefore very important to know at which spatial and temporal scales a mechanical experiment is performed. When focusing on very local (nanoscale) events, different conclusions can be drawn from the measurement of elastic moduli. The percentage of FICs where rupture events were detected is an important quantity that needs to be emphasized: for the myoblasts 46.1% of FICs show disruption events, 26% for the myotubes and 38.5% for the ATP depleted myoblasts (Table 3.4). Even if statistically the local shear modulus of ATP depleted cells is higher, the proportion of disrupted FICs is smaller, and those which are disrupted have a higher density of disruption events. We suspect that ATP depletion does not completely disassemble the actin CSK network but more likely impacts those of the actin stress fibers which are the more dynamic, namely the perinuclear actin stress fibers.

3.3.1.e From ATP depletion to blebbistatin inhibition of NMMII: highlighting the dynamic cross-linker role of NMMII

A set of myoblasts was maintained in GM buffer with blebbistatin (50 μM) (Chapter 5) and histograms of global $\langle G \rangle$ and D_l were computed from undisrupted $N_{peak} = 0$ and disrupted $N_{peak} > 0$ FICs, recorded at a constant scan velocity $V_0 = 1$ μm/s. Given that blebbistatin blocks the NMMII head and their ATPase activity, it decreases drastically the affinity of NMMII for F-actin and blocks its molecular function [Straight, 2003; Kovács, 2004]. Blebbistatin therefore impairs the dynamical building of all the CSK actin stress fibers and notably those of the perinuclear actin cap [Khatau, 2009] (Fig. 3.42). Remarkably, the percentage of FICs showing disrupting events significantly dropped down ($R_D \simeq 5\%$ - 26 FICs among a total sample of 534 FICs). Moreover, we observed a drastic change of the distribution of $\langle G \rangle$ values (Fig. 3.43(a) and (b)) with a significant decrease of the mean global shear modulus values: $\overline{\langle G \rangle}_{[N_{peak}=0]} = 0.95 \pm 0.1$ kPa and $\overline{\langle G \rangle}_{[N_{peak}>0]} = 1.1 \pm 0.5$ kPa (Table 3.4). Also the histogram of dissipation loss D_l is drastically shifted to very low values (Fig. 3.43(c)), meaning that the loss of mechanical energy is very low in blebbistatin treated cells. This confirms our expectations in Section 3.2.3 and the

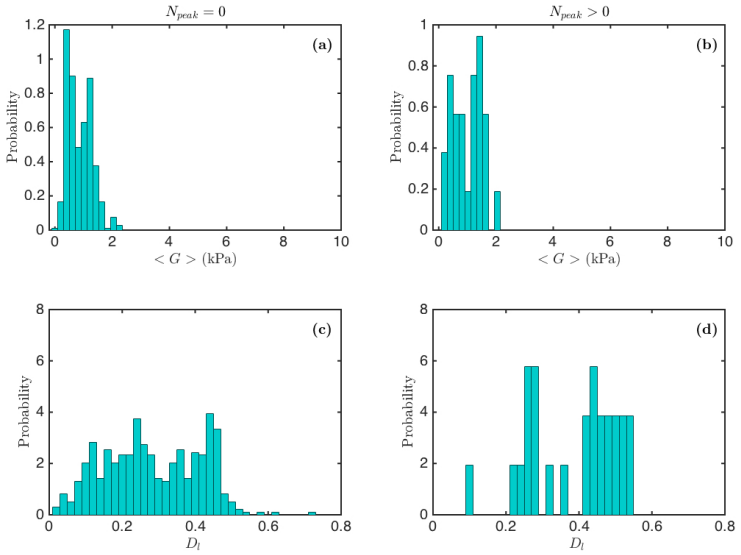

Figure 3.43: **Statistical distributions of $\langle G \rangle$ and D_l captured from 23 myoblasts treated with blebbistatin (534 FICs), distinguishing non-disrupted FICs ($N_{peak} = 0$ - 508 FICs) from disrupted FICs ($N_{peak} > 0$ - 26 FICs).** The myoblasts were adherent on collagen coated petri dishes and maintained in blebbistatin GM buffer at room temperature during AFM FIC capture (Materials and methods - Chapter 5). $\overline{\langle G \rangle}_{[N_{peak}=0]} = 0.95 \pm 0.1$ kPa and $\overline{\langle G \rangle}_{[N_{peak}>0]} = 1.1 \pm 0.5$ kPa, $\overline{D_l}\ _{[N_{peak}=0]} = 0.28 \pm 0.06$ and $\overline{D_l}\ _{[N_{peak}>0]} = 0.4 \pm 0.1$.

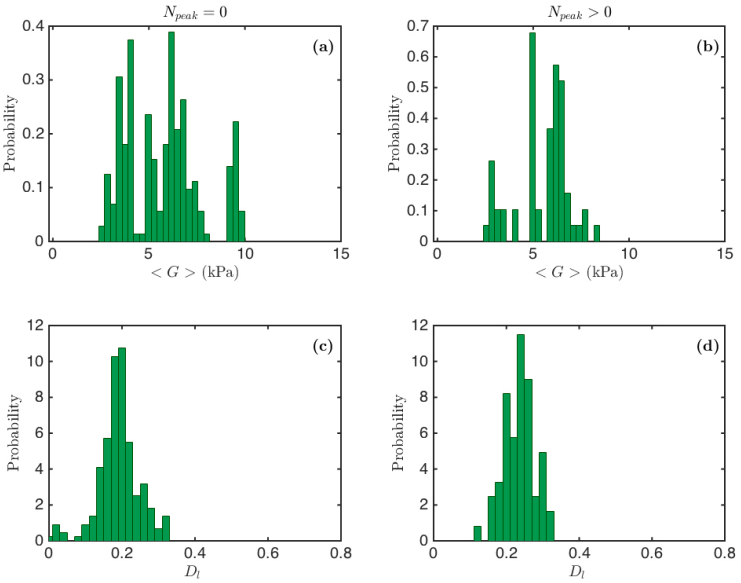

Figure 3.44: **Statistical distributions of $\langle G \rangle$ and D_l captured from 12 myoblasts fixed with paraformaldehyde (4%) in PBS (300 FICs), distinguishing non-disrupted FICs ($N_{peak} = 0$ - 237 FICs) from disrupted FICs ($N_{peak} > 0$ - 63 FICs).** The myoblasts were adherent on collagen coated petri dishes and maintained in PBS buffer during AFM FIC capture (Materials and methods - Chapter 5). $\overline{\langle G \rangle}_{[N_{peak}=0]} = 5.9 \pm 0.6$ kPa and $\overline{\langle G \rangle}_{[N_{peak}>0]} = 5.7 \pm 0.8$ kPa, $\overline{D_l}\ _{[N_{peak}=0]} = 0.17 \pm 0.04$ and $\overline{D_l}\ _{[N_{peak}>0]} = 0.23 \pm 0.05$.

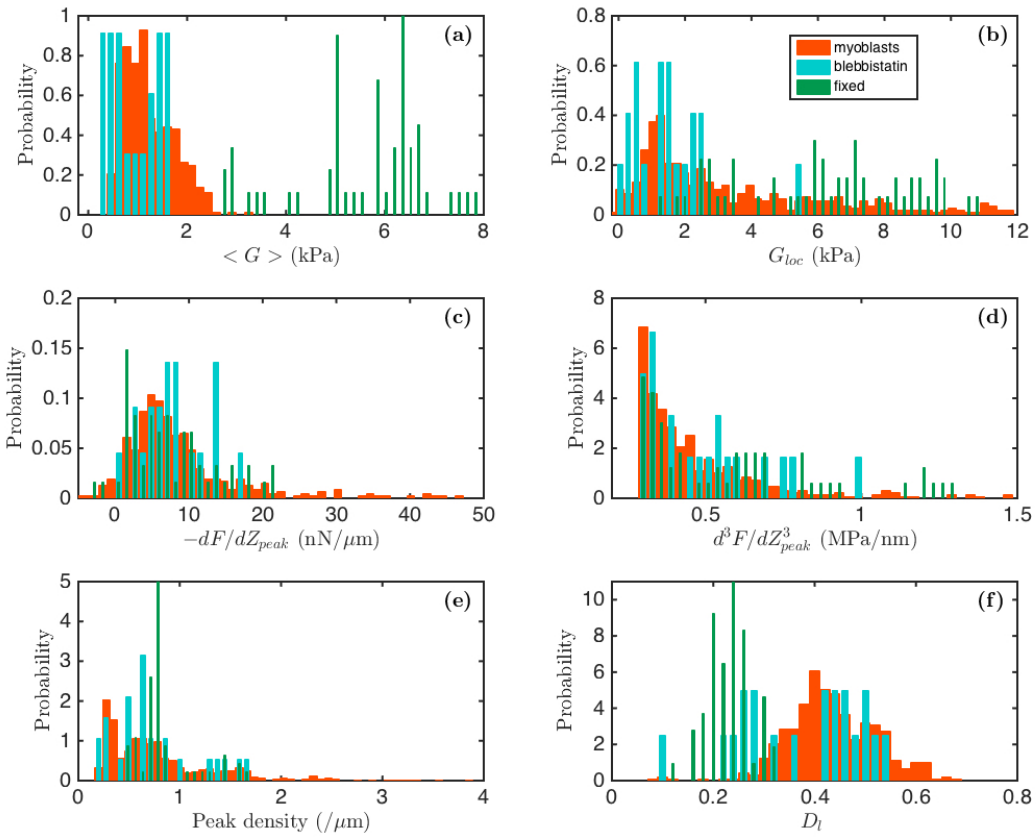

Figure 3.45: **Statistical distributions of global and local features computed from disrupted FICs ($N_{peak} > 0$) sorted out from FICs collected from normal (red), blebbistatin treated (light blue) and fixed (green) C2C12 myoblasts.** (a) $\langle G \rangle_{[N_{peak}>0]}$. (b) G_{loc} (defined in Fig. 3.34). (c) $-dF/dZ_{peak}$. (d) d^3F/dZ^3_{peak}. (e) Peak density $\Lambda_{peak} = N_{peak}/|Z_{setpoint} - Z_c|$. (f) $D_{l\ [N_{peak}>0]}$.

predictions of other rheology studies of blebbistatin treated cells [Balland, 2005]. Actually the softening of blebbistatin treated myoblasts and the reduction of FICs with disrupting events are a strong indication that the major energy consuming mechanisms during adherent cell indentation are given by the rupture of the cross-linked cytoskeleton structures. The morphology of the myoblasts treated with blebbistatin is very different from those of normal myoblasts; actin and straight ventral stress fibers have disappeared and these cells produce very long and curved filopodia containing MTs and thin actin filaments (Fig. 3.42(f-j)). NM-II is therefore essential for the correct building of the cytoskeleton stress fibers and for providing the cell for its necessary mechanical properties for survival, motility and proliferation.

Fixing the cells completely changes their mechanical properties, since it rigidly cross-links their CSK with a chemical agent. These cells are no longer alive and even if they are still commonly used to characterise the morphology of their different filament networks, they cannot be considered as a realistic model system to study the mostly dynamic actin stress network, the perinuclear actin cap that our AFM experiments focused on. C2C12 myoblasts were fixed by a solution of 4 % paraformaldehyde in PBS for 20 minutes at room temperature and switched to PBS buffer before AFM FIC capture (Materials and methods, Chapter 5). The histograms of global shear modulus $\langle G \rangle$ and dissipation loss D_l from undisrupted and disrupted FICs are shown in Fig. 3.44. Fixed cells are definitely much stiffer than normal and ATP depleted myoblasts and myotubes. Their deformation by AFM tip indentation is not consuming much mechanical energy since D_l of undisrupted and disrupted FICs is narrowly distributed around 0.2, with only a very slight increase for FICs with disruption events.

Even if the statistical samples for blebbistating treated cells and fixed cells are much smaller than the other sets of myoblasts and myotubes studied in Sections 3.3.1.c and 3.3.1.d, we have nevertheless reconstructed the corresponding histograms for the local quantities previously reported in Fig. 3.38 and we have compared these histograms to normal myoblasts (Fig. 3.45). The amazing observation is that the very few blebbistatin treated cells that show FICs with disrupted events do not give drastically different local parameters than normal myoblasts, probably these cells may not have been completely transformed by blebbistatin and have kept some of their previous actin stress fiber network characteristic marks. The fixed cells showing disrupted FICs have much larger global $\langle G \rangle$ (Fig. 3.45(a)) and local G_{local} (Fig. 3.45(b)) shear modulus values than all the other considered cell types. If fixed C2C12 myoblasts have a rather low percentage (21%) of disrupted FICs as compared to myoblasts (Table 3.4), the density of disruption events (Fig. 3.45(e)) and their strength (Fig. 3.45(d)) are statistically enhanced.

Chapter 4

Structural and mechanical characterization of human primary myoblasts from healthy donors and patients affected by Duchenne muscular dystrophy

The final aim of this project was to apply the developed AFM protocols to evaluate if and how cell mechanical properties were modified in certain human myopathies. Among the several known myopathies we chose the Duchenne muscular dystrophy (DMD) for several reasons: (i) DMD is a well-characterized disease, its etiology and clinical manifestations are well-known; (ii) its pathogenesis and structural alterations have been studied for decades but they are still not fully understood; (iii) DMD is the most severe disease among muscular dystrophies; (iv) although progresses have been made there is no effective therapy to cure this disease; (v) DMD impacts cell compartments involved in cell mechanics such as the CSK and the cell membrane; (vi) DMD affects also the neuromuscular junctions, and (vii) one can have access to muscle biopsies from patients affected by DMD. In this chapter, we start introducing the musculoskeletal organization and the neuromuscular junctions. We present a general overview of human neuromuscular diseases and dystrophies. Then we focus on the DMD pathology, before comparing the structural properties of human primary myoblasts from healthy donors and the dystrophin-deficient myoblasts from patients affected by DMD. Finally we report the characterization by AFM of the mechanical properties of these two types of cells, taking as reference the results obtained in Chapter 3 for the C2C12 myoblast cell line.

4.1 Skeletal muscle and neuromuscular junction organization

Since the XVIIth century, the muscle tissue has been a topic widely discussed in the biological literature and many strides have been made studying its anatomy, physiology, biochemistry, molecular biology, pathology and biophysics. If the Italian physiologist and physicist Giovanni Alfonso Borelli originally explained muscular movement [Borelli, 2012], the French neurologist

Guillaume-Benjamin-Amand Duchenne [Duchenne, 1867] was the first, with Jean-Martin Charcot, to describe several nervous and muscular disorders. Then, from Archibald Vivian Hill, a British physiologist and biophysicist who received with Otto Meyerhof the 1922 Nobel Prize for Physiology or Medicine for discovering the heat production origin in muscles [Hill, 1959], to Hugh Esmor Huxley, an English molecular biologist who studied the muscle ultrastructure and proposed the sliding-filament theory of muscle contraction [Huxley & Hanson, 1954], many aspects of this highly specialized tissue have been elucidated, such as its anatomical hierarchy, the existence of different types of fibers and their role in the dynamics of muscular contraction.

In humans, the skeletal muscles play an essential role in thermic and energetic body regulation, switching between catabolic and anabolic pathways according to physiological conditions [Argilés, 2016]. This metabolic function is due mainly to the muscle ability of storing glucose in the form of glycogen and amino acids in the form of proteins. Skeletal muscles participate to many vital functions such as movement, posture, breathing, chewing, swallowing, locomotion, ... [Chromiak & Antonio, 2008; Shiozu, 2015]. All these motor functions rely on the muscle fundamental contractile properties which mainly result from the muscle structural organization. As illustrated in Fig. 4.1, skeletal muscles are characterized by a multi-systemic organization: each muscle integrates other different types of tissues, such as blood vessels, nerve fibers, and connective tissues (*i.e.* mysia). The role of nerve fibers will be discussed later in this section. Blood vessels deliver nutrients and oxygen and remove wastes. Connective tissues provide structural organization, protection, communication and mechanical coupling within the musculoskeletal system. Another peculiar characteristic of muscles is their hierarchical organization (Fig. 4.1): bundles of thick (myosin) and thin (actin) filaments together with other proteins organize into the sarcomeric myofibrils; bundles of myofibrils occupying most of the sarcoplasma form myofibers surrounded by sarcolemma; at a higher level, bundles of these myofibers generate muscle fascicles that finally group to form the muscle as an organ. From the smallest scale contractile unit, *i.e.* the sarcomere (the myofibril region between two adjacent Z-disks), to the largest contractile unit which is the muscle, the mechanical, biochemical and electrical couplings involved in this multi-scale structural organization allow thousands of contractile myofibers to work in synchrony.

Muscle contraction also depends on the proper communication between motoneuron axons and the end plates (EP) of muscle fibers through highly specialized synapses called neuromuscular junctions (NMJs). As shown in Fig. 4.2, NMJs enable the communication between the motoneurons, whom cell bodies are located in the spinal cord, and the muscle fibers laying in different regions of the body. This communication permits all the voluntary contractions *via* the transformation of the electrical impulses into muscle contractions. The NMJ structure, function, development together with the associated biochemical and electrophysiological events have been deeply studied for more than 60 years [Hunt & Kuffler, 1950; Duncan, 1983; Bowman, 1988; Hall & Sanes, 1993; Sanes & Lichtman, 1999; Hogg, 2003; Sudhof, 2004; Hughes, 2006; Dani & Bertrand, 2007; Huzé, 2009; Ferraro, 2012; Morel, 2014; Devic, 2014; Rudolf, 2016]. As shown in Fig. 4.2, when the action potential reaches the motoneuron axon terminal, it causes the opening of the voltage-gated Ca^{2+} channels on the plasma membrane of presynaptic nerves and subsequent Ca^{2+} influx. Higher calcium concentration induces the release of the neurotransmitter acetylcholine (ACh) in the synaptic cleft through vesicle fusion induction. Transmission at the post synaptic level in the sarcolemma of muscle cells is improved thanks to deep depressions called synaptic folds where ionotropic nicotinic receptors for ACh (AChRs) are located. The muscle contraction is initiated by a concentration of ACh in the synaptic cleft large enough to

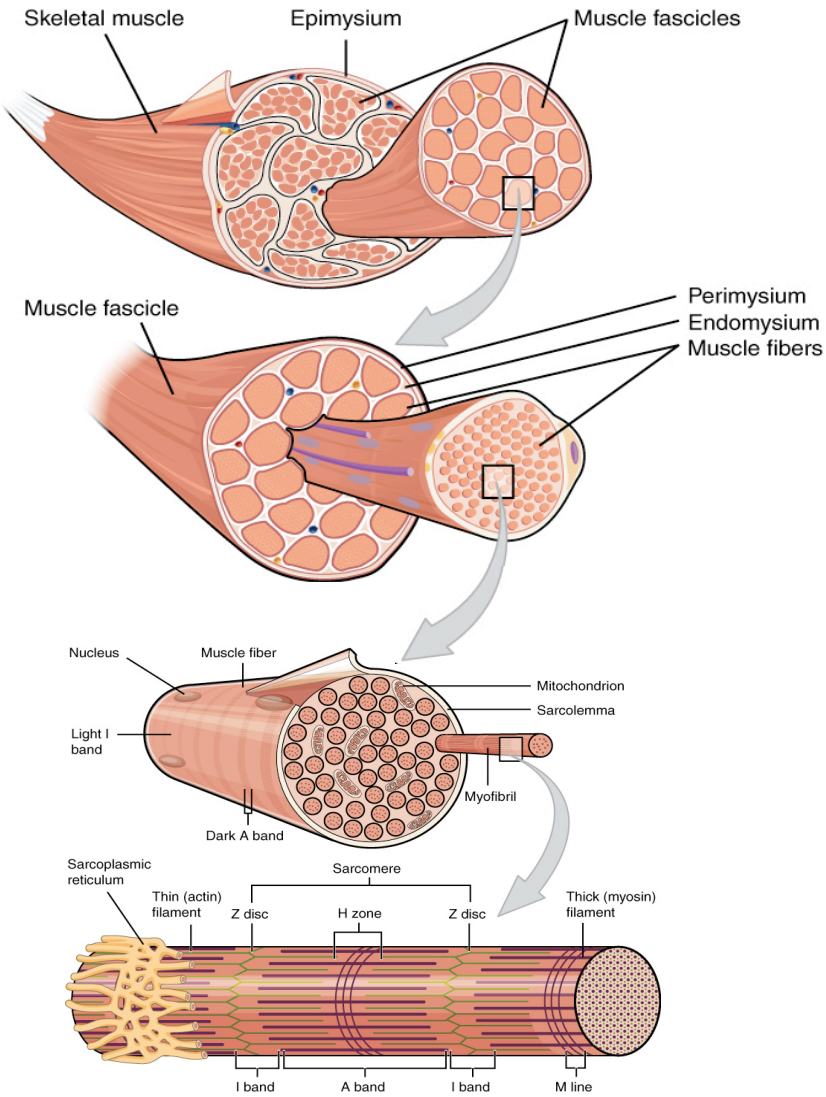

Figure 4.1: **The hierarchical and multi-systemic organization of skeletal muscles.** Schematic representation of the muscle structure from the largest (the muscle as organ) to the smallest (the sarcomere) contractile unit. Adapted from OpenStax College, Anatomy & Physiology [OpenStax-CNX Web site] 2016.

trigger an action potential in the postsynaptic muscle fiber; the term "safety factor" has been introduced to quantify this excess in ACh. For healthy adult mammals, the safety factor varies typically between 3 and 5, meaning from 3-fold to 5-fold the required amount [Wood & Slater, 2001]. The binding of ACh-receptor triggers a cascade of events that increases the permeability of the postsynaptic membrane to Na^+ and K^+, giving birth to a new action potential. This depolarization wave determines the release of calcium ions at the T-tubule level from the terminal cisternae of sarcoplasmic reticulum (SR) into the cytosol. In particular in skeletal muscles, the AChR activation dependent action potential activates dihydropyridine voltage-gated receptors (DHPRs), which in turn activate the SR-located ryanodine receptors (RyRs). RyRs channel activation leads to their opening and consequent release of Ca^{2+} into the cytosol [Lanner, 2010]. Eventually, the increase of intracellular Ca^{2+} concentration caused by the nervous stimulus gen-

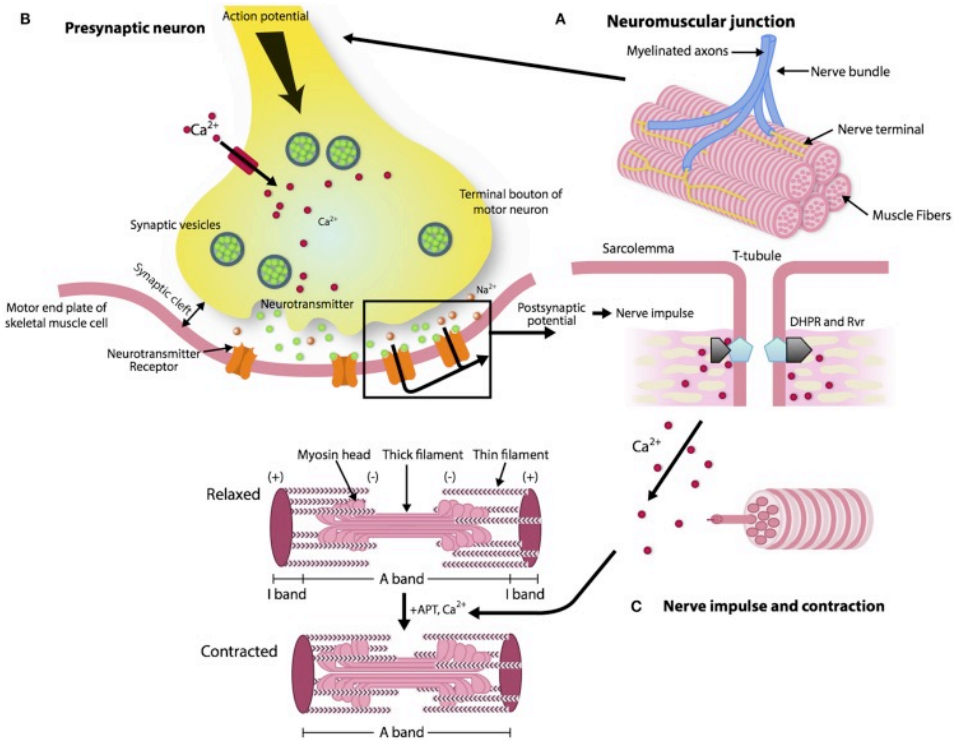

Figure 4.2: **The neuromuscular junction organization.** (A) The motoneuron reaches the myofibers and establishes neuromuscular junctions. (B) The mechanism of acetylcholine release from the presynaptic motor neuron to the synaptic cleft. (C) The transformation of the nerve impulse in calcium-dependent sarcomere contraction. Adapted from Frontiers in Aging Neuroscience [Gonzalez-Freire, 2014].

erates muscle contraction *via* Ca^{2+}-troponin C binding [Gonzalez-Freire, 2014]. Thus, a single muscle contraction represents the culmination of complex interactions between the nervous system and the muscles. Proper neuromuscular transmission, and thus regular muscle contraction, requires correct NMJ development, organization and maturation [Sanes & Lichtman, 1999]. For example, compromised AChR organization and decrease of the safety factor lead to impaired neuromuscular transmission [Wood & Slater, 2001]. NMJs have a dynamic and plastic nature [Fambrough, 1979]; several causes have been associated with altered NMJ organization, such as denervation, aging, overexercising, inactivity and DMD [Jang & Van Remmen, 2011; Kawabuchi, 2011; Sieck, 2012].

As discussed in Chapter 3, satellite cells are located between the basal lamina and the sarcolemma of the muscle fibers. The muscle cell membrane organization is important for proper muscle regeneration. The basement membrane (*i.e.* the basal lamina coupled with reticular lamina) is also important for the muscle integrity, its contraction and communication with bones and nerves *via* neuromuscular and myotendinous junctions. In skeletal muscles, the links between the basement membrane, the sarcolemma and the cytoskeleton have a central role in maintaining muscle structure and function [Campbell & Stull, 2003]. This is not surprising in regard to the vast number of muscular diseases caused by mutations of genes encoding for proteins involved in these three compartments [Blake, 2002; Durbeej & Campbell, 2002; Lovering, 2005]. The structural and functional foci connecting the extracellular basement membrane to the intracellular CSK are the costameres (Fig. 4.3): they include integrins and the dystrophin-

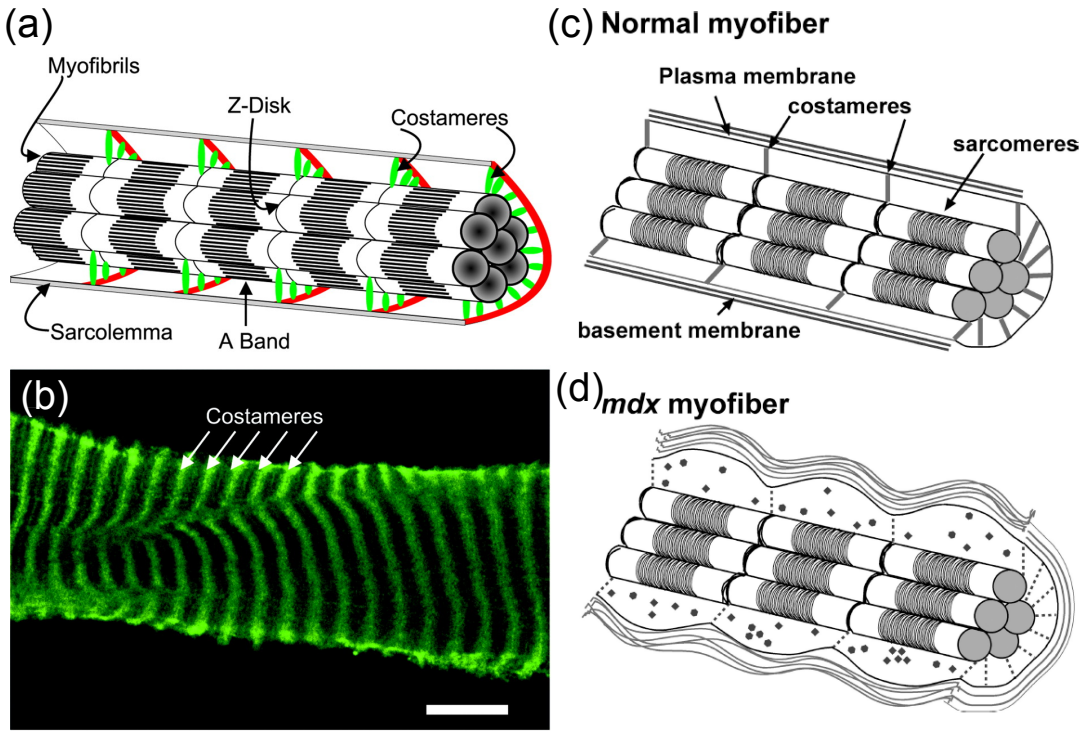

Figure 4.3: **The costameres and their alterations in dystrophin-deficient myofibers.** (a) Schematic representation of the costamere location in a myofiber. (b) Immunoflourescence staining of γ-actin on a mouse myofiber sarcolemma revealing the costamere organization. Scale bar: 10 μm. Schematic representations of normal (c) and dystrophin-deficient *mdx* (d) mouse myofibers. The absence of dystrophin causes costamere disorganization, membrane fragility and permeability with consequent augmentation of Ca^{2+} (filled circles) and reactive oxygen species (diamonds). Figure (a) and (b) were adapted from Journal of Biological Chemistry [Ervasti, 2003]; (c) and (d) were adapted from The Journal of General Physiology [Goldstein & McNally, 2010].

associated protein complex (DAPC). Costameres are aligned with the Z-disks and provide the physical connections between myofibrils, the plasma membrane and the ECM. Costameres have been proved to play a fundamental role not only in the transmission of forces between these compartments, but also in the spatial organization of the myofibrils, in maintaining the myofiber integrity and in signalling pathways. The importance of well-organized costamere foci for muscle function was already clear 13 years ago, when Ervasti [Ervasti, 2003] defined the costamere as the Achilles' heel of skeletal muscles; indeed a high number of disorders are caused by the alteration of costamere components, and such alterations have severe consequences on muscle function. More information about dystrophin, DAPC and costameres will be provided in Section 4.3.2. In summary, a phenomenon as complex as muscle movement and strength are the results of multi-scale, multi-systemic well-organized events that require a better knowledge of each component.

4.2 Overview of neuromuscular diseases and muscular dystrophies

The term neuromuscular diseases (NMDs) encompasses a broad variety of diseases that affect muscle function either directly or indirectly *via* some nervous system/NMJ disorders. Many neurodegenerative diseases do impair the proper function of NMJs, *e.g* amyotrophic lateral sclerosis (ALS) [Boillée, 2006] and spinal muscular atrophy (SMA) [Monani, 2005]. Although NMDs affect roughly 1 % of the population, in most cases, multi-system disorders cause severe clinical conditions [McDonald, 2012]. The main functions of the skeletal muscles were discussed in Section 4.1. Concerning their energy regulatory role, when the body metabolism is unbalanced, for example in the case of some types of cancer, there is a higher energy expenditure relative to the food intake (catabolic wasting) and the muscles experience a severe mass loss [Takemura, 2016]. The loss of muscles accompanying chronic non-muscle diseases is defined as cachexia. Cachexia is an example of secondary muscle disorder related to another pathology. Physiological muscle contractile activity drives it progressively to chronic mechanical and chemical stresses [Tabebordbar, 2013]. Thus, it is not surprising that muscle tissues have their own repair and regenerative mechanisms in addition to those ubiquitous. The muscle regeneration process and the role of satellite cells were discussed in Chapter 3. Membrane repair processes occur in several cell types but they are particularly important in muscles since membrane dysfunctions may cause dystrophic disorders. When small (around 1 μm diameter) membrane lesions take place, the subsequent increases of oxidative agents and intracellular calcium induce a membrane patching mechanism that involves vesicles and SNARE proteins similarly to exocytosis [McNeil & Steinhardt, 2003; Tabebordbar, 2013].

As for other type of diseases, myopathy settles when the damage and the repair mechanisms get unbalanced, leading to a perturbation of normal homeostasis (steady state), which compromises in turn the normal muscle function. More than 100 human NMDs have been identified, as characterized by muscle degenerative impairment and weakness [Tabebordbar, 2013]. According to the etiological factors, neuromuscular disease can be classified in two main groups: "acquired" and "genetic" (inherited) myopathies. Acquired muscle diseases are caused by disparate environmental factors such as infection, injury, too high or too low temperature, poison myotoxins, ischemia/reperfusion damage, improper lifestyle, nutritional deficiencies or excesses, chemical and physical stresses, ... Although the causes can be drastically different, all these factors can lead to muscle cell necrosis [Gutiérrez & Ownby, 2003; Riedemann & Ward, 2003; Tabebordbar, 2013]. For example, among the causes linked to an improper lifestyle, an excessive or inappropriate muscle exercise can lead to the so-called contraction-induced damages [Dalakas, 2011]. Contraction-induce injuries are characterized by myofilament disorganizations, T-tubule damages [Morgan & Allen, 1999] and sarcomere disruptions which may lead to necrosis and local inflammation [Tabebordbar, 2013]. Inflammation itself can be an etiological factor of inflammatory myophaties characterized by chronic, subacute or acute muscle pathology. Inflammatory myophaties are also acquired and treatable [Dalakas, 2011]. Interestingly, if on the one hand excessive muscle activity can cause muscle damages, on the other hand muscle disuse or denervation may cause muscle atrophy (*i.e.* decrease of myofiber size), which can be restored over time with exercise. After development, the number of fibers remains constant because a muscle is made of post mitotic tissues. However, from adulthood to the senescence, the body experiences a dramatic but physiological decrease of muscle mass, from 50 % to 25 % of the total body weight [Romanick, 2013]. Sarcopenia is the term used for muscle loss and weakness

normally observed in aged people because of hormonal and metabolic changes [Rosenberg, 1997; Kalyani, 2014]. Sarcopenia is characterized by a loss of both fiber size and number, along with some weakening of muscle strength. This situation can be aggravated by the concomitance of several chronic diseases [Kalyani, 2014] such as diabetes [Sandri, 2006], obesity [Stenholm, 2009], hyperthyroidism [Riis, 2005], hypercortisolism [Schakman, 2008], vitamin D deficiency [Pfeifer, 2002], hypogonadism [Maggio, 2011] and osteoporosis [Terracciano, 2013]. The most common acquired NMDs are neurophaties including amyotrophic lateral sclerosis (ALS), poliomyelitis, Guillain Barre syndrome, myasthenia gravis, and polymyositis [McDonald, 2012]. Genetic NMDs include spinal muscular atrophy (SMA), Charcot Marie Tooth disease, congenital myasthenia, and Duchenne muscular dystrophy [McDonald, 2012]. Among genetic myophaties, more than 30 congenital myopathies and muscular dystrophies were identified together with several metabolic myopathies.

The term muscular dystrophies (MDs) refers to an heterogeneous group of genetic degenerative neuromuscular disorders, primarily affecting skeletal and cardiac muscles. MDs are characterized by progressive muscular weakness and wasting. Mutation of a gene encoding for either dystrophin, or any other members of the dystrophin-associated protein complex (DAPC, see Section 4.3.2), ECM or the nuclear envelope can cause inherited muscular dystrophies, *e.g.* limb-girdle muscular dystrophy and congenital muscular dystrophy [Blake, 2002; Dalkilic & Kunkel, 2003; Lovering, 2005]. In most cases the mutation affects genes encoding for structural proteins. MD phenotype, characterized by (i) a reduced level of dystrophin and other DAPC proteins and (ii) an increased expression of utrophin, can be caused by mutations of dystrophin transcription regulating proteins such as the mammalian target of rapamycin (mTOR) [Risson, 2009]. MD patients display structural and functional alterations of different muscles: membrane fragility, alteration in myofiber size and infiltration of non-muscle tissues (*e.g.* fatty and connective tissues) [Dalkilic & Kunkel, 2003]. Different gene mutations cause impairment of different muscles at different periods of life with variable severity. MDs were initially classified according to clinical phenotypes before a molecular classification was established. In parallel, to progress in biochemical and molecular analysis methods, the diagnosis of muscular dystrophies also benefited from the increased number of identified MD-correlated gene mutations. The next Section 4.3 is aimed at describing the fundamental pathological aspects of the most severe and common MD: the Duchenne muscular dystrophy (DMD, OMIM 310200).

4.3 The Duchenne muscular dystrophy (DMD)

Although there is evidence of typical clinical manifestations of the DMD in Egyptian wall paintings, the scientific interest in this genetic disease started about 200 years ago, when physicians such as Charles Bell (1830), Gaetano Conte (1836), Mr Padrige (1847) and Edward Meryon (1852) reported some DMD clinical cases [Emery, 2015]. In 1868, Duchenne described for the first time the disease progression on 13 patients, taking into account the histological feature evolution. Duchenne main innovation was the use of muscle biopsy of living patients. From his observations, DMD patients exhibited progressive muscle weakness, initial hypertrophy and subsequent atrophy [Duchenne, 1868]. Over the years, DMD kept on fascinating the scientific community, receiving the emblematic definition of "one of the most interesting and at the same time most sad" disease [Gowers, 1879]. The main breakthrough in DMD research was achieved in the eighties, when among several groups working intensely on the DMD genetics, the Luis Kunkel's laboratory discovered the dystrophin gene (*DMD*) location and its sequence

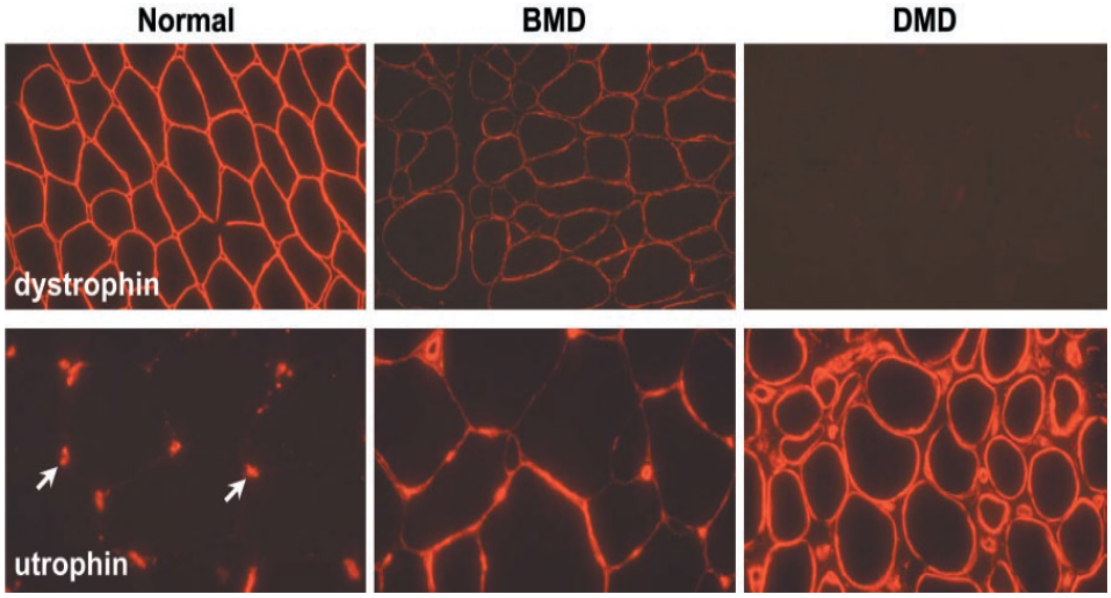

Figure 4.4: **Dystrophin and utrophin location in normal, BMD and DMD muscles.** Immuno-staining of dystrophin (first row) and utrophin (second row) in human muscle biopsy transverse sections in healthy, Becker (BMD) and Duchenne (DMD) tissues. White arrows mark utrophin accumulation in extra-muscular tissues (*i.e.* capillaries of endomyosium). Adapted from Physiological Reviews [Blake, 2002].

using inverse genetics [Kunkel, 2005]. After accumulated efforts, the dystrophin gene was fully characterized: *DMD* is the largest gene in the human genome accounting for about 1 % of the DNA (approximately 2.5 megabases). Located in the short arm of chromosome X at locus 21 (Xp21), *DMD* contains 4 domains and 79 exons [Roberts, 1993; Muntoni, 2003]. The discovery of the dystrophin gene sequence generated enthusiasm in the myology community and permitted the production of antibodies against the dystrophin protein which was finally localized in the intracellular side of the cell membrane [Hoffman, 1987; Watkins, 1988]. Among several scientists who played an important role in the DMD research, Peter Emil Becker deserves some credit for his identification of a more benign form of DMD [Becker, 1962], named the Becker muscular dystrophy (BMD, OMIM 300376). The progressive and lethal DMD kept passionating the scientific (medical) community and over decades a lot of efforts and progresses were made concerning the molecular bases of this disease. Although these findings improved significantly our understanding of DMD and its diagnosis, the DMD pathogenesis leading to progression of the disease is still not completely understood. If DMD patient life expectancy and quality of life have been ameliorated, the therapeutic strategy is still palliative and current therapies cannot prevent DMD patient premature death.

4.3.1 DMD etiology and epidemiology

DMD is an inherited recessive disease caused by the mutation of the dystrophin gene, which leads to dystrophin deficiency in the great majority of cases. In BMD, a milder phenotype is observed with a decreased quantity of truncated semi-functional dystrophin: dystrophin syn-

thesis occurs but the protein exhibits a lower molecular weight due to some damages. Since the dystrophin gene is located in the X chromosome, in most cases DMD disease is carried but not expressed in females (single copy of the gene mutation) whereas males express the disease [Hoogerwaard, 1999]. Only occasionally (8%) females are manifesting carriers showing DMD mild forms because of the physiologic X chromosome inactivation [Song, 2011]. This inactivation, also known as lyonization, prevents double X chromosome product assembly in female placenta by random inactivation of one gene (*i.e.* heterochromatin packaging of the silenced X chromosome). DMD therefore affects almost exclusively males during childhood and it represents $\sim$ 50 % of all dystrophy cases. Both DMD and BMD are caused by heterogeneous genotypes carrying different mutations in the dystrophin gene (*DMD*). In most cases, a DMD (resp. BMD) phenotype is due to one or more exon deletions in the *DMD* that cause (resp. do not cause) the disruption of the reading frame in the spliced mRNA; such a transcript leads to truncated non functional (resp. smaller semi-functional) dystrophin protein [Hoffman, 1987; Monaco, 1988; Carsana, 2005; Bladen, 2015]. Over two thirds of the DMD and BMD mutations are intragenic deletions and duplications [Den Dunnen, 1989; Carsana, 2005; Tayeb, 2010]. The DMD patient studied in this thesis carries intragenic deletions of exons 48-52 in the dystrophin gene. These exons correspond to a central *DMD* region, which contains exons from 45 to 53 and encodes the amino acids 2146-2624 of the dystrophin protein [Carsana, 2005]. In particular, the dystrophin protein amino acids encoded by the 48-52 exons are part of the rod domain (ROD) of the dystrophin enclosing its third hinge (HIII) domain. Deletions of 45–52 exons of *DMD* locus are known to carry premature stop codons and to produce DMD phenotype with undetectable levels of dystrophin in muscle cells [Maggio, 2016]. Note that an *ex novo* mutation has been reported in 30 % of the cases [Garcia, 2014]. DMD incidence, defined as the rate of new case emergence, was estimated in the range from 9.6 to 39 per 100,000 newborn males (or 1:3500) as compared to 1.3 to 1.7 per 100,000 males for BMD [Emery, 1991]. More recently, Mah *et al.* [Mah, 2014] using MEDLINE and EMBASE databases, found that DMD population-based incidence varied between 10.71 and 27.78 per 100,000 males in Europe and North America. They further estimated the prevalence (*i.e.* effective number of living cases) of DMD (resp. BMD) to be 4.78 (resp. 1.53) per 100,000 males. These findings confirm the higher prevalence and incidence of DMD compared to BMD, and suggest a possible overestimation of the DMD incidence in the past decades.

4.3.2 Dystrophin location and function in myofibers and myoblasts

To discuss the DMD pathogenesis, *i.e.* the mechanism whereby the dystrophin gene mutation leads to disease, it is necessary to know the location and the function of the dystrophin protein. Dystrophin is a 110 nm long rod-shaped protein of 427 kDa largely expressed in skeletal and cardiac muscles, as well as in smooth muscles and in brain but in smaller quantities [Hoffman, 1987]. Utrophin is an autosomal homologue of dystrophin with similar structure and function [Love, 1989]. Utrophin is expressed ubiquitously in human adults with higher levels in kidney, liver, lung, stomach, muscles, and brain, fulfilling the same connective role as dystrophin. In normal muscles, utrophin was observed to be associated with nervous and vascular systems (Fig.4.4). In adult skeletal muscle tissues, utrophin has a different location than dystrophin. In particular, it accumulates in proximity to the NMJs in the postsynaptic sarcolemma folds in association with AChRs [Haenggi & Fritschy, 2006] and close to myotendinous junctions [Nguyen, 1991; Blake, 2002]. Over-expression of utrophin in extra-junctional sites is observed in

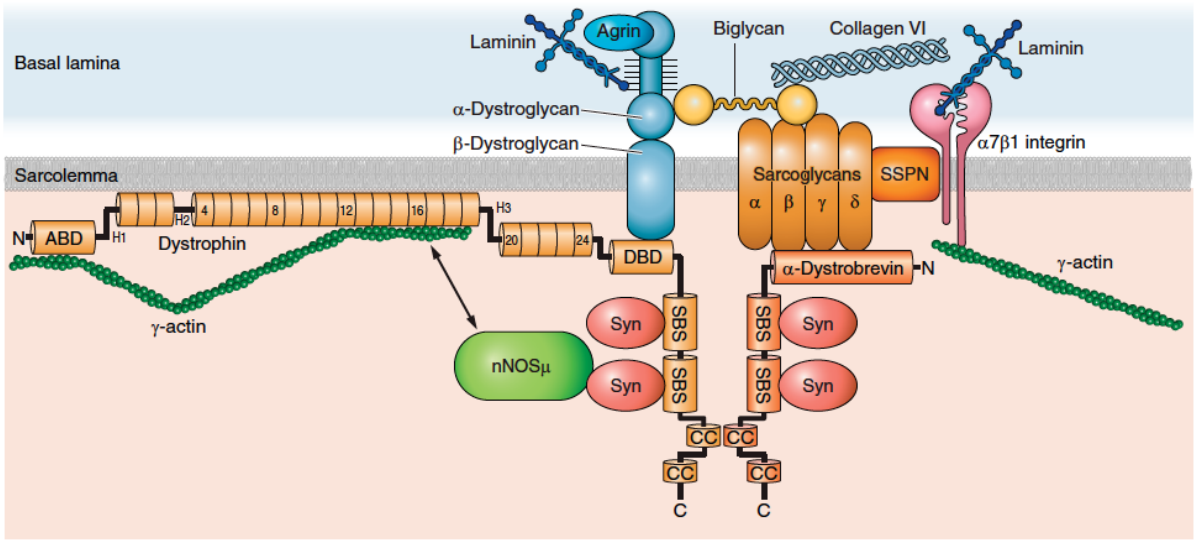

Figure 4.5: **Dystrophin and dystrophin-associated protein complex (DAPC).** Schematic representation of the multi-proteic DAPC complex and the interaction between its components. Dystrophin binds (i) γ-actin with its actin binding domain, (ii) β-dystroglycan *via* its dystroglycan binding domain, and (iii) syntrophin *via* its syntrophin binding sites. Legend: Syn=syntrophin; SSPN=sarcospan; ABD=actin binding domain; DBD=dystroglycan binding domain; SBS=syntrophin binding site; CC=coiled-coil domain; N=amino terminus; C=carboxy terminus. Adapted from Physiological Reviews [Allen, 2016].

certain myophaties, such as BMD and DMD (Fig.4.4).

As sketched in Fig. 4.5, dystrophin bridges the intracellular CSK F-actin with the ECM *via* the DAPC sarcolemma complex in striated skeletal muscle cells. In other words, dystrophin mechanically couples the sarcomeres to the costameres. Although dystrophin was originally defined as a simple structural protein, over time it was shown to be a key member of DAPC. DAPC includes several integral membrane glycoproteins such as dystroglycans, sarcoglycans, integrins, caveolins, dystrobrevins, syntrophins and sarcospans [Campbell & Kahl, 1989; Cohn & Campbell, 2000; Constantin, 2014; Allen, 2016; Chang, 2016]. In particular, dystrophin binds (i) F-actin with its amino terminus and (ii) dystroglycans at the plasma membrane *via* its carboxyl terminus [Blake, 2002]. Dystroglycan complex is connected in turn to the extracellular basal lamina through laminin. The integrity of this multimeric protein complex depends on the structural support of dystrophin; it has been shown that the absence of dystrophin causes the instability of DAPC and the decrease of the number of its components (Section 4.3.4). Because of its configuration, structure and location, the multi-protein DAPC complex is involved in several vital cellular processes. First, DAPC accumulation at costameres ensures mechanoprotection and structural integrity of the sarcolemma. Perturbations of DAPC lead to membrane leakage and altered permeability. DAPC is also thought to be the muscle compartment equivalent to the non-muscle cell focal adhesion sites; thus, it may have a role in mechanosensing, force transmission and transduction during muscle contraction. Moreover, *via* its participation in transmembrane signalling, DAPC plays also a role in the homeostasis maintenance of the intracellular composition [Constantin, 2014]. Notably, as shown in Fig 4.5, several molecular actors of the dystrophin signalling pathway are anchored to the DAPC; among them syntrophins partici-

pate to the recruitment and regulation of several signalling proteins involved in the maturation of NMJs during regeneration through sodium and calcium voltage-gated channels [Hoshino, 2001]. β-dystroglycans are instead involved in the activation of the Rac1 and PAK1 pathways. Dystrophin mechanical role has been clarified: during muscle contraction, dystrophin is necessary to stabilize the sarcolemma and to absorbe mechanical shocks. DMD myofibers show indeed muscle injuries after forced lengthening contractions (*i.e.* eccentric contractions) [Pestronk, 1982; Moens, 1993; Petrof, 1993; Deconinck & Dan, 2007]. These mechanoprotection functions are also due to the recently discovered direct interactions of dystrophin with the membrane phospholipids and the CSK [Le Rumeur, 2010]. In muscle fibers, dystrophin and DAPC accumulate particularly near the neuromuscular and muscle-tendon junctions, stabilizing the membrane through its CSK connections and organizing the distribution of DAPC glycoproteins. It was believed that satellite cells (SCs) were lacking dystrophin, and that the impaired myogenic activity in muscle regeneration observed in DMD patients was caused by an excessive regeneration demand causing stem cell exhaustion [Sacco, 2010]. However, dystrophin was recently shown to be expressed in SCs, especially before undergoing cell division [Dumont, 2015]. Dystrophin was further shown to be critical for the initiation and establishment of the cell polarity, and in turn for the myoblast asymmetric cell division [Ono, 2015]. This type of cell division induces one of the two daughter cells to behave as a progenitor cell (myogenic-committed) while the other one stays as a self-renewing satellite stem cell (not myogenic-committed). The impairment of cell polarization impacts several cellular processes, such as cell migration and cell differentiation which are essential for development and regeneration. Moreover cell polarization incapability has been associated with tissue disorganization and diseases, including cancer [Martin-Belmonte & Perez-Moreno, 2012]. Concerning the impairment of muscle regeneration in DMD patients, the loss of polarity of satellite cells was shown to limit the number of progenitor muscle cells and so myogenesis [Chang, 2016].

4.3.3 Comparison of the cross-linking complexes at the extracellular and nuclear membranes

A wide variety of organisms have syncytia (multinucleated cells), which are formed either when multiple nuclear divisions occur without cell divisions or as a result of cell fusion. Normally, syncytial nuclei are located in specific regions or evenly spaced through the cytoplasm. For instance, a vertebrate myotube has hundreds of nuclei; most are evenly spaced apart; however, a group of 4-8 nuclei clusters at the neuromuscular junction. A correct positioning of these nuclei is therefore very important for both the development and function of the muscle. Two related processes are required to control the specific positioning of these nuclei. First, nuclei must migrate through the cytoplasm to the appropriate positions, and then they must be anchored at that position so they do not drift. These processes are controlled by a combination of forces from microtubule and actin-based networks. The microtubule network is well-known for its active role in positioning the nucleus [Reinsch & Gonczy, 1998; Dupin & Etienne-Manneville, 2011]. Less documented are the roles of the actin and intermediate filament networks in that issue [Starr & Han, 2002; Gundersen & Worman, 2013; Luxton, 2014].

We have previously described the role of dystrophin and its associated dystrophin-glycoprotein complex (DAPC) in connecting the actin cytoskeleton to the extracellular matrix; mutations in any of these components lead to Duchenne or Becker muscular dytrophies. The Syne/ANC-1 anchors have been proposed to directly tether the actin cytoskeleton to the nuclear envelop [Starr

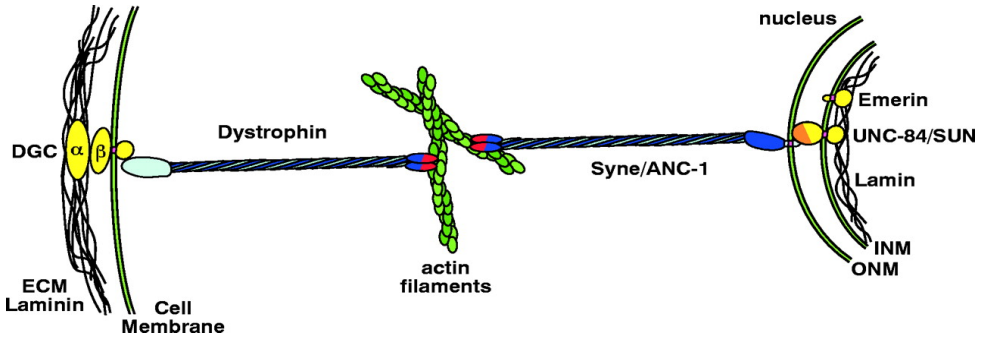

Figure 4.6: **Comparison of dystrophin-glycoprotein complex (DGC or DAPC) and nuclear Syne/ANC-1 and their connection with actin.** Is there a potential role for Syne/ANC-1 in Muscular Dystrophy? This model points out the similarities between the mechanisms of Syne/ANC-1 and dystrophin. Both of these huge proteins bind to actin through N-terminal calponin domains, and extend spectrin repeats through the cytoplasm. They both function as part of a bridge across membranes. Mutations in many of these components lead to muscular dystrophy. Adapted from Journal of Cell Science [Starr & Han, 2003].

& Han, 2003]. It is quite intuitive to compare these two cross-linking mechanisms since their bear striking similarities (Fig. 4.6). Dystrophin and Syne/ANC-1 both bind to actin through an N-terminal CH domain and extend through the cytoplasm towards the plasma or nuclear membranes, respectively. Through their associated proteins, DAPC on the plasma membrane and UNC-84/SUN on the nuclear membrane, dystrophin and Syne/ANC-1 eventually connect to related underlying matrices, either the basement membrane component laminin or the nuclear lamina. As compared to dystrophin which does not have a predicted transmembrane domain, Syne/ANC-1 could circumvent the problem of the double membrane at the nuclear envelope by using its own transmembrane domain to pass through the outer nuclear membrane. It is therefore very likely that this whole complex plays a major role in the positioning of some of the myonuclei beneath the postsynaptic membrane at the NMJ. Actually, only 1% of the muscle fiber surface is synaptic, it is therefore necessary that a concerted mechanism recruits several nuclei in the neighbourhood of the postsynaptic membrane. The sorting and confinement of the larger and rounder nuclei suited for the synthesis of synaptic proteins (such as subunits of the acetylcholine receptor AChR) are controlled by the motoneuron through the proteoglycan agrin and its receptor MuSK (muscle specific tyrosine kinase) which is concentrated in the postsynaptic membrane [Apel, 2000]. Facing the postsynaptic membrane at the NMJ, the nuclear envelope protein Syne-1 was shown to be concentrated in the synaptic nuclei. This protein possesses a group of dystrophin-like spectrin repeats and is associated with the nuclear envelope in skeletal, cardiac and smooth muscle cells. Its similarities with the Klarsicht protein involved in nucleus migration suggest that Syne-1 should play the same role in myotubes. The repositioning of nuclei from center to periphery is predominant for muscle maturity since it conditions the transition from myotube to myofiber transition.

4.3.4 DMD pathogenesis, structural alterations and clinical manifestations

In DMD patients, the absence of dystrophin at the cellular level causes some abnormality of the DAPC which manifests in a decreasing number of its components that experience some degradation by proteasome pathways [Straub & Campbell, 1997]. DAPC and dystrophin were

originally considered as structural compartments. Recently, Allen *et al.* [Allen, 2016] studied DMD early pathogenesis considering the DAPC role in cell signalling. It is clear nowadays that impaired DAPCs cause some membrane mechanical weakening and some permeability increase because of their fundamental role in cell membrane structure and signalling. In most DMD cases, alterations in the calcium transport have been invoked: excessive calcium entry into the cell induces chronic hypercontractile activity, and increased release of creatine kinase (CK) [Cullen & Fulthorpe, 1975; Bodensteiner & Engel, 1978; Blake, 2002; Allen, 2016]. CK is a muscle enzyme that normally increases in blood after exercise (*i.e.* hyperCKemia), together with lactate dehydrogenase (LDH). HyperCKemia is recognized as a marker of muscle damage and is generally observed in DMD and other neuromuscular disorder (NMD) patients. Increased levels of the nitric oxide (NO) and reactive oxygen species (ROS) have also been detected in DMD muscles [Allen, 2016]. NO synthesis is due to the calcium-dependent activation of nitric oxide synthases (NOS), whom the muscle tissue isoform is nNOSμ. ROS synthesis are likely activated by stretch and have a role in the progression of the membrane leakage and calcium intake. Increased level of ROS induces an augmentation of Ca^{2+} and *vice versa*. Moreover, it has been shown that antioxidant treatments can reduce membrane damage following eccentric contractions, cell necrosis and hyperCKemia in *mdx* myofibers [Hnia, 2007; Whitehead, 2008; Tonon, 2012]. The *mdx* mice are one of the mostly used DMD animal model which lacks dystrophin expression and shows a milder phenotype compared to human DMD patients [Durbeej & Campbell, 2002; Willmann, 2009]. Perturbations of the MT compartment (denser and less organised network) were observed in *mdx* myofibers [Prins, 2009]. This disorganization is involved in the Ca^{2+} and ROS signalling alterations [Khairallah, 2012]. Although the complete damage pathways are still debated, it is widely recognized that the alteration of the intracellular calcium concentration induces progressive myofiber damages [Blake, 2002].

At the tissue level, the absence of dystrophin produces muscle degeneration with downstream events such as inflammation, fibrosis and adipose tissue infiltrations. Impairment of muscle regeneration and membrane repair plays a central role in DMD pathogenesis and progression [Wallace & McNally, 2009; Ciciliot & Schiaffino, 2010; Dumont, 2015]. Satellite cell (SCs) differentiation is activated in DMD myofibers due to the muscle inflammation and myofiber necrosis, but the so-produced myotubes do not fuse efficiently, leading to an increased fragility of the myofibers [Head, 2010; Chan & Head, 2011]. Thus, although an exceptionally high number of SCs was observed in DMD patients, in particular in advanced stages of the disease, the muscle regeneration was impaired [Kottlors & Kirschner, 2010; Bankolé, 2013]. The same increased number of satellite cells was found in *mdx* mice as compared to wild type mice [Dumont, 2015]. The failure of DMD muscle repair in due to the ineffectiveness of dystrophin-deficient SCs to establish cell polarity which impairs their asymmetric division leading to an insufficient number of myogenic committed myoblasts [Chang, 2016] (Fig. 4.7). If the SC fate is still not understood, their cell polarity incompetence could explain the degeneration of non-muscle tissues as the brain in DMD patients. These recent findings open new therapeutic strategies targeting the polarity inability of SCs [Shi, 2013]. Moreover, the inability of muscle regeneration likely induces prolongation and intensification of the symptoms, thereby explaining the degenerative nature of this disease.

At the organ level, muscular fragility and weakness have been observed in DMD patients, with unbalance between muscle damage and regeneration causing muscle wasting. Also progressive inflammation leads to muscle function failure. After contraction-induced injury, anomalous muscle weakness was found in DMD muscles due to structural and signalling affections [Lovering,

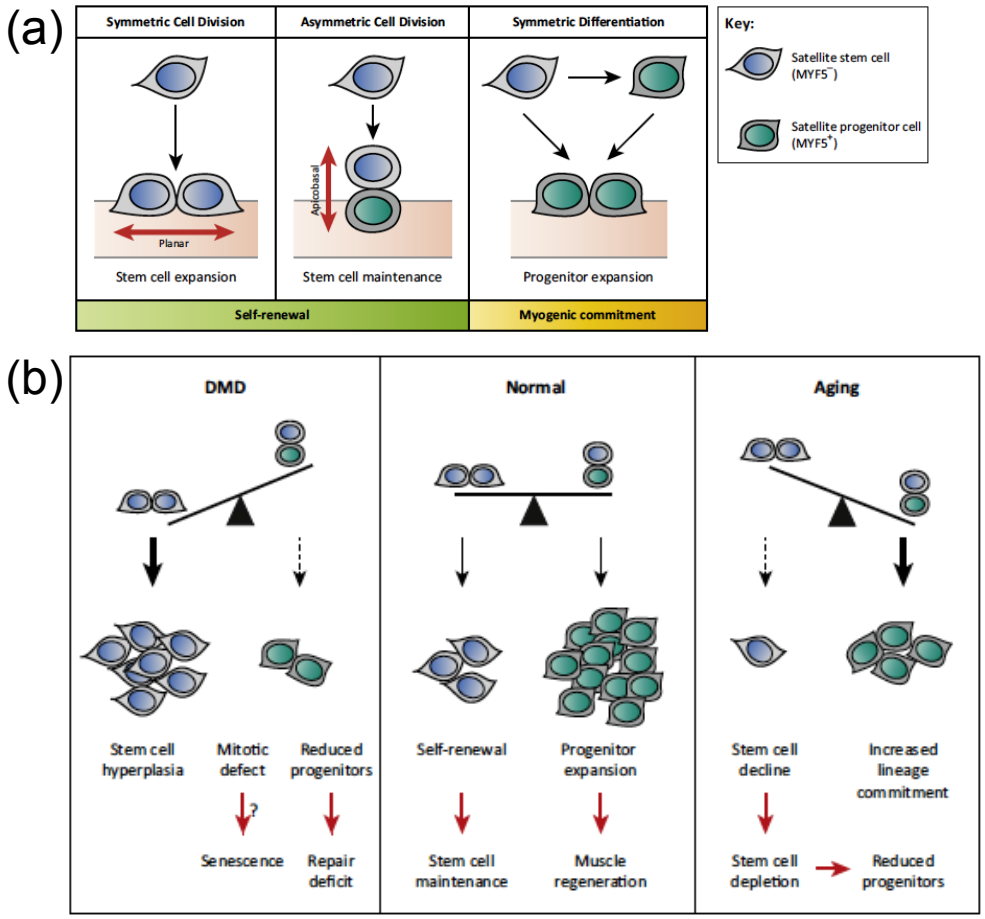

Figure 4.7: **Mechanism of satellite cell division in normal, dystrophin-deficient and aging conditions.** (a) In normal conditions, activated satellite cells divide by symmetric and asymmetric mechanisms in order to maintain the stem cell population and to produce progenitor cells. (b) In DMD, the impairment of asymmetric satellite cell division causes an unbalance between the two division modes which leads to stem cell hyperplasia, reduced progenitors and muscle repair deficit. Adapted from Trends in Molecular Medicine [Chang, 2016].

2009]. NMJ disruption and neuromuscular transmission dysfunction was also observed in DMD and *mdx* mice [Willmann, 2009]. Worsening of structural alterations of NMJs (dispersion of both motor end-plate and AchRs) in *mdx* mice after *in vivo* injury was reported by Pratt *et al.* [Pratt, 2013] with a longer time necessary for muscle force recovery as compared to wild type [Pratt, 2015]. Progressive bone fragility was observed in DMD patients, probably related to decreased muscle motility. Bone demineralization comes along with NMD-related muscle weakness [Hsu, 1981], and this particularly in DMD patients where the disease progression is accompanied by a progressive decrease of the bone density leading to osteoporosis and in turn to a higher predisposition to fractures [McDonald, 2002; Bianchi, 2003; Söderpalm, 2007; Nakagaki & Camilli, 2012].

At the organism level, DMD causes multi-systemic disorders: skeletal, smooth and cardiac muscle dysfunctions, alterations of NMJ, cardiac, respiratory and skeletal complications, and occasionally slight impairment of cognitive functions [Yanagisawa, 2009; McDonald, 2012]. The natural history of DMD patients has been largely reported [Jennekens, 1991; Blake, 2002; Emery,

2015]. DMD newborns are clinically normal until they reach 2 - 5 years, when the first symptoms appear in the form of mobility difficulties. Generally in the following years pseudo-hypertrophy of calf muscles and lower limb weakness become visible, as illustrated in Fig. 4.8 for a 7 year old boy. Progression of limb muscle weakness eventually leads to the confinement in wheelchair

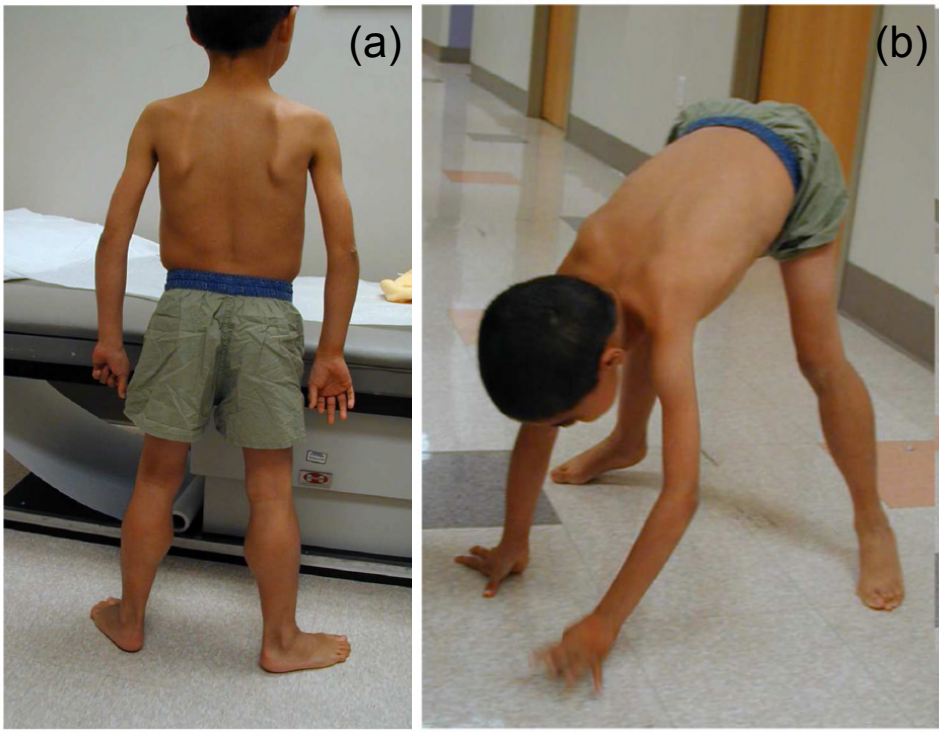

Figure 4.8: **DMD clinical manifestations in childhood.** (a) A seven year old child with typical DMD clinical manifestations: calf hypertrophy, shoulder retraction, scapular winging and equines posturing at the ankles. (b) The same child showing the Gowers' sign: the necessity of using arms to stand up from squatting position because of the limb weakness. Adapted from Physical Medicine and Rehabilitation Clinics [McDonald, 2012]

of the DMD patients before the age of 12 because of the loss of mobility. Disease progression results also in arm weakness. Once the DMD patients are wheelchair-bound, worsening of the musculoskeletal organization and function can cause orthopedic complications such as scoliosis. Thoracic scoliosis curvature aggravates respiratory conditions which may be fatal in patients having already pulmonary critical problems [Hoffman, 1987]. Most DMD patients die in their early twenties due to either chronic respiratory insufficiency (*e.g.* pneumonia) and/or cardiac failure. BMD progression and natural history present the same symptoms and dysfunctions but with later onset and less severe complications; 90 % of BMD patients are alive in their twenties, in some cases they keep a motor activity until mild or late adulthood, and they have a longer life expectancy.

4.3.5 DMD diagnosis and treatment

To distinguish different forms of DM, clinicians need to investigate the patient family history, and to proceed to different musculoskeletal, neurologic and functional exams before suggesting more specific investigations. These informations are very useful to interpret muscle/nerve biopsies and molecular genetic analyses, and thus for the final diagnosis [McDonald, 2012]. The

distinction between BMD and DMD was initially made by observing the patient phenotype and his different clinical manifestations, *e.g.* the later BMD onset and the fact that this form of dystrophy allows mobility until 16 years of age or later. As for other muscular dystrophies, the DMD diagnosis has been improved over the last few decades thanks to biochemical and molecular progress. Because specific disorders present several subtypes and genetic heterogeneity, gene mutation identification is not sufficient to diagnose the specific MD [Kaplan & Hamroun, 2013]. For DMD diagnosis, after the observation of the typical clinical manifestations in children, the complete clinical diagnosis involves different tissular and cellular techniques: (i) blood analysis showing from 50- to 200-fold higher level of CK as compared to standard values; (ii) histological analysis of muscular biopsy revealing typical dystrophic features such as necrosis, muscle degeneration and abnormal regenerative myofibers; (iii) immuno-histochemical analysis displaying total absence of dystrophin, and (iv) genetic screening showing deletion of the DMD gene in most cases.

Once accurate diagnosis is performed, patients are informed about prognosis, natural history of the disease and eligibility for molecular-based therapy such as antisense oligonucleotides or stop codon read-through drugs [McDonald, 2012]. Besides research strategies of clinical trials, DMD therapy currently treats symptomatic downstream events in order to improve life conditions and life expectancy. Since these downstream events affect several systems, the treatment is also multi-systemic : (i) orthopedic, to maintain the ambulatory ability as long as possible and to stabilize the spine affected by scoliosis (physiotherapy, fitting with prosthesis, ...); (ii) respiratory, to prevent and treat infections and to preserve a sufficient respiratory function (ventilation, respiratory physiotherapy, ...); (iii) cardiac (ACE inhibitors and heart protection). Currently, glucocorticoids are one of the mostly used drugs for DMD patients in order to reduce inflammation and to inhibit the immune system response [Manzur, 2008]. Other anti-inflammation drugs used in DMD are TNF-α inhibitors and the cytokine osteopontin, specific against harmful inflammation and fibrosis pathways [Vetrone, 2009; Ermolova, 2014]. Antioxidants are also used in DMD treatment to reduce oxidative damage and necrosis of muscles [Pinto, 2013].

The ongoing research for DMD therapy embraces a wide range of different approaches aiming at treating etiological factors [Partridge, 2011; Tabebordbar, 2013]. Because of their role in the DAPC member degradation, the inhibition of proteasome pathways was shown to increase membrane stability [Bonuccelli, 2003]. Recombinant protein-based treatments are under evaluation to improve DMD clinical conditions. Among them, the use of insulin-like growth factor I (IGF-I) to trigger muscle regeneration *via* satellite cell activation has proved efficient in *mdx* mice [Gregorevic, 2002, 2004], as well as laminin-111 [Rooney, 2009] and utrophin [Squire, 2002]. Inhibitors of myostatin which represses muscle growth, have been positively evaluated in humans [Schuelke, 2004]. For a long time transplantation of satellite cells from a healthy donor has been an attractive strategy. The main drawbacks of this strategy are the difficulty of primary cell population expansion *ex vivo* and the early death of a vast majority of the transferred cells [Miller, 1997; Tremblay & Guerette, 1997]. Transplantations of healthy myoblasts or of skeletal muscle-resident stem cells have already been tested in mice [Watt, 1984], dogs [Bartlett, 1990; Robriquet, 2015, 2016; Lardenois, 2016], monkeys [Kinoshita, 1995], rabbits [Boubaker el Andalousi, 2002] and pigs [Holzer, 2005]. Skuk *et al.* [Skuk, 2010] showed that the transplantation of primary human myoblasts from healthy donors in immunodeficient mice, produced donor-derived satellite cells, myofibers expressing human dystrophin and muscle regeneration by human muscle precursor cells. Tremblay *et al.* [Tremblay, 2009] obtained promising results in a phase Ib clinical trial of myoblast transplantation therapy for DMD accompanied by the

well-known immunosuppressor tacrolimus. Although further clinical trials are necessary to establish the best method, the cell-based therapy and in particular the transplantation of primary myoblasts from healthy donors to myophatic patients represents one of the most promising emerging therapy because of its low risk-to-benefit ratio as compared to other strategies [Skuk, 2004; Black, 2015; Dumont & Rudnicki, 2016]. Recently, several clinical trials of gene-based therapies have been evaluated [Aartsma-Rus & Muntoni, 2013; Fairclough, 2013; Hoffman & Connor, 2013; Rodino-Klapac, 2013]. Most of the tested gene therapies involve the replacement of the dystrophin gene or the repair of its mutation: retroviral transduction, Clustered Regularly Interspaced Short Palindromic Repeats (CRISPR-Cas9) genome editing, liposomes, transposons, ... [Chamberlain, 2002; Allen, 2016]. One of the main issues of this strategy is the huge size of the DMD gene. Adeno-associated viral (AAV) gene therapy was successful in inducing expression of a smaller dystrophin in *mdx* mice ameliorating DMD symptoms [Harper, 2002; Watchko, 2002]. However, in children the expression of this mini-dystrophin was scarce and not permanent [Mendell, 2010]. Sequence-specific nucleases *via* CRISPR-Cas9 adenoviral vectors coupling with transcriptional activator-like effector nucleases (TALENs) have recently succeeded with 37 % of DMD gene expression in human myoblasts [Maggio, 2016]. One of the most promising gene-based therapy is the exon-skipping approach: this strategy involves the use of an anti-sense oligonucleotide which blocks the translation of unwanted exons *via* their binding to specific exons of the RNAm coding for dystrophin (*e.g.* the exon 51 which is mutated in about 15 % DMD males), leading to a smaller but functional dystrophin [Hoffman & McNally, 2014]. Another genetic strategy aims at increasing utrophin expression. This strategy has proven to improve the DMD symptoms in *mdx* [Tinsley, 2011], and just begins to be evaluated in DMD. If some critical issues of DMD gene therapy have been resolved, *e.g.* in producing a smaller but functional protein than the huge DMD gene, several difficulties remain to be overcome such as the rather small amount of expressed functional dystrophin and the short duration of this expression [Mendell, 2013].

None of the tested methods have reached the therapeutic efficacy in terms of improving DMD muscle performance in clinical trials. However, very promising research in this domain are constantly being developed (*in vitro*, *ex vivo*, in animal models and in clinical trials).

4.4 Structural and morphological properties of healthy and DMD primary human myoblasts

As discussed in Chapter 3, the use of cell lines in biology research has several advantages such as the lower cost, the better homogeneity of the cells, their unlimited proliferative potential and the possibility of using the same cell line as a biological model in different laboratories. Thus they represent the most suitable biological sample to test experimental protocols and to collect preliminary results. However, cell lines are immortalized and show modified characteristics as compared to *in vivo* cells; for example their genotype and phenotype homogeneity is the result of several culture selective passages and does not reflect the cell variability in original tissues.

Because of their greater similarity with real biological conditions, primary cells (*i.e.* those derived directly from *in vivo* tissues), and in particular primary human skeletal muscle cells (hSkMCs), turn to be a very useful biological model for both physiological and pathological conditions. Primary cell manipulation is essential not only for fundamental research but also for the development of new therapies. In the context of myophaties, and more precisely in

DMD, transplantation of primary myoblasts from healthy donors to patients and myoblasts-mediated gene therapy represent some of the most promising emerging therapeutic approaches (Section 4.3.5). However in current research, hSkMCs are still more rarely used as compared to cell lines because of experimental difficulties inherent to primary cell culture, *e.g* limited proliferative ability and development of a senescent phenotype similar to *in vivo* phenotype in aging conditions [Bigot, 2008; Pääsuke, 2016]. These difficulties pushed to the development of different complementary approaches of human myoblast culture like the development of immortalized cell lines from primary human cells from healthy donors and patients [Pantic, 2016]. It has been recently shown that one can generate pluripotent stem cells (iPS cells) from the de-differentiation of skin fibroblasts and to drive them to functional myoblasts which differentiate in myotubes carrying the *in vivo* disease defect (insulin resistance in type 2 diabetes) [Iovino, 2016]. In DMD research, Choi *et al.* [Choi, 2016] reported concordant but (inter-patient) variable phenotype of human myoblasts generated using human induced pluripotent stem cells (hiPSCs) of DMD patients.

Primary human myoblasts obtained directly from donor biopsies were driven to proliferation and differentiation into functional myotubes [Malatesta, 2013]. Like other primary human cells, primary human myoblasts showed improved proliferation when supplied with hormones, such as human basic fibroblast growth factor (hbFGF), insulin and epidermal growth factor (EGF). Also some types of petri dish coating can improve primary cell adhesion and proliferation. We monitored under the microscope the culture of healthy donor (HD) and DMD primary human myoblasts on standard, collagen- and matrigel-coated petri dishes (Chapter 5) and we observed that, although both types of cells were able to proliferate and adhere on all types of tested supports, the adhesion and proliferation rates were higher in coated petri dishes. Moreover the time required for cell adhesion on culture substrates was lower in coated substrates. Thus we also chose the collagen coated petri dishes (CCPD) for primary human cell studies for better comparison with the results reported for C2C12 myoblasts in Chapter 3.

4.4.1 Morphology of HD and DMD myoblasts

Following the same protocol as for C2C12 cells (Chapter 3), we observed and quantified the morphology of HD and DMD primary human myoblasts on CCPD, as shown in Figs. 4.9 and 4.10 respectively. These optical microscopy images were recorded before AFM experiments and used to position the AFM cantilever tip on the selected cell region. HD myoblasts appear well-adherent on the culture surface, showing a central nucleus and lamellipodial protrusions (Fig. 4.9). Most of the cells exhibit a fusiform shape and a morphology similar to those of C2C12 myoblasts (Figs. 3.12 and 3.13), but they have a larger size. DMD myoblasts are also adherent on the CCPD, but with only few lamellipodial and thin cytoplasmic protrusions (Fig. 4.10). DMD myoblasts display spindle-shape cell body in most cases, with very elongated fusiform cell protrusions. This cell morphology reminds those of C2C12 myoblasts undergoing cell rounding and subsequent mitosis (Figs. 3.1 and 3.3). Note that a significant amount of cellular debris with elongated or rounded shapes are present in DMD as compared to HD myoblasts images.

We performed a quantitative comparison between HD and DMD cell morphologies measuring the same parameters as we did for C2C12 cells (Chapter 3). The results obtained for cellular and nuclear parameters (length, width and area) are reported in Fig. 4.11, together with those of C2C12 myoblasts for comparison. Primary human myoblasts are slightly longer and show a significantly greater cell area compared to C2C12 murine cells. Importantly, cell length and

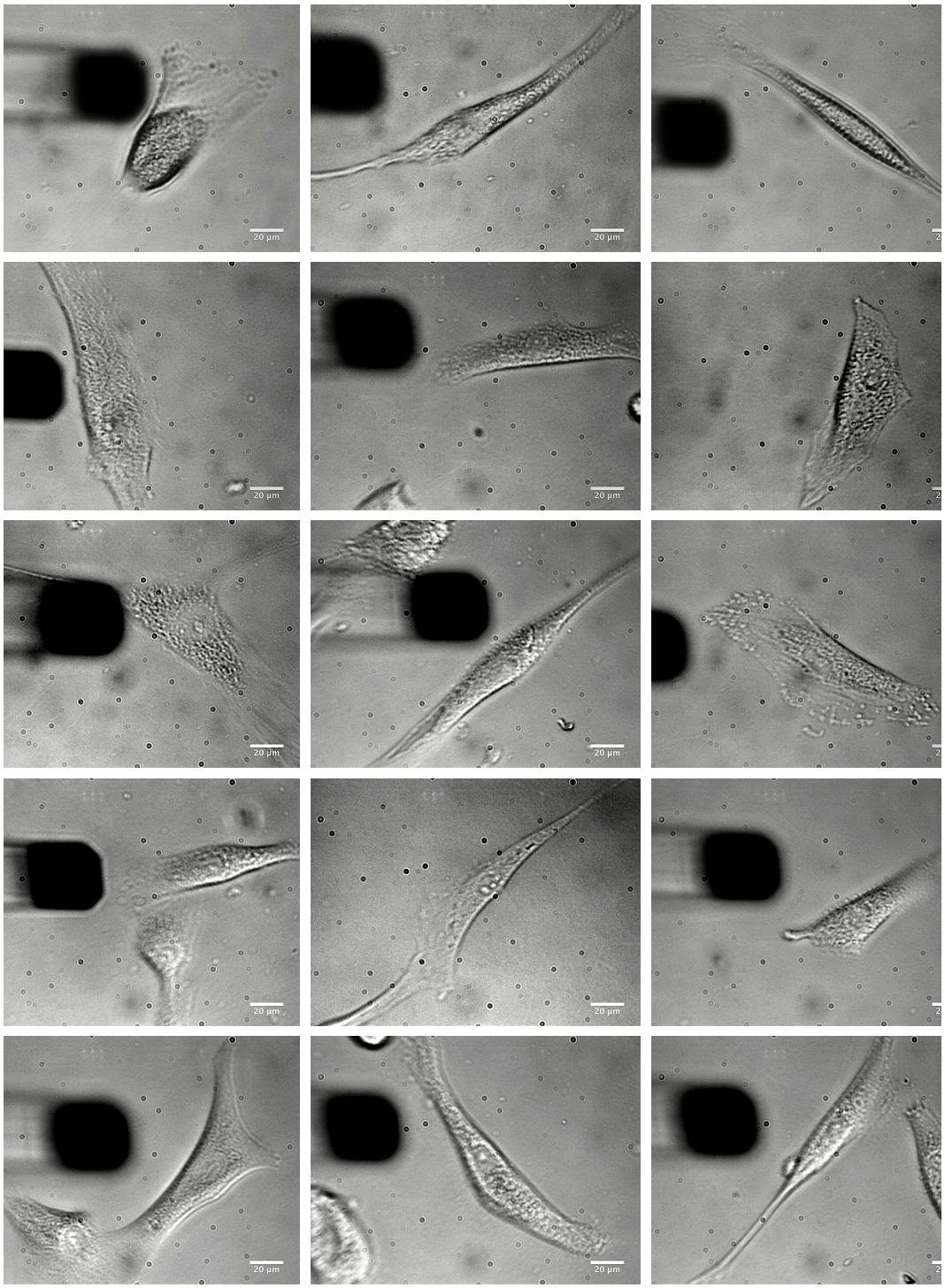

Figure 4.9: **Morphology of human primary myoblasts from a healthy donor**. Optical microscopy images of human primary myoblasts of a healthy donor on a collagen-coated petri dish captured before mechanical AFM experiments. The rectangular AFM cantilever is visible on these images. Scale bars: 20 μm.

width of DMD myoblasts are significantly larger than those of the other two cell types. The

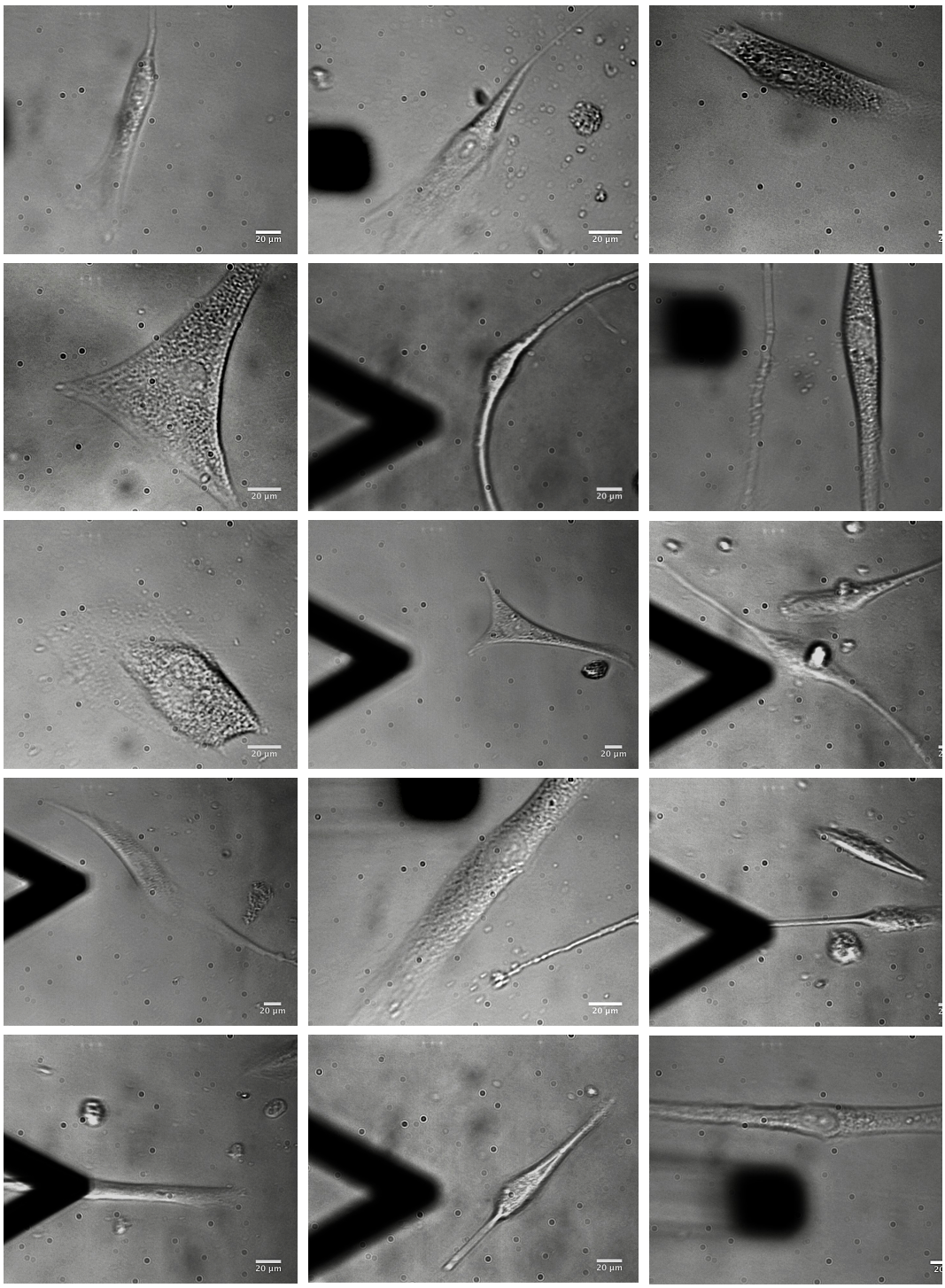

Figure 4.10: **Morphology of human primary myoblasts from a patient affected by Duchenne muscular dystrophy.** Optical microscopy images of human primary myoblasts from a DMD patient on a collagen-coated petri dish captured before mechanical AFM experiments. Rectangular and triangular AFM cantilevers are visible on these images. Scale bars: 20 μm.

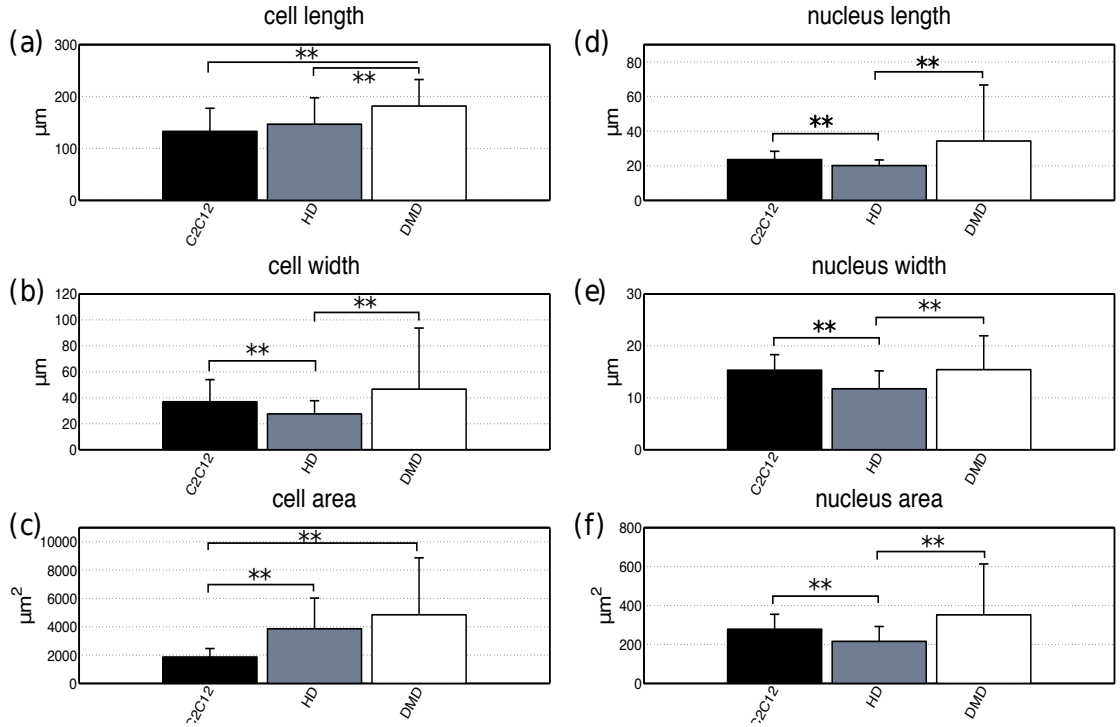

Figure 4.11: **Morphological parameters of C2C12, HD and DMD myoblasts on collagen-coated petri dishes.** Values of length (a), width (b), area (c) of cells, and length (d), width (e), area (f) of their nuclei. Morphological parameters were computed with ImageJ on 25 optical microscopy images. The data are reported as mean ± SD over n= 30 cells for each cell type. With ** are marked significant differences between data distributions ($p \leqslant 0.05$).

mean of cell area of DMD myoblasts ($\sim$ 5000 μm^2) is more than twice the mean area of C2C12 myoblasts ($\sim$ 2000 μm^2). Concerning the nucleus morphology, the HD myoblast nuclei are shorter and narrower with a smaller area as compared to the C2C12 myoblasts. DMD myoblasts instead exhibit bigger nuclei as confirmed by larger values for all three measured parameters. Interestingly, DMD myoblasts have a mean nucleus size more similar to C2C12 than to human HD myoblasts. Concerning the cell and nucleus shapes (Fig. 4.12), it is conspicuous that (i) primary human cells are significantly more elongated (*i.e.* greater cell aspect ratio) as compared to mouse myoblasts; (ii) DMD nuclei are more elongated, and (iii) the ratio between the cell and nucleus areas are significantly different for the three types of cells. In particular, the greatest area ratio is obtained for HD myoblasts, with a mean cell area about 20-fold bigger than the one of their nucleus. Let us point out that the standard deviations of all DMD cell morphological parameters are the largest ones, as an indication of the greater shape variability of DMD myoblasts as compared to C2C12 and HD myoblast cells.

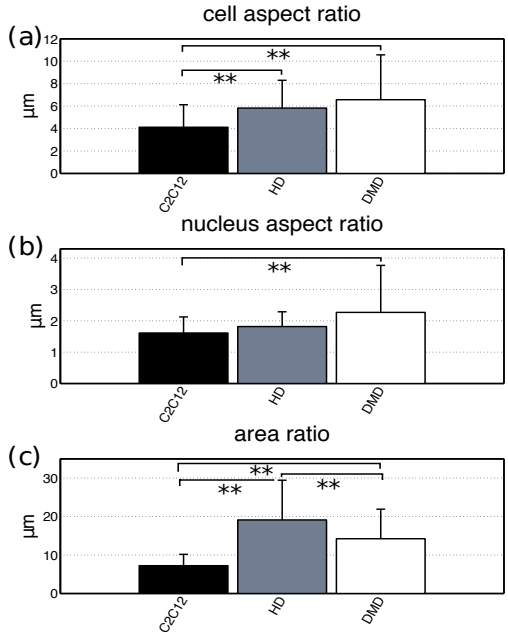

Figure 4.12: **Cell and nucleus aspect ratios of C2C12, HD and DMD myoblasts on collagen-coated petri dishes.** Aspect ratio of the cell (a) and of the nucleus (b) of different types of myoblasts. (c) Ratio between the cell and nucleus areas. These ratios were estimated with ImageJ from 25 optical microscopy images. The data are reported as mean ± SD over n= 30 cells for each cell type. With ** are marked significant differences between data distributions ($p \leqslant 0.05$).

4.5 Application of the AFM-based method to the characterization of healthy and DMD human myoblast mechanical properties

In this section, we compare the mechanical properties of DMD myoblasts to those of HD myoblasts using the AFM indentation method introduced in Chapters 2 and 3. The aim is to measure to which extent the absence or dysfunction of dystrophin impacts the mechanical properties of primary human myoblasts. In Section 4.3.2 and 4.3.4, the dystrophin location and function were discussed together with DMD pathogenesis and structural alterations. Because of its role in cell mechanoprotection and signalling, the lack of dystrophin causes muscle degeneration, sarcolemma fragility, muscle weakness, and impairment of the contractile function. The recently reported effects of the dystrophin deficiency in muscle stem cells (*i.e.* perturbed cell polarization and differentiation) are challenging the previous dogma that dystrophin would be readily found in myotubes/myofibres [Dumont, 2015; Gorecki, 2016]. Do these alterations impact the mechanical properties of human myoblasts? If yes, is it possible to quantify these mechanical perturbations with the previously reported AFM-based method? Does the mechanical characterization of DMD myoblasts provide us complementary information about this disease?

Even if it has been shown that the absence of dystrophin impacts the mechanical properties of murine *mdx* myofibers, contrasting results have been published about the *mdx* muscle cell stiffness measured by AFM. Engler *et al.* [Engler, 2004b] reported larger Young's modulus

($E = 18 \pm 6$ kPa) of *mdx* extensor digitorum longus (EDL) muscle, compared to normal muscles ($E = 12 \pm 4$ kPa). Performing AFM elasticity maps, Canato *et al.* [Canato, 2010] also showed that *mdx* fibers are stiffer ($E \sim 12.5$ kPa) than wild type myofibers ($E \sim 8$ kPa). On the other hand, Pasternak *et al.* [Pasternak, 1995] reported a softer cellular cortex of *mdx* myotubes, as compared to control myotubes. Similarly, Puttini *et al.* [Puttini, 2009] estimated by AFM nano-indentation a smaller Young's modulus of *mdx* myofibers (E = 1.4 ± 0.4 kPa), compared to wild type muscle cells (E = 4.2 ± 1.1 kPa). In particular, they showed not only that *mdx* myofibers have impaired mechanical resistance to deformation, but also that the recovery of dystrophin expression (by exon-skipping) increases the Young's modulus of *mdx* myofibers up to values similar to those of healthy myofibers [Puttini, 2009]. More recently, Van Zwieten *et al.* [Van Zwieten, 2014] reported a proof-of-concept about the application of AFM nano-indentation from muscle biopsies as potential diagnostic tool for human myopathies such as BMD, DMD and limb-girdle muscular dystrophy. They showed that the Young's modulus of DMD myofibers ($E = 1.10 \pm 0.04$ kPa) was smaller than BMD ($E = 2.90 \pm 0.06$ kPa) and healthy muscle fibers ($E = 3.50 \pm 0.1$ kPa). Moreover, their findings indicated a correlation between the severity of the dystrophy and the decrease of the Young's modulus. Contrastingly, through passive stretch-injury experiments, Grange *et al.* [Grange, 2002] did not observe a significant difference between the elastic moduli of *mdx* myofibers and normal maturing myofibers. Similar results were obtained for adult mouse myofibers with small passive stretches (*i.e.* linear elastic stretch range) [Wolff, 2006]. As outlined in Chapters 2 and 3, these contrasting results could be due to several causes including different experimental conditions for the preparation or isolation of muscle fibers, the scale at which the cells or tissues were indented and the analytical methods from which elastic modulus were estimated.

Mechanical characterization of pathological human myoblasts remains rare. Human myoblasts with heterozygous R350P desmin mutation were found stiffer than normal myoblasts, and to present a higher vulnerability (*i.e.* greater susceptibility to stretch-injury and cell death) upon cyclic mechanical stretches [Bonakdar, 2012]. Desmin mutations are known to cause desminopathies, and to be involved in different forms of myopathies and cardiomyopathies [Schröder, 2007]. In contrast, the depletion of plectin on murine myoblasts was shown to cause lower stiffness and decreased cell death in response to stretch, as compared to wild type and to plectin-deficient keratinocytes [Bonakdar, 2015]. The greater vulnerability to mechanical stress of human cells with mutations of intermediate filament proteins corroborated the role of IFs as cellular stress absorbers [Herrmann, 2007]. The conjunction of increased cell stiffness and stretch-induced injury was also observed in differentiated muscle cells [Lieber & Friden, 1993]. The fast and efficient coupling of the myonuclear envelope with the extracellular membrane via CSK filaments is an important factor for the functionality of the NMJ. Two components of the myonuclear envelope, the lamin A and the emerin, were shown to be important for the integrity of skeletal muscle fibers: mutations of either genes can lead to Emery-Dreifuss muscular dystrophies (EDMD) in humans via an alteration of the viscoelastic behavior of the nuclear lamina [Lammerding, 2004; Dutta, 2016].

To summarize, previous mechanical characterizations of DMD myofibers lead to contradictory estimations of their stiffening or softening, as compared to their healthy counterparts. The mechanical properties of primary human DMD myoblasts have rarely been investigated [Nesmith, 2016]. Besides the fact that cellular mechanosensitivity depends on the cell-type, altogether these findings suggest that in human myoblasts, inhibition or activation of different CSK molecular components and linkers should produce different mechanical outcomes. The

cell polarity machinery impairment of DMD myoblasts (as an indication of CSK perturbations) [Dumont, 2015] should also imply some alteration of their mechanical properties, as compared to HD myoblasts.

4.5.1 Mechanical properties of healthy primary human myoblasts

We duplicated the same AFM FIC analytical methods described in Chapter 3, to compare HD and DMD primary human myoblasts. In this section, we first describe the FICs and their derivatives collected from a few adherent myoblasts; then we make a global estimation of the shear modulus $\langle G \rangle$ from undisrupted and disrupted FICs, their dissipation loss and we use the wavelet-based FIC analysis to detect the local disruption events, their strength and their density.

Figs 4.13 and 4.14 show four sets of FICs collected from four different HD myoblasts together with their transmission microscopy images. The first two HD myoblasts 1 and 2 are not broadly spread on the collagen coated substrate. They show very similar fusiform morphologies and their force curves do not show drastic disruption events (Figs 4.13(a,a')). Both these HD myoblasts are also softer than the C2C12 myoblasts illustrated in Figs 3.26, 3.27 and 3.28. The force first-order derivatives of the HD myoblasts 1 and 2 (Fig. 4.13(b,b')) can be fairly well fitted by a straight line, asserting that these two cells behave similarly to an elastic material. The HD myoblasts 3 and 4 have been chosen because they both have a more widely spread morphology. Also HD myoblast 3 seems to be much more mobile with ruffles of its lamellipodia, with a denser or thicker nucleus. It behaves much more hectically than HD myoblast 4 and its FICs display more important disruption events. HD myoblast 4 seems to have a very flat (crunched) nucleus. In both cases, the Z position of the FICs disruption events are not fixed, but seem to change randomly from one load-unload scan to the next one. The 3D representation of the FICs of myoblasts 3 in Fig. 4.15 illustrates some irreproducibility of the occurrence of the disruption events. The HD myoblast 4 disruption events have a lower amplitude (Fig. 4.16(a)), but when using the same 3D representation, we can detect a few disruption events which also occur intermittently (Fig. 4.16(b)). This difference could be explained by a lower HD myoblast 4 activity or motility. In both HD myoblasts 3 and 4, disrupted FICs occur as isolated chronologically, their previous and following FICs being almost undisrupted. This apparent random (intermittent) occurrence of the disrupted FICs contrasts with what we have observed in Chapter 3, in particular with the C2C12 myoblast 6 in Fig. 3.30 where the disruption events seemed to grow progressively from one load-unload scan to the next scan to ultimately disappear after a finite number of scans. A higher regularity of disruption events on successive load-unload scan FICs was also observed with myotubes 1, 2, 3 in Figs 3.31 and 3.32.

type	N cells	N FICs	R_D	$\overline{\langle G \rangle}_{[N_{peak}=0]}$	$\overline{\langle G \rangle}_{[N_{peak}>0]}$	$\overline{D_l}\ _{[N_{peak}=0]}$	$\overline{D_l}\ _{[N_{peak}>0]}$
C2C12	54	1383	46.1	1.57 ± 0.25 kPa	1.26 ± 0.1 kPa	0.39 ± 0.02	0.45 ± 0.02
HD	20	548	20.0	1.0 ± 0.2 kPa	0.9 ± 0.3 kPa	0.28 ± 0.05	0.41 ± 0.06
DMD	24	682	22.0	1.7 ± 0.5 kPa	1.2 ± 0.5 kPa	0.31 ± 0.02	0.36 ± 0.06

Table 4.1: **Compilation of the means of the global quantities $\langle G \rangle$ and D_l for C2C12, HD, and DMD myoblasts**. FICs without ($N_{peak} = 0$) and with ($N_{peak} = 0$) disrupted events are compared. R_D is the percentage of FICs with disruption events. The global Young modulus is given by $\langle E \rangle = 3\langle G \rangle$ (with the Poisson coefficient $\nu = 0.5$).

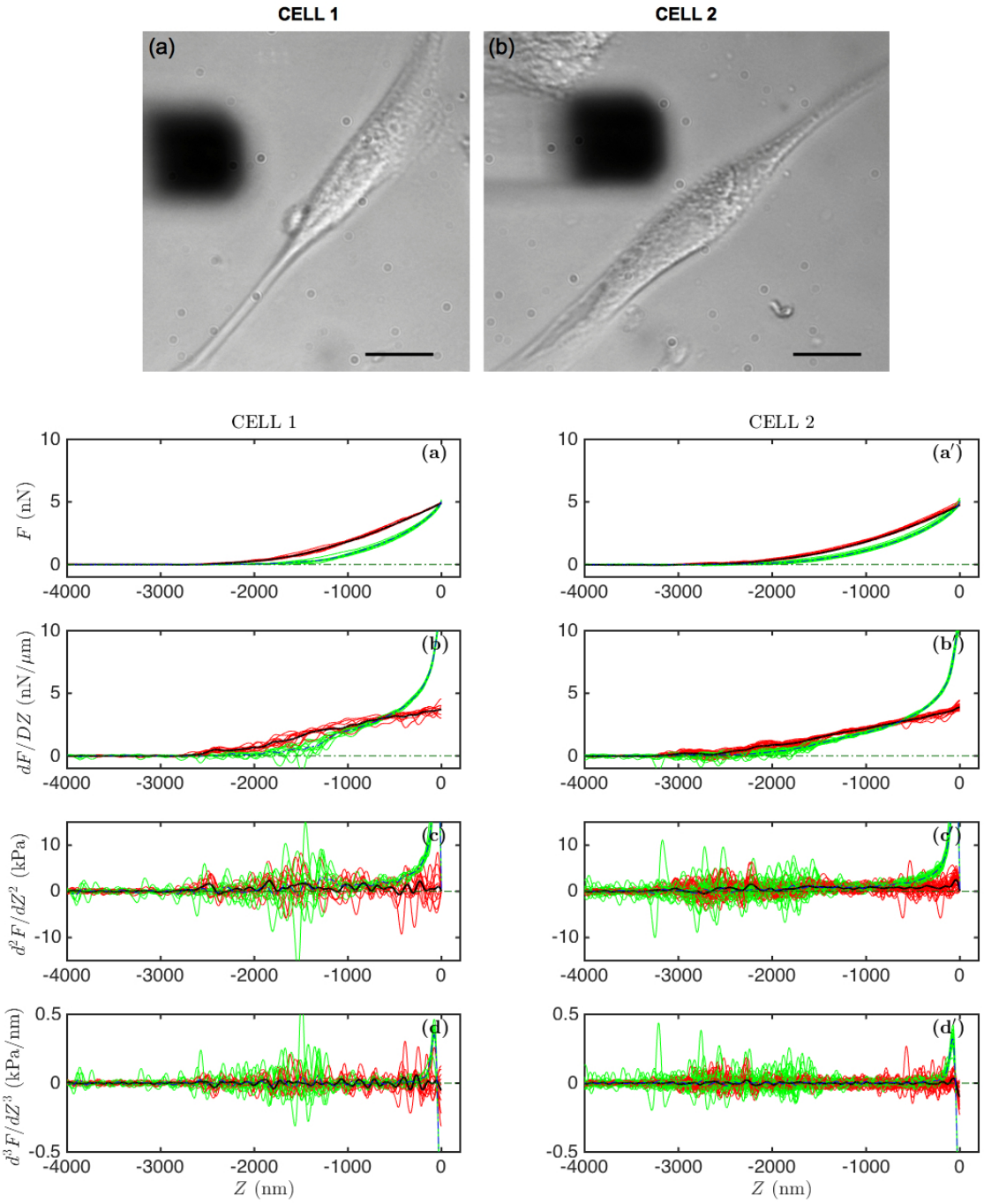

Figure 4.13: **FICs collected from two HD myoblasts (1 and 2).** Top panels: transmission microscopy images of the two HD myoblasts 1 and 2. Scale bar: 30 μm. (a,a') FIC series (30 curves for each cell) were recorded at a scan velocity $V_0 = 1$ μm/s and filtered from the raw FICs using a Gaussian wavelet of width $2\sqrt{2}s_g^{(0)} = 9$ nm (Eq. (5.10)). (b,b') FIC derivatives computed from the raw FICs using a Gaussian derivative wavelet of width $2\sqrt{2}s_g^{(1)} = 110$ nm (Eq. (5.11)). (c,c') Second-order derivatives computed from the raw FICs with a second derivative of a Gaussian wavelet of width $2\sqrt{2}s_g^{(2)} = 110$ nm (Eq. (5.12)). (d,d') Third-order derivatives computed from the raw FICs with a third derivative of a Gaussian wavelet of width $2\sqrt{2}s_g^{(3)} = 110$ nm (Eq. (5.13)). Loading FICs (red) and their average (black); unloading FICs (green).

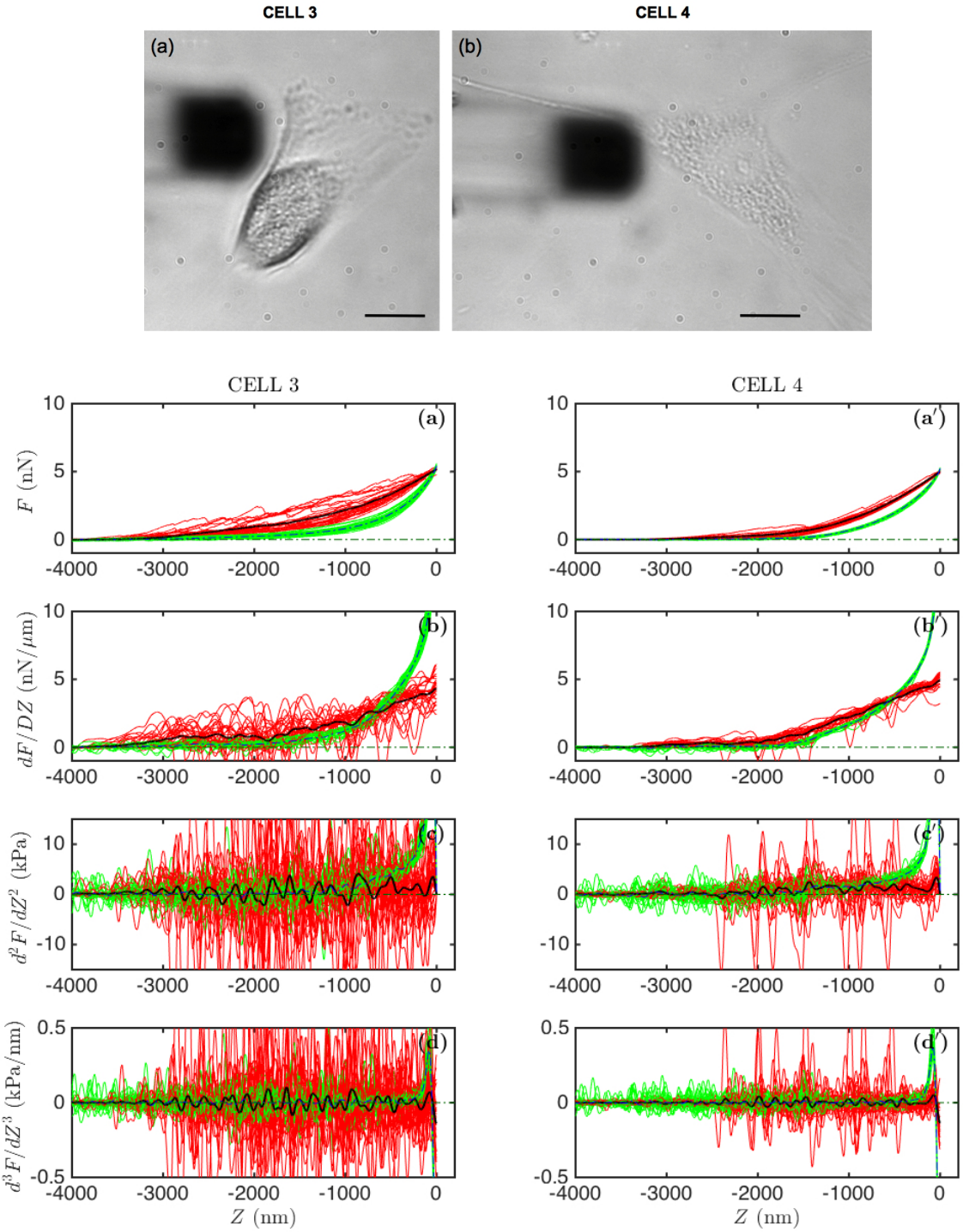

Figure 4.14: **FICs collected from two HD myoblasts (3 and 4).** Top panels: transmission microscopy images of the two HD myoblasts 3 and 4. Scale bar: 30 μm. (a,a') FIC series (30 curves for each cell) were recorded at a scan velocity $V_0 = 1$ μm/s and filtered from the raw FICs using a Gaussian wavelet of width $2\sqrt{2}s_g^{(0)} = 9$ nm (Eq. (5.10)). (b,b') FIC derivatives computed from the raw FICs using a Gaussian derivative wavelet of width $2\sqrt{2}s_g^{(1)} = 110$ nm (Eq. (5.11)). (c,c') Second-order derivatives computed from the raw FICs with a second derivative of a Gaussian wavelet of width $2\sqrt{2}s_g^{(2)} = 110$ nm (Eq. (5.12)). (d,d') Third-order derivatives computed from the raw FICs with a third derivative of a Gaussian wavelet of width $2\sqrt{2}s_g^{(3)} = 110$ nm (Eq. (5.13)). Loading FICs (red) and their average (black); unloading FICs (green).

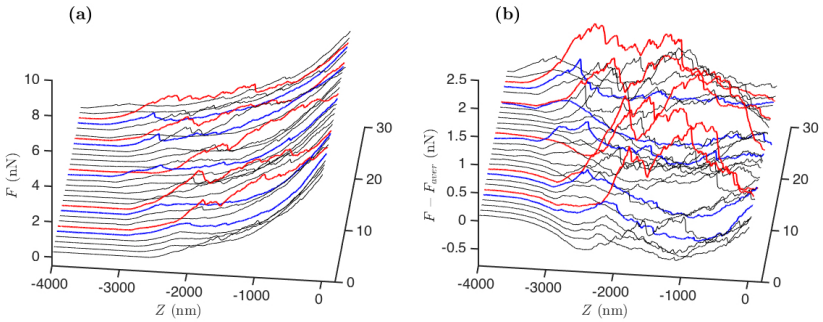

Figure 4.15: **Tracking the disruption events from a series of FICs collected on HD myoblast 3 (Fig. 4.14).** (a) FICs plotted in a 3D representation with their recording index. (b) Difference of the FICs from the averaged FIC. The red curves highlight the mostly disrupted FICs, the blue curves correspond to their neighbouring FICs.

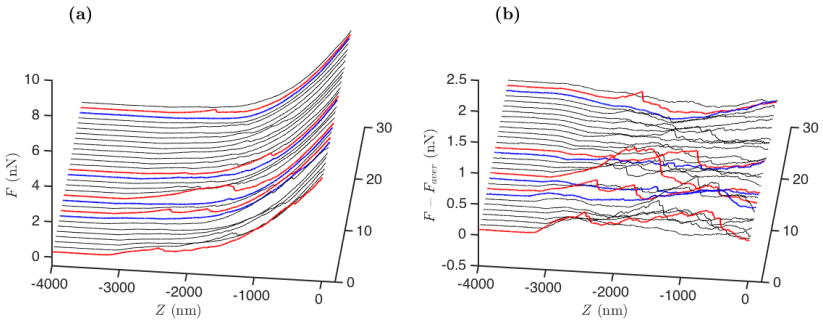

Figure 4.16: **Tracking the disruption events from a series of FICs collected on HD myoblast 4 (Fig. 4.14).** (a) FICs plotted in a 3D representation with their recording index. (b) Difference of the FICs from the averaged FIC. The red curves highlight the mostly disrupted FICs, the blue curves correspond to their neighbouring FICs.

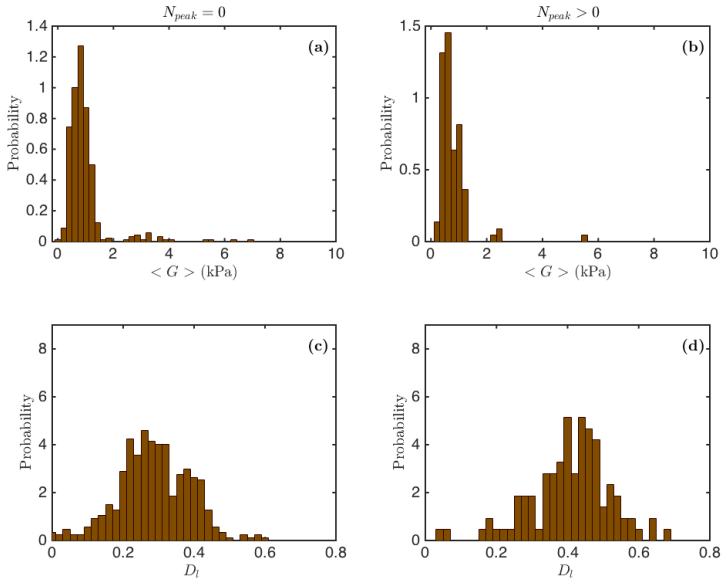

Figure 4.17: **Statistical distributions of $\langle G \rangle$ and D_l captured from 20 human healthy donor (HD) myoblasts (548 FICs), distinguishing non-disrupted FICs ($N_{peak} = 0$ - 440 FICs) from disrupted FICs ($N_{peak} > 0$ - 108 FICs).** The myoblasts were adherent on collagen coated petri dishes and maintained in PM buffer at room temperature during the AFM recording (Materials and methods - Chapter 5). $\overline{\langle G \rangle}_{[N_{peak}=0]} = 1.0 \pm 0.2$ kPa and $\overline{\langle G \rangle}_{[N_{peak}>0]} = 0.9 \pm 0.3$ kPa, $\overline{D_l}_{\ [N_{peak}=0]} = 0.28 \pm 0.05$ and $\overline{D_l}_{\ [N_{peak}>0]} = 0.41 \pm 0.06$.

The percentage of FICs showing disruption events is much smaller for HD myoblasts (20%) than for C2C12 myoblasts (46%), and closer to the proportion observed with myotubes (26%), suggesting that the density of peaks computed from the third-order derivative of the FICs should also decrease (see Fig. 4.23(e)). The mean global shear moduli $\overline{\langle G \rangle}_{[N_{peak}=0]} = 1.0 \pm 0.2$ kPa (Fig. 4.17(a)) and $\overline{\langle G \rangle}_{[N_{peak}>0]} = 0.9 \pm 0.3$ kPa (Fig. 4.17(b)) both are much smaller than their previous estimations from a population of 54 C2C12 myoblasts (Table 4.1). The dissipation loss D_l of undisrupted FICs from HD myoblasts (Fig. 4.17(c)) is much smaller than those from C2C12 myoblasts (Fig. 3.35(c)), corroborating the previous observations from C2C12 myoblast derived cells of Chapter 3 that undisrupted FICs involve less mechanical energy dissipation. 30% of the undisrupted FICs from HD myoblasts presents a dissipation loss $D_l \leq 0.2$, characteristic of what we have observed with blebbistatin treated C2C12 myoblasts and could correspond to situations where the perinuclear actin stress fibers are not (or only partially) established. These cells correspond to the fusiform shapes myoblasts illustrated in Fig. 4.13. Such morphologies are more common with high confluency cell culture, typically when proliferating cells start fusing to form myotubes, their adherence and spreading is then diminished to favor cell fusion.

4.5.2 Mechanical properties of human DMD myoblasts

Four DMD myoblasts (1-4) were selected from a set of 24 cells to construct Figs 4.18, 4.19, 4.20 and 4.21. We choose the DMD myoblasts 1 and 2 because their FICs did not present marked disruption events. However, their morphologies are drastically different, myoblast 1 has a fusiform shape and myoblast 2 looks rather like an asymmetric comet (Fig. 4.18). The FIC derivative corresponding to the DMD myoblast 1 (Fig. 4.18(b)) is quasi-linear, similarly to an elastic material. The FIC derivative corresponding to the DMD myoblast 2 (Fig. 4.18(b')) can be broken down in two regimes, (i) a first regime with a very low slope on the first 1.5 μm indentation, and (ii) a second regime with a steeper slope that lasts for more than 1 μm depth. In that later case, there is no evidence of detectable disruption event. The smoothness of the nucleus texture of DMD myoblast 2 contrasts with the granulosity of the cell cytoplasm; this cell image suggests that the nucleus could have been shrunk to a concentrated core inside a diluted hollow space. Moreover, it is difficult to circumvent the DMD myoblast 2 contour and its membrane (compared to DMD myoblast 1). The difference of the sizes of the central part of DMD myoblasts 1 and 2 is striking and suggests that the nucleus shape variability of DMD myoblasts is greater than for HD myoblasts, in agreement with the estimations of morphological parameters of Figs 4.11.

The DMD myoblasts 3 and 4 are very different from both their morphologies and their FICs where many disruption events appear (Fig. 4.19). Both FIC series (loading curves) do not follow a simple linear trend but rather can be decomposed into distinct regimes, separated by disruption events (Fig. 4.19(b,b')). The DMD myoblast 4 reaches a quasi-constant force derivative after 3 μm of indentation. We could consider the DMD myoblasts 3 and 4 as more motile than the DMD myoblasts 1 and 2. For these two myoblasts, we have also used the same 3D representation of the FICs (Figs 4.20 and 4.21) to illustrate that again for the cells where disrupted events occur, disrupted FICs appear with a higher rate of occurrence, than observed with C2C12 myoblasts. Their repetition in time is not regular, and each disrupted FIC is preceded and followed by an undisrupted FIC. This singularity of the disruption events is characteristic of both HD and DMD myoblasts. It would be interesting to perform longer series of FICs (load-unload scans) to characterize the inter-correlation of the disruption events in one

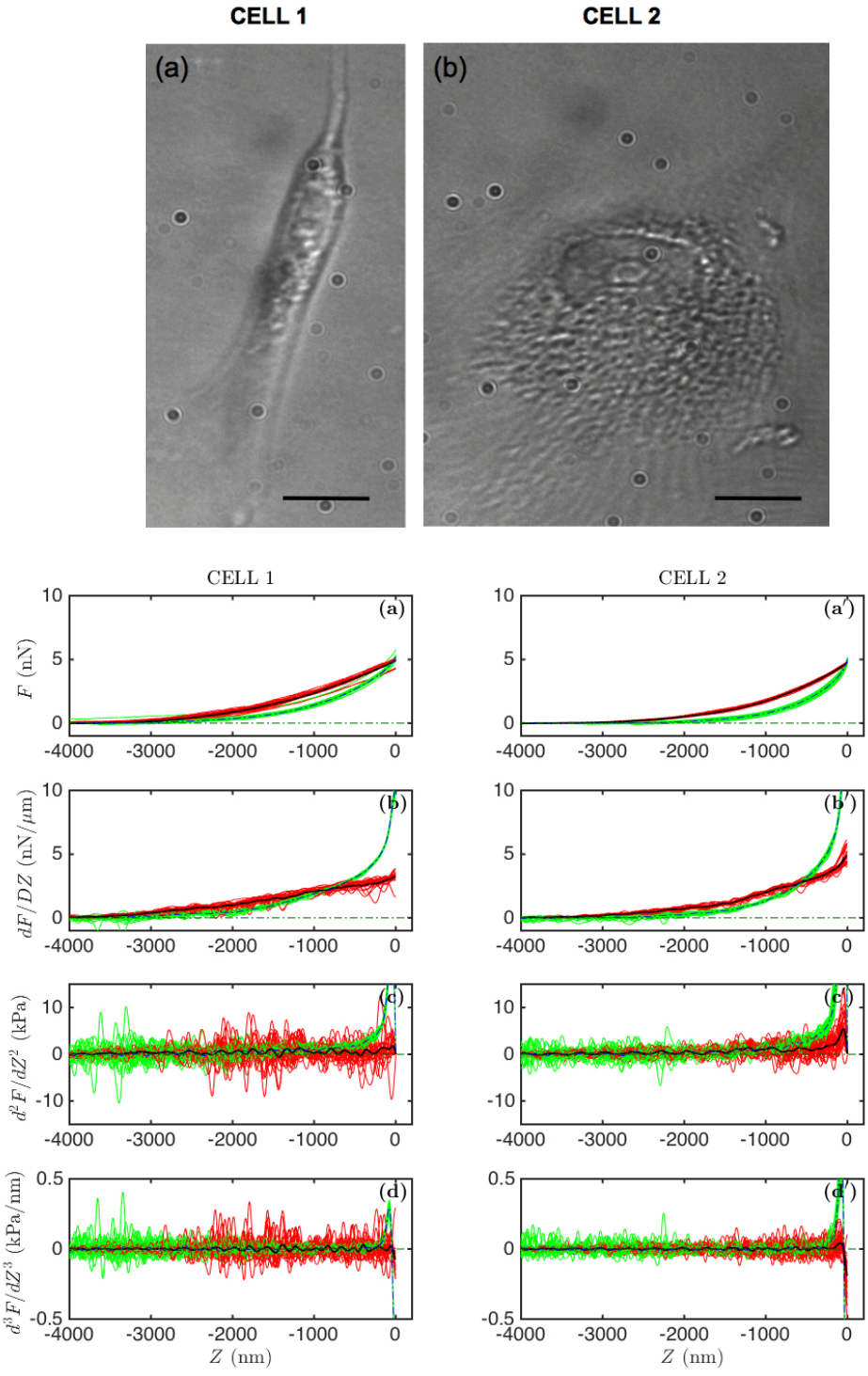

Figure 4.18: **FICs collected from two DMD myoblasts (1 and 2).** Top panels: transmission microscopy images of the two DMD myoblasts 1 and 2. Scale bar: 30 μm. (a,a') FIC series (30 curves for each cell) were recorded at a scan velocity $V_0 = 1$ μm/s and filtered from the raw FICs using a Gaussian wavelet of width $2\sqrt{2}s_g^{(0)} = 9$ nm (Eq. (5.10)). (b,b') FIC derivatives computed from the raw FICs using a Gaussian derivative wavelet of width $2\sqrt{2}s_g^{(1)} = 110$ nm (Eq. (5.11)). (c,c') Second-order derivatives computed from the raw FICs with a second derivative of a Gaussian wavelet of width $2\sqrt{2}s_g^{(2)} = 110$ nm (Eq. (5.12)). (d,d') Third-order derivatives computed from the raw FICs with a third derivative of a Gaussian wavelet of width $2\sqrt{2}s_g^{(3)} = 110$ nm (Eq. (5.13)). Loading FICs (red) and their average (black); unloading FICs (green).

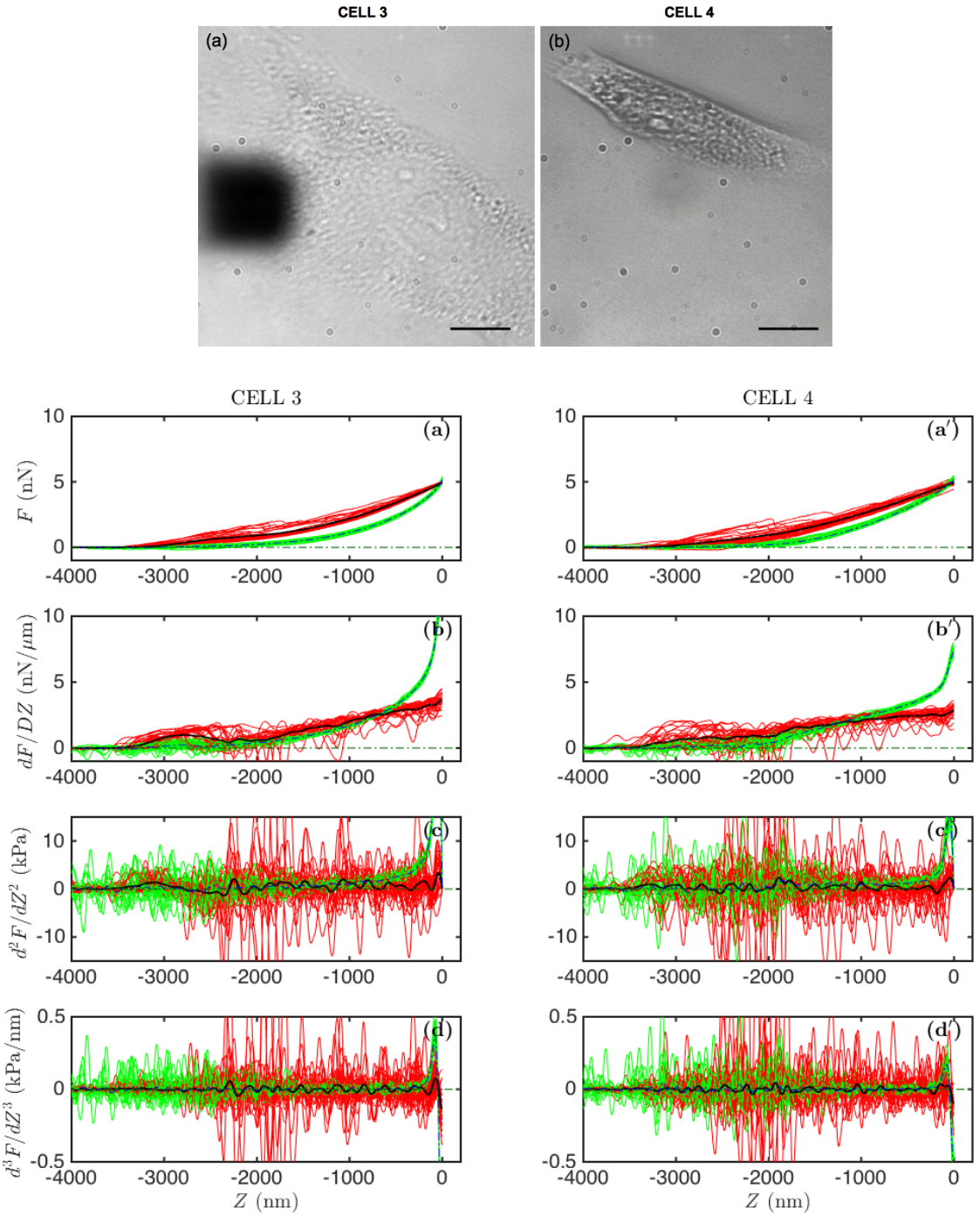

Figure 4.19: **FICs collected from two DMD myoblasts (3 and 4).** Top panels: transmission microscopy images of the two HD myoblasts 3 and 4. Scale bar: 30 μm. (a,a') FIC series (30 curves for each cell) were recorded at a scan velocity $V_0 = 1$ μm/s and filtered from the raw FICs using a Gaussian wavelet of width $2\sqrt{2}s_g^{(0)} = 9$ nm (Eq. (5.10)). (b,b') FIC derivatives computed from the raw FICs using a Gaussian derivative wavelet of width $2\sqrt{2}s_g^{(1)} = 110$ nm (Eq. (5.11)). (c,c') Second-order derivatives computed from the raw FICs with a second derivative of a Gaussian wavelet of width $2\sqrt{2}s_g^{(2)} = 110$ nm (Eq. (5.12)). (d,d') Third-order derivatives computed from the raw FICs with a third derivative of a Gaussian wavelet of width $2\sqrt{2}s_g^{(3)} = 110$ nm (Eq. (5.13)). Loading FICs (red) and their average (black); unloading FICs (green).

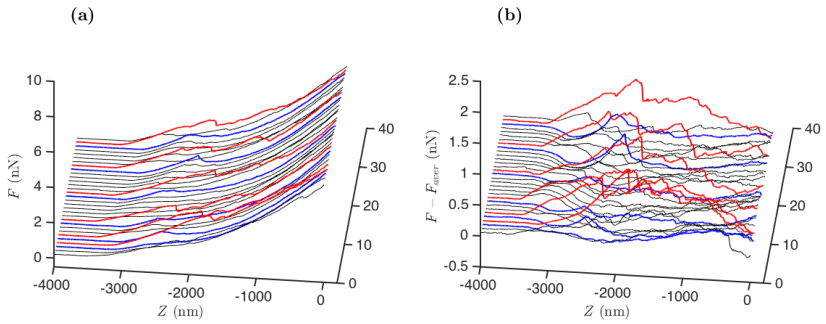

Figure 4.20: **Tracking the disruption events from a series of FICs collected on DMD myoblast 3 (Fig. 4.19).** (a) FICs plotted in a 3D representation with their recording index. (b) Difference of the FICs from the averaged FIC. The red curves highlight the mostly disrupted FICs, the blue curves correspond to their neighbouring FICs.

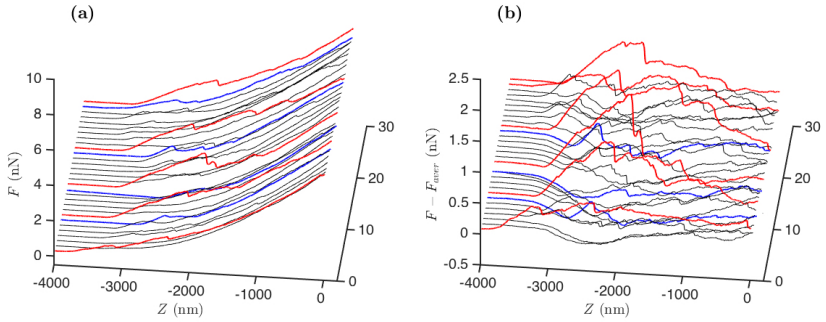

Figure 4.21: **Tracking the disruption events from a series of FICs collected on DMD myoblast 4 (Fig. 4.19).** (a) FICs plotted in a 3D representation with their recording index. (b) Difference of the FICs from the averaged FIC. The red curves highlight the mostly disrupted FICs, the blue curves correspond to their neighbouring FICs.

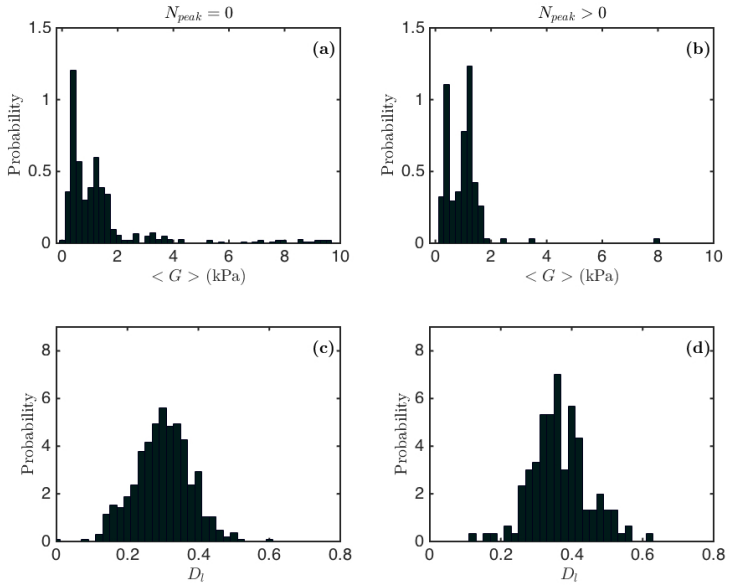

Figure 4.22: **Statistical distributions of $\langle G \rangle$ and D_l captured from 24 human DMD myoblasts (682 FICs), distinguishing non-disrupted FICs ($N_{peak} = 0$ - 530 FICs) from disrupted FICs ($N_{peak} > 0$ - 152 FICs).** The myoblasts were adherent on collagen coated petri dishes and maintained in PM buffer at room temperature during the AFM recording (Materials and methods - Chapter 5). $\overline{\langle G \rangle}_{[N_{peak}=0]} = 1.7 \pm 0.5$ kPa and $\overline{\langle G \rangle}_{[N_{peak}>0]} = 1.2 \pm 0.5$ kPa, $\overline{D_l}_{[N_{peak}=0]} = 0.31 \pm 0.02$ and $\overline{D_l}_{[N_{peak}>0]} = 0.36 \pm 0.06$.

FIC with the ones of the following FICs. The higher apparent temporal occurrence of disruptive FICs observed with primary human myoblasts may indicate that these cells have a more intense remodeling of their actin stress fibers and a greater local extensibility of their actin network. The C2C12 myoblasts are transformed myoblast cells; they have been cultured for months on very stiff and adherent substrates that favor the establishment of highly tensed actin stress fibers at the expense of a higher motility and adaptability of the cell to local deformations.

The fraction of FICs with disruption events for human DMD myoblasts (22.0%) is very small, as previously observed for human HD myoblasts (20.0%), and significantly smaller than for C2C12 myoblasts (46.1%). As compared to HD myoblasts, the mean global shear moduli of DMD myoblasts (Fig. 4.22(a,b)) $\overline{\langle G \rangle}_{[N_{peak}=0]} = 1.7 \pm 0.5$ kPa and $\overline{\langle G \rangle}_{[N_{peak}>0]} = 1.2 \pm 0.5$ kPa increase slightly to become closer to that of C2C12 myoblasts (Table 4.1). The mean dissipation loss $\overline{D_l} = 0.31 \pm 0.02$ of undisrupted FICs from DMD myoblasts (Fig. 4.22(c)) is also smaller than those from C2C12 myoblasts $\overline{D_l} = 0.39 \pm 0.02$ (Fig. 3.35(c)). Again, 30% of the undisrupted FICs from DMD myoblasts present a dissipation loss $D_l \leq 0.2$, similarly to human HD myoblasts and could correspond to situations where the perinuclear actin stress fibers are not (or partially) established. These cells likely correspond to the fusiform shaped myoblast illustrated in Fig. 4.18(a).

4.5.3 Comparison of the statistics and strength of disruption events from HD and DMD myoblasts

Finally we reconstructed the local disruption event feature distributions from the three sets of myoblasts (C2C12, human HD and human DMD) on a single figure (Fig 4.23) for better comparison. The red bars correspond to C2C12 myoblasts, the brown bars to human HD myoblasts and the black bars to human DMD myoblasts. Clearly, we observe in Fig. 4.23(a) that both HD and DMD myoblasts are softer than C2C12 myoblasts. The disrupted FICs with $\langle G \rangle \geq 2$ kPa have disappeared (Fig 4.23(a)). The same remark holds true for the distributions of the local shear modulus G_{loc} which are bounded to values smaller than 3 kPa (Fig 4.23(b)). We note also that the distribution of local shear modulus for human HD myoblasts is slightly shifted to the right compared to the same distribution for DMD myoblasts. This is an indication that locally, the human HD myoblasts can sustain larger pressure from the cantilever before rupture. However, the highest local shear moduli FICs encountered with C2C12 myoblasts have almost completely disappeared, confirming the global softening of both HD and DMD human primary myoblasts. The first and third derivatives of the FICs are also interesting to comment, since even if the human primary myoblasts behave as softer locally and globally, the strength of the rupture events that they can sustain are are not so different from that of C2C12 myoblasts, their distributions are quite superimposed (Fig 4.23(c,d)). This is confirmed by the reconstruction of the histograms of $-dF/dZ$ in a log-log representation in Fig. 4.24(c). The scatter point plot of $-dF/dZ$ versus d^3F/dZ^3 (Fig. 4.24(b)), together with the log-normal distribution representation of $log_{10}(-dF/dZ)$ (Fig. 4.24(c)) confirm the strong similarity of the characteristics of disruption events on these three cell types.

Fluorescence images of the actin and microtubule filaments from HD and DMD primary human myoblasts strikingly corroborate our interpretation of the AFM FIC analysis (Figs. 4.25 and 4.26). As compared to C2C12 myoblasts (Figs 3.7, 3.8, 3.41(GM) and 3.42(a-e)), primary human myoblasts do not show the perinuclear actin stress fibers previously observed with this mouse cell line, their ventral stress fibers are also less distinguishable, and the density of periph-

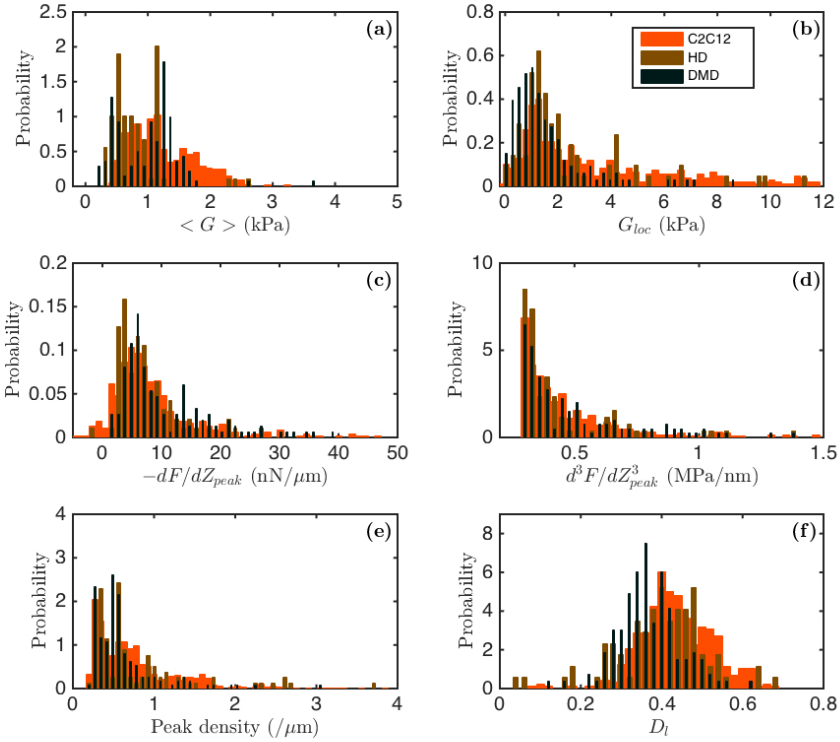

Figure 4.23: **Statistical distributions of global and local features computed from disrupted FICs ($N_{peak} > 0$) sorted out from FICs collected from C2C12 normal (red), HD (brown) and DMD (black) myoblasts.** (a) $\langle G \rangle_{[N_{peak}>0]}$. (b) G_{loc} (defined in Fig. 3.34). (c) $-dF/dZ_{peak}$. (d) d^3F/dZ^3_{peak}. (e) Peak density $\Gamma_{peak} = N_{peak}/|Z_{setpoint} - Z_c|$. (f) $D_{l\ [N_{peak}>0]}$.

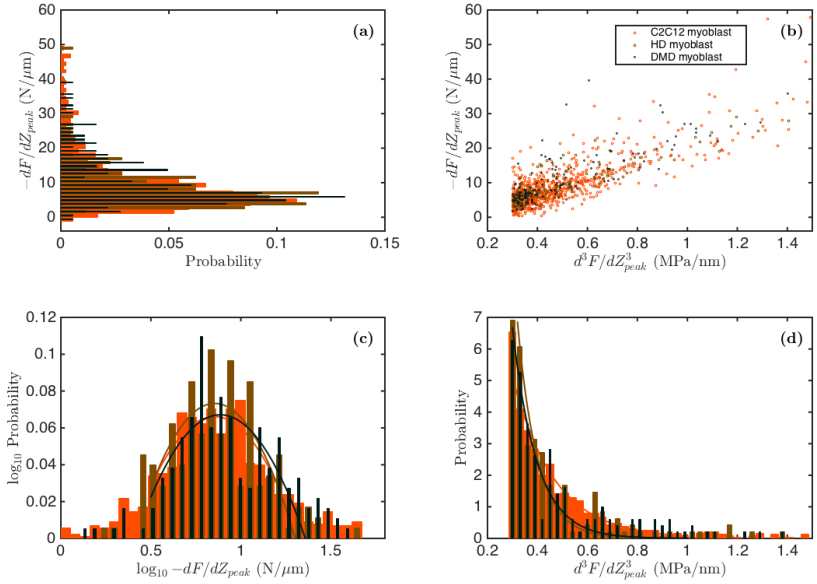

Figure 4.24: **Statistical distributions of $-dF/dZ_{peak}$ and $\Gamma_{peak} = d^3F/dZ^3_{peak}$ collected from C2C12 myoblast (red), HD myoblast (brown) and DMD (black) myoblast FICs.** (a) $-dF/dZ_{peak}$. (b) Scatter point plot of $-dF/dZ_{peak}$ versus $\Gamma_{peak} = d^3F/dZ^3_{peak}$. (c) Log-normal distribution of $\log_{10}(-dF/dZ_{peak})$ and its parametrization with parabola functions. (d) Exponential distribution of $\Gamma_{peak} = d^3F/dZ^3_{peak}$.

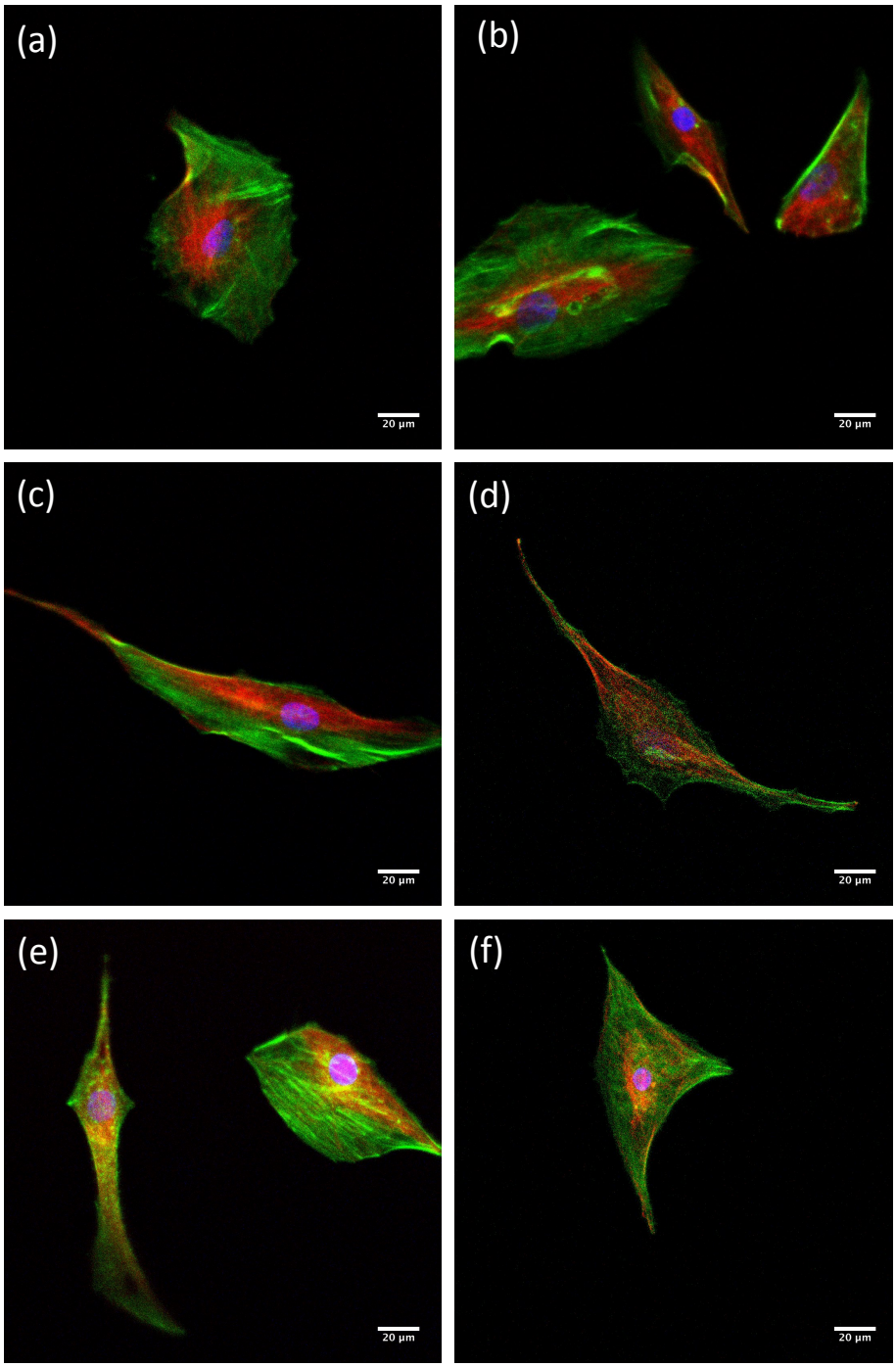

Figure 4.25: **Immuno-fluorescence confocal images of primary human myoblasts of healthy donors adherent on CCPD.** Staining: F-actin (phalloidin-Alexa Fluor 488, green), β-tubulin (anti-β-tubulin Cy3-conjugate, red) and nucleus (DAPI, blue). Scale bars: 20 μm.

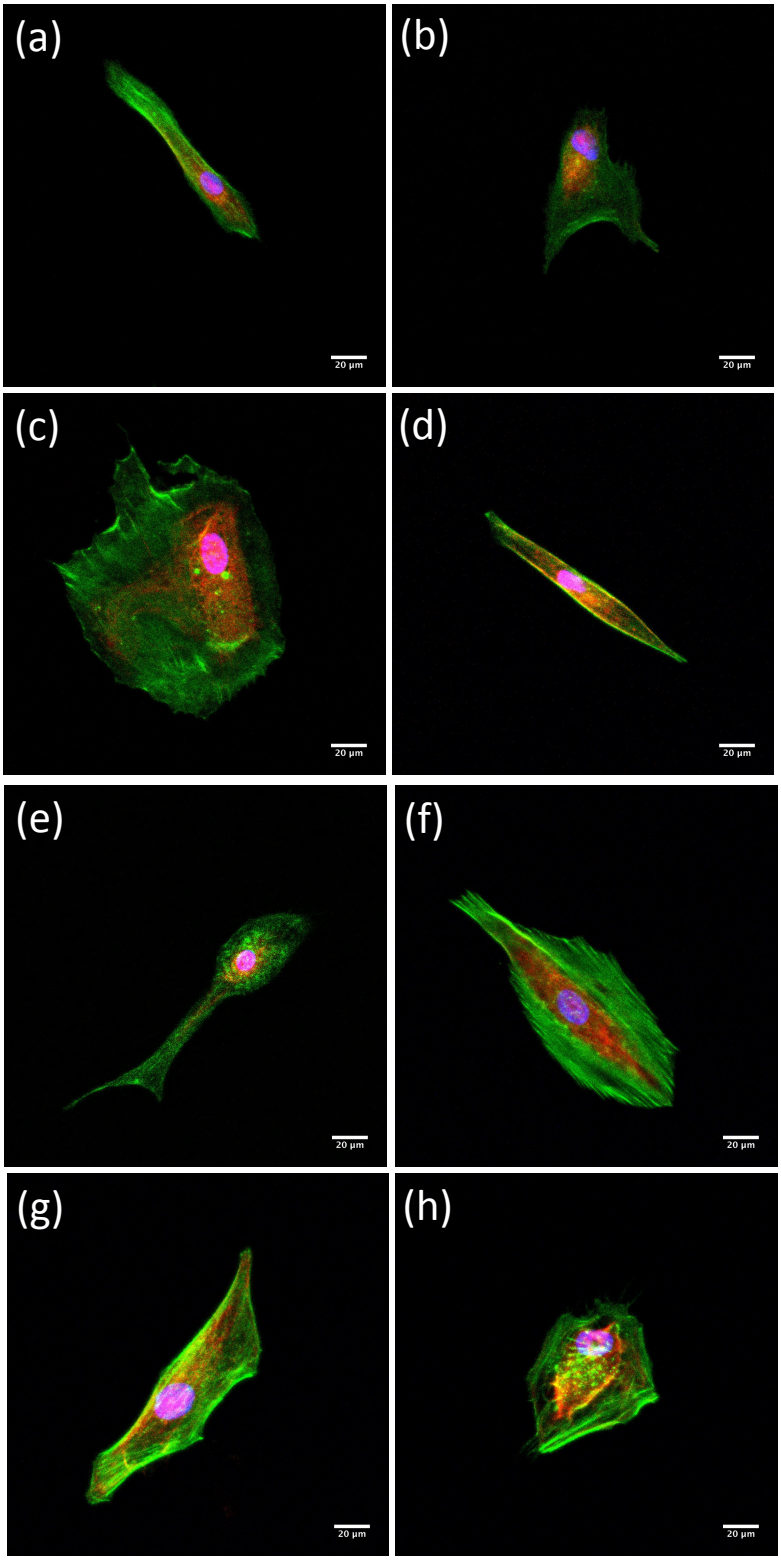

Figure 4.26: **Immuno-fluorescence confocal images of primary human myoblasts of patients affected by Duchenne muscular dystrophy, adherent on CCPD.** Staining: F-actin (phalloidin-Alexa Fluor 488, green), β-tubulin (anti-β-tubulin Cy3-conjugate, red) and nucleus (DAPI, blue). Scale bars: 20 μm.

eral stress fibers changes considerably from one cell to another one. Interestingly, comparing the cells which are mostly spread on the collagen substrate (Figs 4.25(a,b) and 4.26(c) with Fig. 3.42(d,e)), we note that the human primary myoblasts seem to be more motile, they have only very localized and short actin stress fibers that do not cross over the nucleus. More surprinsingly, in these examples, the perinuclear actin appears instead as punctuate aggregates suggesting that there is an accumulation of small actin filaments which could not be mobilized by myosin motors to build larger stress fiber structures. Comparing the adherent C2C12 myoblast in Fig. 3.42(d) and the rightmost adherent HD primary human myoblast in Fig. 4.25(e) is really astonishing. The HD human myoblast has a more circular nucleus of size about half the one of a C2C12 myoblast. This confirms the fact that the perinuclear actin stress fibers are not (or very little) assembled in human primary myoblasts and that they do not press on the nucleus. Back to Fig. 3.41 where we followed the transformation of C2C12 myoblasts during ATP depletion, we note that even after ATP depletion, C2C12 myoblast nuclei retained their ellipsoidal shape and large diameters. These strong differences between C2C12 myoblasts and human primary myoblasts cannot be explained by a global deficiency of the primary human myoblasts in their energetic metabolism (ATP failure). These differences rather seem to be constitutive, the primary myoblasts have not the same contractility and actin stress fiber-focal adhesion machinery as the one C2C12 myoblast acquired in laboratory cultures. This explains that some caution has to be taken when comparing primary mouse myoblasts with primary human myoblasts before concluding on their cytoskeleton and mechanical properties.

The parametrization of the distribution of d^3F/dZ^3 gives a faster exponential decay for both HD and DMD myoblasts than for C2C12 myoblasts, with a characteristic amplitude $\tau_\Gamma \lesssim 0.1$ MPa/nm (about half its value for C2C12 myoblasts). This means that if the smallest peaks (corresponding to smaller values of $\Gamma_{peak} = d^3F/dZ^3$) are more likely to occur during successive load-unload scans, the FICs with larger amplitude peaks are more isolated FICs without clear precursor and successor FICs in human primary myoblasts than in C2C12 myoblasts. This suggests that the FICs with strong disruption events are unrelated to the next strong disruption events, as if the internal dynamics of the human primary myoblasts could recover faster from a previously disrupted local CSK domain. These observations require further confirmation when increasing the statistical size of the sampled cells.

From these indentation experiments on a rather small sample size, we have however reached the evidence that trying to compare the mechanics of human myoblasts from both healthy donor and DMD patients adherent on collagen coated surfaces may not be the best way to distinguish the presence or the lack of connection of the dystrophin-glycoprotein complex to either the extracellular laminin and/or the intracellular actin CSK. Actually, we should have probed the cells with cantilever tips with specific coatings (agrin or laminin) and let them adhere on the cell extracellular matrix and pulled out the AFM cantilever to test the robustness of the attachement (if any) of the cells with their actin network. The collagen adherent assays that we have chosen push the cells to construct actin stress fibers by the stimulation of focal adhesion *via* integrins, which do not produce the same actin stress fiber architecture as the one which must be established below the postsynaptic membrane of the NMJ. Actually, the transmembrane integrins which work in synergy with the dystrophin-dystroglycan complex for the connection of the intracellular CSK to extracellular laminin (α_3, α_6, α_7) are different from those which interact with type I collagen (α_1, α_2, α_{10}, α_{11}) [Hynes, 2002; Leitinger, 2011]. The integrin-binding specificities of laminins are primarily governed by their α-chains. Surprisingly, the increased staining intensities in $\alpha_7\beta_1$ in DMD patients and *mdx* mice, was suggested as an

alternative treatment to dystrophin or utrophin restoration by myoblast or virally mediated gene transfer. Burkin *et al.* [Burkin, 2001] showed that the percentage of muscle fibers with centrally located nuclei, was equivalent in the double mutants (dystrophin-utrophin) and those over-expressing the α_7 subunit, with however a 3-fold life-span increase together with a higher mobility of the mice over-expressing the α_7 subunit. This supports the view that the $\alpha_7\beta_1$ and the DGC complex are distinctive receptors (although very close to each other) but that an increased amount of $\alpha_7\beta_1$ is capable of stabilizing muscle function and improving the dystrophin-deficient phenotype. The richness and diversity of membrane integral proteins that link the CSK to the extracellular matrix in myotubes and myoblasts make these cells very sensitive to environmental cues. There is a strong topological and mechanical impact of the myoblast micro-environment on their differentiation and survival rate [Chiron, 2012]; actually a dynamic regulation of the cell-matrix stiffness determines the differentiation of myoblasts in myocytes. It should therefore be very interesting to test different micro-environments for their chemical composition (collagen, fibrin, fibronectin, laminin), their rigidity and their geometry (2D to 3D) to find those which could offer the best discrimination of HD and DMD myoblasts. Because we started working with primary human myoblasts in the last year of our experimental data collection, and because we did not have as much cell materials with primary cells, as compared to the C2C12 cell line, we could not perform all these tests on cell micro-environments.

Chapter 5

Materials and methods

5.1 Cell culture and differentiation

5.1.1 C2C12 myoblast culture

The C2C12 mouse cell line (American Type Culture Collection, Manassas, VA, number CRL-1772) was cultured in growth medium (GM) composed of high glucose (4,5 g/L) Dulbecco's Modified Eagle Medium with L-glutamine (DMEM, PAA, GE Healthcare Life Science, Munich, Germany) supplemented with 20 % fetal bovine serum (FBS, PAA), 1 % penicillin-streptomycin antibiotics (100 U/ml penicillin and 100 μg/ml streptomycin, Gibco, Thermo Fisher Scientific) and 10 mM HEPES (Gibco, Thermo Fisher Scientific). The GM was stored at 4°C up to 1 month; fresh GM medium was discarded and replaced every 2 days. The C2C12 cell line was maintained in a 5 % CO_2 atmosphere at 37 °C inside 90 mm diameter petri dishes until $\sim$ 70 % confluency. To avoid that 60-70 % confluent myoblasts differentiate spontaneously, the dishes were washed with preheated PBS and cells were detached from the dish bottom with 0.25 % trypsin-EDTA (Gibco, Thermo Fisher Scientific) for 3 minutes at 37 °C. Then the cells were harvested and either re-plated at lower concentration or frozen for storing.

In order to test the impact of different culture substrates on C2C12 myoblast morphology and differentiation, these cells were grown in GM at 37 °C with 5 % CO_2 on different adhesion supports: gold coated micro-slides, standard (SPD) and collagen coated petri dishes (CCPD). For AFM experiments, C2C12 myoblast cells ($\sim$ 1.5 10^5 cells from passages 10 to 14) were seeded on CCPDs (35 mm diameter) in GM and kept at least 24 hours at 37 °C with 5 % CO_2. Then the medium was changed and replaced by 2 ml of GM and the petri dish was transferred to the AFM. Each sample was used within 2 to 3 hours and discarded afterwards.

5.1.2 C2C12 myoblast differentiation

To induce myogenic differentiation, when C2C12 myoblasts grown on CCPD petri dishes reached 60 % confluency, the growth medium (GM) was replaced by the differentiation medium (DM) (differentiation time t_D), following to the standard protocol [Szustakowski, 2006; Lee, 2015; McClure, 2016; Shiozaki, 2016]. $\sim$ 60 % confluency was chosen because myogenic C2C12 myoblasts usually undergo one last mitosis before their withdrawal from the cell cycle. DM was composed of high glucose (4,5 g/L) Dulbecco's Modified Eagle Medium with L-glutamine (DMEM, PAA), supplemented with 2 % Donor Horse Serum (HS, PAA), 1 % penicillin-streptomycin antibiotics (100 U/ml penicillin and 100 μg/ml streptomycin, Gibco) and 10 mM HEPES (Gibco).

The C2C12 myoblast cells were maintained in DM at 37 °C with 5 % CO_2 for at least 5 days and the DM was replaced each 2 days. Different culture supports were used (glass bottom petri dishes, SPDs and CCPDs) to compare their impact on C2C12 cell myogenic differentiation.

C2C12 myoblast cell differentiation process was monitored by DIC and time-lapse video recording (121 hours recording, starting 1 hour before t_D). Multinucleated myotubes were observed with fluorescence confocal microscopy and probed by AFM at their 5th day of differentiation. A fusion index, defined as the percentage of nuclei contained in myotubes compared to the total number of nuclei observed in each image field, was used to quantify the degree of myotube formation in different culture conditions [Lee, 2013; Kamli, 2014]. The mean fusion index for each condition was averaged on 5 images selected at random (with the same magnification).

5.1.3 Primary human myoblast culture

Purified primary human myoblasts from a healthy donor (HD, Y075) and a patient affected by the Duchenne muscular dystrophy (DMD, V024) biopsies were courteously donated from Hospices Civils de Lyon (Centre de Biotechnologie Cellulaire, Groupement Hospitalier Est, Bron, France) after patient informed consent in accordance with the Declaration of Helsinki. When the biopsies were performed, the DMD patient was around 3 years old while the healthy donor was 72 year old. The DMD patient carried deletions of axons 48-52 in the dystrophin gene. Both types of cells were grown in proliferation medium (PM) at 37 °C with 5 % CO_2 on CCPDs. PM was composed of high glucose (4,5 g/L) Dulbecco's Modified Eagle Medium with L-glutamine (DMEM, PAA), supplemented with 20 % fetal bovine serum (FBS, PAA), 1 % penicillin-streptomycin antibiotics (100 U/ml penicillin and 100 μg/ml streptomycin, Gibco), insulin (10 μg/ml, Sigma), human basic fibroblast growth factor (hbFGF, 25 ng/ml, Sigma) and epidermal growth factor (EGF, 10 ng/ml, Sigma). The filtered PM was stored at 4 °C up to 1 month; fresh PM was replaced every 2 days. HD and DMD myoblasts were dissociated from the culture substrates either for routine subculture or for cryopreservation using 0.05% trypsin-EDTA (Gibco) for 3-5 minutes at 37 °C after replacement of PM with preheated PBS.

HD and DMD primary human myoblasts were seeded (2.5 x 10^4 cells from 2nd and 3th passages) on CCPDs (35 mm diameter) in PM and kept at 37 °C with 5 % CO_2 at least 24 hours before AFM recording. Then the medium was changed and replaced by 2 ml of PM and the petri dish was transferred to the AFM. Each sample was used within 2 to 3 hours and discarded afterwards.

5.1.4 Cell fixation

C2C12 myoblasts grown on CCPDs (35 mm diameter) were rinsed twice with preheated PBS and fixed with freshly made 4 % paraformaldehyde (PFA, Fluka, St. Louis, MO) in PBS for 20 minutes at room temperature (24 °C). Then the sample was maintained in 2 ml PBS before AFM measurements which lasted $\sim$ 4 hours at room temperature.

5.1.5 ATP depletion

Cultured cells use a combination of oxidative and glycolytic energy metabolism for ATP production. It is therefore necessary to inhibit both pathways to achieve a complete ATP depletion [Mandel, 1986]. We used concomitantly the inhibitor of mitochondrial electron transport chain

(ETC) complex III (antimycin A, AMA) [Nakayama, 1956; Pham, 2000; Ma, 2011; Rakhmatullina, 2015] and the glycolysis inhibitor (2-deoxy-D-glucose, 2-DG) [Bright, 1995; Pelicano, 2006; Fokt, 2009]. The ATP depletion buffer composition was: 140 mM NaCl, 5 mM KCl, 1 mM $MgCl_2$, 2 mM $CaCl_2$, 10 mM HEPES, 6 mM 2-DG (Sigma), 5 μM AMA (Sigma). The filtered solution was adjusted to pH 7.4 and stored at -20 °C. To induce ATP depletion C2C12 myoblasts were rinsed 2 times with preheated PBS before replacing the GM with the same amount of preheated freshly thawed ATP depletion buffer (2 ml). Cells were then kept in ATP depletion buffer for 15 minutes before use to allow the cellular ATP concentration to decrease below 7 % of its initial concentration as described by Theander et al. [Theander, 2002]. The AFM measurements were performed on each fixed cell sample within 2 ml of ATP-depletion buffer at room temperature for 2-3 hours, before throwing it away.

5.1.6 Blebbistatin treatment

C2C12 myoblasts were treated with (S)-(-)-Blebbistatin (Santa Cruz Biotechnology, Texas, USA) to inhibit the activity of the non-muscle myosin II [Straight, 2003; Allingham, 2005]. Aliquots of 100 μM blebbistatin dissolved in dimethylsulfoxide (DMSO) were stored at -20 °C. 2 ml volumes of GM supplemented with 50 μM blebbistatin were freshly prepared before use according to Griffin et al. [Griffin, 2004]. The GM of C2C12 myoblast was discarded and replaced with the same amount (2 ml) of preheated GM containing blebbistatin 20 minutes before fluorescent staining and AFM. During AFM experiments C2C12 cells were kept in 2 ml GM with 50 μM blebbistatin for approximately 2 hours and 30 minutes at room temperature.

5.2 Sample preparation

5.2.1 Collagen coating of petri dishes

Type I collagen aqueous solution (3 mg/ml) from bovine skin and tendon BioReagent (Sigma Aldrich, St. Louis, MO) was diluted in ultra-pure water up to the working concentration of 100 μg/ml before deposition on 35 mm diameter petri dishes. After 3 hours of contact with this solution (8 μg/ cm^2) at 37 °C to allow proteins to bind, the dishes were dried overnight at room temperature (24 °C) under hood and rinsed with Dulbecco's Phosphate Buffer Saline (PBS, Sigma) before use.

5.2.2 Gold coated micro-slide cleaning and cell deposition

High RI (1.648) coverslips were coated with a 1.5 nm chromium layer and a 45 nm gold layer by cathodic sputtering. Each gold coated micro-slide was cleaned carefully before cell deposition by rinsing with ethanol and drying under a stream of nitrogen. The slides were further cleaned by placing them in a UV ozone cleaner for 20 minutes and soaked in ultra pure ethanol for 30 minutes to deactivate the surfaces. All the slide manipulations were performed with a pair of flat-ended tweezers. 2.5 10^4 C2C12 myoblasts were seeded on the gold surface within their culture medium and kept 4 hours at 37 °C and 5 % CO_2 to let them adhere on the gold substrate before time-lapse DIC or SSPM microscopy imaging.

5.2.3 SSPM cell chamber preparation

Cleaned gold coated micro-slide were seeded with 2.5 x 10^4 C2C12 myoblasts and let in the culture medium for 4 hours at 37 °C with 5 % CO_2. The chamber for SSPM was sealed with a double face sticky spacer (Gene Frame, Thermo Fisher Scientific, Massachusetts, USA) after cell adhesion (bottom face: a gold coated coverslip, upper face: a second glass coverslip - volume of the chamber: 1cm×1cm×250 μm=25 μl). Two types of SSPM observations were performed: (i) time-lapse living myoblast SSPM imaging and (ii) fixed myoblast imaging for reconstruction of high resolution Z scans and extraction of optical index values. The fixation of myoblasts was performed with 4 % paraformaldehyde (PFA, Sigma) for 20 minutes at room temperature after rinsing the sample twice with preheated PBS. Fixed myoblasts were covered with 25 μl of PBS while living myoblasts were maintained in 25 μl of culture medium.

5.3 Optical microscopies for cell visualisation

5.3.1 Differential interference contrast microscopy

Differential interference contrast (DIC) microscopy imaging and time-lapse recording were performed with an inverted Zeiss Axiovert 135 microscope available of the imaging platform PLATIM (UMS3444, BioSciences Gerland, Lyon, France), equipped with a charge-coupled device (CCD) camera Leica DC350 FX (Leica Microsystems GmbH, Germany) and 2.5X/0.075 NA, 10X/0.25 NA, 20X/0.75 and 40X/1.3 NA (NA= numerical aperture) Zeiss objectives. For each specimen and each magnification, 10 images of 1388 x 1040 pixels were captured. Time-lapse videos were carried out by recording 1 DIC image of 1388 x 1040 pixels every 30 seconds during 8 hours. DIC images were processed with ImageJ 1.47v program (i) to transform them for further Matlab analysis (high rate video recording at 30 frames per second) or (ii) to estimate the morphological parameters such as the length (the longest side), the width (the shortest side) and the area of cells and of their nuclei (ImageJ measurement toolbox). Morphological measurements were carried out on 30 cells (n= 30) for each experimental condition. The cell (resp. nucleus) aspect ratio was calculated as the ratio between the cell (resp. nucleus) length and its width. The area ratio, defined as the ratio between the cell and the nucleus areas, was also computed for 30 cells for each condition. Statistical analysis was performed with Matlab R2012a (MathWorks, Natick, MA) and the data were reported as mean ± standard deviation (SD) for each condition. Statistical significant difference (marked as **) between two datasets was determined by paired Student's t-test with $p < 0.05$ and applied to compare all datasets.

5.3.2 Fluorescence confocal microscopy

Fluorescence confocal microscopy imaging was performed with the inverted scanning confocal microscope Confocal Spectral LSM710 (ZEISS, Oberkochan, Germany) available at the imaging platform PLATIM, equipped with a motorized X-Y stage and a set of ZEISS objectives with magnification from 10X to 63X. Fluorescent images (1224 x 900 pixels) were collected using a 405 nm blue-violet laser diode to visualize DAPI and AMCA, a 488 nm argon laser to detect Alexa Fluor 488, and a 561 nm diode-pumped solid state (DPSS) laser to capture Cy3. The excitation and the fluorescence signal acquisition of each fluorophore was executed in sequential multi-tracking channels in order to avoid bleed-through crossover artefacts. Saturation was checked and avoided using range indicators of the Zen software. The scan speed and image

averaging were optimized before image acquisition in order to have the highest signal-to-noise ratio for a minimum cost of time. Z-Stack images of 9 μm $\pm$ 3 μm depth with 0.5 μm interval between each slice were acquired with the Zen software. ImageJ 1.47v processing program was used to analyze the confocal microscopy images and to reconstruct the Z projections of stained cells.

5.3.2.a Fluorescent staining

Fluorescent labelling of specific intracellular structure of C2C12 cells was performed combining immunofluorescence and non-antibody labelling techniques. Adherent C2C12 myoblasts ($\sim 10^5$) and confluent myotubes on 35 mm diameter CCPD were rinsed twice with preheated PBS and fixed with freshly made 4 % paraformaldehyde (PFA, Fluka) in PBS for 20 minutes at room temperature (RT). The samples were then permeabilized with 0.05 % Triton X-100 (Euromedex, Souffelweyersheim, France) in PBS for 10 minutes at RT before being saturated with 1 % bovine serum albumins (BSA, Sigma) in PBS and kept 30 minutes at RT. The samples were stained either for F-actin, β-tubulin and nucleus, or for the three cytoskeleton filaments according to the two following protocols. In the fist case, after incubation with mouse monoclonal Cy3-conjugate anti-β-tubulin (Sigma) diluted 1:200 in 1 % BSA PBS for 1 hour at RT in a humid and dark chamber, the cells were incubated with phalloidin-Alexa Fluor 488 (Molecular Probes, Life Technologies Carlsband, CA) diluted 1:100 in 1 % BSA PBS for 15 minutes at RT in a humid and dark chamber. Finally, the samples were sealed with glass cover-slides and VectaShield mounting medium (Vector Laboratories, Burlingame, CA) with DAPI (4',6-diamino-2- phenylindole) and stored at least for 10 minutes at 4 °C. In the second case before β-tubulin staining, the cells were incubated with mouse monoclonal anti-desmin (DAKO, Agilent Technologies, California, USA) diluted 1:200 in 1 % BSA PBS over night in humid chamber at 4 °C. The day after, incubation with AMCA-conjugated goat secondary antibody anti mouse (Jackson ImmunoResearch, Suffolk, UK) diluted 1:1000 in 1 % BSA PBS was carried out for 1 hour at RT in a humid and dark chamber. Then the labelling of β-tubulin and F-actin was performed similarly to previous protocol before sealing the samples with glass cover-slides and VectaShield mounting medium without DAPI and storing them at least 10 minutes at 4 °C. In both protocols the samples were gently rinsed with PBS 3 times for 5 minutes between each step.

5.3.3 Surface plasmon microscopy

Scanning surface plasmon microscopy (SSPM) is an optical microscopy technique that uses the surface plasmon resonance (SPR) to detect minute index variations at the interface between a gold layer and a dielectric medium [Otto, 1968; Kretschmann & Raether, 1968; Raether, 1988]. In particular, SSPM exploits guided transverse electromagnetic surface waves that propagate along a metal-dielectric interface surface named plasmon polaritons (SPP). Different SSPM set-ups have been developed in the team at ENS Lyon, Laboratory of Physics from the early 2000s and applied to nanoparticles, biological macromolecules and living cell imaging [Elezgaray & Argoul, 2005; Berguiga, 2007; Zhang, 2007; Berguiga, 2009; Roland, 2009, 2010; Elezgaray, 2010; Argoul, 2010; Berguiga, 2011; Argoul, 2012; Berguiga, 2013a,b; Boyer-Provera, 2013; Elezgaray, 2014; Berguiga, 2016]. A SSPM coupled to an inverted microscope stand [Berguiga, 2016], equipped with a high numerical aperture objective lens, a radial polarization illumination, a fibered heterodyne interferometer and a 3D (X, Y, Z) piezoelectric scanning device was used for time-lapse imaging of living adherent C2C12 myoblasts deposited on gold coated glass surfaces and con-

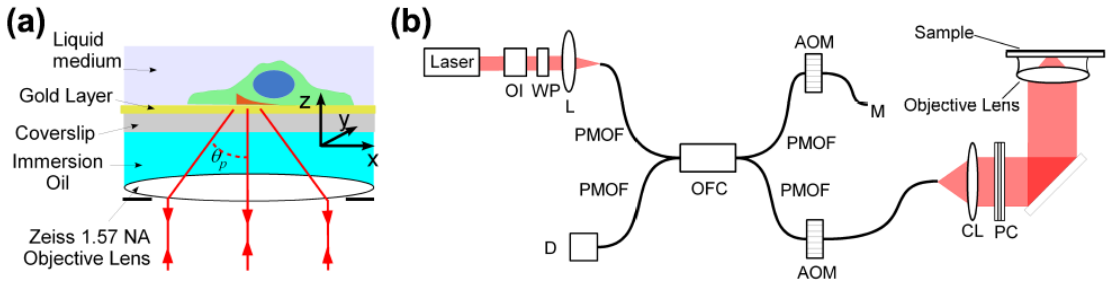

Figure 5.1: **SSPM set-up.** (a) Sample configuration with the SPP excitation through a 1.57 numerical aperture (NA) (Carl Zeiss Microscopy GmbH) objective lens. (b) Microscope set-up with the fibered heterodyne interferometer: OI: optical isolator, WP: $\lambda/2$ wave-plates, L: lens, PMOF: polarization-maintaining optical fiber, OFC: optical fiber coupler, AOM: acousto-optic modulator, D: detector, CL: collimating lens. Adapted from [Berguiga, 2016].

fined inside sealed chambers (Section 5.2.3). The SSPM set-up is shown in Fig 5.1. The high numerical aperture (NA) objective lens is coupled to the liquid chamber with an index-matching oil (Carl Zeiss Microscopy GmbH). The combination of a radial polarization illumination and a fibered heterodyne interferometer improved the spatial resolution and the temporal stability of this microscope respectively. This is particularly interesting for the characterization of the dynamics of living cells, given that a full resolution (500x500 pixels) image capture takes about one minute. The range of temporal scales affordable by this microscopy is more than three decades (one minute to $\sim$ 3000 minutes), without detectable drift of the optical set-up. The scanning height Z was set at 0.4 μm to optimize the imaging contrast in the near field of SPP [Berguiga, 2016]. SSPM images were recorded on living C2C12, at room temperature, during 50 hours with a time step of 65 s. More information about this SSPM instrument and its application on monitoring the temporal deformation of C2C12 myoblast adhesion dynamic and protrusion contours during their migration on gold surface can be found in [Berguiga, 2016] and [Streppa, 2016].

5.4 Atomic force microscopy

5.4.1 AFM equipment

A CellHesion 200 Atomic Force Microscope (AFM, JPK Instruments, Berlin, Germany) coupled to a transmission inverted microscope and a CCD camera (The Imaging Source Europe, Bremen, Germany) was used for nano-indentation experiments. The apparatus was equipped with a X-Y Motor Precision Stage (JPK) with 20×20 mm motorised stage, a vibration isolation table (Melles Griot, Albuquerque, NM), a foam-based acoustic isolation system and a white light LED illumination (Thorlabs, Model MCWHLS, Newton, New Jersey). The AFM Z-piezotransducer with movement range of 100 μm was controlled by a closed loop feedback system with sub-nanometric precision. Proportional gain (P gain) was settled at 20 and integral gain (I gain) at 0.002.

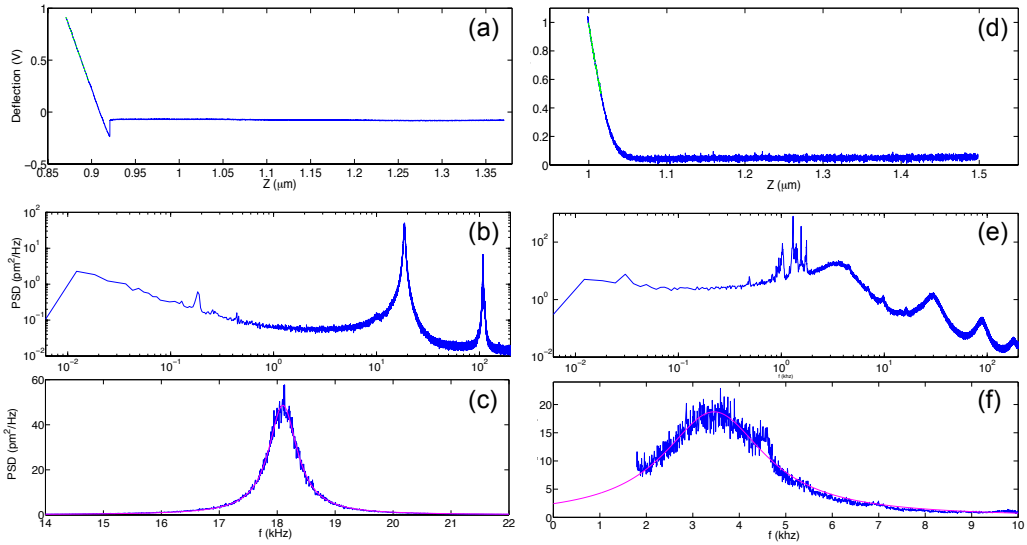

Figure 5.2: **Illustration of a SNL-10 triangular cantilever calibration**. Calibration of the same AFM probe in air (a - c) and in liquid (d - f). Estimation of the deflection sensitivity of the cantilever using the slope of the loading curves of FICs recorded when indenting (a) a clean glass surface in air and (d) a collagen coated petri dish in growth medium (GM). Power spectral density of the same cantilever thermal (unforced) fluctuations in air (b) and in GM (e). First mode resonance peaks (blue) and their fittings with Lorentzian functions (magenta) in air (c) and liquid (f). Air (resp. liquid) deflection sensitivity: 41.7 nm/V (resp. 32.4 nm/V); first mode resonance frequency: 18.1 kHz (resp. 3.9 kHz); $k = 0.068$ N/m (resp. 0.05 N/m).

5.4.2 AFM probes and their calibration

We used two types of AFM probes: (i) triangular gold-coated silicon nitride cantilevers from Sharp Nitride Lever (SNL-10, Bruker, Camarillo, CA) with nominal spring constant of 0.06 N/m (min= 0.03 N/m; max= 0.12 N/m) and typical resonant frequency in air: 18 ± 6 kHz; (ii) rectangular partially gold-coated quartz cantilevers (qp-CONT 20, Nanosensors^{TM}, Neuchatel, Switzerland) with nominal spring constant of 0.1 N/m (min = 0.08 N/m; max= 0.15 N/m) and typical resonant frequency in air: 30 ± 4 kHz. Before each experiment, cantilever calibration was carefully performed both in air, to verify the correct positioning of the probe and the proper system alignment, and in liquid to estimate the cantilever spring constant (k). First, the deflection sensitivity (nm/V) of the cantilever-photodiode system was evaluated using the in-contact part of force indentation curves (FICs) on a clean glass surface (5 FICs collected in both air and in liquid). Then the cantilever spring constant was estimated in air and in liquid by the thermal noise method as shown in Fig. 5.2 [Sader, 1995; Hutter, 2005; Sader, 2012]. From the thermal fluctuations of the cantilever, we can get an estimation of its spring constant k [Sader, 1995], assuming energy equipartition and harmonic oscillations:

$$k = \frac{k_B T}{\langle d^2 \rangle} , \tag{5.1}$$

where $\langle d^2 \rangle$ is the mean square displacement of the cantilever from its neutral position, T the absolute temperature in Kelvin and k_B the Boltzmann's constant. Since AFM cantilevers have

different geometries and several vibration modes, a correction factor β_n must be included in Eq. 5.1 [Stark, 2001]:

$$k = \frac{k_B T}{\langle d^2 \rangle} \beta_n \ , \tag{5.2}$$

where the factor β_n varies according to the vibration mode and the cantilever geometry. The value $\beta_n = 0.817$ (resp. 0.778) was used for rectangular (resp. triangular) cantilevers.

To summarise, we computed the power spectral density (PSD) of the AFM cantilever stochastic fluctuations 100 μm away from the sample surface (Figs 5.2(b, e)), showing the two first mode peaks of a triangular AFM cantilever (SNL-10 Bruker) in air and in liquid. By fitting the first mode peak with a Lorentzian function we computed the area under the resonance peak which is equivalent to $\langle d^2 \rangle$, from which the cantilever spring constant k was calculated with Eq. (5.2). These computations were performed with home-made programs written in Matlab.

5.4.3 AFM FIC recording

5.4.3.a FICs recorded with different cantilever scan velocities

Force indentation curves (FICs) were recorded with conical tip located at the far end of triangular cantilever SNL-10, (nominal $k \sim 0.06$ N/m) when indenting both C2C12 myoblasts and myotubes on different spots above their nuclear region (nuclear domain - NUC-D). The distance between the different probed spots was ~ 2 μm. Five different ranges of increasing indentation velocities (V_0) were tested: for myoblasts (i) 0.1, 0.25, 0.5, 1, 2, 4, 6, 8 and 10 μm/s; (ii) 0.1, 0.25, 0.5, 1, 2 and 4 μm/s; (iii) 0.1, 0.25, 0.5, 1, 2, 4, 8, 16, 32 and 64 μm/s; for myotubes (iv) from 0.25 to 8 μm/s with an interval of 0.25 μm/s and (v) 0.25, 0.5, 1, 2, 4 and 8 μm/s. For each speed, 10 FICs were collected with a force set point of 9 ± 1 nN. Between each 10 FIC recording series, the sampling rate was adjusted to collect the same amount of data points (20000 ± 200) for each FIC. For technical reasons, the cantilever vertical travel range ΔZ was enlarged at the highest velocities to avoid spending too much time for scan at lower speeds, *e. g.* $\Delta Z = 3$ μm for $V_0 = 0.1$ μm/s, 4 μm for $V_0 = 0.25$ and 0.5 μm/s, 5 μm for $V_0 = 1$, 2, 4 and 6 μm/s, 10 μm for $V_0 > 6$ μm/s.

5.4.3.b FICs recorded at fixed cantilever scan velocities

Single FICs were recorded on the same cellular location (30 curves on each position), indenting different zones above the nucleus (NUC-D) and the cytoskeleton (cytoskeletal domain - CYT-D). The same FIC recording was used for normal, fixed, ATP depleted and blebbistatin treated C2C12 myoblasts. In some cases, the same cell was indented before and after treatment, such as in the cases of ATP depletion and blebbistatin treatment. C2C12 myotubes at the 5th day of differentiation were also probed in their NUC-D and CYT-D domains with single FICs repeated 30 times, as well HD and DMD myoblasts. The force set-point was fixed to 8 ± 2 nN to probe NUC-D and at 3 ± 1 nN to probe CYT-D. The indentation scan velocity V_0 was fixed (1 μm/s), the cantilever displacement range ΔZ was limited to 6 ± 2 μm and the time rate FIC recording was chosen to store 20000 ± 200 data points for each FIC (loading and unloading).

5.4.3.c Maps of FICs acquisition

Maps of FICs were recorded using a square grid of 25 μm^2 (10×10 pixels). Due to the limited resolution of our $X - Y$ JPK Motorized Precision stage, we fixed a minimum pixel

separation = 500 nm. The grid was constructed starting at the upper left corner and scanning with alternating directions on successive lines. Given a fixed pause of 2 s to move from one pixel to the next one, a full map took 20 minutes (10×10 pixel grid). The force set-point was fixed to 3 nN and 100 FICs were recorded for each map. The indentation speed was fixed to 1 μm/s, the cantilever displacement length ΔZ to 6 μm and 20000 $\pm$ 200 data points were recorded for each FIC. AFM FIC maps were collected for C2C12 myoblasts, myotubes at the 5_{th} day of differentiation and daily during the differentiation process.

5.4.4 FIC analysis

The analysis of FICs required a set of numerical treatments to extract the correct mechanical parameters describing the relaxation response (under constant velocity indentation) of a living cell.

5.4.4.a Hydrodynamic drag and baseline drift correction

The first step was to eliminate the drift of the FICs which may result from either a misalignment of the laser photodiode beam on the tip of the cantilever or from an hydrodynamic drag produced by the liquid surrounding the cantilever. This second aspect is discussed in Section 2.6.3. The elimination of the drift coming for optical misalignments was performed from a parametrisation of the sum of the loading and unloading curves, far from the contact zone of these curves. If we can assume that the hydrodynamic drag inflects similarly the loading and the unloading curves, by summing them we simply eliminate it and we can correct other sources of drift of the FICs.

Once this correction was performed, we concentrated on the hydrodynamic drag correction. For that purpose, we computed the difference of the loading and unloading curves, far from the contact zone (more than 500 nm before the contact point). This difference is equal to twice the hydrodynamic drag F_d (Eqs (2.58) and (2.61)). We considered a length of the FIC out-of-contact zone shorter than 1-2 μm that allowed us to approximate Eq. (2.61) by a linear equation (Eq. (2.62)), from which we could determine the parameter H^*_{off}.

5.4.4.b Wavelet-based decomposition of FICs

The second step was to filter the signal to get rid of the background noise and to transform the FIC in order to facilitate its modeling. We used the continuous wavelet transform that indeed performed both tasks simultaneously. We applied the wavelet transform systematically on each FIC before any further analysis and modeling attempt.

The wavelet transform is a mathematical time-frequency (time-scale) decomposition of signals introduced in the early 1980s [Grossmann & Morlet, 1984]. The wavelet transform has been applied to a great variety of situations in physics, physical chemistry, biology, signal and image processing, material engineering, mechanics, economics, epidemics ... [Meyer, 1992; Daubechies, 1992; Arneodo, 1995; Mallat, 1998; Arneodo, 2002, 2008, 2011]. Real experimental signals are very often nonstationary (they contain transient components), and when they are complex or singular, they may also involve a rather wide range of frequencies. It also happens that experimental signals display characteristic frequencies that drift in time. Standard Fourier analysis is therefore inadequate in that situations, since it provides only statistical information about the relative contributions of the frequencies involved in the analyzed signal. The possibility

to perform simultaneously a temporal and frequency decomposition of a given signal was first proposed by Gabor for the theory of communication [Gabor, 1946]. Later on, two distinct approaches (based on different wavelet transforms) were developed in parallel: (i) a continuous wavelet transform (CWT) [Grossmann & Morlet, 1984; Mallat, 1998] and (ii) a discrete wavelet transform (DWT) [Daubechies, 1992]. For singular (self-similar or multi-fractal) signals or images, the CWT transform rapidly became a predilection mathematical microscope to perform space-scale analysis and to characterize scale invariance properties. In particular it was used to elaborate a statistical physics formalism of multifractals [Muzy, 1994; Delour, 2001; Audit, 2002; Arneodo, 1995, 2008].

For about 30 years, my host team has been pioneering the use of the CWT for biological applications, on both 1D signals and 2D images [Arneodo, 2002, 2008, 2011]. As far as 1D signals are concerned, the CWT was applied to AFM force curves collected from single living plant cells [Digiuni, 2015], living hematopoietic stem cells [Laperrousaz, 2016a,b] and to AFM fluctuation signals to characterize the passive microrheology of living myoblasts [Martinez-Torres, 2016]. The 1D CWT was also generalized to 2D (and to 3D) CWT and it proved again its versatility and power for analyzing AFM topographic images of biosensors [Roland, 2009], fluorescence microscopy images of chromosome territories [Khalil, 2007] and diffraction phase microscopy of living cells [Martinez-Torres, 2014, 2015]. We did not use the 2D CWT in this PhD thesis. I will therefore simply revisit here the 1D CWT formalism with special emphasis on the analyzing wavelets we used to analyze the AFM force indentation curves.

Within the norm $\mathcal{L}^1$, the one-dimensional WT of a signal $F(Z)$ reads:

$$W_\psi[F](b,s) = \frac{1}{s}\int_{-\infty}^{\infty} F(Z)\psi^*(\frac{Z-b}{s})dZ \ , \tag{5.3}$$

where b is a spatial coordinate (homologous to Z) and s (> 0) a scale parameter. A typical admissible (of null integral) analyzing wavelet $\psi(Z)$ is the second derivative of a Gaussian $g^{(0)}(Z) = e^{-Z^2/2}$, also called the Mexican hat wavelet:

$$g^{(2)}(Z) = -\frac{d^2}{dZ^2}g^{(0)}(Z) = e^{-Z^2/2}(1-Z^2) \ . \tag{5.4}$$

Via two integrations by part, it is straightforward to demonstrate that the WT $W_{g^{(2)}}[F](b,s)$ of F with the second derivative of a Gaussian wavelet at scale s is precisely the second derivative of a smoothed version $W_{g^{(0)}}[F](b,s)$ of F by a Gaussian function at the same scale s:

$$W_{g^{(2)}}[F](b,s) = s^2\frac{d^2}{db^2}W_{g^{(0)}}[F](b,s) \ . \tag{5.5}$$

Let us define the first derivative of the Gaussian function:

$$g^{(1)}(Z) = -\frac{d}{dZ}g^{(0)}(Z) = Ze^{-Z^2/2} \ , \tag{5.6}$$

and its third derivative:

$$g^{(3)}(Z) = -\frac{d^3}{dZ^3}g^{(0)}(Z) = Z(3-Z^2)e^{-Z^2/2} \ . \tag{5.7}$$

With the first and the third derivatives of F we can write similar relations to Eq. (5.5) for the

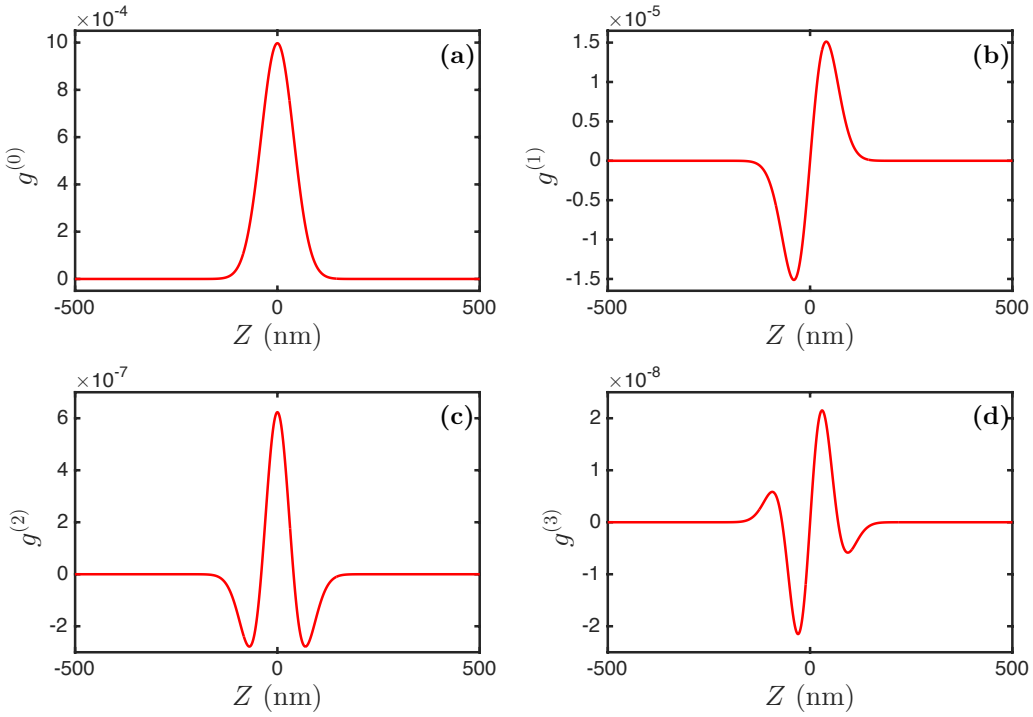

Figure 5.3: **Analyzing wavelets constructed from a Gaussian function** (a) Gaussian function $g^{(0)}$. (b) First derivative of a Gaussian $g^{(1)}$ (Eq. (5.6)). (c) Second derivative of a Gaussian $g^{(2)}$ (Eq. (5.4)). (d) Third derivative of a Gaussian $g^{(3)}$ (Eq. (5.7)).

WTs of the odd order derivatives of F [Muzy, 1994; Arneodo, 2002, 2011]:

$$W_{g^{(1)}}[F](b,s) = s\frac{d}{db}W_{g^{(0)}}[F](b,s)\ , \tag{5.8}$$

and

$$W_{g^{(3)}}[F](b,s) = s^3\frac{d^3}{db^3}W_{g^{(0)}}[F](b,s)\ . \tag{5.9}$$

These four analyzing wavelets are shown in Fig. 5.3. The zero and second-order derivatives of the Gaussian ($g^{(0)}$ and $g^{(2)}$) are symmetric functions, the first and the third-order derivatives ($g^{(1)}$ and $g^{(3)}$) are asymmetric. When we increase the order of derivation the number of extrema of the wavelet increases from 1 to 4.

Let us point out that the validity of the WT definition (Eq. (5.3)) was further extended for distributions including Dirac distributions [Mallat & Hwang, 1992; Muzy, 1994]. The interest of the WT method is two-fold. The first advantage is to use the same smoothing function to filter out the experimental background noise and to compute higher-order derivatives (for instance up to third-order in this study) at well defined smoothing scales s_g. The second advantage relies on the power of the WT to detect local singularities (including rupture events in the FICs) and to quantify their force via the estimate of local Hölder exponents from the behavior across scales of the WT modulus maxima (WTMM) [Mallat & Hwang, 1992; Muzy, 1994; Mallat, 1998; Delour, 2001; Audit, 2002; Arneodo, 2002, 2008, 2011]. In this study, we used modified versions of the definition (Eq. (5.3)) of the WT to get a direct measure of F in nN ($T_{g^{(0)}}[F](b,s)$),

dF/dZ in nN/nm ($T_{g^{(1)}}[F](b,s)$), d^2F/dZ^2 in Pascal ($T_{g^{(2)}}[F](b,s)$) and d^3F/dZ^3 in Pascal/nm ($T_{g^{(3)}}[F](b,s)$), once smoothed by a Gaussian window ($g^{(0)}(Z)$) of width s:

$$T_{g^{(0)}}[F](b,s) = W_{g^{(0)}}[F](b,s) \ , \tag{5.10}$$

$$T_{g^{(1)}}[F](b,s) = \frac{1}{s} W_{g^{(1)}}[F](b,s) \ , \tag{5.11}$$

$$T_{g^{(2)}}[F](b,s) = \frac{1}{s^2} W_{g^{(2)}}[F](b,s) \ , \tag{5.12}$$

$$T_{g^{(3)}}[F](b,s) = \frac{1}{s^3} W_{g^{(3)}}[F](b,s) \ . \tag{5.13}$$

Fig. 5.4 illustrates on a single FIC (loading and unloading curves) the computation of the wavelet-based force derivatives and their parametrization with a nonlinear elasto-plastic model (Eq. (2.64)). The first derivative of the FIC (Fig. 5.4(d)) is preferred to the FIC (Fig. 5.4(b)) for the parametrization because it is more efficient to distinguish the two classes of behaviour (elasto-plastic nonlinear deformation or viscoelastic exponential type relaxation). To perform this systematic classification of FICs numerically, we also computed the second and third derivatives of the FIC (Fig. 5.4(c,e,f)).

5.4.4.c Contact point detection

A key issue in the analysis of AFM FICs is the determination of the scan position Z_c where the cantilever tip comes in contact with the tested material, such as a living cell. This quantity is used in particular as a lower bound for the work integral Eq. (2.70) and as an upper bound for hydrodynamic drag correction. To master this question, we used a wavelet transform decomposition of the FICs (Section 5.4.4.b). For a given width of the analyzing wavelets $g^{(0)}$ and $g^{(1)}$, we computed the smoothed force $T_{g^{(0)}}[F]$ and its derivative $T_{g^{(1)}}[F]$, and we estimated the contact position Z_c where these two functions cross a given threshold. These thresholds were estimated from different values s_g, as a compromise to keep the transition from out-of-contact to in-contact as sharp as possible in the force derivative $T_{g^{(1)}}[F]$ and to smooth the background noise. For all the force curves analyzed in this work, we used a lower threshold of $5\ 10^{-5}$ nN/nm with a $g^{(1)}$ wavelet size of $2\sqrt{2}s_{g^{(0)}} = 110$ nm.

5.4.4.d Cantilever spring constant correction

When the force derivative is no longer negligible as compared to the cantilever spring constant k, the FICs must be corrected according to the following equation [Cappella & Dietler, 1999]:

$$Z - Z_c = h + F/k \ . \tag{5.14}$$

The nominal spring constant of the cantilever ($k \in$ [0.04nN/nm to 0.1 nN/nm]) was chosen large enough for the cantilever deflection to be small compared to the cell deformation. Nevertheless, we have subtracted the correcting term from the FICs for energy integral computation. Note that this correcting term does not affect the computation of the second-order derivative of the force.

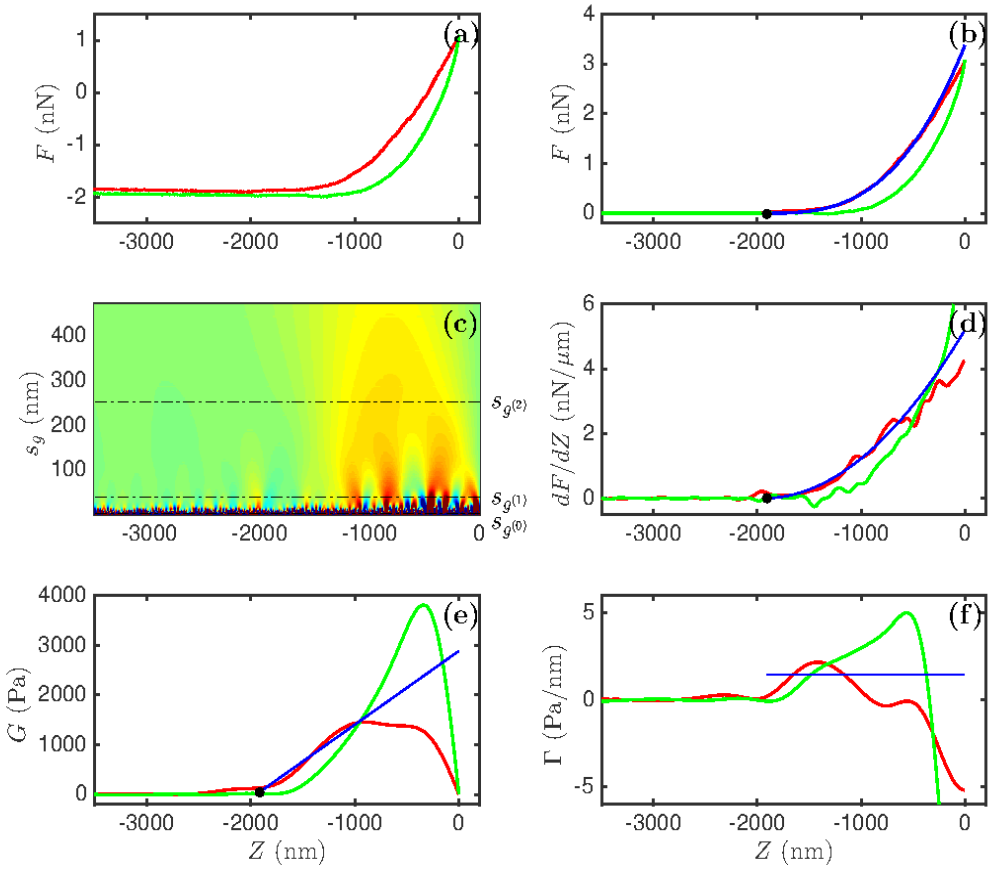

Figure 5.4: **Illustration of the wavelet-based analysis of AFM FICs.** (a) Raw FICs recorded from a living myoblast cell (loading curve: red, unloading curve: green). (b) FICs after tilt and hydrodynamic drag correction. These FICs have also been filtered by a Gaussian of width $2\sqrt{2}s_{g^{(0)}} = 9$ nm. (c) Scale-space representation of the wavelet transform of the loading FIC with the second derivative $g^{(2)}$ of the Gaussian function. The wavelet scales $s_{g^{(0)}}$, $s_{g^{(1)}}$ and $s_{g^{(2)}}$ ($s_{g^{(2)}} = s_{g^{(3)}}$) used for the FIC are outlined with black dashed-dotted lines. Rainbow colorscale from black to red: [-5000, 5000]. (d) First derivative of the loading FIC, computed with the first derivative $g^{(1)}$ of the Gaussian function of width $2\sqrt{2}s_{g^{(1)}} = 110$ nm. (e) Second derivative of the loading FIC, computed with the second derivative $g^{(2)}$ of the Gaussian function of width $2\sqrt{2}s_{g^{(2)}} = 710$ nm and expressed in Pa units (Eq. (5.19)) (f) Third derivative of the loading FIC, computed with the third derivative $g^{(3)}$ of the Gaussian function of width $2\sqrt{2}s_{g^{(3)}} = 710$ nm and expressed in Pa/nm units (Eq. (5.20)). The blue curves correspond to a nonlinear elasto-plastic parametrization performed on the first derivative of the FIC (Eq. (2.64)).

5.4.4.e Integral representation of force-indentation curves

Viscoelasticity theories developed in the second half of the twentieth century [Graham, 1965, 1967; Cheng & Cheng, 2004] have led to general hereditary integral representation of stress-strain relationships for the indentation of linear viscoelastic materials by axisymmetric indenters:

$$F(t) = \frac{4}{1-\nu} C_n \int_0^t G_r(t-\tau) \frac{dh^{(n+1)/n}(\tau)}{d\tau} d\tau \ , \tag{5.15}$$

where $G(t)$ is the stress relaxation modulus, F is the loading force, h describes the displacement of the indenter $h = Z - Z_c$, and n is a positive integer which depends on the shape of the indenter. The stress relaxation modulus $G(t)$ retains the strain-rate memory of the deformation. For a pyramidal indenter tip, we have $n = 1$ and $C_1 = \tan\theta/\pi$, where θ is the nominal tip half-angle:

$$F(t) = \frac{4\tan\theta}{\pi(1-\nu)} \int_0^t G_r(t-\tau) \frac{dh^2(\tau)}{d\tau} d\tau \ . \tag{5.16}$$

Since the cantilever is swept at constant velocity V_0, $dZ = V_0 dt$, the stress relaxation modulus G can be rewritten as (Eq. (2.53)):

$$G(Z) = \frac{\pi(1-\nu)}{8\tan\theta} \frac{d^2F(Z)}{dZ^2} \ , \tag{5.17}$$

meaning that the variation of G with Z is an important quantity which keeps the memory of the whole deformation. Eq. (5.17) establishes that the stress relaxation modulus can be obtained from the second order derivative of the FIC with respect to Z, without assuming *a-priori* a particular viscoelastic or plastic cellular model. This approach is therefore particularly attractive for living cells which cannot be wittled down to a combination of springs and dashpots. However, even if Eqs (5.15) to (5.17) are limited to linear viscoelastic regimes, we can still use Eq. (5.17) to compute the local curvature of FICs.

To distinguish between strain-stiffening and strain-softening behavior, we have also used the sign of the local curvature of the FIC derivative defined from the third-order derivative of the FIC $\Gamma(Z)$:

$$\Gamma(Z) = \frac{\pi(1-\nu)}{8\tan\theta} \frac{d^3F(Z)}{dZ^3} \ . \tag{5.18}$$

From Eqs (5.12) and (5.17), the shear relaxation modulus can be computed as:

$$G(Z) = \frac{\pi(1-\nu)}{8\tan\alpha} T_{g^{(2)}}[F](Z,s) \ . \tag{5.19}$$

In the same way, from Eqs (5.13) and (5.18) its derivative $\Gamma(Z)$ can be computed as:

$$\Gamma(Z) = \frac{\pi(1-\nu)}{8\tan\alpha} T_{g^{(3)}}[F](Z,s) \ . \tag{5.20}$$

Chapter 6

Conclusions and perspectives

6.1 Conclusions

This multidisciplinary thesis was aimed at developing an innovative AFM-based method for characterizing the mechanical properties of single muscle precursor cells, focusing on their global and local dynamical mechanical responses upon indentation with sharp tip cantilevers. The final ambition of this work was the application of this method to compare the mechanical behavior of normal (HD) and dystrophic (DMD) primary human myoblasts.

The guiding principle that came out from Chapters 2 and 3 was to demonstrate from indentation experiments, mathematical analysis and modeling that a layer of adsorbed living cells is not an homogeneous, time invariant and reproducible system and that it can behave contrastingly as elastic, viscoelastic or elastoplastic, depending not only on the state of the cell and its environment but also on the temporal and spatial scales at which an AFM cantilever interacts with it.

- A larger distances, before the direct contact with the cells adherent on collagen coated coverslips, the cell layer introduces an additional damping term to the classical solid wall damping force due to its viscoelasticity. Interestingly, we demonstrated that this additional damping force still exists at very low scan velocity (namely from 0.5 to 1 μm/s) and therefore that it was essential to subtract this damping force from the AFM force indentation curves (before but also after cantilever tip contact with the cells).

- In close contact with the cell, for rather deep cell indentations above the perinuclear area, studying the modification of the force-indentation curves (FICs) provided the evidence that some cells (two myoblasts in this example) tend to adopt an elastic to elasto-plastic response and that other cells (two myotubes in this example) instead behave as viscoelastic. Actually, beyond this simplistic classification based only on a global (large scale response) and averaged response (over several FICs), we realized that some cells were able to sustain the deformation for long distances (elastic or slightly elastoplastic responses over the whole indentation) whereas other cells reached quite rapidly a saturation of their force curve derivatives which was suspected to be the signature of a progressive loss of their initial compliance to deformation.

From these conclusions, we elaborated in Chapter 3 on a completely original space-scale analysis of the FICs based on the application of the wavelet transform with analysing wavelets of different orders. This analysis allowed us to focus on the local events (non stationarity of the FICs,

change of curvature of the FICS, disruption events) for each FIC and to follow their temporal changes from one load-unload force scan to the next one on a given cell. This meticulous study enlightened unexpected phenomena (disruption events) which could occur at shallow or deep indentation depths, depending on the apparent compliance of the considered cells. At that stage of our study, the notion of global stiffness of the cells was no longer telling us how they could sustain the deformation in time, since our statistical analysis on a larger set of cells showed that the accumulation of disruption events would finally end on the saturation of the force first-order derivatives, that we had interpreted as a viscoelastic response of the cell.

Interestingly, our initial simplistic classification in elastoplastic and viscoelastic cells (Chapter 2) turned out to be cell-type independent. In particular, among myoblasts (resp. myotubes), ~ 46 % (resp. ~ 26 %) of the FICs showed these local failure events, while the cells (indifferently myoblasts or myotubes) which were able to sustain large local deformations without failures appeared stiffer and more elastic upon indentations. These findings indicated that myoblasts and myotubes probably share common cytoskeleton (CSK) features, such as the cross-linkage of the perinuclear CSK F-actin stress-fiber network (that ensures the elasticity of this region surrounding the nucleus). In particular, the decreased local rupture probability observed in myotubes could be interpreted as an incomplete reorganization of the perinuclear F-actin stress fibers.

Globally, considering undisrupted FICs, the myotubes behaved as more elastic $\overline{\langle E \rangle} = 3\overline{\langle G \rangle} = 9.3 \pm 1.2$ kPa (assuming a constant Poisson coefficient $\nu = 0.5$) with a smaller dissipation loss $\overline{D_l} = 0.28 \pm 0.02$, as compared to myoblasts $\overline{\langle E \rangle} = 4.7 \pm 0.7$ kPa with a higher dissipation loss $\overline{D_l} = 0.39 \pm 0.02$. Interestingly, the depletion of ATP resource in myoblasts did not change much their elasticity $\overline{\langle E \rangle} \sim 4.2 \pm 0.6$ kPa, with a slight increase of their dissipation loss $\overline{D_l} = 0.44 \pm 0.06$. From the FICs with disrupted events, the dissipation loss for ATP depleted myoblasts was more noticeably increased $\overline{D_l} = 0.52 \pm 0.06$, which means that the recovery of the deformation (during unloading) may even be more sensitive to the activity of molecular motors (NMM II) that assist the F-actin stress fibers reassembly. The complete inhibition of myosin (both as a molecular motor and as an actin filaments cross-linker) by blebbistatin confirmed the fact that both passive and active F-actin cross-linkers are necessary for a full mechanical function accomplishment.

Altogether these findings showed that (i) perinuclear cross-linked actin stress fibers are key actors of C2C12 myoblast mechanical resistance to deformation, (ii) the molecular motor NMM II activity is necessary for building correctly the perinuclear actin stress fibers and ensuring that this network can be rapidly remodeled after local failures upon indentation, (iii) F-actin cross-linkers (active and passive) are the cement that build the CSK local stiffness. We focused specifically on F-actin stress fibers in this work, considering that the two other microtubule and interfilament networks likely play the role of slower longer-range cross-linking machineries as global modulators of the cell compressibility, without changing the characteristic features (local disruption events) that were observed in FICs.

The application of our AFM-based method on normal and dystrophic primary human myoblasts revealed that both DMD and HD cells are softer with less frequent FIC disruption events as compared to C2C12 normal myoblasts. Combining these indentation experiments with confocal fluorescence imaging led us to interpret this drastic change of the mechanical properties of these myoblasts by a loss of the perinuclear actin stress fiber characteristic network of C2C12 adherent myoblasts, similarly to blebbistatin treated C2C12 myoblasts. This preliminary result on primary myoblasts (we could only test ~ 20 cells of each type) was rather encouraging on the possibility to rapidly distinguish normal from pathological cells with our AFM indentation technique assisted with wavelet-based local detection of FICs disruption events. It also opened

many perspectives that will be described in the next section.

6.2 Perspectives

This thesis not only provides an alternative approach for single cell mechanics investigations but it also raises new fundamental questions that will hopefully be resolved by this local cell deformation and rupture analysis.

- *Can we generalise this methodology to other cells (adherent and non adherent)?*
  This method could be generalised to adherent cells with a well-organized actin cap, such as mouse embryonic fibroblasts, mouse myoblasts, human lung and foreskin fibroblasts, human umbilical vein endothelial cells, human ovarian epithelial cells [Kim, 2013], and more generally to mechano-sensitive animal cells. Given that the actin cap is involved in the regulation of the nuclear shape [Khatau, 2009] and in the force transmission from the extracellular matrix to the nucleus [Kim, 2013], this AFM-method could be very efficient for probing the effects of different stimuli (*e.g.* different culture adhesion substrates) on this CSK compartment. Also, by coupling AFM to confocal fluorescence microscopy, one should be able to visualise simultaneously the spatial reorganisation of the perinuclear actin stress fibers upon a local deformation by an AFM tip. Furthermore, since previous CSK structural studies have shown that the perinuclear actin cap is altered or totally absent in several disease (*e.g.* murine and human laminopathies, HeLa cervical cancer line, MCF-7 breast adenocarcinoma and U2OS osteosarcoma) [Kim, 2013], it could be very interesting to study quantitatively how these actin-cap alterations impact the mechanics of the perinuclear cytoskeleton network in these diseases.

- *As far as the interpretation of local rheology experiments is concerned, what can we learn from the large indentation experiments reported in this thesis?*
  We have also performed AFM based passive microrheology experiments of living myoblasts (keeping a constant force load on the cell while recording the error signal of the AFM cantilever tip) which were first published in [Martinez-Torres, 2016]. Complementary AFM cantilever fluctuation signals were recorded in 2015 which were analysed during last year within a multi-fractal formalism. This work was developed by the team of A. Arneodo and F. Argoul in Bordeaux and is presently under progress.

- *How the other cytoskeleton network filaments do interact with the perinuclear actin stress fibers to assist the maintenance of the cytoskeleton cohesion locally?*
  The MT network is strongly reorganised during myotube formation. While in non differentiated myoblasts, MTs nucleate from the centrosome and remain anchored to it, in differentiated myoblasts and myotubes, the nuclear envelope accumulates centrosomal proteins (*i.e.* pericentrin) and becomes the main MT organising center. In multinucleate myotubes, most of the MTs remain attached to the nuclear envelope and are organised in long parallel arrays. The dynein/dynactin complex is a major MT motor that is required for nucleus centration during the differentiation of myoblasts into myotubes. Both dynein and kinesin are involved in the spreading of the myonuclei and their migration to the myofiber periphery and their clustering under the neuromuscular junction. Comparing the impact of MT and/or dynein inhibitors on myoblast mechanical properties with actin and myosin inhibitors should therefore be very interesting. Our dynamical analysis of AFM

FICs should allow us to distinguish which of these two network systems is time-limiting and to which extent the MTs assist the perinuclear actin stress fiber recovery after rupture.

- *Would it be possible to build from these experiments a nonlinear dynamical modeling of living cells that would extend traditional nonlinear viscoelastic models?*
  To help this modeling, it will be important to increase the number of indentations (load-unload scans) to reconstruct (F, δ, t) maps on longer time intervals. A few time-lapse indentation experiments on the perinuclear regions of mouse myoblasts and myotubes were already performed, but the indentation depth was too small to properly sense the perinuclear cytoskeleton network.

- *Could we reconstruct spatial maps of cell dissipation or disruption events from living cells that would point out loci of higher fragility? Do the cells use this fragility to respond more rapidly to deformations?*
  The reconstruction of these maps should help us understanding how the perinuclar actin stress fiber breaks propagate in time and in space. Unfortunately, during this thesis, we could collect only a few FIC maps from living myoblasts, but again these indentations were rather superficial and could not be compared to the FICs which have been analysed in this manuscript.

- *Can this method be used in the future as a diagnostic tool for myopathies?*
  The inability of DMD myoblasts to properly polarize and differentiate in contractile myotubes has been recently reported, together with their impaired actin CSK and nucleus organizations [Chang, 2016; Nesmith, 2016]. However, the reported actin network perturbations were not linked to a specific cell compartment or actin filament structure. Our analysis on primary DMD myoblasts suggests a CSK alteration specific to the perinuclear stress fibers. Since the loss of perinuclear actin stress fibers was observed also in normal human myoblasts, it is important to confirm if this dramatic CSK modification is general to human primary myoblasts or if it simply results from the choice of the healthy donor or the culture conditions. The best way to answer this question is not only to probe more cells, but also to analyze primary human myoblasts from a larger group of donors (*i.e.* with different ages, sex, life style, ...) and to compare the impact of different adhesion substrates on their actin CSK. If we can correlate the CSK actin stress fiber impairment to pathologic situations (*e.g.* DMD and other dystrophies, degenerative disorders and aging), the perinuclear actin stress fiber compartment could become a new potential target for diagnosis and therapeutic purposes.

Other very exciting future long-term prospects for DMD myoblast (or myotube) mechanical studies could be to test the efficacy of actin stress fiber stimulating factors (*e.g.* sphingosine 1-phosphate S1P [Formigli, 2005], overexpression of NMMII or α-actinin), in order to assist the recovery of: (i) a proper contractile actin SF organization, (ii) normal myoblast mechanical properties, (iii) an efficient cell polarization, and (iv) an effective myogenesis. Improving muscle regeneration could help decrease the severity of the muscular function impairment and improve the DMD patient prognosis.

Bibliography

Aartsma-Rus, A. & Muntoni, F. (2013). 194th ENMC International Workshop. 3rd workshop on exon skipping: towards clinical application of antisense-mediated exon skipping for Duchenne muscular dystrophy. 8–10 December 2012, Naarden, The Netherlands. *Neuromuscular Disorders*, 23(11), 934–944.

Abidine, Y., Laurent, V., Michel, R., Duperray, A., & Verdier, C. (2013). Microrheology of complex systems and living cells using AFM. *Computer Methods in Biomechanics and Biomedical Engineering*, 16(sup1), 15–16.

Affonce, D. A. & Lutchen, K. R. (2006). New perspectives on the mechanical basis for airway hyperreactivity and airway hypersensitivity in asthma. *Journal of Applied Physiology*, 101(6), 1710–1719.

Akiyama, N., Ohnuki, Y., Kunioka, Y., Saeki, Y., & Yamada, T. (2006). Transverse stiffness of myofibrils of skeletal and cardiac muscles studied by atomic force microscopy. *The Journal of Physiological Sciences*, 56(2), 145–151.

Al-Rekabi, Z. & Pelling, A. E. (2013). Cross talk between matrix elasticity and mechanical force regulates myoblast traction dynamics. *Physical Biology*, 10(6), 066003.

Alcaraz, J., Buscemi, L., Puig-de Morales, M., Colchero, J., Baro, A., & Navajas, D. (2002). Correction of microrheological measurements of soft samples with atomic force microscopy for the hydrodynamic drag on the cantilever. *Langmuir*, 18(3), 716–721.

Alenghat, F. J. & Ingber, D. E. (2002). Mechanotransduction: all signals point to cytoskeleton, matrix, and integrins. *Science's STKE : Signal Transduction Knowledge Environment*, 119(6), 1–4.

Alessandrini, A. & Facci, P. (2005). AFM: a versatile tool in biophysics. *Measurement Science and Technology*, 16(6), R65–R92.

Allbrook, D., Han, M., & Hellmuth, A. (1971). Population of muscle satellite cells in relation to age and mitotic activity. *Pathology*, 3(3), 233–243.

Allen, D. G., Whitehead, N. P., & Froehner, S. C. (2016). Absence of dystrophin disrupts skeletal muscle signaling: roles of Ca^{2+}, reactive oxygen species, and nitric oxide in the development of muscular dystrophy. *Physiological Reviews*, 96(1), 253–305.

Allen, R. E., Rankin, L. L., Greene, E. A., Boxhorn, L. K., Johnson, S. E., Taylor, R. G., & Pierce, P. R. (1991). Desmin is present in proliferating rat muscle satellite cells but not in bovine muscle satellite cells. *Journal of Cellular Physiology*, 149(3), 525–535.

Allingham, J. S., Smith, R., & Rayment, I. (2005). The structural basis of blebbistatin inhibition and specificity for myosin II. *Nature Structural & Molecular Biology*, 12(4), 378–379.

Ambro, L., Pevala, V., Bauer, J., & Kutejová, E. (2012). The influence of ATP-dependent proteases on a variety of nucleoid-associated processes. *Journal of Structural Biology*, 179(2), 181–192.

Amm, I., Sommer, T., & Wolf, D. H. (2014). Protein quality control and elimination of protein waste: The role of the ubiquitin–proteasome system. *Biochimica et Biophysica Acta (BBA)-Molecular Cell Research*, 1843(1), 182–196.

Ananthakrishnan, R., Guck, J., Wottawah, F., Schinkinger, S., Lincoln, B., Romeyke, M., Moon, T., & Käs, J. (2006). Quantifying the contribution of actin networks to the elastic strength of fibroblasts. *Journal of Theoretical Biology*, 242(2), 502–516.

Andrés, V. & Walsh, K. (1996). Myogenin expression, cell cycle withdrawal, and phenotypic differentiation are temporally separable events that precede cell fusion upon myogenesis. *The Journal of Cell Biology*, 132(4), 657–666.

Apel, E. D., Lewis, R. M., Grady, R. M., & Sanes, J. R. (2000). Syne-1, a dystrophin- and Klarsicht-related protein associated with synaptic nuclei at the neuromuscular junction. *Journal of Biological Chemistry*, 275(41), 31986–31995.

Arce, F. T., Whitlock, J. L., Birukova, A. A., Birukov, K. G., Arnsdorf, M. F., Lal, R., Garcia, J. G., & Dudek, S. M. (2008). Regulation of the micromechanical properties of pulmonary endothelium by S1P and thrombin: role of cortactin. *Biophysical Journal*, 95(2), 886–894.

Argilés, J. M., Campos, N., Lopez-Pedrosa, J. M., Rueda, R., & Rodriguez-Mañas, L. (2016). Skeletal muscle regulates metabolism via inter-organ crosstalk: roles in health and disease. *Journal of the American Medical Directors Association*, 17(9), 789–796.

Argoul, F., Arneodo, A., Elezgaray, J., & Kuhn, A. (1997). Dynamical characterization of electroless deposition in the diffusion-limited regime. *Fractals*, 5(01), 75–86.

Argoul, F., Monier, K., Roland, T., Elezgaray, J., & Berguiga, L. (2010). High resolution surface plasmon microscopy for cell imaging. In *SPIE Photonics Europe* (pp. 771506–771506). Bellingham WA, USA: International Society for Optics and Photonics.

Argoul, F., Roland, T., Fahys, A., Berguiga, L., & Elezgaray, J. (2012). Uncovering phase maps from surface plasmon resonance images: Towards a sub-wavelength resolution. *Comptes Rendus Physique*, 13(8), 800–814.

Arneodo, A., Audit, B., Decoster, N., Muzy, J.-F., & Vaillant, C. (2002). Wavelet based multifractal formalism: applications to DNA sequences, satellite images of the cloud structure, and stock market data. In *The Science of Disasters* (pp. 26–102). Berlin, DE: Springer Verlag.

Arneodo, A., Audit, B., Kestener, P., & Roux, S. (2008). Wavelet-based multifractal analysis. *Scholarpedia*, 3(3), 4103.

Arneodo, A., Bacry, E., & Muzy, J. (1995). The thermodynamics of fractals revisited with wavelets. *Physica A*, 213(1-2), 232–275.

Arneodo, A., Vaillant, C., Audit, B., Argoul, F., d'Aubenton Carafa, Y., & Thermes, C. (2011). Multi-scale coding of genomic information: From DNA sequence to genome structure and function. *Physics Reports*, 498(2), 45–188.

Atkinson, S., Hosford, M., & Molitoris, B. (2004). Mechanism of actin polymerization in cellular ATP depletion. *Journal of Biological Chemistry*, 279(7), 5194–5199.

Attard, P. (2007). Measurement and interpretation of elastic and viscoelastic properties with the atomic force microscope. *Journal of Physics: Condensed Matter*, 19(47), 473201.

Audit, B., Bacry, E., Muzy, J.-F., & Arneodo, A. (2002). Wavelet-based estimators of scaling behavior. *IEEE Transactions on Information Theory*, 48(11), 2938–2954.

Baas, D., Caussanel-Boude, S., Guiraud, A., Calhabeu, F., Delaune, E., Pilot, F., Chopin, E., Machuca-Gayet, I., Vernay, A., Bertrand, S., Rual, J.-F., Jurdic, P., Hill, D. E., Vidal, M., Schaeffer, L., & Goillot, E. (2012). CKIP-1 regulates mammalian and zebrafish myoblast fusion. *Journal of Cell Science*, 125(16), 3790–3800.

Babahosseini, H., Ketene, A. N., Schmelz, E. M., Roberts, P. C., & Agah, M. (2014). Biomechanical profile of cancer stem-like/tumor-initiating cells derived from a progressive ovarian cancer model. *Nanomedicine: Nanotechnology, Biology and Medicine*, 10(5), e1013–e1019.

Bacabac, R., Smit, T., Cowin, S., Van Loon, J., Nieuwstadt, F., Heethaar, R., & Klein-Nulend, J. (2005). Dynamic shear stress in parallel-plate flow chambers. *Journal of Biomechanics*, 38(1), 159–167.

Bacallao, R., Garfinkel, A., Monke, S., Zampighi, G., & Mandel, L. (1994). ATP depletion: a novel method to study junctional properties in epithelial tissues. I. rearrangement of the actin cytoskeleton. *Journal of Cell Science*, 107(12), 3301–3313.

Bailey, R. G., Turner, R. D., Mullin, N., Clarke, N., Foster, S. J., & Hobbs, J. K. (2014). The interplay between cell wall mechanical properties and the cell cycle in Staphylococcus aureus. *Biophysical Journal*, 107(11), 2538–2545.

Ball, E. H. & Singer, S. (1981). Association of microtubules and intermediate filaments in normal fibroblasts and its disruption upon transformation by a temperature-sensitive mutant of Rous sarcoma virus. *Proceedings of the National Academy of Sciences USA*, 78(11), 6986–6990.

Balland, M., Richert, A., & Gallet, F. (2005). The dissipative contribution of myosin II in the cytoskeleton dynamics of myoblasts. *European Biophysics Journal*, 34(3), 255–261.

Bankolé, L.-C., Feasson, L., Ponsot, E., & Kadi, F. (2013). Fibre type-specific satellite cell content in two models of muscle disease. *Histopathology*, 63(6), 826–832.

Bartlett, R. J., Sharp, N. J. H., Hung, W.-Y., Kornegay, J. N., & Roses, A. D. (1990). *Molecular Markers for Myoblast Transplantation in GRMD*, (pp. 273–278). Springer US, Boston, MA.

Baskurt, O. & Meiselman, H. (2003). Blood rheology and hemodynamics. *Seminars in Thrombosis and Hemostasis*, 29(5), 435–450.

Bear, J., Svitkina, T., Krause, Mand Schafer, D., Loureiro, J., Strasser, G., Maly, I., Chaga, O., Cooper, J., & Borisy, G. (2002). Antagonism between Ena/VASP proteins and actin filament capping regulates fibroblast motility. *Cell*, 109(4), 509–521.

Becker, P. (1962). Two families of benign sex-linked recessive muscular dystrophy. *Revue Canadienne de Biologie/éditée par l'Université de Montréal*, 21, 551.

Bendris, N., Lemmers, B., & Blanchard, J. M. (2015). Cell cycle, cytoskeleton dynamics and beyond: the many functions of cyclins and CDK inhibitors. *Cell Cycle*, 14(12), 1786–1798.

Berg, J., Tymoczko, J., & L., S. (2002). *Biochemistry. 5th edition. Metabolism Is Composed of Many Coupled, Interconnecting Reactions.* W H Freeman, New York.

Berger, S., Schäfer, G., Kesper, D. A., Holz, A., Eriksson, T., Palmer, R. H., Beck, L., Klämbt, C., Renkawitz-Pohl, R., & Önel, S.-F. (2008). WASP and SCAR have distinct roles in activating the Arp2/3 complex during myoblast fusion. *Journal of Cell Science*, 121(8), 1303–1313.

Bergert, M., Chandradoss, S. D., Desai, R. A., & Paluch, E. (2012). Cell mechanics control rapid transitions between blebs and lamellipodia during migration. *Proceedings of the National Academy of Sciences USA*, 109(36), 14434–14439.

Berguiga, L., Boyer-Provera, E., Elezgaray, J., & Argoul, F. (2013a). Sensing nanometer depth of focused optical fields with scanning surface plasmon microscopy. *Plasmonics*, 8(2), 715–722.

Berguiga, L., Boyer-Provera, E., Martinez-Torres, C., Elezgaray, J., Arneodo, A., & Argoul, F. (2013b). Guided wave microscopy: mastering the inverse problem. *Optics Letters*, 38(21), 4269–4272.

Berguiga, L., Elezgaray, J., Hugo, N., Roland, T., & Argoul, F. (2009). Advances in surface plasmon resonance-based high throughput biochips. *Frontiers of Physics in China*, 4(4), 469–480.

Berguiga, L., Roland, T., Monier, K., Elezgaray, J., & Argoul, F. (2011). Amplitude and phase images of cellular structures with a scanning surface plasmon microscope. *Optics Express*, 19(7), 6571–6586.

Berguiga, L., Streppa, L., Boyer-Provera, E., Martinez-Torres, C., Schaeffer, L., Elezgaray, J., Arneodo, A., & Argoul, F. (2016). Time-lapse scanning surface plasmon microscopy of living adherent cells with a radially polarized beam. *Applied Optics*, 55(6), 1216–1227.

Berguiga, L., Zhang, S., Argoul, F., & Elezgaray, J. (2007). High-resolution surface-plasmon imaging in air and in water: $V(Z)$ curve and operating conditions. *Optics Letters*, 32(5), 509–511.

Berry, C. C., Campbell, G., Spadiccino, A., Robertson, M., & Curtis, A. S. (2004). The influence of microscale topography on fibroblast attachment and motility. *Biomaterials*, 25(26), 5781–5788.

Bershadsky, A. & Gelfand, V. (1983). Role of ATP in the regulation of stability of cytoskeletal structures. *Cell Biology International Reports*, 7(3), 173–187.

Bershadsky, A., Gelfand, V., Svitkina, T., & Tint, I. (1980). Destruction of microfilament bundles in mouse embryo fibroblasts treated with inhibitors of energy metabolism. *Experimental Cell Research*, 127(2), 421–429.

Bershadsky, A., Kozlov, M., & Geiger, B. (2006). Adhesion-mediated mechanosensitivity: a time to experiment, and a time to theorize. *Current Opinion in Cell Biology*, 18(5), 472–481.

Bettadapur, A., Suh, G. C., Geisse, N. A., Wang, E. R., Hua, C., Huber, H. A., Viscio, A. A., Kim, J. Y., Strickland, J. B., & McCain, M. L. (2016). Prolonged culture of aligned skeletal myotubes on micromolded gelatin hydrogels. *Scientific Reports*, 6, 28855.

Betz, T., Lenz, M., Joanny, J.-F., & Sykes, C. (2009). ATP-dependent mechanics of red blood cells. *Proceedings of the National Academy of Sciences USA*, 106(36), 15320–15325.

Bhana, B., Iyer, R. K., Chen, W. L. K., Zhao, R., Sider, K. L., Likhitpanichkul, M., Simmons, C. A., & Radisic, M. (2010). Influence of substrate stiffness on the phenotype of heart cells. *Biotechnology and Bioengineering*, 105(6), 1148–1160.

Bhuanantanondh, P., Grecov, D., & Kwok, E. (2012). Rheological study of viscosupplements and synovial fluid in patients with osteoarthritis. *Journal of Medical and Biological Engineering*, 32(1), 12–16.

Biagini, E., Valgimigli, M., Smits, P., Poldermans, D., Schinkel, A., Rizzello, V., Bountioukos, M., & Serruys, P. (2006). Stress and tissue doppler echocardiographic evidence of effectiveness of myoblast transplantation in patients with ischaemic heart failure. *European Journal of Heart Failure*, 8(6), 641–648.

Bianchi, M., Mazzanti, A., Galbiati, E., Saraifoger, S., Dubini, A., Cornelio, F., & Morandi, L. (2003). Bone mineral density and bone metabolism in Duchenne muscular dystrophy. *Osteoporosis International*, 14(9), 761–767.

Bigot, A., Jacquemin, V., Debacq-Chainiaux, F., Butler-Browne, G. S., Toussaint, O., Furling, D., & Mouly, V. (2008). Replicative aging down-regulates the myogenic regulatory factors in human myoblasts. *Biology of the Cell*, 100(3), 189–199.

Bingham, E. C. (1922). *Fluidity and Plasticity*. New York: McGraw Hill.

Binnig, G., Quate, C. F., & Gerber, C. (1986). Atomic force microscope. *Physical Review Letters*, 56(9), 930.

Birukova, A. A., Arce, F. T., Moldobaeva, N., Dudek, S. M., Garcia, J. G., Lal, R., & Birukov, K. G. (2009). Endothelial permeability is controlled by spatially defined cytoskeletal mechanics: atomic force microscopy force mapping of pulmonary endothelial monolayer. *Nanomedicine: Nanotechnology, Biology and Medicine*, 5(1), 30–41.

Bischoff, R. (1990). Interaction between satellite cells and skeletal muscle fibers. *Development*, 109(4), 943–952.

Bischofs, I. B. & Schwarz, U. S. (2003). Cell organization in soft media due to active mechanosensing. *Proceedings of the National Academy of Sciences USA*, 100(16), 9274–9279.

Black, A. B., Dahlenburg, H., Pepper, K., Nacey, C., Pontow, S., Kuhn, M. A., Belafsky, P. C., & Nolta, J. A. (2015). Human myoblast and mesenchymal stem cell interactions visualized by videomicroscopy. *Human Gene Therapy Methods*, 26(6), 193–196.

Bladen, C. L., Salgado, D., Monges, S., Foncuberta, M. E., Kekou, K., Kosma, K., Dawkins, H., Lamont, L., Roy, A. J., Chamova, T., Guergueltcheva, V., Chan, S., Korngut, L., Campbell, C., Dai, Y., Wang, J., Barisic, N., Brabec, P., Lahdetie, J., Walter, M. C., Schreiber-Katz, O., Karcagi, V., Garami, M., Viswanathan, V., Bayat, F., Buccella, F., Kimura, E., Koeks, Z., van den Bergen, J. C., Rodrigues, M., Roxburgh, R., Lusakowska, A., Kostera-Pruszczyk, A., Zimowski, J., Santos, R., Neagu, E., Artemieva, S., Rasic, V. M., Vojinovic, D., Posada, M., Bloetzer, C., Jeannet, P. Y., Joncourt, F., Diaz-Manera, J., Gallardo, E., Karaduman, A. A., Topaloglu, H., El Sherif, R., Stringer, A., Shatillo, A. V., Martin, A. S., Peay, H. L., Bellgard, M. I., Kirschner, J., Flanigan, K. M., Straub, V., Bushby, K., Verschuuren, J., Aartsma-Rus, A., Béroud, C., & Lochmuller, H. (2015). The TREAT-NMD DMD global database: Analysis of more than 7,000 Duchenne muscular dystrophy mutations. *Human Mutation*, 36(4), 395–402.

Blake, D. J., Weir, A., Newey, S. E., & Davies, K. E. (2002). Function and genetics of dystrophin and dystrophin-related proteins in muscle. *Physiological Reviews*, 82(2), 291–329.

Blanchoin, L., Boujemaa-Paterski, R., Sykes, C., & Plastino, J. (2014). Actin dynamics, architecture, and mechanics in cell motility. *Physiological Reviews*, 94(1), 235–263.

Blanchoin, L. & Michelot, A. (2012). Actin cytoskeleton: a team effort during actin assembly. *Current Biology*, 22(16), R643–R645.

Blanchoin, L. & Pollard, T. D. (2002). Hydrolysis of ATP by polymerized actin depends on the bound divalent cation but not profilin. *Biochemistry*, 41(2), 597–602.

Blau, H., Chiu, C., & Webster, C. (1983). Cytoplasmic activation of human nuclear genes in stable heterocaryons. *Cell*, 32(4), 1171–1180.

Bloch, B. & Dintenfass, L. (1963). Rheological study of human synovial fluid. *Australian and New Zealand Journal of Surgery*, 33(2), 108–113.

Bloomfield, I., Johnston, I., & Bilston, L. (1998). Effects of proteins, blood cells and glucose on the viscosity of cerebrospinal fluid. *Pediatric Neurosurgery*, 28(5), 246–251.

Bodensteiner, J. B. & Engel, A. G. (1978). Intracellular calcium accumulation in Duchenne dystrophy and other myopathies: a study of 567,000 muscle fibers in 114 biopsies. *Neurology*, 28(5), 439–439.

Boillée, S., Velde, C. V., & Cleveland, D. W. (2006). ALS: a disease of motor neurons and their nonneuronal neighbors. *Neuron*, 52(1), 39–59.

Boisvert, F.-M., van Koningsbruggen, S., Navascués, J., & Lamond, A. I. (2007). The multifunctional nucleolus. *Nature Reviews Molecular Cell Biology*, 8(7), 574–585.

Bonakdar, N., Luczak, J., Lautscham, L., Czonstke, M., Koch, T. M., Mainka, A., Jungbauer, T., Goldmann, W. H., Schröder, R., & Fabry, B. (2012). Biomechanical characterization of a desminopathy in primary human myoblasts. *Biochemical and Biophysical Research Communications*, 419(4), 703–707.

Bonakdar, N., Schilling, A., Spörrer, M., Lennert, P., Mainka, A., Winter, L., Walko, G., Wiche, G., Fabry, B., & Goldmann, W. H. (2015). Determining the mechanical properties of plectin in mouse myoblasts and keratinocytes. *Experimental Cell Research*, 331(2), 331–337.

Bonora, M., Patergnani, S., Rimessi, A., De Marchi, E., Suski, J. M., Bononi, A., Giorgi, C., Marchi, S., Missiroli, S., Poletti, F., Wieckowski, M. R., & Pinton, P. (2012). ATP synthesis and storage. *Purinergic Signalling*, 8(3), 343–357.

Bonuccelli, G., Sotgia, F., Schubert, W., Park, D. S., Frank, P. G., Woodman, S. E., Insabato, L., Cammer, M., Minetti, C., & Lisanti, M. P. (2003). Proteasome inhibitor (MG-132) treatment of *mdx* mice rescues the expression and membrane localization of dystrophin and dystrophin-associated proteins. *The American Journal of Pathology*, 163(4), 1663–1675.

Borelli, G. A. (2012). *On the Movement of Animals*. Springer-Verlag, Heidelberg, Berlin.

Borisy, G. G. & Svitkina, T. M. (2000). Actin machinery: pushing the envelope. *Current Opinion in Cell Biology*, 12(1), 104–112.

Boubaker el Andalousi, R., Daussin, P.-A., Micallef, J.-P., Roux, C., Nougues, J., Chammas, M., Nougues, Y., & Bacou, F. (2002). Changes in mass and performance in rabbit muscles after muscle damage with or without transplantation of primary satellite cells. *Cell Transplantation*, 11(2), 169–180.

Bowman, W., Marshall, I., Gibb, A., & Harborne, A. (1988). Feedback control of transmitter release at the neuromuscular junction. *Trends in Pharmacological Sciences*, 9(1), 16–20.

Boyer-Provera, E., Rossi, A., Oriol, L., Dumontet, C., Plesa, A., Berguiga, L., Elezgaray, J., Arneodo, A., & Argoul, F. (2013). Wavelet-based decomposition of high resolution surface plasmon microscopy $V(Z)$ curves at visible and near infrared wavelengths. *Optics Express*, 21(6), 7456–7477.

Brenner, H. (1961). The slow motion of a sphere through a viscous fluid towards a plane surface. *Chemical Engineering Science*, 16(3-4), 242–251.

Bright, R. T., Salvaterra, C. G., Rubin, L. J., & Yuan, X.-J. (1995). Inhibition of glycolysis by 2-DG increases Ca^{2+} in pulmonary arterial smooth muscle cells. *American Journal of Physiology-Lung Cellular and Molecular Physiology*, 269(2), L203–L208.

Buckingham, M., Bajard, L., Chang, T., Daubas, P., Hadchouel, J., Meilhac, S., Montarras, D., Rocancourt, D., & Relaix, F. (2003). The formation of skeletal muscle: from somite to limb. *Journal of Anatomy*, 202(1), 59–68.

Buckley, I. K. & Porter, K. R. (1967). Cytoplasmic fibrils in living cultured cells. *Protoplasma*, 64(4), 349–380.

Bui, A. & Nguyen, M. (2004). Prediction of viscosity of glucose and calcium chloride solutions. *Journal of Food Engineering*, 62(4), 345–349.

Burattini, S., Ferri, P., Battistelli, M., Curci, R., Luchetti, F., & Falcieri, E. (2004). C2C12 murine myoblasts as a model of skeletal muscle development: morpho-functional characterization. *European Journal of Histochemistry: EJH*, 48(3), 223.

Burkin, D. J., Wallace, G. Q., Nicol, K. J., Kaufman, D. J., & Kaufman, S. J. (2001). Enhanced expression of the $\alpha_7\beta_1$ integrin reduces muscular dystrophy and restores viability in dystrophic mice. *Journal of Cell Biology*, 152(6), 1207–1218.

Burnstock, G., Arnett, T. R., & Orriss, I. R. (2013). Purinergic signalling in the musculoskeletal system. *Purinergic Signalling*, 9(4), 541–572.

Burnstock, G. & Verkhratsky, A. (2012). *Purinergic Signalling and the Nervous System*. New York: Springer Science & Business Media.

Burridge, K. & Wittchen, E. S. (2013). The tension mounts: stress fibers as force-generating mechanotransducers. *The Journal of Cell Biology*, 200(1), 9–19.

Campbell, K. P. & Kahl, S. D. (1989). Association of dystrophin and an integral membrane glycoprotein. *Nature*, 338(6212), 259–262.

Campbell, K. P. & Stull, J. T. (2003). Skeletal muscle basement membrane-sarcolemma-cytoskeleton interaction minireview series. *Journal of Biological Chemistry*, 278(15), 12599–12600.

Canato, M., Dal Maschio, M., Sbrana, F., Raiteri, R., Reggiani, C., Vassanelli, S., & Megighian, A. (2010). Mechanical and electrophysiological properties of the sarcolemma of muscle fibers in two murine models of muscle dystrophy: Col6a1-/- and *mdx*. *BioMed Research International*, 2010, 981945.

Capetanaki, Y., Bloch, R. J., Kouloumenta, A., Mavroidis, M., & Psarras, S. (2007). Muscle intermediate filaments and their links to membranes and membranous organelles. *Experimental Cell Research*, 313(10), 2063–2076.

Cappella, B. & Dietler, G. (1999). Force-distance curves by atomic force microscopy. *Surface Science Reports*, 34(1), 1–104.

Carsana, A., Frisso, G., Tremolaterra, M., Lanzillo, R., Vitale, D., Santoro, L., & Salvatore, F. (2005). Analysis of dystrophin gene deletions indicates that the hinge III region of the protein correlates with disease severity. *Annals of Human Genetics*, 69(3), 253–259.

Cartagena, A. & Raman, A. (2014). Local viscoelastic properties of live cells investigated using dynamic and quasi-static atomic force microscopy methods. *Biophysical Journal*, 106(5), 1033–1043.

Ceruti, S., Giammarioli, A. M., Camurri, A., Falzano, L., Rufini, S., Frank, C., Fiorentini, C., Malorni, W., & Abbracchio, M. P. (2000). Adenosine-and 2-chloro-adenosine-induced cytopathic effects on myoblastic cells and myotubes: involvement of different intracellular mechanisms. *Neuromuscular Disorders*, 10(6), 436–446.

Chaki, S. P., Barhoumi, R., Berginski, M. E., Sreenivasappa, H., Trache, A., Gomez, S. M., & Rivera, G. M. (2013). Nck enables directional cell migration through the coordination of polarized membrane protrusion with adhesion dynamics. *Journal of Cell Science*, 126(7), 1637–1649.

Chamberlain, J. S. (2002). Gene therapy of muscular dystrophy. *Human Molecular Genetics*, 11(20), 2355–2362.

Chan, S. & Head, S. (2011). The role of branched fibres in the pathogenesis of Duchenne muscular dystrophy. *Experimental Physiology*, 96(6), 564–571.

Chang, L. & Goldman, R. D. (2004). Intermediate filaments mediate cytoskeletal crosstalk. *Nature Reviews Molecular Cell Biology*, 5(8), 601–613.

Chang, N. C., Chevalier, F. P., & Rudnicki, M. A. (2016). Satellite cells in muscular dystrophy - lost in polarity. *Trends in Molecular Medicine*, 22(6), 479–496.

Chanliaud, E., Burrows, K., Jeronimidis, G., & Gidley, M. (2002). Mechanical properties of primary plant cell wall analogues. *Planta*, 215(6), 989–996.

Charest, J., García, A., & King, W. (2007). Myoblast alignment and differentiation on cell culture substrates with microscale topography and model chemistries. *Biomaterials*, 28(13), 2202–2210.

Charge, S. B. & Rudnicki, M. A. (2004). Cellular and molecular regulation of muscle regeneration. *Physiological Reviews*, 84(1), 209–238.

Charras, G. T. & Horton, M. A. (2002a). Determination of cellular strains by combined atomic force microscopy and finite element modeling. *Biophysical Journal*, 83(2), 858–879.

Charras, G. T. & Horton, M. A. (2002b). Single cell mechanotransduction and its modulation analyzed by atomic force microscope indentation. *Biophysical Journal*, 82(6), 2970–2981.

Chen, J. (2014). Nanobiomechanics of living cells: a review. *Interface Focus*, 4(2), 20130055.

Chen, J., Dong, R., Ge, J., Guo, B., & Ma, P. X. (2015). Biocompatible, biodegradable, and electroactive polyurethane-urea elastomers with tunable hydrophilicity for skeletal muscle tissue engineering. *ACS Applied Materials & Interfaces*, 7(51), 28273–28285.

Cheng, Y. & Cheng, C. (2004). Scaling, dimensional analysis, and indentation measurements. *Materials Science and Engineering: R: Reports*, 44(4), 91–149.

Cheng, Y. & Yang, F. (2009). Obtaining shear relaxation modulus and creep compliance of linear viscoelastic materials from instrumented indentation using axisymmetric indenters of power-law profiles. *Journal of Materials Research*, 24(10), 3013–3017.

Chesarone, M. A., DuPage, A. G., & Goode, B. L. (2010). Unleashing formins to remodel the actin and microtubule cytoskeletons. *Nature Reviews Molecular Cell Biology*, 11(1), 62–74.

Chiron, S., Tomczak, C., Duperray, A., Lainé, J., Bonne, G., Eder, A., Hansen, A., Eschenhagen, T., Verdier, C., & Coirault, C. (2012). Complex interactions between human myoblasts and the surrounding 3D fibrin-based matrix. *PLoS ONE*, 7(4), 2–9.

Choi, I. Y., Lim, H., Estrellas, K., Mula, J., Cohen, T. V., Zhang, Y., Donnelly, C. J., Richard, J.-P., Kim, Y. J., Kim, H., Kazuki, Y., Oshimura, M., Li, H. L., Hotta, A., Rothstein, J., Maragakis, N., Wagner, K. R., & Lee, G. (2016). Concordant but varied phenotypes among Duchenne muscular dystrophy patient-specific myoblasts derived using a human iPSC-based model. *Cell Reports*, 15(10), 2301–2312.

Christensen, R. (2012). *Theory of Viscoelasticity: an Introduction*. New York: Dover Publications.

Chromiak, J. A. & Antonio, J. (2008). Skeletal muscle plasticity. In *Essentials of Sports Nutrition and Supplements* (pp. 21–52). Springer Science Business Media, Totowa, NJ.

Ciciliot, S. & Schiaffino, S. (2010). Regeneration of mammalian skeletal muscle: basic mechanisms and clinical implications. *Current Pharmaceutical Design*, 16(8), 906–914.

Ciecierska, A., Chodkowska, K., Motyl, T., & Sadkowski, T. (2013). Myogenic cells applications in regeneration of post-infarction cardiac tissue. *Journal of Physiology and Pharmacology*, 64, 401–408.

Cohn, R. D. & Campbell, K. P. (2000). Molecular basis of muscular dystrophies. *Muscle & Nerve*, 23(10), 1456–1471.

Collinsworth, A., Zhang, S., Kraus, W., & Truskey, G. (2002). Apparent elastic modulus and hysteresis of skeletal muscle cells throughout differentiation. *American Journal of Physiology-Cell Physiology*, 283(4), C1219–C1227.

Coluccio, L. M. (2007). *Myosins: a Superfamily of Molecular Motors*, volume 7. New York: Springer Science & Business Media.

Constantin, B. (2014). Dystrophin complex functions as a scaffold for signalling proteins. *Biochimica et Biophysica Acta (BBA)-Biomembranes*, 1838(2), 635–642.

Converti, A., Zilli, M., Arni, S., Di Felice, R., & Del Borghi, M. (1999). Estimation of viscosity of highly viscous fermentation media containing one or more solutes. *Biochemical Engineering Journal*, 4(1), 81–85.

Cooper, G. M. & Hausman, R. E. (2000). *The Cell: A Molecular Approach*. Sinauer Associates Sunderland (MA).

Cooper, J. A. & Schafer, D. A. (2000). Control of actin assembly and disassembly at filament ends. *Current Opinion in Cell Biology*, 12(1), 97–103.

Cooper, M. (2003). The man who knew too much: The strange and inventive life of Robert Hooke, 1635-1703. *The English Historical Review*, 118(479), 1391–1393.

Cooper, S., Maxwell, A., Kizana, E., Ghoddusi, M., Hardeman, E., Alexander, I., Allen, D., & North, K. (2004). C2C12 co-culture on a fibroblast substratum enables sustained survival of contractile, highly differentiated myotubes with peripheral nuclei and adult fast myosin expression. *Cell motility and the Cytoskeleton*, 58(3), 200–211.

Corriden, R. & Insel, P. A. (2010). Basal release of ATP: an autocrine-paracrine mechanism for cell regulation. *Science Signaling*, 3(104), re1.

Costa, K. D. (2004a). Single-cell elastography: probing for disease with the atomic force microscope. *Disease Markers*, 19(2-3), 139–154.

Costa, M., Escaleira, R., Cataldo, A., Oliveira, F., & Mermelstein, C. (2004b). Desmin: molecular interactions and putative functions of the muscle intermediate filament protein. *Brazilian Journal of Medical and Biological Research*, 37(12), 1819–1830.

Costa, M. L. (2014). Cytoskeleton and adhesion in myogenesis. *ISRN Developmental Biology*, 2014, 713631.

Craig, V. S. & Neto, C. (2001). In situ calibration of colloid probe cantilevers in force microscopy: Hydrodynamic drag on a sphere approaching a wall. *Langmuir*, 17(19), 6018–6022.

Cramer, L. P. & Mitchison, T. (1997). Investigation of the mechanism of retraction of the cell margin and rearward flow of nodules during mitotic cell rounding. *Molecular Biology of the Cell*, 8(1), 109–119.

Crick, F. (1970). Central dogma of molecular biology. *Nature*, 227(5258), 561–563.

Crick, F. H. (1958). On protein synthesis. In *Symposia of the Society for Experimental Biology*, volume 12 (pp. 138–63).

Cross, S. E., Jin, Y.-S., Rao, J., & Gimzewski, J. K. (2007). Nanomechanical analysis of cells from cancer patients. *Nature Nanotechnology*, 2(12), 780–783.

Crouzier, T., Fourel, L., Boudou, T., Albigès-Rizo, C., & Picart, C. (2011). Presentation of BMP-2 from a soft biopolymeric film unveils its activity on cell adhesion and migration. *Advanced Materials*, 23(12).

Crouzier, T., Ren, K., Nicolas, C., Roy, C., & Picart, C. (2009). Layer-by-layer films as a biomimetic reservoir for rhBMP-2 delivery: controlled differentiation of myoblasts to osteoblasts. *Small*, 5(5), 598–608.

Cullen, M. & Fulthorpe, J. (1975). Stages in fibre breakdown in Duchenne muscular dystrophy: an electron-microscopic study. *Journal of the Neurological Sciences*, 24(2), 179–200.

Curci, R., Battistelli, M., Burattini, S., D'Emilio, A., Ferri, P., Lattanzi, D., Ciuffoli, S., Ambrogini, P., Cuppini, R., & Falcieri, E. (2008). Surface and inner cell behaviour along skeletal muscle cell in vitro differentiation. *Micron*, 39(7), 843–851.

Curtis, A. & Wilkinson, C. (1997). Topographical control of cells. *Biomaterials*, 18(24), 1573–1583.

Dahl, K. N., Ribeiro, A. J., & Lammerding, J. (2008). Nuclear shape, mechanics, and mechanotransduction. *Circulation Research*, 102(11), 1307–1318.

Dalakas, M. (2011). Review: an update on inflammatory and autoimmune myopathies. *Neuropathology and Applied Neurobiology*, 37(3), 226–242.

D'Albis, A., Lenfant-Guyot, M., Janmot, C., Chanoine, C., Weinman, J., & Gallien, C. L. (1987). Regulation by thyroid hormones of terminal differentiation in the skeletal dorsal muscle: I. Neonate mouse. *Developmental Biology*, 123(1), 25–32.

Dalby, M. J. (2009). Nanostructured surfaces: cell engineering and cell biology. *Nanomedicine*, 4(3), 247–248.

Dalkilic, I. & Kunkel, L. M. (2003). Muscular dystrophies: genes to pathogenesis. *Current Opinion in Genetics & Development*, 13(3), 231–238.

Dani, J. A. & Bertrand, D. (2007). Nicotinic acetylcholine receptors and nicotinic cholinergic mechanisms of the central nervous system. *The Annual Review of Pharmacology and Toxicology*, 47, 699–729.

Darling, E. M. & Di Carlo, D. (2015). High-throughput assessment of cellular mechanical properties. *Annual Review of Biomedical Engineering*, 17, 35–62.

Darling, E. M., Topel, M., Zauscher, S., Vail, T. P., & Guilak, F. (2008). Viscoelastic properties of human mesenchymally-derived stem cells and primary osteoblasts, chondrocytes, and adipocytes. *Journal of Biomechanics*, 41(2), 454–464.

Daubechies, I. (1992). *Ten Lectures on Wavelets, vol. 61 of CBMS-NSF Regional Conference Series in Applied Mathematics*. Philadelphia, CA, USA: SIAM.

De Almeida Ribeiro, E., Pinotsis, N., Ghisleni, A., Salmazo, A., Konarev, P. V., Kostan, J., Sjöblom, B., Schreiner, C., Polyansky, A. A., Gkougkoulia, E. A., Holt, M. R., Aachmann, F. L., Zagrović, B., Bordignon, E., Pirker, K. F., Svergun, D. I., Gautel, M., & Djinović-Carugo, K. (2014). The structure and regulation of human muscle α-actinin. *Cell*, 159(6), 1447–1460.

Deconinck, N. & Dan, B. (2007). Pathophysiology of Duchenne muscular dystrophy: current hypotheses. *Pediatric Neurology*, 36(1), 1–7.

Defranchi, E., Bonaccurso, E., Tedesco, M., Canato, M., Pavan, E., Raiteri, R., & Reggiani, C. (2005). Imaging and elasticity measurements of the sarcolemma of fully differentiated skeletal muscle fibres. *Microscopy Research and Technique*, 67(1), 27–35.

Delour, J., Muzy, J., & Arneodo, A. (2001). Intermittency of 1d velocity spatial profiles in turbulence: a magnitude cumulant analysis. *The European Physical Journal B*, 23(2), 243–248.

Den Dunnen, J., Grootscholten, P., Bakker, E., Blonden, L., Ginjaar, H., Wapenaar, M., Van Paassen, H., Van Broeckhoven, C., Pearson, P., & Van Ommen, G. (1989). Topography of the Duchenne muscular dystrophy (DMD) gene: FIGE and cDNA analysis of 194 cases reveals 115 deletions and 13 duplications. *American Journal of Human Genetics*, 45(6), 835–847.

Deroanne, C. F., Lapiere, C. M., & Nusgens, B. V. (2001). In vitro tubulogenesis of endothelial cells by relaxation of the coupling extracellular matrix-cytoskeleton. *Cardiovascular Research*, 49(3), 647–658.

Desai, A. & Mitchison, T. J. (1997). Microtubule polymerization dynamics. *Annual Review of Cell and Developmental Biology*, 13(1), 83–117.

Despeyroux, A. & Ambari, A. (2012). Slow motion of a sphere towards a plane through confined non-Newtonian fluid. *Journal of Non-Newtonian Fluid Mechanics*, 167-168, 38–45.

Devic, P., Petiot, P., Simonet, T., Stojkovic, T., Delmont, E., Franques, J., Magot, A., Vial, C., Lagrange, E., Nicot, A., Risson, V., Eymard, V., & Schaeffer, L. (2014). Antibodies to clustered acetylcholine receptor: expanding the phenotype. *European Journal of Neurology*, 21(1), 130–134.

Devin, A. & Rigoulet, M. (2007). Mechanisms of mitochondrial response to variations in energy demand in eukaryotic cells. *American Journal of Physiology-Cell Physiology*, 292(1), C52–C58.

Dib, N., Michler, R. E., Pagani, F. D., Wright, S., Kereiakes, D. J., Lengerich, R., Binkley, P., Buchele, D., Anand, I., Swingen, C., Di Carli, M. F., Thomas, J. D., Jaber, W. A., Opie, S. R., Campbell, A., McCarthy, P., Yeager, M., Dilsizian, V., Griffith, B. P., Korn, R., Kreuger, S. K., Ghazoul, M., MacLellan, W. R., Fonarow, G., Eisen, H. J., Dinsmore, J., & Diethrich, E. (2005). Safety and feasibility of autologous myoblast transplantation in patients with ischemic cardiomyopathy: Four-year follow-up. *Circulation*, 112(12), 1748–1755.

Digiuni, S., Berne-Dedieu, A., Martinez-Torres, C., Szecsi, J., Bendahmane, M., Arneodo, A., & Argoul, F. (2015). Single cell wall nonlinear mechanics revealed by a multi-scale analysis of AFM force-indentation curves. *Biophysical Journal*, 108, 2235–2248.

Discher, D. E., Janmey, P., & Wang, Y.-L. (2005). Tissue cells feel and respond to the stiffness of their substrate. *Science*, 310(5751), 1139–1143.

Doberstein, S. K., Fetter, R. D., Mehta, A. Y., & Goodman, C. S. (1997). Genetic analysis of myoblast fusion: blown fuse is required for progression beyond the prefusion complex. *The Journal of Cell Biology*, 136(6), 1249–1261.

Doherty, J., Lenhart, K., Cameron, M., Mack, C., Conlon, F., & Taylor, J. (2011). Skeletal muscle differentiation and fusion are regulated by the BAR-containing Rho-GTPase-activating protein (Rho-GAP), GRAF1. *Journal of Biological Chemistry*, 286(29), 25903–25921.

Dong, C., Skalak, R., & Sung, K. (1990). Cytoplasmic rheology of passive neutrophils. *Biorheology*, 28(6), 557–567.

Duan, R. & Gallagher, P. J. (2009). Dependence of myoblast fusion on a cortical actin wall and nonmuscle myosin IIA. *Developmental Biology*, 325(2), 374–385.

Duchenne, G. (1868). Recherches sur la paralysie musculaire pseudo-hypertrophique ou paralysie myo-sclérosique. *Extrait des Archives Générales de Médecine*.

Duchenne, G. B. A. (1867). *Physiologie des mouvements démontrée a l'aide de l'expérimentation électrique et de l'observation clinique et applicable a l'étude des paralysies et des déformations*. Baillière et Fils, Paris, France.

Dumont, N. A. & Rudnicki, M. A. (2016). Targeting muscle stem cell intrinsic defects to treat Duchenne muscular dystrophy. *Regenerative Medicine*, 1, 16006.

Dumont, N. A., Wang, Y. X., von Maltzahn, J., Pasut, A., Bentzinger, C. F., Brun, C. E., & Rudnicki, M. A. (2015). Dystrophin expression in muscle stem cells regulates their polarity and asymmetric division. *Nature Medicine*, 21(12), 1455–1463.

Duncan, C. (1983). Role of calcium in triggering the release of transmitters at the neuromuscular junction. *Cell Calcium*, 4(3), 171–193.

Dupin, I. & Etienne-Manneville, S. (2011). Nuclear positioning: Mechanisms and functions. *International Journal of Biochemistry and Cell Biology*, 43(12), 1698–1707.

Durbeej, M. & Campbell, K. P. (2002). Muscular dystrophies involving the dystrophin–glycoprotein complex: an overview of current mouse models. *Current Opinion in Genetics & Development*, 12(3), 349–361.

Durrani, S., Konoplyannikov, M., Ashraf, M., & Haider, K. H. (2010). Skeletal myoblasts for cardiac repair. *Regenerative Medicine*, 5(6), 919–932.

Dutta, S., Bhattacharyya, M., & Sengupta, K. (2016). Implications and assessment of the elastic behavior of lamins in laminopathies. *Cells*, 5(4), 37.

Duxbury, M. S., Ashley, S. W., & Whang, E. E. (2004). Inhibition of pancreatic adenocarcinoma cellular invasiveness by blebbistatin: a novel myosin II inhibitor. *Biochemical and Biophysical Research Communications*, 313(4), 992–997.

Edinger, A. L. & Thompson, C. B. (2004). Death by design: apoptosis, necrosis and autophagy. *Current Opinion in Cell Biology*, 16(6), 663–669.

Elezgaray, J. & Argoul, F. (2005). Topography reconstruction from surface plasmon resonance data. *Journal of Optics A: Pure and Applied Optics*, 7(9), 472.

Elezgaray, J., Berguiga, L., & Argoul, F. (2014). Plasmon-based tomographic microscopy. *Journal of the Optical Society of America*, 31(1), 155–161.

Elezgaray, J., Roland, T., Berguiga, L., & Argoul, F. (2010). Modeling of the scanning surface plasmon microscope. *Journal of the Optical Society of America*, 27(3), 450–457.

Embry, A., Mohammadi, H., Niu, X., Liu, L., Moe, B., Miller-Little, W., Lu, C. Y., Bruggeman, L. A., McCulloch, C. A., Janmey, P. A., & Miller, R. T. (2016). Biochemical and cellular determinants of renal glomerular elasticity. *PloS One*, 11(12), e0167924.

Emery, A. E. (1991). Population frequencies of inherited neuromuscular diseases—A world survey. *Neuromuscular Disorders*, 1(1), 19–29.

Emery, A. E., Muntoni, F., & Quinlivan, R. C. (2015). *Duchenne Muscular Dystrophy*. Oxford Monographs on Medical Genetics. OUP Oxford, UK.

Engler, A., Bacakova, L., Newman, C., Hategan, A., Griffin, M., & Discher, D. (2004a). Substrate compliance versus ligand density in cell on gel responses. *Biophysical Journal*, 86(1), 617–628.

Engler, A., Griffin, M., Sen, S., Bönnemann, C., Sweeney, H., & Discher, D. (2004b). Myotubes differentiate optimally on substrates with tissue-like stiffness pathological implications for soft or stiff microenvironments. *The Journal of Cell Biology*, 166(6), 877–887.

Engler, A. J., Rehfeldt, F., Sen, S., & Discher, D. E. (2007). Microtissue elasticity: measurements by atomic force microscopy and its influence on cell differentiation. *Methods in Cell Biology*, 83, 521–545.

Engler, A. J., Sen, S., Sweeney, H. L., & Discher, D. E. (2006). Matrix elasticity directs stem cell lineage specification. *Cell*, 126(4), 677–689.

Ermolova, N., Martinez, L., Vetrone, S., Jordan, M., Roos, K., Sweeney, H., & Spencer, M. (2014). Long-term administration of the TNF blocking drug Remicade (cV1q) to *mdx* mice reduces skeletal and cardiac muscle fibrosis, but negatively impacts cardiac function. *Neuromuscular Disorders*, 24(7), 583–595.

Ervasti, J. M. (2003). Costameres: the Achilles' heel of Herculean muscle. *Journal of Biological Chemistry*, 278(16), 13591–13594.

Fairclough, R. J., Wood, M. J., & Davies, K. E. (2013). Therapy for Duchenne muscular dystrophy: renewed optimism from genetic approaches. *Nature Reviews Genetics*, 14(6), 373–378.

Fambrough, D. M. (1979). Control of acetylcholine receptors in skeletal muscle. *Physiological Reviews*, 59(1), 165–227.

Ferraro, E., Molinari, F., & Berghella, L. (2012). Molecular control of neuromuscular junction development. *Journal of Cachexia, Sarcopenia and Muscle*, 3(1), 13–23.

Ferreira, L. M. (2010). Cancer metabolism: the Warburg effect today. *Experimental and Molecular Pathology*, 89(3), 372–380.

Findley, W. & Davis, F. (2013). *Creep and Relaxation of Nonlinear Viscoelastic Materials*. New York: Dover Publication Inc.

Firat-Karalar, E. N. & Welch, M. D. (2011). New mechanisms and functions of actin nucleation. *Current Opinion in Cell Biology*, 23(1), 4–13.

Flanagan, L. A., Ju, Y.-E., Marg, B., Osterfield, M., & Janmey, P. A. (2002). Neurite branching on deformable substrates. *Neuroreport*, 13(18), 2411.

Fletcher, D. A. & Geissler, P. L. (2009). Active biological materials. *Annual Review of Physical Chemistry*, 60, 469.

Fletcher, D. A. & Mullins, R. D. (2010). Cell mechanics and the cytoskeleton. *Nature*, 463(7280), 485–492.

Flügge, W. (1975). *Viscoelasticity*. Berlin, DE: Springer-Verlag.

Fokt, I., Szymanski, S., Skora, S., Cybulski, M., Madden, T., & Priebe, W. (2009). D-Glucose-and D-mannose-based antimetabolites. part 2. facile synthesis of 2-deoxy-2-halo-D-glucoses and-D-mannoses. *Carbohydrate Research*, 344(12), 1464–1473.

Formigli, L., Meacci, E., Sassoli, C., Chellini, F., Giannini, R., Quercioli, F., Tiribilli, B., Squecco, R., Bruni, P., Francini, F., (2005). Sphingosine 1-phosphate induces cytoskeletal reorganization in C2C12 myoblasts: physiological relevance for stress fibres in the modulation of ion current through stretch-activated channels. *Journal of Cell Science*, 118(6), 1161–1171.

Fourel, L., Valat, A., Faurobert, E., Guillot, R., Bourrin-Reynard, I., Ren, K., Lafanechère, L., Planus, E., Picart, C., & Albiges-Rizo, C. (2016). β3 integrin-mediated spreading induced by matrix-bound BMP-2 controls Smad signaling in a stiffness-independent manner. *The Journal of Cell Biology*, 212(6), 693–706.

Frederix, P., Bosshart, P., & Engel, A. (2009). Atomic force microscopy of biological membranes. *Biophysical Journal*, 96(2), 329–338.

Frey, P. A. & Arabshahi, A. (1995). Standard free energy change for the hydrolysis of the alpha, beta-phosphoanhydride bridge in ATP. *Biochemistry*, 34(36), 11307–11310.

Friedl, P. & Wolf, K. (2003). Tumour-cell invasion and migration: diversity and escape mechanisms. *Nature Reviews Cancer*, 3(5), 362–374.

Friedl, P., Wolf, K., & Lammerding, J. (2011). Nuclear mechanics during cell migration. *Current Opinion in Cell Biology*, 23(1), 55–64.

Gabor, D. (1946). Theory of communication. *Journal of the Institution of Electrical Engineering*, 93, 429–457.

Gandevia, S., Herbert, R., & Leeper, J. (1998). Voluntary activation of human elbow flexor muscles during maximal concentric contractions. *The Journal of Physiology*, 512(2), 595–602.

Garcia, S., De Haro, T., Zafra-Ceres, M., Poyatos, A., Gomez-Capilla, J. A., & Gomez-Llorente, C. (2014). Identification of *de novo* mutations of Duchenne/Becker muscular dystrophies in southern Spain. *International Journal of Medical Sciences*, 11(10), 988.

Gareis, H., Moshe, S., Baratta, R., Best, R., & D'Ambrosia, R. (1992). The isometric length-force models of nine different skeletal muscles. *Journal of Biomechanics*, 25(8), 903–916.

Gavara, N. & Chadwick, R. S. (2012). Determination of the elastic moduli of thin samples and adherent cells using conical atomic force microscope tips. *Nature Nanotechnology*, 7(11), 733–736.

Gébrane-Younès, J., Fomproix, N., & Hernandez-Verdun, D. (1997). When rDNA transcription is arrested during mitosis, UBF is still associated with non-condensed rDNA. *Journal of Cell Science*, 110(19), 2429–2440.

Geiger, B. & Bershadsky, A. (2002). Exploring the neighborhood: adhesion-coupled cell mechanosensors. *Cell*, 110(2), 139–142.

Georges, P. C. & Janmey, P. A. (2005). Cell type-specific response to growth on soft materials. *Journal of Applied Physiology*, 98(4), 1547–1553.

Ghassemi, S., Meacci, G., Liu, S., Gondarenko, A. A., Mathur, A., Roca-Cusachs, P., Sheetz, M. P., & Hone, J. (2012). Cells test substrate rigidity by local contractions on submicrometer pillars. *Proceedings of the National Academy of Sciences USA*, 109(14), 5328–5333.

Ghibaudo, M., Trichet, L., Le Digabel, J., Richert, A., Hersen, P., & Ladoux, B. (2009). Substrate topography induces a crossover from 2D to 3D behavior in fibroblast migration. *Biophysical Journal*, 97(1), 357–368.

Gibson, M. C., Patel, A. B., Nagpal, R., & Perrimon, N. (2006). The emergence of geometric order in proliferating metazoan epithelia. *Nature*, 442(7106), 1038–1041.

Gilbert, S. F. (2003). *Developmental Biology, Seventh Edition*. Sinauer Associates Inc. Sunderland MA.

Gimbrone, M. A., Topper, J. N., Nagel, T., Anderson, K. R., & Garcia-Cardeña, G. (2000). Endothelial dysfunction, hemodynamic forces, and atherogenesisa. *Annals of the New York Academy of Sciences*, 902(1), 230–240.

Glascott, P. A., McSorley, K. M., Mittal, B., Sanger, J. M., & Sanger, J. W. (1987). Stress fiber reformation after ATP depletion. *Cell Motility and the Cytoskeleton*, 8(2), 118–129.

Glerum, J., Van Mastrigt, R., & Van Koeveringe, A. (1990). Mechanical properties of mammalian single smooth muscle cells III. Passive properties of pig detrusor and human a terme uterus cells. *Journal of Muscle Research & Cell Motility*, 11(5), 453–462.

Goldfarb, L., Vicart, P., Goebel, H., & Dalakas, M. (2004). Desmin myopathy. *Brain*, 127(4), 723–734.

Goldman, R. D., Milsted, A., Schloss, J. A., Starger, J., & Yerna, M.-J. (1979). Cytoplasmic fibers in mammalian cells: cytoskeletal and contractile elements. *Annual Review of Physiology*, 41(1), 703–722.

Goldstein, J. A. & McNally, E. M. (2010). Mechanisms of muscle weakness in muscular dystrophy. *The Journal of General Physiology*, 136(1), 29–34.

Goley, E. D. & Welch, M. D. (2006). The Arp2/3 complex: an actin nucleator comes of age. *Nature Reviews Molecular Cell Biology*, 7(10), 713–726.

Gonzalez-Freire, M., de Cabo, R., Studenski, S. A., & Ferrucci, L. (2014). The neuromuscular junction: Aging at the crossroad between nerves and muscle. *Frontiers in Aging Neuroscience*, 6(208), 1–11.

Gorecki, D. C. (2016). Dystrophin: the dead calm of a dogma. *Rare Diseases*, 4(1), e1153777.

Gowers, W. R. (1879). *Pseudo-hypertrophic Muscular Paralysis: a Clinical Lecture*. J. & A. Churchill, London, UK.

Grabe, M., Wang, H., & Oster, G. (2000). The mechanochemistry of V-ATPase proton pumps. *Biophysical Journal*, 78(6), 2798–2813.

Graham, G. A. C. (1965). The contact problem in the linear theory of viscoelasticity. *International Journal of Engineering Science*, 3(1), 27–46.

Graham, G. A. C. (1967). The contact problem in the linear theory of viscoelasticity when the time dependent contact area has any number of maxima and minima. *International Journal of Engineering Science*, 5(6), 495–514.

Grange, R. W., Gainer, T. G., Marschner, K. M., Talmadge, R. J., & Stull, J. T. (2002). Fast-twitch skeletal muscles of dystrophic mouse pups are resistant to injury from acute mechanical stress. *American Journal of Physiology-Cell Physiology*, 283(4), C1090–C1101.

Greaves, G. N., Greer, A., Lakes, R., & Rouxel, T. (2011). Poisson's ratio and modern materials. *Nature Materials*, 10(11), 823–837.

Gregorevic, P., Plant, D. R., Leeding, K. S., Bach, L. A., & Lynch, G. S. (2002). Improved contractile function of the *mdx* dystrophic mouse diaphragm muscle after insulin-like growth factor-I administration. *The American Journal of Pathology*, 161(6), 2263–2272.

Gregorevic, P., Plant, D. R., & Lynch, G. S. (2004). Administration of insulin-like growth factor-I improves fatigue resistance of skeletal muscles from dystrophic *mdx* mice. *Muscle & Nerve*, 30(3), 295–304.

Griffin, M. A., Sen, S., Sweeney, H. L., & Discher, D. E. (2004). Adhesion-contractile balance in myocyte differentiation. *Journal of Cell Science*, 117(24), 5855–5863.

Grossmann, A. & Morlet, J. (1984). Decomposition of Hardy functions into square integrable wavelets of constant shape. *SIAM Journal on Mathematical Analysis*, 15(4), 723–736.

Grover, C. N., Gwynne, J. H., Pugh, N., Hamaia, S., Farndale, R. W., Best, S. M., & Cameron, R. E. (2012). Crosslinking and composition influence the surface properties, mechanical stiffness and cell reactivity of collagen-based films. *Acta Biomaterialia*, 8(8), 3080–3090.

Gundersen, G. G., Khawaja, S., & Bulinski, J. C. (1989). Generation of a stable, posttranslationally modified microtubule array is an early event in myogenic differentiation. *The Journal of Cell Biology*, 109(5), 2275–2288.

Gundersen, G. G. & Worman, H. J. (2013). Nuclear positioning. *Cell*, 152(6), 1376–1389.

Gundry, R. L., Raginski, K., Tarasova, Y., Tchernyshyov, I., Bausch-Fluck, D., Elliott, S. T., Boheler, K. R., Van Eyk, J. E., & Wollscheid, B. (2009). The mouse C2C12 myoblast cell surface N-linked glycoproteome identification, glycosite occupancy, and membrane orientation. *Molecular & Cellular Proteomics*, 8(11), 2555–2569.

Gutiérrez, J. M. & Ownby, C. L. (2003). Skeletal muscle degeneration induced by venom phospholipases A2: insights into the mechanisms of local and systemic myotoxicity. *Toxicon*, 42(8), 915–931.

Guttridge, D., Albanese, C., Reuther, J., Pestell, R., & Baldwin, A. (1999). NF-κB controls cell growth and differentiation through transcriptional regulation of cyclin D1. *Molecular and Cellular Biology*, 19(8), 5785–5799.

Haase, K. & Pelling, A. E. (2015). Investigating cell mechanics with atomic force microscopy. *Journal of The Royal Society Interface*, 12(104), 20140970.

Haenggi, T. & Fritschy, J.-M. (2006). Role of dystrophin and utrophin for assembly and function of the dystrophin glycoprotein complex in non-muscle tissue. *Cellular and Molecular Life Sciences CMLS*, 63(14), 1614–1631.

Hall, Z. W. & Sanes, J. R. (1993). Synaptic structure and development: the neuromuscular junction. *Cell*, 72, 99–121.

Hansen-Smith, F. M., Picou, D., & Golden, M. (1979). Muscle satellite cells in malnourished and nutritionally rehabilitated children. *Journal of the Neurological Sciences*, 41(2), 207–221.

Happel, J. & Brenner, H. (1983). *Low Reynolds Number Hydrodynamics*. The Hague, The Netherlands: Martinus Nijhoff Publishers.

Harada, T., Swift, J., Irianto, J., Shin, J.-W., Spinler, K. R., Athirasala, A., Diegmiller, R., Dingal, P. D. P., Ivanovska, I. L., & Discher, D. E. (2014). Nuclear lamin stiffness is a barrier to 3D migration, but softness can limit survival. *The Journal of Cell Biology*, 204(5), 669–682.

Harasim, M., Wunderlich, B., Peleg, O., Kröger, M., & Bausch, A. R. (2013). Direct observation of the dynamics of semiflexible polymers in shear flow. *Physical Review Letters*, 110(10), 108302.

Harn, H. I., Wang, Y.-K., Hsu, C.-K., Ho, Y.-T., Huang, Y.-W., Chiu, W.-T., Lin, H.-H., Cheng, C.-M., Tang, M.-J., (2015). Mechanical coupling of cytoskeletal elasticity and force generation is crucial for understanding the migrating nature of keloid fibroblasts. *Experimental Dermatology*, 24(8), 579–584.

Harper, S. Q., Hauser, M. A., DelloRusso, C., Duan, D., Crawford, R. W., Phelps, S. F., Harper, H. A., Robinson, A. S., Engelhardt, J. F., Brooks, S. V., & Chamberlain, J. S. (2002). Modular flexibility of dystrophin: implications for gene therapy of Duchenne muscular dystrophy. *Nature Medicine*, 8(3), 253–261.

Hartman, M. A. & Spudich, J. A. (2012). The myosin superfamily at a glance. *Journal of Cell Science*, 125(7), 1627–1632.

Hawke, T. J. & Garry, D. J. (2001). Myogenic satellite cells: physiology to molecular biology. *Journal of Applied Physiology*, 91(2), 534–551.

Hawkins, D. & Bey, M. (1997). Muscle and tendon force-length properties and their interactions *in vivo*. *Journal of Biomechanics*, 30(1), 63–70.

Hayashi, K. & Iwata, M. (2015). Stiffness of cancer cells measured with an AFM indentation method. *Journal of the Mechanical Behavior of Biomedical Materials*, 49, 105–111.

Head, S. I. (2010). Branched fibres in old dystrophic *mdx* muscle are associated with mechanical weakening of the sarcolemma, abnormal Ca^{2+} transients and a breakdown of Ca^{2+} homeostasis during fatigue. *Experimental Physiology*, 95(5), 641–656.

Helfand, B. T., Chang, L., & Goldman, R. D. (2004). Intermediate filaments are dynamic and motile elements of cellular architecture. *Journal of Cell Science*, 117(2), 133–141.

Helmke, B. P. & Davies, P. F. (2002). The cytoskeleton under external fluid mechanical forces: hemodynamic forces acting on the endothelium. *Annals of Biomedical Engineering*, 30(3), 284–296.

Herget-Rosenthal, S., Hosford, M., Kribben, A., Atkinson, S. J., Sandoval, R. M., & Molitoris, B. A. (2001). Characteristics of EYFP-actin and visualization of actin dynamics during ATP depletion and repletion. *American Journal of Physiology-Cell Physiology*, 281(6), C1858–C1870.

Hernandez-Verdun, D. (2011). Assembly and disassembly of the nucleolus during the cell cycle. *Nucleus*, 2(3), 189–194.

Herrmann, H., Bär, H., Kreplak, L., Strelkov, S. V., & Aebi, U. (2007). Intermediate filaments: from cell architecture to nanomechanics. *Nature Reviews Molecular Cell Biology*, 8(7), 562–573.

Heydemann, A. & McNally, E. M. (2007). Consequences of disrupting the dystrophin-sarcoglycan complex in cardiac and skeletal myopathy. *Trends in Cardiovascular Medicine*, 17(2), 55–59.

Hieter, P. & Griffiths, T. (1999). Polyploidy–more is more or less. *Science*, 285(5425), 210–211.

Hill, A. V. (1959). The heat production of muscle and nerve, 1848-1914. *Annual Review of Physiology*, 21(1), 1–19.

Hinderliter, P., Minard, K., Orr, G., Chrisler, W., Thrall, B., Pounds, J., & Teeguarden, J. (2010). ISDD: A computational model of particle sedimentation, diffusion and target cell dosimetry for in vitro toxicity studies. *Particle and Fibre Toxicology*, 7(1), 1.

Hinshaw, D. B., Armstrong, B. C., Beals, T. F., & Hyslop, P. A. (1988). A cellular model of endothelial cell ischemia. *Journal of Surgical Research*, 44(5), 527–537.

Hiramoto, Y. (1987). Mechanical properties of the protoplasm of echinoderm eggs at various stages of cell cycle. In *Biomechanics of Cell Division* (pp. 13–35). Plenum Press, New York (NY).

Hnia, K., Hugon, G., Rivier, F., Masmoudi, A., Mercier, J., & Mornet, D. (2007). Modulation of p38 mitogen-activated protein kinase cascade and metalloproteinase activity in diaphragm muscle in response to free radical scavenger administration in dystrophin-deficient *mdx* mice. *The American Journal of Pathology*, 170(2), 633–643.

Hodges, C. (2002). Measuring forces with the AFM: Polymeric surfaces in liquids. *Advances in Colloid and Interface Science*, 99(1), 13–75.

Hoebertz, A., Mahendran, S., Burnstock, G., & Arnett, T. R. (2002). ATP and UTP at low concentrations strongly inhibit bone formation by osteoblasts: a novel role for the P2Y2 receptor in bone remodeling. *Journal of Cellular Biochemistry*, 86(3), 413–419.

Hoffman, B. D. & Crocker, J. C. (2009). Cell mechanics: dissecting the physical responses of cells to force. *Annual Review of Biomedical Engineering*, 11, 259–288.

Hoffman, B. D., Massiera, G., Van Citters, K. M., & Crocker, J. C. (2006). The consensus mechanics of cultured mammalian cells. *Proceedings of the National Academy of Sciences USA*, 103(27), 10259–10264.

Hoffman, E. P., Brown, R. H., & Kunkel, L. M. (1987). Dystrophin: the protein product of the Duchenne muscular dystrophy locus. *Cell*, 51(6), 919–928.

Hoffman, E. P. & Connor, E. M. (2013). Orphan drug development in muscular dystrophy: update on two large clinical trials of dystrophin rescue therapies. *Discovery Medicine*, 16(89), 233–239.

Hoffman, E. P. & McNally, E. M. (2014). Exon-skipping therapy for muscular dystrophy: A roadblock, detour, or bump in the road? *Science Translational Medicine*, 6(230), 230fs14.

Hofmann, U. G., Rotsch, C., Parak, W. J., & Radmacher, M. (1997). Investigating the cytoskeleton of chicken cardiocytes with the atomic force microscope. *Journal of Structural Biology*, 119(2), 84–91.

Hogg, R., Raggenbass, M., & Bertrand, D. (2003). Nicotinic acetylcholine receptors: from structure to brain function. In *Reviews of Physiology, Biochemistry and Pharmacology* (pp. 1–46). Springer, Heidelberg, Berlin.

Hoh, H. & Engel, A. (1993). Friction effects on force measurements with an atomic force microscop. *Langmuir*, 9, 3310–3312.

Hoh, J. H. & Schoenenberger, C.-A. (1994). Surface morphology and mechanical properties of MDCK monolayers by atomic force microscopy. *Journal of Cell Science*, 107(5), 1105–1114.

Holmes, K. C., Popp, D., Gebhard, W., & Kabsch, W. (1990). Atomic model of the actin filament. *Nature*, 347(6288), 44–49.

Holzer, N., Hogendoorn, S., Zürcher, L., Garavaglia, G., Yang, S., König, S., Laumonier, T., & Menetrey, J. (2005). Autologous transplantation of porcine myogenic precursor cells in skeletal muscle. *Neuromuscular Disorders*, 15(3), 237–244.

Hoogerwaard, E., Bakker, E., Ippel, P., Oosterwijk, J., Majoor-Krakauer, D., Leschot, N., Van Essen, A., Brunner, H., Van der Wouw, P., Wilde, A., & de Visser, M. (1999). Signs and symptoms of Duchenne muscular dystrophy and Becker muscular dystrophy among carriers in The Netherlands: a cohort study. *The Lancet*, 353(9170), 2116–2119.

Horsley, V., Jansen, K. M., Mills, S. T., & Pavlath, G. K. (2003). IL-4 acts as a myoblast recruitment factor during mammalian muscle growth. *Cell*, 113(4), 483–494.

Hoshino, S., Ohkoshi, N., Ishii, A., Kameya, S., Takeda, S., & Shoji, S. (2001). The expression of dystrophin and α1-syntrophin during skeletal muscle regeneration. *Journal of Muscle Research & Cell Motility*, 22(2), 185–191.

Hsu, J. (1981). Skeletal changes in children with neuromuscular disorders. *Progress in Clinical and Biological Research*, 101, 553–557.

Hu, X., Park, S., Gil, E., Xia, X., Weiss, A., & Kaplan, D. (2011). The influence of elasticity and surface roughness on myogenic and osteogenic-differentiation of cells on silk-elastin biomaterials. *Biomaterials*, 32(34), 8979–8989.

Huang, G. & Lu, H. (2006). Measurement of Young's relaxation modulus using nanoindentation. *Mechanics of Time-Dependent Materials*, 10(3), 229–243.

Hughes, B. W., Kusner, L. L., & Kaminski, H. J. (2006). Molecular architecture of the neuromuscular junction. *Muscle & Nerve*, 33(4), 445–461.

Hunt, C. C. & Kuffler, S. W. (1950). Pharmacology of the neuromuscular junction. *Pharmacological Reviews*, 2(1), 96–120.

Hunter, S. (1960). The Hertz problem for a rigid spherical indenter and a viscoelastic half-space. *Journal of the Mechanics and Physics of Solids*, 8(4), 219–234.

Hutter, J. & Bechhoefer, J. (1993). Calibration of atomic-force microscope tips. *Review of Scientific Instruments*, 64(7), 1868–1873.

Hutter, J. L. (2005). Comment on tilt of atomic force microscope cantilevers: effect on spring constant and adhesion measurements. *Langmuir*, 21(6), 2630–2632.

Huxley, H. & Hanson, J. (1954). Changes in the cross-striations of muscle during contraction and stretch and their structural interpretation. *Nature*, 173, 973–976.

Huzé, C., Bauché, S., Richard, P., Chevessier, F., Goillot, E., Gaudon, K., Ammar, A. B., Chaboud, A., Grosjean, I., Lecuyer, H.-A., Bernard, V., Rouche, A., Alexandri, N., Kuntzer, T., Fardeau, M., Fournier, E., Brancaccio, A., Ruegg, M. A., Koenig, J., Eymard, B., Schaeffer, L., & Hantai, D. (2009). Identification of an agrin mutation that causes congenital myasthenia and affects synapse function. *The American Journal of Human Genetics*, 85(2), 155–167.

Hynes, R. O. (2002). Integrins : bidirectional, allosteric signaling machines. *Cell*, 110(1), 673–687.

Ingber, D. (2003a). Mechanobiology and diseases of mechanotransduction. *Annals of Medicine*, 35(8), 564–577.

Ingber, D. (2003b). Tensegrity II. How structural networks influence cellular information processing networks. *Journal of Cell Science*, 116(8), 1397–1408.

Inoue, S., Frank, V., Hörning, M., Kaufmann, S., Yoshikawa, H., Madsen, J., Lewis, A., Armes, S., & Tanaka, M. (2015). Live cell tracking of symmetry break in actin cytoskeleton triggered by abrupt changes in micromechanical environments. *Biomaterials Science*, 3(12), 1539–1544.

Iovino, S., Burkart, A. M., Warren, L., Patti, M. E., & Kahn, C. R. (2016). Myotubes derived from human-induced pluripotent stem cells mirror *in vivo* insulin resistance. *Proceedings of the National Academy of Sciences USA*, 113(7), 1889–1894.

Jahraus, A., Egeberg, M., Hinner, B., Habermann, A., Sackman, E., Pralle, A., Faulstich, H., Rybin, V., Defacque, H., & Griffiths, G. (2001). ATP-dependent membrane assembly of F-actin facilitates membrane fusion. *Molecular Biology of the Cell*, 12(1), 155–170.

Jamison, C., Marangoni, R., & Glaser, A. (1968). Viscoelastic properties of soft tissue by discrete model characterization. *Journal of Engineering for Industry*, 90(2), 239–247.

Jang, Y. C. & Van Remmen, H. (2011). Age-associated alterations of the neuromuscular junction. *Experimental Gerontology*, 46(2), 193–198.

Janmey, P. A. & McCulloch, C. A. (2007). Cell mechanics: integrating cell responses to mechanical stimuli. *Annual Review of Biomedical Engineering*, 9, 1–34.

Janovjak, H., Struckmeier, J., & Müller, D. J. (2005). Hydrodynamic effects in fast AFM single-molecule force measurements. *European Biophysics Journal*, 34(1), 91–96.

Jansen, K. A., Donato, D. M., Balcioglu, H. E., Schmidt, T., Danen, E. H., & Koenderink, G. H. (2015). A guide to mechanobiology: where biology and physics meet. *Biochimica et Biophysica Acta (BBA)-Molecular Cell Research*, 1853(11), 3043–3052.

Jennekens, F., Ten Kate, L., De Visser, M., & Wintzen, A. (1991). Diagnostic criteria for Duchenne and Becker muscular dystrophy and myotonic dystrophy. *Neuromuscular Disorders*, 1(6), 389–391.

Jirmanová, I. & Thesleff, S. (1972). Ultrastructural study of experimental muscle degeneration and regeneration in the adult rat. *Zeitschrift für Zellforschung und Mikroskopische Anatomie*, 131(1), 77–97.

Johansson, F., Carlberg, P., Danielsen, N., Montelius, L., & Kanje, M. (2006). Axonal outgrowth on nano-imprinted patterns. *Biomaterials*, 27(8), 1251 – 1258.

Jonckheere, A. I., Smeitink, J. A., & Rodenburg, R. J. (2012). Mitochondrial ATP synthase: architecture, function and pathology. *Journal of Inherited Metabolic Disease*, 35(2), 211–225.

Kalderon, N. & Gilula, N. B. (1979). Membrane events involved in myoblast fusion. *The Journal of Cell Biology*, 81(2), 411–425.

Kalyani, R. R., Corriere, M., & Ferrucci, L. (2014). Age-related and disease-related muscle loss: the effect of diabetes, obesity, and other diseases. *The Lancet Diabetes & Endocrinology*, 2(10), 819–829.

Kamli, M. R., Kim, J., Pokharel, S., Jan, A. T., Lee, E. J., & Choi, I. (2014). Expressional studies of the aldehyde oxidase (AOX1) gene during myogenic differentiation in C2C12 cells. *Biochemical and Biophysical Research Communications*, 450(4), 1291–1296.

Kaplan, J.-C. & Hamroun, D. (2013). The 2014 version of the gene table of monogenic neuromuscular disorders (nuclear genome). *Neuromuscular Disorders*, 23(12), 1081–1111.

Karimi, A., Navidbakhsh, M., Alizadeh, M., & Razaghi, R. (2014). A comparative study on the elastic modulus of polyvinyl alcohol sponge using different stress-strain definitions. *Biomedical Engineering/Biomedizinische Technik*, 59(5), 439–446.

Katagiri, T., Yamaguchi, A., Komaki, M., Abe, E., Takahashi, N., Ikeda, T., Rosen, V., Wozney, J. M., Fujisawa-Sehara, A., & Suda, T. (1994). Bone morphogenetic protein-2 converts the differentiation pathway of C2C12 myoblasts into the osteoblast lineage. *The Journal of Cell Biology*, 127(6), 1755–1766.

Kaufman, S. J. & Foster, R. F. (1988). Replicating myoblasts express a muscle-specific phenotype. *Proceedings of the National Academy of Sciences USA*, 85(24), 9606–9610.

Kaufmann, U., Kirsch, J., Irintchev, A., Wernig, A., & Starzinski-Powitz, A. (1999). The M-cadherin catenin complex interacts with microtubules in skeletal muscle cells: implications for the fusion of myoblasts. *Journal of Cell Science*, 112(1), 55–68.

Kawabuchi, M., Tan, H., & Wang, S. (2011). Age affects reciprocal cellular interactions in neuromuscular synapses following peripheral nerve injury. *Ageing Research Reviews*, 10(1), 43–53.

Keating, T. J. & Borisy, G. G. (1999). Centrosomal and non-centrosomal microtubules. *Biology of the Cell*, 91(4-5), 321–329.

Kelly, G. M., Kilpatrick, J. I., Van Es, M. H., Weafer, P. P., Prendergast, P. J., & Jarvis, S. P. (2011). Bone cell elasticity and morphology changes during the cell cycle. *Journal of Biomechanics*, 44(8), 1484–1490.

Kesper, D. A., Stute, C., Buttgereit, D., Kreisköther, N., Vishnu, S., Fischbach, K.-F., & Renkawitz-Pohl, R. (2007). Myoblast fusion in Drosophila melanogaster is mediated through a fusion-restricted myogenic-adhesive structure (furmas). *Developmental Dynamics*, 236(2), 404–415.

Khairallah, R. J., Shi, G., Sbrana, F., Prosser, B. L., Borroto, C., Mazaitis, M. J., Hoffman, E. P., Mahurkar, A., Sachs, F., Sun, Y., (2012). Microtubules underlie dysfunction in Duchenne muscular dystrophy. *Science Signaling*, 5(236).

Khalil, A., Grant, J. L., Caddle, L. B., Atzema, E., Mills, K. D., & Arneodo, A. (2007). Chromosome territories have a highly nonspherical morphology and nonrandom positioning. *Chromosome Research*, 15, 899–916.

Khatau, S. B., Hale, C. M., Stewart-Hutchinson, P., Patel, M. S., Stewart, C. L., Searson, P. C., Hodzic, D., & Wirtz, D. (2009). A perinuclear actin cap regulates nuclear shape. *Proceedings of the National Academy of Sciences USA*, 106(45), 19017–19022.

Khatau, S. B., Kim, D.-H., Hale, C. M., Bloom, R. J., & Wirtz, D. (2010). The perinuclear actin cap in health and disease. *Nucleus*, 1(4), 337–342.

Kiecker, C., Bates, T., & Bell, E. (2016). Molecular specification of germ layers in vertebrate embryos. *Cellular and Molecular Life Sciences*, 73(5), 923–947.

Kim, D.-H., Chambliss, A. B., & Wirtz, D. (2013). The multi-faceted role of the actin cap in cellular mechanosensation and mechanotransduction. *Soft Matter*, 9(23), 5516–5523.

Kim, D.-H., Khatau, S. B., Feng, Y., Walcott, S., Sun, S. X., Longmore, G. D., & Wirtz, D. (2012). Actin cap associated focal adhesions and their distinct role in cellular mechanosensing. *Scientific Reports*, 2, 555.

Kim, S. & Coulombe, P. A. (2007). Intermediate filament scaffolds fulfill mechanical, organizational, and signaling functions in the cytoplasm. *Genes & Development*, 21(13), 1581–1597.

Kinoshita, I., Vilquin, J.-T., Gravel, C., Roy, R., & Tremblay, J. (1995). Myoblast allo-transplantation in primates. *Muscle & Nerve*, 18(10), 1217–1218.

Kirby, B. J. (2010). *Micro- and Nanoscale Fluid Mechanics: Transport in Microfluidic Devices*. Cambridge, UK: Cambridge University Press.

Kirmizis, D. & Logothetidis, S. (2010). Atomic force microscopy probing in the measurement of cell mechanics. *International Journal of Nanomedicine*, 5(137), e45.

Klein-Nulend, J., Bacabac, R., Veldhuijzen, J., & Van Loon, J. (2003). Microgravity and bone cell mechanosensitivity. *Advances in Space Research*, 32(8), 1551–1559.

Knauss, W. G., Emri, I., & Lu, H. (2008). *Mechanics of Polymers: Viscoelasticity*. New York: Springer Science+Business Media.

Knight, B., Laukaitis, C., Akhtar, N., Hotchin, N. A., Edlund, M., & Horwitz, A. R. (2000). Visualizing muscle cell migration in situ. *Current Biology*, 10(10), 576–585.

Kolb, H.-A. & Wakelam, M. J. (1983). Transmitter-like action of ATP on patched membranes of cultured myoblasts and myotubes. *Nature*, 303(5918), 621–623.

Konigsberg, I. R. (1963). Clonal analysis of myogenesis. *Science*, 140(3573), 1273–1284.

Konigsberg, U. R., Lipton, B. H., & Konigsberg, I. R. (1975). The regenerative response of single mature muscle fibers isolated in vitro. *Developmental Biology*, 45(2), 260–275.

Kottlors, M. & Kirschner, J. (2010). Elevated satellite cell number in Duchenne muscular dystrophy. *Cell and Tissue Research*, 340(3), 541–548.

Kovács, M., Tóth, J., Hetényi, C., Málnási-Csizmadia, A., & Sellers, J. (2004). Mechanism of blebbistatin inhibition of myosin II. *Journal of Biological Chemistry*, 279(34), 35557–35563.

Kretschmann, E. & Raether, H. (1968). Radiative decay of non radiative surface plasmons excited by light. *Zeitschrift für Naturforschung A*, 23(12), 2135–2136.

Kumar, A., Khandelwal, N., Malya, R., Breid, M. B., & Boriek, A. M. (2004). Loss of dystrophin causes aberrant mechanotransduction in skeletal muscle fibers. *The FASEB Journal*, 18(1), 102–113.

Kumar, S. & Weaver, V. M. (2009). Mechanics, malignancy, and metastasis: the force journey of a tumor cell. *Cancer and Metastasis Reviews*, 28(1-2), 113–127.

Kumar, V., Abbas, A. K., Fausto, N., & Aster, J. C. (2014). *Robbins and Cotran Pathologic Basis of Disease*. Elsevier Health Sciences, Philadelphia, PA.

Kunkel, L. M. (2005). Cloning of the DMD Gene. *The American Journal of Human Genetics*, 76(2), 205–214.

Kuznetsova, T. G., Starodubtseva, M. N., Yegorenkov, N. I., Chizhik, S. A., & Zhdanov, R. I. (2007). Atomic force microscopy probing of cell elasticity. *Micron*, 38(8), 824–833.

Kwon, O., Phillips, C. L., & Molitoris, B. A. (2002). Ischemia induces alterations in actin filaments in renal vascular smooth muscle cells. *American Journal of Physiology-Renal Physiology*, 282(6), F1012–F1019.

Ladoux, B. & Nicolas, A. (2012). Physically based principles of cell adhesion mechanosensitivity in tissues. *Reports on Progress in Physics*, 75(11), 116601.

Lai, S., Wang, Y., Wirtz, D., & Hanes, J. (2009). Micro-and macrorheology of mucus. *Advanced Drug Delivery Reviews*, 61(2), 86–100.

Lakes, R. (1993). Advances in negative Poisson's ratio materials. *Advanced Materials*, 5(4), 293–296.

Lakes, R. (2009). *Viscoelastic Materials*. Cambridge, UK: Cambridge University Press.

Lammerding, J., C, S. P., Takahashi, T., Kozlov, S., Sullivan, T., D, K. R., Stewart, C. L., & Lee, R. T. (2004). Lamin A/C deficiency causes defective nuclear mechanics and mechanotransduction. *Journal of Clinical Investigation*, 113(3), 370–378.

Lämmermann, T., Bader, B. L., Monkley, S. J., Worbs, T., Wedlich-Söldner, R., Hirsch, K., Keller, M., Förster, R., Critchley, D. R., Fässler, R., & Sixt, M. (2008). Rapid leukocyte migration by integrin-independent flowing and squeezing. *Nature*, 453(7191), 51–55.

Lanner, J. T., Georgiou, D. K., Joshi, A. D., & Hamilton, S. L. (2010). Ryanodine receptors: structure, expression, molecular details, and function in calcium release. *Cold Spring Harbor Perspectives in Biology*, 2(11), a003996.

Laperrousaz, B., Berguiga, L., Nicolini, F. E., Martinez-Torres, C., Arneodo, A., Maguer-Satta, V., & Argoul, F. (2016a). Revealing stiffening and brittlening of chronic myelogenous leukemia hematopoietic primary cells through their temporal response to shear stress. *Physical Biology*, 13, 03LT01.

Laperrousaz, B., Drillon, G., Berguiga, L., Nicolini, F., Audit, B., Maguer-Satta, V., Arneodo, A., & Argoul, F. (2016b). From elasticity to inelasticity in cancer cell mechanics: A loss of scale-invariance. *AIP Conference Proceedings*, 1760, 020040.

Lardenois, A., Jagot, S., Lagarrigue, M., Guével, B., Ledevin, M., Larcher, T., Dubreil, L., Pineau, C., Rouger, K., & Guével, L. (2016). Quantitative proteome profiling of dystrophic dog skeletal muscle reveals a stabilized muscular architecture and protection against oxidative stress after systemic delivery of MuStem cells. *Proteomics*, 16, 2028–2042.

Laurent, V. M., Duperray, A., Rajan, V. S., & Verdier, C. (2014). Atomic force microscopy reveals a role for endothelial cell ICAM-1 expression in bladder cancer cell adherence. *PloS One*, 9(5), e98034.

Laurin, M., Fradet, N., Blangy, A., Hall, A., Vuori, K., & Côté, J.-F. (2008). The atypical Rac activator Dock180 (Dock1) regulates myoblast fusion in vivo. *Proceedings of the National Academy of Sciences USA*, 105(40), 15446–15451.

Lazarides, E. (1980). *Desmin and Intermediate Filaments in Muscle Cells*, (pp. 124–131). Springer Berlin Heidelberg: Berlin, Heidelberg.

Lazarides, E. (1982). Intermediate filaments: a chemically heterogeneous, developmentally regulated class of proteins. *Annual Review of Biochemistry*, 51(1), 219–250.

Lazarides, E. & Hubbard, B. D. (1976). Immunological characterization of the subunit of the 100 A filaments from muscle cells. *Proceedings of the National Academy of Sciences USA*, 73(12), 4344–4348.

Le Digabel, J., Ghibaudo, M., Trichet, L., Richert, A., & Ladoux, B. (2010). Microfabricated substrates as a tool to study cell mechanotransduction. *Medical & Biological Engineering & Computing*, 48(10), 965–976.

Le Grand, F. & Rudnicki, M. A. (2007). Skeletal muscle satellite cells and adult myogenesis. *Current Opinion in Cell Biology*, 19(6), 628–633.

Le Rumeur, E., Winder, S. J., & Hubert, J.-F. (2010). Dystrophin: more than just the sum of its parts. *Biochimica et Biophysica Acta (BBA)-Proteins and Proteomics*, 1804(9), 1713–1722.

Lee, E. J., Bhat, A. R., Kamli, M. R., Pokharel, S., Chun, T., Lee, Y.-H., Nahm, S.-S., Nam, J. H., Hong, S. K., Yang, B., Chung, K. Y., Kim, S. H., & Choi, I. (2013). Transthyretin is a key regulator of myoblast differentiation. *PloS One*, 8(5), e63627.

Lee, J., Tachibana, Hand Morinaga, Y., Fujimura, Y., & Yamada, K. (2009). Modulation of proliferation and differentiation of C2C12 skeletal muscle cells by fatty acids. *Life Sciences*, 84(13), 415–420.

Lee, L. M. & Liu, A. P. (2014). The application of micropipette aspiration in molecular mechanics of single cells. *Journal of Nanotechnology in Engineering and Medicine*, 5(4), 040902.

Lee, S.-W., Won, J.-Y., Yang, J., Lee, J., Kim, S.-Y., Lee, E. J., & Kim, H.-S. (2015). AKAP6 inhibition impairs myoblast differentiation and muscle regeneration: Positive loop between AKAP6 and myogenin. *Scientific Reports*, 5, 16523.

Leitch, A. R. (2000). Higher levels of organization in the interphase nucleus of cycling and differentiated cells. *Microbiology and Molecular Biology Reviews*, 64(1), 138–152.

Leite, F., Riul, J., & Herrmann, P. (2003). Mapping of adhesion forces on soil minerals in air and water by atomic force spectroscopy (AFS). *Journal of Adhesion Science and Technology*, 17(16), 2141–2156.

Leite, F. L., Mattoso, L. H. C., Oliveira Jr, O. N., & Herrmann Jr, P. S. P. (2007). The atomic force spectroscopy as a tool to investigate surface forces: Basic principles and applications. In A. Mendez-Vilas & J. Diaz (Eds.), *Modern Research and Educational Topics in Microscopy* (pp. 747–757). Badajoz, Spain: Formatex.

Leitinger, B. (2011). Transmembrane collagen receptors. *Annual Review of Cell and Developmental Biology*, 27, 265–290.

Lekka, M., Laidler, P., Gil, D., Lekki, J., Stachura, Z., & Hrynkiewicz, A. (1999). Elasticity of normal and cancerous human bladder cells studied by scanning force microscopy. *European Biophysics Journal*, 28(4), 312–316.

Lepper, C., Partridge, T. A., & Fan, C.-M. (2011). An absolute requirement for Pax7-positive satellite cells in acute injury-induced skeletal muscle regeneration. *Development*, 138(17), 3639–3646.

Li, H., Choudhary, S. K., Milner, D. J., Munir, M. I., Kuisk, I. R., & Capetanaki, Y. (1994). Inhibition of desmin expression blocks myoblast fusion and interferes with the myogenic regulators MyoD and myogenin. *The Journal of Cell Biology*, 124(5), 827–841.

Li, M., Liu, L., Xiao, X., Xi, N., & Wang, Y. (2016). Effects of methotrexate on the viscoelastic properties of single cells probed by atomic force microscopy. *Journal of Biological Physics*, 42(4), 551–569.

Li, Q., Lee, G., Ong, C., & Lim, C. (2008). AFM indentation study of breast cancer cells. *Biochemical and Biophysical Research Communications*, 374(4), 609–613.

Li, S., Patwardhan, A., Amirouche, F., Havey, R., & Meade, K. (1995). Limitations of the standard linear solid model of intervertebral discs subject to prolonged loading and low-frequency vibration in axial compression. *Journal of Biomechanics*, 28(7), 779–790.

Lieber, R. L. & Friden, J. (1993). Muscle damage is not a function of muscle force but active muscle strain. *Journal of Applied Physiology*, 74(2), 520–526.

Lieber, S. C., Aubry, N., Pain, J., Diaz, G., Kim, S.-J., & Vatner, S. F. (2004). Aging increases stiffness of cardiac myocytes measured by atomic force microscopy nanoindentation. *American Journal of Physiology-Heart and Circulatory Physiology*, 287(2), H645–H651.

Limouze, J., Straight, A. F., Mitchison, T., & Sellers, J. R. (2004). Specificity of blebbistatin, an inhibitor of myosin II. *Journal of Muscle Research & Cell Motility*, 25(4-5), 337–341.

Limpert, E., Stahel, W., & Abbt, M. (2001). Lognormal distributions across the sciences: keys and clues. *BiosScience*, 51(5), 341–352.

Liu, H., Wen, J., Xiao, Y., Liu, J., Hopyan, S., Radisic, M., Simmons, C. A., & Sun, Y. (2014). In situ mechanical characterization of the cell nucleus by atomic force microscopy. *ACS Nano*, 8(4), 3821–3828.

Liu, R., Roman, M., & Yang, G. (2010). Correction of the viscous drag induced errors in macromolecular manipulation experiments using atomic force microscope. *Review of Scientific Instruments*, 81(6), 1–5.

Liu, Y.-J., Le Berre, M., Lautenschlaeger, F., Maiuri, P., Callan-Jones, A., Heuzé, M., Takaki, T., Voituriez, R., & Piel, M. (2015). Confinement and low adhesion induce fast amoeboid migration of slow mesenchymal cells. *Cell*, 160(4), 659–672.

Lo, C.-M., Wang, H.-B., Dembo, M., & Wang, Y.-l. (2000). Cell movement is guided by the rigidity of the substrate. *Biophysical Journal*, 79(1), 144–152.

Lodish, H., Baltimore, D., Berk, A., Zipursky, S. L., Matsudaira, P., & Darnell, J. (2000). *Molecular Cell Biology*. WH Freeman, New York.

Love, D. R., Hill, D. F., Dickson, G., Spurr, N. K., Byth, B. C., Marsden, R. F., Walsh, F. S., Edwards, Y. H., & Davies, K. E. (1989). An autosomal transcript in skeletal muscle with homology to dystrophin. *Nature*, 339(6219), 55–58.

Lovering, R. M., Michaelson, L., & Ward, C. W. (2009). Malformed *mdx* myofibers have normal cytoskeletal architecture yet altered EC coupling and stress-induced Ca^{2+} signaling. *American Journal of Physiology-Cell Physiology*, 297(3), C571–C580.

Lovering, R. M., Porter, N. C., & Bloch, R. J. (2005). The muscular dystrophies: from genes to therapies. *Physical Therapy*, 85(12), 1372–1388.

Lu, H., Wang, B., Ma, J., Huang, G., & Viswanathan, H. (2003). Measurement of creep compliance of solid polymers by nanoindentation. *Mechanics of Time-Dependent Materials*, 7(3-4), 189–207.

Lu, Z. & Smith, D. (1991). Adenosine 5'-triphosphate increases acetylcholine channel opening frequency in rat skeletal muscle. *The Journal of Physiology*, 436(1), 45–56.

Lüders, J. (2016). *The Microtubule Cytoskeleton: Organisation, Function and Role in Disease*. Springer-Verlag, Wien.

Lunt, S. Y. & Vander Heiden, M. G. (2011). Aerobic glycolysis: meeting the metabolic requirements of cell proliferation. *Annual Review of Cell and Developmental biology*, 27, 441–464.

Luo, Q., Kuang, D., Zhang, B., & Song, G. (2016). Cell stiffness determined by atomic force microscopy and its correlation with cell motility. *Biochimica et Biophysica Acta (BBA)-General Subjects*, 1860(9), 1953–1960.

Luxton, G. G., Gomes, E. R., Folker, E. S., Worman, H., & Gundersen, G. G. (2014). *Nucleus*, 2(3), 173–181.

Ma, X., Jin, M., Cai, Y., Xia, H., Long, K., Liu, J., Yu, Q., & Yuan, J. (2011). Mitochondrial electron transport chain complex III is required for antimycin A to inhibit autophagy. *Chemistry & Biology*, 18(11), 1474–1481.

Ma, X., Kovács, M., Conti, M. A., Wang, A., Zhang, Y., Sellers, J. R., & Adelstein, R. S. (2012). Nonmuscle myosin II exerts tension but does not translocate actin in vertebrate cytokinesis. *Proceedings of the National Academy of Sciences USA*, 109(12), 4509–4514.

Maeda, N. & Senden, T. (2000). Method for the calibration of force microscopy cantilevers via hydrodynamic drag. *Langmuir*, 16(24), 9282–9286.

Maggio, I., Stefanucci, L., Janssen, J. M., Liu, J., Chen, X., Mouly, V., & Gonçalves, M. A. (2016). Selection-free gene repair after adenoviral vector transduction of designer nucleases: rescue of dystrophin synthesis in DMD muscle cell populations. *Nucleic Acids Research*, 44(3), 1449–1470.

Maggio, M., Ceda, G. P., Lauretani, F., Bandinelli, S., Metter, E. J., Guralnik, J. M., Basaria, S., Cattabiani, C., Luci, M., Dall'Aglio, E., Vignali, A., Volpi, R., Valenti, G., & Ferrucci, L. (2011). Gonadal status and physical performance in older men. *The Aging Male*, 14(1), 42–47.

Mah, J. K., Korngut, L., Dykeman, J., Day, L., Pringsheim, T., & Jette, N. (2014). A systematic review and meta-analysis on the epidemiology of Duchenne and Becker muscular dystrophy. *Neuromuscular Disorders*, 24(6), 482–491.

Maheshwari, G., Brown, G., Lauffenburger, D. A., Wells, A., & Griffith, L. G. (2000). Cell adhesion and motility depend on nanoscale RGD clustering. *Journal of Cell Science*, 113(10), 1677–1686.

Malatesta, M., Giagnacovo, M., Cardani, R., Meola, G., & Pellicciari, C. (2013). *Human Myoblasts from Skeletal Muscle Biopsies: In Vitro Culture Preparations for Morphological and Cytochemical Analyses at Light and Electron Microscopy*. Humana Press, Totowa, NJ.

Mallat, S. (1998). *A Wavelet Tour of Signal Processing*. New York, USA: Academic Press.

Mallat, S. & Hwang, W. L. (1992). Singularity detection and processing with wavelets. *IEEE Transactions on Information Theory*, 38(2), 617–643.

Mancini, A., El Bounkari, O., Norrenbrock, A., Scherr, M., Schaefer, D., Eder, M., Banham, A., Pulford, K., Lyne, L., Whetton, A. D., & Tamura, T. (2007). FMIP controls the adipocyte lineage commitment of C2C12 cells by downmodulation of C/EBPalpha. *Oncogene*, 26(7), 1020–1027.

Mandel, L. J. (1986). Energy metabolism of cellular activation, growth, and transformation. *Current Topics in Membranes and Transport*, 27, 261–291.

Mandel, L. J., Bacallao, R., & Zampighi, G. (1993). Uncoupling of the molecular 'fence' and paracellular 'gate' functions in epithelial tight junctions. *Nature*, 361, 552–555.

Mangan, M. E. & Olmsted, J. (1996). A muscle-specific variant of microtubule-associated protein 4 (MAP4) is required in myogenesis. *Development*, 122(3), 771–781.

Manzur, A. Y., Kuntzer, T., Pike, M., & Swan, A. V. (2008). Glucocorticoid corticosteroids for Duchenne muscular dystrophy. *Cochrane Database of Systematic Reviews*, 1(CD003725).

Marko, J. F. & Poirier, M. G. (2003). Micromechanics of chromatin and chromosomes. *Biochemistry and Cell Biology*, 81(3), 209–220.

Martin-Belmonte, F. & Perez-Moreno, M. (2012). Epithelial cell polarity, stem cells and cancer. *Nature Reviews Cancer*, 12(1), 23–38.

Martinello, T., Baldoin, M. C., Morbiato, L., Paganin, M., Tarricone, E., Schiavo, G., Bianchini, E., Sandonà, D., & Betto, R. (2011). Extracellular ATP signaling during differentiation of C2C12 skeletal muscle cells: role in proliferation. *Molecular and Cellular Biochemistry*, 351(1-2), 183–196.

Martinez-Torres, C., Arneodo, A., Streppa, L., Argoul, P., & Argoul, F. (2016). Passive microrheology of soft materials with atomic force microscopy: A wavelet-based spectral analysis. *Applied Physics Letters*, 108(3), 034102.

Martinez-Torres, C., Berguiga, L., Streppa, L., Boyer-Provera, E., Schaeffer, L., Elezgaray, J., Arneodo, A., & Argoul, F. (2014). Diffraction phase microscopy: retrieving phase contours on living cells with a wavelet-based space-scale analysis. *Journal of Biomedical Optics*, 19(3), 036007–036007.

Martinez-Torres, C., Laperrousaz, B., Berguiga, L., Boyer-Provera, E., Elezgaray, J., Nicolini, F. E., Maguer-Satta, V., Arneodo, A., & Argoul, F. (2015). Deciphering the internal complexity of living cells with quantitative phase microscopy: a multiscale approach. *Journal of Biomedical Optics*, 20(9), 096005–096005.

Massiera, G., Van Citters, K. M., Biancaniello, P. L., & Crocker, J. C. (2007). Mechanics of single cells: rheology, time dependence, and fluctuations. *Biophysical Journal*, 93(10), 3703–3713.

Mathur, A., Collinsworth, A., Reichert, W., Kraus, W., & Truskey, G. (2001). Endothelial, cardiac muscle and skeletal muscle exhibit different viscous and elastic properties as determined by atomic force microscopy. *Journal of Biomechanics*, 34(12), 1545–1553.

Mathur, A. B., Truskey, G. A., & Reichert, W. M. (2000). Atomic force and total internal reflection fluorescence microscopy for the study of force transmission in endothelial cells. *Biophysical Journal*, 78(4), 1725–1735.

Mauro, A. (1961). Satellite cell of skeletal muscle fibers. *The Journal of Biophysical and Biochemical Cytology*, 9(2), 493–495.

McClure, M. J., Clark, N. M., Hyzy, S. L., Chalfant, C. E., Olivares-Navarrete, R., Boyan, B. D., & Schwartz, Z. (2016). Role of integrin $\alpha 7\beta 1$ signaling in myoblast differentiation on aligned polydioxanone scaffolds. *Acta Biomaterialia*, 39, 44–54.

McDonald, C. M. (2012). Clinical approach to the diagnostic evaluation of hereditary and acquired neuromuscular diseases. *Physical Medicine and Rehabilitation Clinics of North America*, 23(3), 495–563.

McDonald, D. G., Kinali, M., Gallagher, A. C., Mercuri, E., Muntoni, F., Roper, H., Jardine, P., Jones, D. H., & Pike, M. (2002). Fracture prevalence in Duchenne muscular dystrophy. *Developmental Medicine & Child Neurology*, 44(10), 695–698.

McGann, C. J., Odelberg, S. J., & Keating, M. T. (2001). Mammalian myotube dedifferentiation induced by newt regeneration extract. *Proceedings of the National Academy of Sciences USA*, 98(24), 13699–13704.

McGeachie, J. K. & Grounds, M. D. (1987). Initiation and duration of muscle precursor replication after mild and severe injury to skeletal muscle of mice. *Cell and Tissue Research*, 248(1), 125–130.

McNeil, P. L. & Steinhardt, R. A. (2003). Plasma membrane disruption: repair, prevention, adaptation. *Annual Review of Cell and Developmental Biology*, 19(1), 697–731.

Meiselman, H. J., Evans, E. A., & Hochmuth, R. M. (1978). Membrane mechanical properties of ATP-depleted human erythrocytes. *Blood*, 52(3), 499–504.

Melki, R., Fievez, S., & Carlier, M.-F. (1996). Continuous monitoring of Pi release following nucleotide hydrolysis in actin or tubulin assembly using 2-amino-6-mercapto-7-methylpurine ribonucleoside and purine-nucleoside phosphorylase as an enzyme-linked assay. *Biochemistry*, 35(37), 12038–12045.

Menasché, P., Hagège, A. A., Scorsin, M., Pouzet, B., Desnos, M., Duboc, D., Schwartz, K., Vilquin, J.-T., & Marolleau, J.-P. (2001). Myoblast transplantation for heart failure. *The Lancet*, 357(9252), 279–280.

Menasché, P., Hagege, A. A., Vilquin, J.-T., Desnos, M., Abergel, E., Pouzet, B., Bel, A., Sarateanu, S., Scorsin, M., Schwartz, K., Bruneval, P., Benbunan, M., Marolleau, J.-P., & Duboc, D. (2003). Autologous skeletal myoblast transplantation for severe postinfarction left ventricular dysfunction. *Journal of the American College of Cardiology*, 41(7), 1078–1083.

Mendell, J. R., Campbell, K., Rodino-Klapac, L., Sahenk, Z., Shilling, C., Lewis, S., Bowles, D., Gray, S., Li, C., Galloway, G., Malik, V., Coley, B., Clark, K. R., Li, J., Xiao, X., Samulski, J., McPhee, S. W., Samulski, R. J., & Walker, C. M. (2010). Dystrophin immunity in Duchenne's muscular dystrophy. *New England Journal of Medicine*, 363(15), 1429–1437.

Mendell, J. R., Rodino-Klapac, L. R., Sahenk, Z., Roush, K., Bird, L., Lowes, L. P., Alfano, L., Gomez, A. M., Lewis, S., Kota, J., Malik, V., Shontz, K., Walker, C. M., Flanigan, K. M., Corridore, M., Kean, J. R., Allen, H. D., Shilling, C., Melia, K. R., Sazani, P., Saoud, J. B., & Kaye, E. M. (2013). Eteplirsen for the treatment of Duchenne muscular dystrophy. *Annals of Neurology*, 74(5), 637–647.

Mendez-Mendez, J., Alonso-Rasgado, M., Faria, E. C., Flores-Johnson, E., & Snook, R. (2014). Numerical study of the hydrodynamic drag force in atomic force microscopy measurements undertaken in fluids. *Micron*, 66, 37–46.

Mermelstein, C. S., Andrade, L. R., Portilho, D. M., & Costa, M. L. (2006). Desmin filaments are stably associated with the outer nuclear surface in chick myoblasts. *Cell and Tissue Research*, 323(2), 351–357.

Meyer, Y. (1992). *Wavelets and Applications*. Berlin, DE: Springer-Verlag.

Meyers, M. A., Chen, P.-Y., Lin, A. Y.-M., & Seki, Y. (2008). Biological materials: structure and mechanical properties. *Progress in Materials Science*, 53(1), 1–206.

Mian, I., Pierre-Louis, W. S., Dole, N., Gilberti, R. M., Dodge-Kafka, K., & Tirnauer, J. S. (2012). LKB1 destabilizes microtubules in myoblasts and contributes to myoblast differentiation. *PloS One*, 7(2), e31583.

Mihai, C., Bao, S., Lai, J.-P., Ghadiali, S. N., & Knoell, D. L. (2012). PTEN inhibition improves wound healing in lung epithelia through changes in cellular mechanics that enhance migration. *American Journal of Physiology-Lung Cellular and Molecular Physiology*, 302(3), L287–L299.

Miller, R., Sharma, K. R., Pavlath, G., Gussoni, E., Mynhier, M., Yu, P., Lanctot, A., Greco, C., Steinman, L., & Blau, H. (1997). Myoblast implantation in Duchenne muscular dystrophy: the San Francisco study. *Muscle & Nerve*, 20(4), 469–478.

Millon-Frémillon, A., Bouvard, D., Grichine, A., Manet-Dupé, S., Block, M. R., & Albiges-Rizo, C. (2008). Cell adaptive response to extracellular matrix density is controlled by ICAP-1-dependent β_1-integrin affinity. *The Journal of Cell Biology*, 180(2), 427–441.

Mitchison, T. & Kirschner, M. (1984). Dynamic instability of microtubule growth. *Nature*, 312(5991), 237–242.

Mizuno, D., Tardin, C., Schmidt, C. F., & MacKintosh, F. C. (2007). Nonequilibrium mechanics of active cytoskeletal networks. *Science*, 315(5810), 370–373.

Mizuno, Y., Suzuki, M., Nakagawa, H., Ninagawa, N., & Torihashi, S. (2009). Switching of actin isoforms in skeletal muscle differentiation using mouse ES cells. *Histochemistry and Cell Biology*, 132(6), 669–672.

Modulevsky, D. J., Tremblay, D., Gullekson, C., Bukoresthliev, N. V., & Pelling, A. E. (2012). The physical interaction of myoblasts with the microenvironment during remodeling of the cytoarchitecture. *PloS One*, 7(9), e45329.

Moeendarbary, E. & Harris, A. R. (2014). Cell mechanics: principles, practices, and prospects. *Wiley Interdisciplinary Reviews: Systems Biology and Medicine*, 6(5), 371–388.

Moens, P., Baatsen, P., & Maréchal, G. (1993). Increased susceptibility of EDL muscles from *mdx* mice to damage induced by contractions with stretch. *Journal of Muscle Research & Cell Motility*, 14(4), 446–451.

Mohun, T. (1992). Muscle differentiation. *Current Opinion in Cell Biology*, 4(6), 923–928.

Molitoris, B. A., Geerdes, A., & McIntosh, J. (1991). Dissociation and redistribution of Na^+, K^+-ATPase from its surface membrane actin cytoskeletal complex during cellular ATP depletion. *Journal of Clinical Investigation*, 88(2), 462.

Monaco, A. P., Bertelson, C. J., Liechti-Gallati, S., Moser, H., & Kunkel, L. M. (1988). An explanation for the phenotypic differences between patients bearing partial deletions of the DMD locus. *Genomics*, 2(1), 90–95.

Monani, U. R. (2005). Spinal muscular atrophy: a deficiency in a ubiquitous protein; a motor neuron-specific disease. *Neuron*, 48(6), 885–895.

Moore, S. W., Roca-Cusachs, P., & Sheetz, M. P. (2010). Stretchy proteins on stretchy substrates: the important elements of integrin-mediated rigidity sensing. *Developmental Cell*, 19(2), 194–206.

Morel, V., Lepicard, S., Rey, A. N., Parmentier, M.-L., & Schaeffer, L. (2014). Drosophila Nesprin-1 controls glutamate receptor density at neuromuscular junctions. *Cellular and Molecular Life Sciences*, 71(17), 3363–3379.

Morgan, D. & Allen, D. (1999). Early events in stretch-induced muscle damage. *Journal of Applied Physiology*, 87(6), 2007–2015.

Moss, F. & Leblond, C. (1970). Nature of dividing nuclei in skeletal muscle of growing rats. *The Journal of Cell Biology*, 44(2), 459–461.

Mullis, K., Faloona, F., Scharf, S., Saiki, R., Horn, G., & Erlich, H. (1986). Specific enzymatic amplification of DNA in vitro: the polymerase chain reaction. In *Cold Spring Harbor Symposia on Quantitative Biology*, volume 51 (pp. 263–273). New York, NY: Cold Spring Harbor Laboratory Press.

Mulvaney, D., Marple, D., & Merkel, R. (1988). Proliferation of skeletal muscle satellite cells after castration and administration of testosterone propionate. *Experimental Biology and Medicine*, 188(1), 40–45.

Muntoni, F., Torelli, S., & Ferlini, A. (2003). Dystrophin and mutations: one gene, several proteins, multiple phenotypes. *The Lancet Neurology*, 2(12), 731–740.

Murphy, M. M., Lawson, J. A., Mathew, S. J., Hutcheson, D. A., & Kardon, G. (2011). Satellite cells, connective tissue fibroblasts and their interactions are crucial for muscle regeneration. *Development*, 138(17), 3625–3637.

Musa, H., Orton, C., Morrison, E., & Peckham, M. (2003). Microtubule assembly in cultured myoblasts and myotubes following nocodazole induced microtubule depolymerisation. *Journal of Muscle Research & Cell Motility*, 24(4-6), 303–310.

Muzy, J.-F., Bacry, E., & Arneodo, A. (1994). The multifractal formalism revisited with wavelets. *International Journal of Bifurcation and Chaos*, 4(02), 245–302.

Nagayama, K., Nagano, Y., Sato, M., & Matsumoto, T. (2006). Effect of actin filament distribution on tensile properties of smooth muscle cells obtained from rat thoracic aortas. *Journal of Biomechanics*, 39(2), 293–301.

Nakagaki, W. R. & Camilli, J. A. (2012). Bone tissue and muscle dystrophin deficiency in *mdx* mice. *Joint Bone Spine*, 79(2), 129–133.

Nakayama, K., Okamoto, F., & Harada, Y. (1956). Antimycin A: isolation from a new Streptomyces and activity against rice plant blast fungi. *The Journal of Antibiotics*, 9(2), 63–66.

Nawaz, S., Sánchez, P., Bodensiek, K., Li, S., Simons, M., & Schaap, I. (2012). Cell visco-elasticity measured with AFM and optical trapping at sub-micrometer deformations. *PLoS One*, 7(9), e45297.

Nelson, D. L., Cox, M. M., & Lehninger, A. L. (2013). *Lehninger Principles of Biochemistry*. New York: W.H. Freeman.

Nelson, D. L., Lehninger, A. L., & Cox, M. M. (2008). *Lehninger Principles of Biochemistry*. Macmillan, New York.

Nemir, S. & West, J. (2010). Synthetic materials in the study of cell response to substrate rigidity. *Annals of Biomedical Engineering*, 38(1), 2–20.

Nesmith, A. P., Wagner, M. A., Pasqualini, F. S., O'Connor, B. B., Pincus, M. J., August, P. R., & Parker, K. K. (2016). A human in vitro model of duchenne muscular dystrophy muscle formation and contractility. 215(1), 47–56.

Newton, I., Bernoulli, D., MacLaurin, C., & Euler, L. (1833). *Philosophiae Naturalis Principia Mathematica*, volume 1. excudit G. Brookman; impensis TT et J. Tegg, Londini.

Nguyen, T., Ellis, J., Love, D., Davies, K., Gatter, K., Dickson, G., & Morris, G. (1991). Localization of the DMDL gene-encoded dystrophin-related protein using a panel of nineteen monoclonal antibodies: presence at neuromuscular junctions, in the sarcolemma of dystrophic skeletal muscle, in vascular and other smooth muscles, and in proliferating brain cell lines. *The Journal of Cell Biology*, 115(6), 1695–1700.

Nigg, E. A. (2001). Mitotic kinases as regulators of cell division and its checkpoints. *Nature Reviews Molecular Cell Biology*, 2(1), 21–32.

Nogales, E. & Wang, H.-W. (2006). Structural intermediates in microtubule assembly and disassembly: how and why? *Current Opinion in Cell Biology*, 18(2), 179–184.

Nowak, S. J., Nahirney, P. C., Hadjantonakis, A.-K., & Baylies, M. K. (2009). Nap1-mediated actin remodeling is essential for mammalian myoblast fusion. *Journal of Cell Science*, 122(18), 3282–3293.

Nyland, L. R. & Maughan, D. W. (2000). Morphology and transverse stiffness of Drosophila myofibrils measured by atomic force microscopy. *Biophysical Journal*, 78(3), 1490–1497.

O'Connor, C. (2008a). Cell division: Stages of mitosis. *Nature Education*, 1(1), 188.

O'Connor, R. S., Steeds, C. M., Wiseman, R. W., & Pavlath, G. K. (2008b). Phosphocreatine as an energy source for actin cytoskeletal rearrangements during myoblast fusion. *The Journal of Physiology*, 586(12), 2841–2853.

Ogneva, I. V., Lebedev, D. V., & Shenkman, B. S. (2010). Transversal stiffness and Young's modulus of single fibers from rat soleus muscle probed by atomic force microscopy. *Biophysical Journal*, 98(3), 418–424.

Okano, T., Satoh, S., Oka, T., & Matsuda, T. (1997). Tissue engineering of skeletal muscle highly dense, highly oriented hybrid muscular tissues biomimicking native tissues. *Asaio Journal*, 43(5), M753.

Olson, M. O., Dundr, M., & Szebeni, A. (2000). The nucleolus: an old factory with unexpected capabilities. *Trends in Cell Biology*, 10(5), 189–196.

Ono, Y., Urata, Y., Goto, S., Nakagawa, S., Humbert, P. O., Li, T.-S., & Zammit, P. S. (2015). Muscle stem cell fate is controlled by the cell-polarity protein Scrib. *Cell Reports*, 10(7), 1135–1148.

Oster, G. & Wang, H. (2003). Rotary protein motors. *Trends in Cell Biology*, 13(3), 114–121.

Ostrovidov, S., Shi, X., Zhang, L., Liang, X., Kim, S. B., Fujie, T., Ramalingam, M., Chen, M., Nakajima, K., Al-Hazmi, F., Bae, H., Memic, A., & Khademhosseini, A. (2014). Myotube formation on gelatin nanofibers–multi-walled carbon nanotubes hybrid scaffolds. *Biomaterials*, 35(24), 6268–6277.

Otto, A. (1968). Excitation of nonradiative surface plasma waves in silver by the method of frustrated total reflection. *Zeitschrift für Physik*, 216(4), 398–410.

Pääsuke, R., Eimre, M., Piirsoo, A., Peet, N., Laada, L., Kadaja, L., Roosimaa, M., Pääsuke, M., Märtson, A., Seppet, E., & Paju, K. (2016). Proliferation of human primary myoblasts is associated with altered energy metabolism in dependence on ageing *in vivo* and *in vitro*. *Oxidative Medicine and Cellular Longevity*, 2016, ID 8296150.

Pajerowski, J. D., Dahl, K. N., Zhong, F. L., Sammak, P. J., & Discher, D. E. (2007). Physical plasticity of the nucleus in stem cell differentiation. *Proceedings of the National Academy of Sciences USA*, 104(40), 15619–15624.

Pal, S. (2014). *Design of Artificial Human Joints & Organs*. New York: Springer Science+Business Media.

Palchesko, R. N., Zhang, L., Sun, Y., & Feinberg, A. W. (2012). Development of polydimethylsiloxane substrates with tunable elastic modulus to study cell mechanobiology in muscle and nerve. *PloS One*, 7(12), e51499.

Pan, C., Kumar, C., Bohl, S., Klingmueller, U., & Mann, M. (2009). Comparative proteomic phenotyping of cell lines and primary cells to assess preservation of cell type-specific functions. *Molecular & Cellular Proteomics*, 8(3), 443–450.

Pantic, B., Borgia, D., Giunco, S., Malena, A., Kiyono, T., Salvatori, S., De Rossi, A., Giardina, E., Sangiuolo, F., Pegoraro, E., Vergani, L., & Botta, A. (2016). Reliable and versatile immortal muscle cell models from healthy and myotonic dystrophy type 1 primary human myoblasts. *Experimental Cell Research*, 342(1), 39–51.

Parise, G., McKinnell, I. W., & Rudnicki, M. A. (2008). Muscle satellite cell and atypical myogenic progenitor response following exercise. *Muscle & Nerve*, 37(5), 611–619.

Parre, E. & Geitmann, A. (2005a). More than a leak sealant. the mechanical properties of callose in pollen tubes. *Plant Physiology*, 137(1), 274–286.

Parre, E. & Geitmann, A. (2005b). Pectin and the role of the physical properties of the cell wall in pollen tube growth of solanum chacoense. *Planta*, 220(4), 582–592.

Partridge, T. A. (2011). Impending therapies for Duchenne muscular dystrophy. *Current Opinion in Neurology*, 24(5), 415–422.

Pasapera, A. M., Schneider, I. C., Rericha, E., Schlaepfer, D. D., & Waterman, C. M. (2010). Myosin II activity regulates vinculin recruitment to focal adhesions through FAK-mediated paxillin phosphorylation. *The Journal of Cell Biology*, 188(6), 877–890.

Pasternak, C., Wong, S., & Elson, E. L. (1995). Mechanical function of dystrophin in muscle cells. *The Journal of Cell Biology*, 128(3), 355–361.

Peckham, M. (2008). Engineering a multi-nucleated myotube, the role of the actin cytoskeleton. *Journal of Microscopy*, 231(3), 486–493.

Peeters, E. A., Oomens, C. W., Bouten, C. V., Bader, D. L., & Baaijens, F. P. (2005). Viscoelastic properties of single attached cells under compression. *Journal of Biomechanical Engineering*, 127(2), 237–243.

Pelham, R. J. & Wang, Y.-l. (1997). Cell locomotion and focal adhesions are regulated by substrate flexibility. *Proceedings of the National Academy of Sciences USA*, 94(25), 13661–13665.

Pelicano, H., Martin, D., Xu, R., & Huang, P. (2006). Glycolysis inhibition for anticancer treatment. *Oncogene*, 25(34), 4633–4646.

Pellegrin, S. & Mellor, H. (2007). Actin stress fibres. *Journal of Cell Science*, 120, 3491–3499.

Pelling, A. E. & Horton, M. A. (2008). An historical perspective on cell mechanics. *Pflügers Archiv-European Journal of Physiology*, 456(1), 3–12.

Pestronk, A., Parhad, I. M., Drachman, D. B., & Price, D. L. (1982). Membrane myopathy: morphological similarities to Duchenne muscular dystrophy. *Muscle & Nerve*, 5(3), 209–214.

Petrof, B. J., Shrager, J. B., Stedman, H. H., Kelly, A. M., & Sweeney, H. L. (1993). Dystrophin protects the sarcolemma from stresses developed during muscle contraction. *Proceedings of the National Academy of Sciences USA*, 90(8), 3710–3714.

Peyton, S. R. & Putnam, A. J. (2005). Extracellular matrix rigidity governs smooth muscle cell motility in a biphasic fashion. *Journal of Cellular Physiology*, 204(1), 198–209.

Pfeifer, M., Begerow, B., & Minne, H. (2002). Vitamin D and muscle function. *Osteoporosis International*, 13(3), 187–194.

Pham, N.-A., Robinson, B. H., & Hedley, D. W. (2000). Simultaneous detection of mitochondrial respiratory chain activity and reactive oxygen in digitonin-permeabilized cells using flow cytometry. *Cytometry*, 41(4), 245–251.

Pharr, G., Oliver, W., & Brotzen, F. (1992). On the generality of the relationship among contact stiffness, contact area, and elastic modulus during indentation. *Journal of Materials Research*, 7(03), 613–617.

Phillip, J. M., Aifuwa, I., Walston, J., & Wirtz, D. (2015). The mechanobiology of aging. *Annual Review of Biomedical Engineering*, 17, 113.

Phillips, W. D. & Bennett, M. R. (1987). Elimination of distributed synaptic acetylcholine receptor clusters on developing avian fast-twitch muscle fibres accompanies loss of polyneuronal innervation. *Journal of Neurocytology*, 16(6), 785–797.

Phillipson, M. & Kubes, P. (2011). The neutrophil in vascular inflammation. *Nature Medicine*, 17(11), 1381–1390.

Pinto, R. D. S. M., Ferretti, R., Moraes, L. H. R., Santo Neto, H., Marques, M. J., & Minatel, E. (2013). N-Acetylcysteine treatment reduces TNF-α levels and myonecrosis in diaphragm muscle of *mdx* mice. *Clinical Nutrition*, 32(3), 472–475.

Pinyol, R., Haeckel, A., Ritter, A., Qualmann, B., & Kessels, M. (2007). Regulation of N-WASP and the Arp2/3 complex by Abp1 controls neuronal morphology. *PloS One*, 2(5), e400.

Pizon, V., Gerbal, F., Diaz, C. C., & Karsenti, E. (2005). Microtubule-dependent transport and organization of sarcomeric myosin during skeletal muscle differentiation. *The EMBO Journal*, 24(21), 3781–3792.

Pollard, T. & Borisy, G. (2003). Cellular motility driven by assembly and disassembly of actin filaments. *Cell*, 112(4), 453–465.

Pollard, T. D. (1986). Rate constants for the reactions of ATP-and ADP-actin with the ends of actin filaments. *The Journal of Cell Biology*, 103(6), 2747–2754.

Pollard, T. D., Blanchoin, L., & Mullins, R. D. (2000). Molecular mechanisms controlling actin filament dynamics in nonmuscle cells. *Annual Review of Biophysics and Biomolecular Structure*, 29(1), 545–576.

Porter, J. (1976). Antony van Leeuwenhoek: tercentenary of his discovery of bacteria. *Bacteriological Reviews*, 40(2), 260.

Praetorius, H. A. & Leipziger, J. (2009). ATP release from non-excitable cells. *Purinergic Signalling*, 5(4), 433–446.

Pratt, S. J., Shah, S. B., Ward, C. W., Inacio, M. P., Stains, J. P., & Lovering, R. M. (2013). Effects of *in vivo* injury on the neuromuscular junction in healthy and dystrophic muscles. *The Journal of Physiology*, 591(2), 559–570.

Pratt, S. J., Shah, S. B., Ward, C. W., Kerr, J. P., Stains, J. P., & Lovering, R. M. (2015). Recovery of altered neuromuscular junction morphology and muscle function in *mdx* mice after injury. *Cellular and Molecular Life Sciences*, 72(1), 153–164.

Prins, K. W., Humston, J. L., Mehta, A., Tate, V., Ralston, E., & Ervasti, J. M. (2009). Dystrophin is a microtubule-associated protein. *The Journal of Cell Biology*, 186(3), 363–369.

Puttini, S., Lekka, M., Dorchies, O. M., Saugy, D., Incitti, T., Ruegg, U. T., Bozzoni, I., Kulik, A. J., & Mermod, N. (2009). Gene-mediated restoration of normal myofiber elasticity in dystrophic muscles. *Molecular Therapy*, 17(1), 19–25.

Qing, L., Dongdong, K., Bingyu, Z., & Guanbin, S. (2016). Cell stiffness determined by atomic force microscopy and its correlation with cell motility. *Biochimica et Biophysica Acta (BBA) - General Subjects*, 1860(9), 1953–1960.

Querfurth, H. W., Suhara, T., Rosen, K. M., McPhie, D. L., Fujio, Y., Tejada, G., Neve, R. L., Adelman, L. S., & Walsh, K. (2001). β-Amyloid peptide expression is sufficient for myotube death: implications for human inclusion body myopathy. *Molecular and Cellular Neuroscience*, 17(5), 793–810.

Radmacher, M., Fritz, M., Kacher, C., Cleveland, J., & Hansma, P. (1996). Measuring the viscoelastic properties of human platelets with the atomic force microscope. *Biophysical Journal*, 70(1), 556–567.

Raether, H. (1988). *Surface Plasmons on Smooth Surfaces*. Berlin, DE: Springer.

Rajagopalan, P., Marganski, W. A., Brown, X. Q., & Wong, J. Y. (2004). Direct comparison of the spread area, contractility, and migration of balb/c 3T3 fibroblasts adhered to fibronectin-and RGD-modified substrata. *Biophysical Journal*, 87(4), 2818–2827.

Rakhmatullina, D., Ponomareva, A., Gazizova, N., & Minibayeva, F. (2015). Mitochondrial morphology and dynamics in Triticum aestivum roots in response to rotenone and antimycin A. *Protoplasma*, (pp. 1–10).

Ralston, H., Inman, V., Strait, L., & Shaffrath, M. (1947). Mechanics of human isolated voluntary muscle. *American Journal of Physiology–Legacy Content*, 151(2), 612–620.

Ramón-Azcón, J., Ahadian, S., Estili, M., Liang, X., Ostrovidov, S., Kaji, H., Shiku, H., Ramalingam, M., Nakajima, K., & Sakka, Y. (2013). Dielectrophoretically aligned carbon nanotubes to control electrical and mechanical properties of hydrogels to fabricate contractile muscle myofibers. *Advanced Materials*, 25(29), 4028–4034.

Rassier, D. (2010). *Muscle Biophysics: From Molecules to Cells*, volume 682. Springer Science & Business Media,New York, NY.

Reiner, M. (1960). *Deformation, Strain and Flow: An Elementary Introduction to Rheology*. New York, London: Interscience.

Reinsch, S. & Gonczy, P. (1998). Mechanisms of nuclear positioning. *Journal of Cell Science*, 111, 2283–2295.

Reznik, M. (1969). Thymidine-3H uptake by satellite cells of regenerating skeletal muscle. *The Journal of Cell Biology*, 40(2), 568.

Rho, J., Ashman, R., & Turner, C. (1993). Young's modulus of trabecular and cortical bone material: ultrasonic and microtensile measurements. *Journal of Biomechanics*, 26(2), 111–119.

Richardson, B. E., Beckett, K., Nowak, S. J., & Baylies, M. K. (2007). SCAR/WAVE and Arp2/3 are crucial for cytoskeletal remodeling at the site of myoblast fusion. *Development*, 134(24), 4357–4367.

Rico, F., Roca-Cusachs, P., Gavara, N., Farré, R., Rotger, M., & Navajas, D. (2005). Probing mechanical properties of living cells by atomic force microscopy with blunted pyramidal cantilever tips. *Physical Review E*, 72(2), 021914.

Ridley, A. J. (2011). Life at the leading edge. *Cell*, 145(7), 1012–1022.

Ridley, A. J., Schwartz, M. A., Burridge, K., Firtel, R. A., Ginsberg, M. H., Borisy, G., Parsons, J. T., & Horwitz, A. R. (2003). Cell migration: integrating signals from front to back. *Science*, 302(5651), 1704–1709.

Riedemann, N. C. & Ward, P. A. (2003). Complement in ischemia reperfusion injury. *The American Journal of Pathology*, 162(2), 363–367.

Riis, A. L. D., Jørgensen, J. O. L., Gjedde, S., Nørrelund, H., Jurik, A. G., Nair, K. S., Ivarsen, P., Weeke, J., & Møller, N. (2005). Whole body and forearm substrate metabolism in hyperthyroidism: evidence of increased basal muscle protein breakdown. *American Journal of Physiology-Endocrinology and Metabolism*, 288(6), E1067–E1073.

Risson, V., Mazelin, L., Roceri, M., Sanchez, H., Moncollin, V., Corneloup, C., Richard-Bulteau, H., Vignaud, A., Baas, D., Defour, A., Freyssenet, D., Tanti, J.-F., Le-Marchand-Brustel, Y., Ferrier, B., Conjard-Duplany, A., Romanino, K., Bauché, S., Hantai, D., Mueller, M., Kozma, S. C., Thomas, G., Ruegg, M. A., Ferry, A., Pende, M., Bigard, X., Koulmann, N., Schaeffer, L., & Gangloff, Y.-G. (2009). Muscle inactivation of mTOR causes metabolic and dystrophin defects leading to severe myopathy. *The Journal of Cell Biology*, 187(6), 859–874.

Roberts, R. G., Coffey, A. J., Bobrow, M., & Bentley, D. R. (1993). Exon structure of the human dystrophin gene. *Genomics*, 16(2), 536–538.

Robriquet, F., Babarit, C., Larcher, T., Dubreil, L., Ledevin, M., Goubin, H., Rouger, K., & Guével, L. (2016). Identification in GRMD dog muscle of critical miRNAs involved in pathophysiology and effects associated with MuStem cell transplantation. *BMC Musculoskeletal Disorders*, 17, 209.

Robriquet, F., Lardenois, A., Babarit, C., Larcher, T., Dubreil, L., Leroux, I., Zuber, C., Ledevin, M., Deschamps, J.-Y., Fromes, Y., Yan, C., Laetitia, G., & Karl, R. (2015). Differential gene expression profiling of dystrophic dog muscle after MuStem cell transplantation. *PloS One*, 10(5), e0123336.

Rodino-Klapac, L. R., Mendell, J. R., & Sahenk, Z. (2013). Update on the treatment of Duchenne muscular dystrophy. *Current Neurology and Neuroscience Reports*, 13(3), 1–7.

Rodriguez, M. L., McGarry, P. J., & Sniadecki, N. J. (2013). Review on cell mechanics: experimental and modeling approaches. *Applied Mechanics Reviews*, 65(6), 060801.

Roland, T., Berguiga, L., Elezgaray, J., & Argoul, F. (2010). Scanning surface plasmon imaging of nanoparticles. *Physical Review B*, 81(23), 235419.

Roland, T., Khalil, A., Tanenbaum, A., Berguiga, L., Delichère, P., Bonneviot, L., Elezgaray, J., Arneodo, A., & Argoul, F. (2009). Revisiting the physical processes of vapodeposited thin gold films on chemically modified glass by atomic force and surface plasmon microscopies. *Surface Science*, 603(22), 3307–3320.

Romanazzo, S., Forte, G., Ebara, M., Uto, K., Pagliari, S., Aoyagi, T., Traversa, E., & Taniguchi, A. (2012). Substrate stiffness affects skeletal myoblast differentiation in vitro. *Science and Technology of Advanced Materials*, 13(6), 064211.

Romanick, M., Thompson, L. V., & Brown-Borg, H. M. (2013). Murine models of atrophy, cachexia, and sarcopenia in skeletal muscle. *Biochimica et Biophysica Acta (BBA)-Molecular Basis of Disease*, 1832(9), 1410–1420.

Rooney, J. E., Gurpur, P. B., & Burkin, D. J. (2009). Laminin-111 protein therapy prevents muscle disease in the *mdx* mouse model for Duchenne muscular dystrophy. *Proceedings of the National Academy of Sciences USA*, 106(19), 7991–7996.

Rosenberg, I. H. (1997). Sarcopenia: origins and clinical relevance. *The Journal of Nutrition*, 127(5), 990S–991S.

Rosenblatt, J., Peluso, P., & Mitchison, T. (1995). The bulk of unpolymerized actin in Xenopus egg extracts is ATP-bound. *Molecular Biology of the Cell*, 6(2), 227–236.

Rosenbluth, M. J., Lam, W. A., & Fletcher, D. A. (2006). Force microscopy of nonadherent cells: a comparison of leukemia cell deformability. *Biophysical Journal*, 90(8), 2994–3003.

Roters, A. & Johannsmann, D. (1996). Distance-dependent noise measurements in scanning force microscopy. *Journal of Physics: Condensed Matter*, 8(41), 7561–7577.

Rotsch, C., Jacobson, K., & Radmacher, M. (1999). Dimensional and mechanical dynamics of active and stable edges in motile fibroblasts investigated by using atomic force microscopy. *Proceedings of the National Academy of Sciences USA*, 96(3), 921–926.

Rozhok, S., Sun, P., Piner, R., Lieberman, M., & Mirkin, C. (2004). AFM study of water meniscus formation between an AFM tip and NaCl substrate. *The Journal of Physical Chemistry B*, 108(23), 7814–7819.

Rudnicki, M., Le Grand, F., McKinnell, I., & Kuang, S. (2008). The molecular regulation of muscle stem cell function. In *Cold Spring Harbor Symposia on Quantitative Biology*, volume 73 (pp. 323–331).

Rudolf, R., Deschenes, M. R., & Sandri, M. (2016). Neuromuscular junction degeneration in muscle wasting. *Current Opinion in Clinical Nutrition & Metabolic Care*, 19(3), 177–181.

Sacco, A., Mourkioti, F., Tran, R., Choi, J., Llewellyn, M., Kraft, P., Shkreli, M., Delp, S., Pomerantz, J. H., Artandi, S. E., & Blau, H. M. (2010). Short telomeres and stem cell exhaustion model Duchenne muscular dystrophy in *mdx*/mTR mice. *Cell*, 143(7), 1059–1071.

Sader, J. (1998). Frequency response of cantilever beams immersed in viscous fluids with applications to the atomic force microscope. *Journal of Applied Physics*, 84(1), 64–76.

Sader, J., Chon, J., & Mulvaney, P. (1999). Calibration of rectangular atomic force microscope cantilevers. *Review of Scientific Instruments*, 70(10), 3967–3969.

Sader, J. E., Hughes, B. D., Sanelli, J. A., & Bieske, E. J. (2012). Effect of multiplicative noise on least-squares parameter estimation with applications to the atomic force microscope. *Review of Scientific Instruments*, 83(5), 055106.

Sader, J. E., Larson, I., Mulvaney, P., & White, L. R. (1995). Method for the calibration of atomic force microscope cantilevers. *Review of Scientific Instruments*, 66(7), 3789–3798.

Safi, A., Vandromme, M., Caussanel, S., Valdacci, L., Baas, D., Vidal, M., Brun, G., Schaeffer, L., & Goillot, E. (2004). Role for the pleckstrin homology domain-containing protein CKIP-1 in phosphatidylinositol 3-kinase-regulated muscle differentiation. *Molecular and Cellular Biology*, 24(3), 1245–1255.

Sako, A., Memeledje, A., & Assamoi, P. (2010). Measurement of the viscosity of mousse myoblasts modified with the aß cristalline through the technique of micromanipulation by the means of micropipette. *Asian J. Applied Sciences*, 3, 250–261.

Sambasivan, R., Yao, R., Kissenpfennig, A., Van Wittenberghe, L., Paldi, A., Gayraud-Morel, B., Guenou, H., Malissen, B., Tajbakhsh, S., & Galy, A. (2011). Pax7-expressing satellite cells are indispensable for adult skeletal muscle regeneration. *Development*, 138(17), 3647–3656.

Sandri, M., Lin, J., Handschin, C., Yang, W., Arany, Z. P., Lecker, S. H., Goldberg, A. L., & Spiegelman, B. M. (2006). PGC-1alpha protects skeletal muscle from atrophy by suppressing FoxO3 action and atrophy-specific gene transcription. *Proceedings of the National Academy of Sciences USA*, 103(44), 16260–16265.

Sanes, J. R. & Lichtman, J. W. (1999). Development of the vertebrate neuromuscular junction. *Annual Review of Neuroscience*, 22(1), 389–442.

Sanger, J. W., Chowrashi, P., Shaner, N. C., Spalthoff, S., Wang, J., Freeman, N. L., & Sanger, J. M. (2002). Myofibrillogenesis in skeletal muscle cells. *Clinical Orthopaedics and Related Research*, 403, S153–S162.

Sanjeevi, R., Somanathan, N., & Ramaswamy, D. (1982). A viscoelastic model for collagen fibres. *Journal of Biomechanics*, 15(3), 181–183.

Santos, N. & Castanho, M. A. (2004). An overview of the biophysical applications of atomic force microscopy. *Biophysical Chemistry*, 107(2), 133–149.

Sanz-Moreno, V. & Marshall, C. J. (2010). The plasticity of cytoskeletal dynamics underlying neoplastic cell migration. *Current Opinion in Cell Biology*, 22(5), 690–696.

Sarangapani, K., Torun, H., Finkler, O., Zhu, C., & Degertekin, L. (2010). Membrane-based actuation for high-speed single molecule force spectroscopy studies using AFM. *European Biophysics Journal*, 39(8), 1219–1227.

Sasaki, N. (2012). *Viscoelastic Properties of Biological Materials from Viscoelasticity - From Theory to Biological Applications*. InTech, DOI: 10.5772/49979.

Sauer, F. C. (1935). Mitosis in the neural tube. *Journal of Comparative Neurology*, 62(2), 377–405.

Sbrana, F., Sassoli, C., Meacci, E., Nosi, D., Squecco, R., Paternostro, F., Tiribilli, B., Zecchi-Orlandini, S., Francini, F., & Formigli, L. (2008). Role for stress fiber contraction in surface tension development and stretch-activated channel regulation in C2C12 myoblasts. *American Journal of Physiology-Cell Physiology*, 295(1), C160–C172.

Schaefer, A., te Riet, J., Ritz, K., Hoogenboezem, M., Anthony, E. C., Mul, F. P., de Vries, C. J., Daemen, M. J., Figdor, C. G., van Buul, J. D., & Hordijk, P. (2014). Actin-binding proteins differentially regulate endothelial cell stiffness, ICAM-1 function and neutrophil transmigration. *Journal of Cell Science*, 127(20), 4470–4482.

Schäfer, G., Weber, S., Holz, A., Bogdan, S., Schumacher, S., Müller, A., Renkawitz-Pohl, R., & Önel, S.-F. (2007). The Wiskott–Aldrich syndrome protein (WASP) is essential for myoblast fusion in Drosophila. *Developmental Biology*, 304(2), 664–674.

Schakman, O., Gilson, H., & Thissen, J.-P. (2008). Mechanisms of glucocorticoid-induced myopathy. *Journal of Endocrinology*, 197(1), 1–10.

Schapery, R. (1984). Correspondence principles and a generalized J integral for large deformation and fracture analysis of viscoelastic media. *International Journal of Fracture*, 25(3), 195–223.

Schenk, M., Füting, M., & Reichelt, R. (1998). Direct visualization of the dynamic behavior of a water meniscus by scanning electron microscopy. *Journal of Applied Physics*, 84(9), 4880–4884.

Schloss, J. A., Milsted, A., & Goldman, R. D. (1977). Myosin subfragment binding for the localization of actin-like microfilaments in cultured cells. a light and electron microscope study. *The Journal of Cell Biology*, 74(3), 794–815.

Schröder, R., Vrabie, A., & Goebel, H. H. (2007). Primary desminopathies. *Journal of Cellular and Molecular Medicine*, 11(3), 416–426.

Schuelke, M., Wagner, K. R., Stolz, L. E., Hübner, C., Riebel, T., Kömen, W., Braun, T., Tobin, J. F., & Lee, S.-J. (2004). Myostatin mutation associated with gross muscle hypertrophy in a child. *New England Journal of Medicine*, 350(26), 2682–2688.

Schultz, E. (1974). A quantitative study of the satellite cell population in postnatal mouse lumbrical muscle. *The Anatomical Record*, 180(4), 589–595.

Schultz, E., Gibson, M. C., & Champion, T. (1978). Satellite cells are mitotically quiescent in mature mouse muscle: an EM and radioautographic study. *Journal of Experimental Zoology*, 206(3), 451–456.

Semsarian, C., Sutrave, P., Richmond, D. R., & Graham, R. M. (1999). Insulin-like growth factor (IGF-I) induces myotube hypertrophy associated with an increase in anaerobic glycolysis in a clonal skeletal-muscle cell model. *Biochemical Journal*, 339(2), 443–451.

Sept, D. (2007). Microtubule polymerization: one step at a time. *Current Biology*, 17(17), R764–R766.

Sharples, A. P. & Stewart, C. E. (2011). Myoblast models of skeletal muscle hypertrophy and atrophy. *Current Opinion in Clinical Nutrition & Metabolic Care*, 14(3), 230–236.

Shelden, E. A., Weinberg, J. M., Sorenson, D. R., Edwards, C. A., & Pollock, F. M. (2002). Site-specific alteration of actin assembly visualized in living renal epithelial cells during ATP depletion. *Journal of the American Society of Nephrology*, 13(11), 2667–2680.

Shi, H., Verma, M., Zhang, L., Dong, C., Flavell, R. A., & Bennett, A. M. (2013). Improved regenerative myogenesis and muscular dystrophy in mice lacking Mkp5. *The Journal of Clinical Investigation*, 123(5), 2064–2077.

Shibeshi, S. & Collins, W. (2005). The rheology of blood flow in a branched arterial system. *Applied Rheology*, 15(6), 398.

Shilton, B. H. (2015). Active transporters as enzymes: an energetic framework applied to major facilitator superfamily and ABC importer systems. *Biochemical Journal*, 467(2), 193–199.

Shimizu, S., Yanagimoto, T., & Sakai, M. (1999). Pyramidal indentation load–depth curve of viscoelastic materials. *Journal of Materials Research*, 14(10), 4075–4086.

Shin, Y. C., Lee, J. H., Jin, L., Kim, M. J., Kim, Y.-J., Hyun, J. K., Jung, T.-G., Hong, S. W., & Han, D.-W. (2015). Stimulated myoblast differentiation on graphene oxide-impregnated PLGA-collagen hybrid fibre matrices. *Journal of Nanobiotechnology*, 13(21), 1–11.

Shinin, V., Gayraud-Morel, B., Gomès, D., & Tajbakhsh, S. (2006). Asymmetric division and cosegregation of template DNA strands in adult muscle satellite cells. *Nature Cell Biology*, 8(7), 677–682.

Shiozaki, K., Harasaki, Y., Fukuda, M., Yoshinaga, A., Ryuzono, S., Chigwechokha, P. K., Komatsu, M., & Miyagi, T. (2016). Positive regulation of myoblast differentiation by medaka neu3b sialidase through gangliosides desialylation. *Biochimie*, 123, 65–72.

Shiozu, H., Higashijima, M., & Koga, T. (2015). Association of sarcopenia with swallowing problems, related to nutrition and activities of daily living of elderly individuals. *Journal of Physical Therapy Science*, 27(2), 393–396.

Shutova, M., Yang, C., Vasiliev, J. M., & Svitkina, T. (2012). Functions of non muscle myosin in assembly of the cellular contractile system. *PLoS One*, 7(7), e40814.

Sieck, D. C., Zhan, W.-Z., Fang, Y.-H., Ermilov, L. G., Sieck, G. C., & Mantilla, C. B. (2012). Structure–activity relationships in rodent diaphragm muscle fibers vs. neuromuscular junctions. *Respiratory Physiology & Neurobiology*, 180(1), 88–96.

Sim, E., Haider, H., Aziz, S., Ooi, O., & Law, P. K. (2004). Myoblast transplantation on the beating heart. *International Surgery*, 90(3), 148–150.

Simon, A., Cohen-Bouhacina, T., Porte, M., Aime, J., Amedee, J., Bareille, R., & Baquey, C. (2003). Characterization of dynamic cellular adhesion of osteoblasts using atomic force microscopy. *Cytometry Part A*, 54(1), 36–47.

Sirghi, L., Ponti, J., Broggi, F., & Rossi, F. (2008). Probing elasticity and adhesion of live cells by atomic force microscopy indentation. *European Biophysics Journal*, 37(6), 935–945.

Skuk, D. (2004). Myoblast transplantation for inherited myopathies: a clinical approach. *Expert Opinion on Biological Therapy*, 4(12), 1871–1885.

Skuk, D., Paradis, M., Goulet, M., Chapdelaine, P., Rothstein, D. M., & Tremblay, J. P. (2010). Intramuscular transplantation of human postnatal myoblasts generates functional donor-derived satellite cells. *Molecular Therapy*, 18(9), 1689–1697.

Small, J. & Sobieszek, A. (1977). Studies on the function and composition of the 10-NM (100-A) filaments of vertebrate smooth muscle. *Journal of Cell Science*, 23(1), 243–268.

Smith, D., Ziebert, F., Humphrey, D., Duggan, C., Steinbeck, M., Zimmermann, W., & Käs, J. (2007). Molecular motor-induced instabilities and cross linkers determine biopolymer organization. *Biophysical Journal*, 93(12), 4445–4452.

Sneddon, I. (1965). The relation between load and penetration in the axisymmetric boussinesq problem for a punch of arbitrary profile. *International Journal of Engineering Science*, 3(1), 47–57.

Söderpalm, A.-C., Magnusson, P., Åhlander, A.-C., Karlsson, J., Kroksmark, A.-K., Tulinius, M., & Swolin-Eide, D. (2007). Low bone mineral density and decreased bone turnover in Duchenne muscular dystrophy. *Neuromuscular Disorders*, 17(11), 919–928.

Sokolov, I., Dokukin, M., & Guz, N. (2013). Method for quantitative measurements of the elastic modulus of biological cells in AFM indentation experiments. *Methods*, 60(2), 202–213.

Song, T.-J., Lee, K.-A., Kang, S.-W., Cho, H., & Choi, Y.-C. (2011). Three cases of manifesting female carriers in patients with Duchenne muscular dystrophy. *Yonsei Medical Journal*, 52(1), 192–195.

Sparrow, J. C. & Schöck, F. (2009). The initial steps of myofibril assembly: integrins pave the way. *Nature Reviews Molecular Cell Biology*, 10(4), 293–298.

Spedden, E. & Staii, C. (2013). Neuron biomechanics probed by atomic force microscopy. *International Journal of Molecular Sciences*, 14(8), 16124–16140.

Squire, S., Raymackers, J.-M., Vandebrouck, C., Potter, A., Tinsley, J., Fisher, R., Gillis, J.-M., & Davies, K. (2002). Prevention of pathology in *mdx* mice by expression of utrophin: analysis using an inducible transgenic expression system. *Human Molecular Genetics*, 11(26), 3333–3344.

Sroka, J., Krecioch, I., Zimolag, E., Lasota, S., Rak, M., Kedracka-Krok, S., Borowicz, P., Gajek, M., & Madeja, Z. (2016). Lamellipodia and membrane blebs drive efficient electrotactic migration of rat walker carcinosarcoma cells WC 256. *PloS One*, 11(2), e0149133.

Stark, R., Drobek, T., & Heckl, W. (2001). Thermomechanical noise of a free v-shaped cantilever for atomic-force microscopy. *Ultramicroscopy*, 86(1), 207–215.

Starr, D. & Han, M. (2002). Role of ANC-1 in tethering nuclei to the actin cytoskeleton. *Science*, 298(5592), 406–409.

Starr, D. A. & Han, M. (2003). Anchors away: an actin based mechanism of nuclear positioning. *Journal of Cell Science*, 116, 211–216.

Stenholm, S., Alley, D., Bandinelli, S., Griswold, M., Koskinen, S., Rantanen, T., Guralnik, J., & Ferrucci, L. (2009). The effect of obesity combined with low muscle strength on decline in mobility in older persons: results from the InCHIANTI Study. *International Journal of Obesity*, 33(6), 635–644.

Stewart, M. P., Helenius, J., Toyoda, Y., Ramanathan, S. P., Muller, D. J., & Hyman, A. A. (2011). Hydrostatic pressure and the actomyosin cortex drive mitotic cell rounding. *Nature*, 469(7329), 226–230.

Stoker, M., O'Neill, C., Berryman, S., & Waxman, V. (1968). Anchorage and growth regulation in normal and virus-transformed cells. *International Journal of Cancer*, 3(5), 683–693.

Straight, A. F., Cheung, A., Limouze, J., Chen, I., Westwood, N. J., Sellers, J. R., & Mitchison, T. J. (2003). Dissecting temporal and spatial control of cytokinesis with a myosin II inhibitor. *Science*, 299(5613), 1743–1747.

Straub, V. & Campbell, K. P. (1997). Muscular dystrophies and the dystrophin-glycoprotein complex. *Current Opinion in Neurology*, 10(2), 168–175.

Straube, A. & Merdes, A. (2007). EB3 regulates microtubule dynamics at the cell cortex and is required for myoblast elongation and fusion. *Current Biology*, 17(15), 1318–1325.

Streppa, L., Berguiga, L., Provera, E. B., Ratti, F., Goillot, E., Torres, C. M., Schaeffer, L., Elezgaray, J., Arneodo, A., & Argoul, F. (2016). Tracking in real time the crawling dynamics of adherent living cells with a high resolution surface plasmon microscope. In *SPIE BIOS International Society for Optics and Photonics* (pp. 97240G–97240G).

Sudhof, T. C. (2004). The synaptic vesicle cycle. *Annual Review of Neuroscience*, 27, 509.

Sun, S., Wong, S., Mak, A., & Cho, M. (2014). Impact of oxidative stress on cellular biomechanics and Rho signaling in C2C12 myoblasts. *Journal of Biomechanics*, 47(15), 3650–3656.

Sutton, T. A. & Molitoris, B. A. (1998). Mechanisms of cellular injury in ischemic acute renal failure. *Seminars in Nephrology*, 18(5), 490–497.

Suzuki, K. & Takahashi, K. (2003). Reduced cell adhesion during mitosis by threonine phosphorylation of β1 integrin. *Journal of Cellular Physiology*, 197(2), 297–305.

Swailes, N. T., Colegrave, M., Knight, P. J., & Peckham, M. (2006). Non-muscle myosins 2A and 2B drive changes in cell morphology that occur as myoblasts align and fuse. *Journal of Cell Science*, 119(17), 3561–3570.

Swaney, K. F., Huang, C.-H., & Devreotes, P. N. (2010). Eukaryotic chemotaxis: a network of signaling pathways controls motility, directional sensing, and polarity. *Annual Review of Biophysics*, 39, 265.

Szustakowski, J. D., Lee, J.-H., Marrese, C. A., Kosinski, P. A., Nirmala, N., & Kemp, D. M. (2006). Identification of novel pathway regulation during myogenic differentiation. *Genomics*, 87(1), 129–138.

Tabebordbar, M., Wang, E. T., & Wagers, A. J. (2013). Skeletal muscle degenerative diseases and strategies for therapeutic muscle repair. *Annual Review of Pathology: Mechanisms of Disease*, 8, 441–475.

Takemoto, K., Mizutani, T., Tamura, K., Takeda, K., Haga, H., Kawabata, K., (2012). The number of cyclic stretch regulates cellular elasticity in C2C12 myoblasts. *Open Journal of Cell Biology*, 1(1), 1–10.

Takemura, Y., Sasaki, M., Goto, K., Takaoka, A., Ohi, A., Kurihara, M., Nakanishi, N., Nakano, Y., & Hanaoka, J. (2016). Energy metabolism and nutritional status in hospitalized patients with lung cancer. *Journal of Clinical Biochemistry and Nutrition*, 59(2), 122–129.

Tan, J., Kalapesi, F., & Coroneo, M. (2006). Mechanosensitivity and the eye: cells coping with the pressure. *British Journal of Ophthalmology*, 90(3), 383–388.

Tassin, A.-M., Maro, B., & Bornens, M. (1985). Fate of microtubule-organizing centers during myogenesis in vitro. *The Journal of Cell Biology*, 100(1), 35–46.

Tayeb, M. T. (2010). Deletion mutations in Duchenne muscular dystrophy (DMD) in western Saudi children. *Saudi Journal of Biological Sciences*, 17(3), 237–240.

Teixeira, A., McKie, G., Foley, J., Bertics, P., Nealey, P., & Murphy, C. (2006). The effect of environmental factors on the response of human corneal epithelial cells to nanoscale substrate topography. *Biomaterials*, 27(21), 3945–3954.

Terracciano, C., Celi, M., Lecce, D., Baldi, J., Rastelli, E., Lena, E., Massa, R., & Tarantino, U. (2013). Differential features of muscle fiber atrophy in osteoporosis and osteoarthritis. *Osteoporosis International*, 24(3), 1095–1100.

Theander, S., Lew, D., & Nüße, O. (2002). Granule-specific ATP requirements for Ca^{2+}-induced exocytosis in human neutrophils. evidence for substantial ATP-independent release. *Journal of Cell Science*, 115(14), 2975–2983.

Théry, M. & Bornens, M. (2006). Cell shape and cell division. *Current Opinion in Cell Biology*, 18(6), 648–657.

Thomas, M., Langley, B., Berry, C., Sharma, M., Kirk, S., Bass, J., & Kambadur, R. (2000). Myostatin, a negative regulator of muscle growth, functions by inhibiting myoblast proliferation. *Journal of Biological Chemistry*, 275(51), 40235–40243.

Thoumine, O. & Ott, A. (1997). Time scale dependent viscoelastic and contractile regimes in fibroblasts probed by microplate manipulation. *Journal of Cell Science*, 110(17), 2109–2116.

Tinsley, J. M., Fairclough, R. J., Storer, R., Wilkes, F. J., Potter, A. C., Squire, S. E., Powell, D. S., Cozzoli, A., Capogrosso, R. F., Lambert, A., Wilson, F. X., Wren, S. P., De Luca, A., & Davies, K. E. (2011). Daily treatment with SMTC1100, a novel small molecule utrophin upregulator, dramatically reduces the dystrophic symptoms in the *mdx* mouse. *PloS One*, 6(5), e19189.

Titushkin, I. & Cho, M. (2007). Modulation of cellular mechanics during osteogenic differentiation of human mesenchymal stem cells. *Biophysical Journal*, 93(10), 3693–3702.

Tojkander, S., Gateva, G., & Lappalainen, P. (2012). Actin stress fibers - assembly, dynamics and biological roles. *Journal of Cell Science*, 125, 1855–1864.

Tolstonog, G. V., Sabasch, M., & Traub, P. (2002). Cytoplasmic intermediate filaments are stably associated with nuclear matrices and potentially modulate their DNA-binding function. *DNA and Cell Biology*, 21(3), 213–239.

Tomaiuolo, G. (2014). Biomechanical properties of red blood cells in health and disease towards microfluidics. *Biomicrofluidics*, 8(5), 051501.

Tonon, E., Ferretti, R., Shiratori, J. H., Santo Neto, H., Marques, M. J., & Minatel, E. (2012). Ascorbic acid protects the diaphragm muscle against myonecrosis in *mdx* mice. *Nutrition*, 28(6), 686–690.

Törnroth-Horsefield, S. & Neutze, R. (2008). Opening and closing the metabolite gate. *Proceedings of the National Academy of Sciences USA*, 105(50), 19565–19566.

Tremblay, J. & Guerette, B. (1997). Myoblast transplantation: a brief review of the problems and of some solutions. *BAM-PADOVA*, 7, 221–220.

Tremblay, J. P., Skuk, D., Palmieri, B., & Rothstein, D. M. (2009). A case for immunosuppression for myoblast transplantation in Duchenne muscular dystrophy. *Molecular Therapy*, 17(7), 1122.

Trensz, F., Lucien, F., Couture, V., Söllrald, T., Drouin, G., Rouleau, A.-J., Grandbois, M., Lacraz, G., & Grenier, G. (2015). Increased microenvironment stiffness in damaged myofibers promotes myogenic progenitor cell proliferation. *Skeletal Muscle*, 5(5), 1–16.

Tripathy, S. & Berger, E. (2009). Measuring viscoelasticity of soft samples using atomic force microscopy. *Journal of Biomechanical Engineering*, 131(9), 094507.

Tschumperlin, D. J. (2013). Fibroblasts and the ground they walk on. *Physiology*, 28(6), 380–390.

Tsukamoto, T. & Nigam, S. K. (1997). Tight junction proteins form large complexes and associate with the cytoskeleton in an ATP depletion model for reversible junction assembly. *Journal of Biological Chemistry*, 272(26), 16133–16139.

Vahabi, S. (2013). Atomic force microscopy application in biological research : a review study. *International Journal of Molecular Sciences*, 38(2), 76–83.

Van Citters, K. M., Hoffman, B. D., Massiera, G., & Crocker, J. C. (2006). The role of F-actin and myosin in epithelial cell rheology. *Biophysical Journal*, 91(10), 3946–3956.

Van Der Ven, P. F., Ehler, E., Perriard, J.-C., & Fürst, D. O. (1999). Thick filament assembly occurs after the formation of a cytoskeletal scaffold. *Journal of Muscle Research & Cell Motility*, 20(5-6), 569–579.

Van Zwieten, R. W., Puttini, S., Lekka, M., Witz, G., Gicquel-Zouida, E., Richard, I., Lobrinus, J. A., Chevalley, F., Brune, H., Dietler, G., Kulik, A., Kuntzer, T., & Mermod, N. (2014). Assessing dystrophies and other muscle diseases at the nanometer scale by atomic force microscopy. *Nanomedicine*, 9(4), 393–406.

Vargas-Pinto, R., Gong, H., Vahabikashi, A., & Johnson, M. (2013). The effect of the endothelial cell cortex on atomic force microscopy measurements. *Biophysical Journal*, 105(2), 300–309.

Vetrone, S. A., Montecino-Rodriguez, E., Kudryashova, E., Kramerova, I., Hoffman, E. P., Liu, S. D., Miceli, M. C., & Spencer, M. J. (2009). Osteopontin promotes fibrosis in dystrophic mouse muscle by modulating immune cell subsets and intramuscular TGF-β. *The Journal of Clinical Investigation*, 119(6), 1583–1594.

Vicente-Manzanares, M., Ma, X., Adelstein, R. S., & Horwitz, A. R. (2009). Non-muscle myosin II takes centre stage in cell adhesion and migration. *Nature Reviews Molecular Cell Biology*, 10(11), 778–790.

Vincent, J. (2012). *Structural Biomaterials*. Princeton and Oxford: Princeton University Press.

Vinogradova, O. I., Butt, H. J., Yakubov, G. E., & Feuillebois, F. (2001). Dynamic effects on force measurements. I. Viscous drag on the atomic force microscope cantilever. *Review of Scientific Instruments*, 72(5), 2330–2339.

Wallace, G. Q. & McNally, E. M. (2009). Mechanisms of muscle degeneration, regeneration, and repair in the muscular dystrophies. *Annual Review of Physiology*, 71, 37–57.

Wang, D., Zheng, W., Xie, Y., Gong, P., Zhao, F., Yuan, B., Ma, W., Cui, Y., Liu, W., Sun, Y., (2014). Tissue-specific mechanical and geometrical control of cell viability and actin cytoskeleton alignment. *Scientific Reports*, 4(6160), 1–6.

Wang, H.-B., Dembo, M., & Wang, Y.-L. (2000). Substrate flexibility regulates growth and apoptosis of normal but not transformed cells. *American Journal of Physiology-Cell Physiology*, 279(5), C1345–C1350.

Watchko, J., O'Day, T., Wang, B., Zhou, L., Tang, Y., Li, J., & Xiao, X. (2002). Adeno-associated virus vector-mediated minidystrophin gene therapy improves dystrophic muscle contractile function in *mdx* mice. *Human Gene Therapy*, 13(12), 1451–1460.

Watkins, S. C., Hoffman, E. P., Slayter, H. S., & Kunkel, L. M. (1988). Immuno-electron microscopic localization of dystrophin in myofibres. *Nature*, 333(6176), 863–866.

Watt, D. J., Jennifer, E., & Partridge, T. A. (1984). Use of mononuclear precursor cells to insert allogeneic genes into growing mouse muscles. *Muscle & Nerve*, 7(9), 741–750.

Weed, R. I., LaCelle, P. L., & Merrill, E. W. (1969). Metabolic dependence of red cell deformability. *Journal of Clinical Investigation*, 48(5), 795.

Wegner, A. & Engel, J. (1975). Kinetics of the cooperative association of actin to actin filament. *Biophysical Chemistry*, 3(3), 215–225.

Weisenhorn, A., Maivald, P., Butt, H.-J., & Hansma, P. (1992). Measuring adhesion, attraction, and repulsion between surfaces in liquids with an atomic-force microscope. *Physical Review B*, 45(19), 11226.

Whipple, R. A., Matrone, M. A., Cho, E. H., Balzer, E. M., Vitolo, M. I., Yoon, J. R., Ioffe, O. B., Tuttle, K. C., Yang, J., & Martin, S. S. (2010). Epithelial-to-mesenchymal transition promotes tubulin detyrosination and microtentacles that enhance endothelial engagement. *Cancer Research*, 70(20), 8127–8137.

Whitehead, N. P., Pham, C., Gervasio, O. L., & Allen, D. G. (2008). N-Acetylcysteine ameliorates skeletal muscle pathophysiology in *mdx* mice. *The Journal of Physiology*, 586(7), 2003–2014.

Wickstead, B. & Gull, K. (2011). The evolution of the cytoskeleton. *The Journal of Cell Biology*, 194(4), 513–525.

Wilkinson, P. (1996). Cell locomotion and chemotaxis: basic concepts and methodological approaches. *Methods*, 10(1), 74–81.

Willmann, R., Possekel, S., Dubach-Powell, J., Meier, T., & Ruegg, M. A. (2009). Mammalian animal models for Duchenne muscular dystrophy. *Neuromuscular Disorders*, 19(4), 241–249.

Wolff, A. V., Niday, A. K., Voelker, K. A., Call, J. A., Evans, N. P., Granata, K. P., & Grange, R. W. (2006). Passive mechanical properties of maturing extensor digitorum longus are not affected by lack of dystrophin. *Muscle & Nerve*, 34(3), 304–312.

Wood, S. J. & Slater, C. R. (2001). Safety factor at the neuromuscular junction. *Progress in Neurobiology*, 64(4), 393–429.

Xue, B. & Robinson, R. C. (2013). Guardians of the actin monomer. *European Journal of Cell Biology*, 92(10), 316–332.

Yaffe, D. (1969). Cellular aspects of muscle differentiation in vitro. *Current Topics in Developmental Biology*, 4, 37–77.

Yaffe, D. & Saxel, O. (1977). Serial passaging and differentiation of myogenic cells isolated from dystrophic mouse muscle. *Nature*, 270(5639), 725–727.

Yamaguchi, H. & Condeelis, J. (2007). Regulation of the actin cytoskeleton in cancer cell migration and invasion. *Biochimica et Biophysica Acta (BBA)-Molecular Cell Research*, 1773(5), 642–652.

Yamakita, Y., Totsukawa, G., Yamashiro, S., Fry, D., Zhang, X., Hanks, S. K., & Matsumura, F. (1999). Dissociation of FAK/p130CAS/c-Src complex during mitosis: role of mitosis-specific serine phosphorylation of FAK. *The Journal of Cell Biology*, 144(2), 315–324.

Yamane, Y., Shiga, H., Haga, H., Kawabata, K., Abe, K., & Ito, E. (2000). Quantitative analyses of topography and elasticity of living and fixed astrocytes. *Journal of Electron Microscopy*, 49(3), 463–471.

Yanagisawa, A., Bouchet, C., Quijano-Roy, S., Vuillaumier-Barrot, S., Clarke, N., Odent, S., Rodriguez, D., Romero, N. B., Osawa, M., Endo, T., Lia, T. A., Seta, N., & Guicheney, P. (2009). POMT2 intragenic deletions and splicing abnormalities causing congenital muscular dystrophy with mental retardation. *European Journal of Medical Genetics*, 52(4), 201–206.

Yanniotis, S., Skaltsi, S., & Karaburnioti, S. (2006). Effect of moisture content on the viscosity of honey at different temperatures. *Journal of Food Engineering*, 72(4), 372–377.

Yeung, T., Georges, P. C., Flanagan, L. A., Marg, B., Ortiz, M., Funaki, M., Zahir, N., Ming, W., Weaver, V., & Janmey, P. A. (2005). Effects of substrate stiffness on cell morphology, cytoskeletal structure, and adhesion. *Cell Motility and The Cytoskeleton*, 60(1), 24–34.

Yin, H., Price, F., & Rudnicki, M. A. (2013). Satellite cells and the muscle stem cell niche. *Physiological Reviews*, 93(1), 23–67.

Yokokawa, M., Takeyasu, K., & Yoshimura, S. (2008). Mechanical properties of plasma membrane and nuclear envelope measured by scanning probe microscope. *Journal of Microscopy*, 232(1), 82–90.

Yoshida, N., Yoshida, S., Koishi, K., Masuda, K., & Nabeshima, Y.-I. (1998). Cell heterogeneity upon myogenic differentiation: down-regulation of MyoD and Myf-5 generates 'reserve cells'. *Journal of Cell Science*, 111(6), 769–779.

Yoshikawa, Y., Yasuike, T., Yagi, A., & Yamada, T. (1999). Transverse elasticity of myofibrils of rabbit skeletal muscle studied by atomic force microscopy. *Biochemical and Biophysical Research Communications*, 256(1), 13–19.

Young, J. D. (2013). Metabolic flux rewiring in mammalian cell cultures. *Current Opinion in Biotechnology*, 24(6), 1108–1115.

Yu, H. W., Chen, Y.-Q., Huang, C.-M., Liu, C.-Y., Chiou, A., Wang, Y.-K., Tang, M.-J., & Kuo, J.-C. (2015). β-PIX controls intracellular viscoelasticity to regulate lung cancer cell migration. *Journal of Cellular and Molecular Medicine*, 19(5), 934–947.

Yu, L., Chen, X., Wang, L., & Chen, S. (2016). The sweet trap in tumors: aerobic glycolysis and potential targets for therapy. *Oncotarget*, 7(25), 38908–38926.

Yu, Y., Liu, B., Mersmann, H., & Ding, S. (2006). Porcine peroxisome proliferator-activated receptor γ induces transdifferentiation of myocytes into adipocytes. *Journal of Animal Science*, 84(10), 2655–2665.

Zaman, M. H., Trapani, L. M., Sieminski, A. L., MacKellar, D., Gong, H., Kamm, R. D., Wells, A., Lauffenburger, D. A., & Matsudaira, P. (2006). Migration of tumor cells in 3D matrices is governed by matrix stiffness along with cell-matrix adhesion and proteolysis. *Proceedings of the National Academy of Sciences USA*, 103(29), 10889–10894.

Zanou, N. & Gailly, P. (2013). Skeletal muscle hypertrophy and regeneration: interplay between the myogenic regulatory factors (MRFs) and insulin-like growth factors (IGFs) pathways. *Cellular and Molecular Life Sciences*, 70(21), 4117–4130.

Zatsiorsky, V. & Prilutsky, B. (2012). *Biomechanics of Skeletal Muscles*. Human Kinetics, Pudsey, UK.

Zhang, B., Luo, Q., Mao, X., Xu, B., Yang, L., Ju, Y., & Song, G. (2014). A synthetic mechano-growth factor E peptide promotes rat tenocyte migration by lessening cell stiffness and increasing F-actin formation via the FAK-ERK1/2 signaling pathway. *Experimental Cell Research*, 322(1), 208–216.

Zhang, J., Kraus, W., & Truskey, G. (2004). Stretch-induced nitric oxide modulates mechanical properties of skeletal muscle cells. *American Journal of Physiology-Cell Physiology*, 287(2), C292–C299.

Zhang, S., Berguiga, L., Elezgaray, J., Roland, T., Faivre-Moskalenko, C., & Argoul, F. (2007). Surface plasmon resonance characterization of thermally evaporated thin gold films. *Surface Science*, 601(23), 5445–5458.

Zheng, Y., Wen, J., Nguyen, J., Cachia, M. A., Wang, C., & Sun, Y. (2015). Decreased deformability of lymphocytes in chronic lymphocytic leukemia. *Scientific Reports*, 5, 7613.

Zigmond, S. (1989). Cell locomotion and chemotaxis. *Current Opinion in Cell Biology*, 1(1), 80–86.

Zou, C., Luo, Q., Qin, J., Shi, Y., Yang, L., Ju, B., & Song, G. (2013). Osteopontin promotes mesenchymal stem cell migration and lessens cell stiffness via integrin β1, FAK, and ERK pathways. *Cell Biochemistry and Biophysics*, 65(3), 455–462.